The Role of Rift Obliquity in Formation of the Gulf of California

By

Scott Edmund Kelsey Bennett
B.S. (California State University, Northridge) 2004
M.S. (University of North Carolina, Chapel Hill) 2009

DISSERTATION

Submitted in partial satisfaction of the requirements for the degree of

DOCTOR OF PHILOSOPHY

in

Geology

in the

OFFICE OF GRADUATE STUDIES

of the

UNIVERSITY OF CALIFORNIA

DAVIS

Approved:

_____
Michael E. Oskin, Chair

_____
Sarah M. Roeske

_____
Magali I. Billen

Committee in Charge

2013

ACKNOWLEDGMENTS

I must express my tremendous gratitude to my advisor, Mike Oskin, for several years of continuous support, mentoring, and friendship. Mike is a spectacular teacher and I owe much of my growth over these past years to his savvy and insightful advising. My dissertation research in the Gulf of California relied heavily upon the previous research that Mike conducted during his own PhD research. I had to learn to suppress shock and gracefully accept when several months of my detailed field mapping turned out to verify Mike's reconnaissance interpretations from remote-sensing or a one-day island transect hike a decade ago.

Many other scientific collaborators and colleagues were vital to my accomplishments over the past four years here at UC Davis. I truly enjoyed exploring the Sonoran desert with Becky Dorsey and Mike Darin, my collaborators from the University of Oregon. Their passion for Gulf of California geology is second to none. Some of the big-picture revelations of my dissertation research emerged thanks to the collaborative Gulf of California-Salton Trough (GCAST) paleo-tectonic reconstruction project with Mike Oskin, Becky Dorsey, Mike Darin, as well as Paul Umhoefer and Lisa Skinner, collaborators at Northern Arizona University. My research findings would not have been possible without the high-quality geochronologic results obtained by Alexander Iriondo, my collaborator from Universidad Nacional Autónoma de México, Juriquilla.

Conversations with several other colleagues were key to my development as a geologist during my time at UC Davis, including Sarah Roeske and Magali Billen, my dissertation committee, and also Eric Cowgill, Jeff Unruh, and Jeff Mount. Many thanks to Joe Kirschvink and others at the CalTech Paleomagnetics Laboratory, including Tim Raub, Steve Skinner, and Sarah Slotznick, for their assistance while working in their laboratory. I was fortunate enough to

participate in the MARGINS program (National Science Foundation) community of scientists during its 10-year focused research campaign in the Gulf of California. It was an amazing time to be a geologist working in the Gulf. I benefited greatly from my interactions with numerous MARGINS scientists, including Joann Stock, Arturo Martín-Barajas, John Fletcher, Danny Brothers, Jared Kluesner, Nathaniel Miller, Donna Shillington, Cindy Ebinger, Kathy Marsaglia, Chris Henry, Graham Kent, Julia Morgan, Ramon, Arrowsmith, Maggie Benoit, Lori Summa, and many others.

The completion of my field research in northwestern Mexico would not have been possible without numerous kind and helpful folks. Foremost, I must thank the Molina Villa-Lobos family (Ernesto, Francisco, and Esequel) of the of the native Cumcaác (Seri) tribe for their superb boatmanship and safekeeping during my field research on Isla Tiburón. I am very thankful to the Cumcaác tribe for granting permission and access to conduct my research on their beautiful, native land. Months of isolated field mapping on Isla Tiburón and reconnaissance tuff hunting in remote north-central Baja California would have been impossible without the underpaid, but highly-appreciated, support from several field assistants, including (2009) Jordan Ford (2010) Dan Hadley, Eric Stevens, Anne Gauer, Monica Iglecia (my then fiancé), and (2011) Michael Tappa. Many of the critical details I report regarding the Southwest Isla Tiburón marine basin are, in part, thanks to the concurrent undergraduate theses conducted by Nick Buckmaster (UC Davis) and Molly Keogh (U of Oregon). Irreplaceable logistical support was provided by the Prescott College-Kino Bay Center for Cultural and Ecological Studies, a spectacular desert research station in Bahía Kino, Mexico. I am ever so grateful to the boat support and friendly accommodations provided by the Prescott College staff, Ed Boyer, Lorayne Meltzer, Tad Pfister, Tom Donovan, Cosme Becerra, Gregory Smart, and many others. I was fortunate to overlap with

several friendly research scientist and students at the Prescott research station, including, Abram Fleishman, Naomi Blinick, Marlu Robledo, Andrea Galindo, Héctor Pérez, Emily Weyl, Danny Linder, and many others who ventured into the desert and across the ocean with me. I would also like to thank UC Davis Fleet Services for providing hearty vehicles and fulfilling several odd requests during my extended travel into Mexico.

There are also many people to thank for their generous support at home in California. Firstly, I thank my parents, Susan and Edmund, for their never-ending support. I have my mother to thank for convincing me to partake on this journey called college and my father for teaching me to be inquisitive about our natural world. I also thank the faculty and staff of the UC Davis Geology Department for their continuous support. I appreciate the efforts of my teammates on the award-winning UC Davis Geothermal Team, Maya Wildgoose, Andrew Fowler, Carolyn Cantwell, Leslie Barnes, and the guidance of professors Peter Schiffman, Robert Zierenberg, Bill Glassley, and Jim McClain. Support from fellow graduate students came in many flavors, from our 'weekly' Georide cycling trips, to our Write-Or-Die writing groups, and co-TAing numerous and memorable undergraduate geology field trips across California and Nevada. Much thanks goes out to Austin Elliott, Adam Forte, Cara Harwood, Mark Stelten, Gary Eppich, Nicole Longinotti, Jacob Selander, Maya Wildgoose, Leslie Moclock, Chris Bowles, Tracy Compton, Sarah Gaudio, Peter Gold, and many, many others. Lastly, I owe tremendous gratitude to my wife, Monica Iglecia. Her endless love and support, both in the field and at home, has been fundamental to my achievements throughout graduate school. Amongst the many things I have to be grateful for, having Monica as a partner, friend, and sweetheart is at the top.

ABSTRACT

The Gulf of California illustrates how highly oblique rift geometries, where transform faults are kinematically linked to large-offset normal faults in adjacent pull-apart basins, enhance the ability of continental lithosphere to rupture and, ultimately, hasten the formation of new oceanic basins. The Gulf of California rift has accommodated oblique divergence of the Pacific and North America tectonic plates in northwestern Mexico since Miocene time. Due to its infancy, the rifted margins of the Gulf of California preserve a rare onshore record of early continental break-up processes from which to investigate the role of rift obliquity in strain localization. Using new high-precision paleomagnetic vectors from tectonically stable sites in north-central Baja California, I compile a paleomagnetic transect of Miocene ignimbrites across northern Baja California and Sonora that reveals the timing and distribution of dextral shear associated with inception of this oblique rift. I integrate detailed geologic mapping, basin analysis, and geochronology of pre-rift and syn-rift volcanic units to determine the timing of fault activity on Isla Tiburón, a proximal onshore exposure of the rifted North America margin, adjacent to the axis of the Gulf of California. The onset of strike-slip faulting on Isla Tiburón, ca. 8 - 7 Ma, was synchronous with the onset of transform faulting along a significant length of the nascent plate boundary within the rift. This tectonic transition coincides with a clockwise azimuthal shift in Pacific-North America relative motion that increased rift obliquity. I constrain the earliest marine conditions on southwest Isla Tiburón to ca. 6.4 - 6.0 Ma, coincident with a regional latest Miocene marine incursion in the northern proto-Gulf of California. This event likely flooded a narrow, incipient topographic depression along a ~650 km-long portion of the latest Miocene plate boundary and corresponds in time and space with formation of a newly-constrained ~50-100 kilometer-wide transtensional belt of focused strike-slip faulting, basin

formation, and rotating crustal blocks. This proto-Gulf of California shear zone, embedded within the wider Mexican Basin and Range extensional province and connected to the San Andreas fault in southern California, hosted subsequent localization of the plate boundary and rupture of the continental lithosphere.

TABLE OF CONTENTS

ACKNOWLEDGMENTS ii

ABSTRACT v

1 Paleomagnetic evidence of oblique rift localization in the Gulf of California 1

1.1 ABSTRACT 2

1.2 INTRODUCTION 2

1.3 PALEOMAGNETISM OF REGIONAL IGNIMBRITES 5

1.4 PALEOMAGNETIC METHODS 7

1.5 PALEOMAGNETIC TRANSECT ACROSS THE GULF OF CALIFORNIA 20

1.6 DISCUSSION AND CONCLUSIONS 22

2 Stratigraphy and structural development of the late Miocene to Pliocene Southwest Isla Tiburón marine basin, and implications for the formation of the Gulf of California 28

2.1 ABSTRACT 29

2.2 INTRODUCTION 30

2.3 PREVIOUS WORK AND CONTROVERSIAL RESULTS 33

2.4 METHODS 37

2.4a Geologic, Structural, and Stratigraphic Mapping 37

2.4b Geochronology 40

2.5 STRATIGRAPHY AND GEOCHRONOLOGY 41

2.5a Basement Rocks 41

2.5b Arc-Related Volcanic Rocks 41

2.5c Pre-Basin, Syn-Rift Volcanic Rocks 43

2.5c1 Tuff of Hast Pitzcal (Tthp) 46

2.5c2 Tuff of Ensenada Blanca (Tteb) 46

2.5c3 Tuffs of Arroyo El Canelo (Ttec) 49

2.5d Southwest Isla Tiburón (SWIT) Marine Basin 50

2.5d1 Unnamed Air-Fall Tuffs (Ttua) 50

2.5d2 Marine Sandstone (Tsm) 50

2.5d3 Landslide Breccia (Tbx) 51

2.5d4 Sedimentary Breccia (Tbxs) 51

2.5d5 Lower Marine Conglomerate and Sandstone (Tcml) 53

2.5d6 Shelly Calcarenitic Sandstone (Tcsh) 53

2.5d7 Tuff of Arroyo Sauzal (Ttas) 57

2.5d8 Tuff of Oyster Amphitheater (Ttoa) 58

2.5d9 Marine Tuffaceous Sandstone (Tsmt) 58

2.5d10 Middle Marine Conglomerate and Sandstone (Tcmm) 59

2.5d11 Upper Marine Conglomerate and Sandstone (Tcmu) 60

2.5d12 Non-marine Conglomerate and Sandstone (Tcnm) 63

2.5e Capping Rhyodacite of Cerro Starship (*Tcsf*) and Related Volcanic Units (*Tcsp*, *Tcsd*) 66

2.5f Quaternary Sediments and Volcanic Rocks 71

2.6 FAULTING AND FOLDING 72

2.7 DISCUSSION 74

2.7a Timing of Marine Deposition on Isla Tiburón 74

2.7a1 Age of the Base of Marine Strata 75

2.7a2 Age and Emplacement of the Rhyodacite of Cerro Starship 79

2.7a3 Reinterpretation of Late Miocene Igneous Units 81

2.7a4 Tectonic-Sedimentary Setting and Thickness of Marine Strata on Southwest Isla Tiburón 83

2.7b Implications for Gulf of California Marine Incursion 87

2.7b1 Synchronous Marine Incursion Into the Northern Proto-Gulf of California 87

2.7b2 Speculative Origins of Reworked Middle Miocene Microfossils 94

2.7b3 Tectonic Evolution of Gulf of California 96

2.8 CONCLUSIONS 97

3 Onset of transform faulting in the northern Gulf of California: Implications for oblique rifting and late Miocene localization of the Pacific-North America plate boundary 108

3.1 ABSTRACT 109

3.2 INTRODUCTION 110

3.3 TECTONIC SETTING 115

3.3a Gulf of California 115

3.3b Sonoran Margin 116

3.4 METHODS 120

3.4a Geologic, Structural, and Stratigraphic Mapping 120

3.4b Geochronology 125

3.5 LA CRUZ FAULT STUDY AREA 125

3.5a Stratigraphy and Geochronology 132

3.5a1 Basement Rocks 132

3.5a2 Early to Middle Miocene Volcanic and Sedimentary Rocks 133

3.5a3 Latest(?) Middle Miocene Syn-Rift Rocks 137

3.5a4 Late Miocene to Pliocene(?) La Cruz Basin 139

3.5a5 Quaternary Deposits 143

3.5b Faulting and Folding 143

3.5b1 La Cruz fault 144

3.5b2 Additional Strike-slip Faults 145

3.5b3 Sauzal Fault 146

3.5b4 Colorado Fault 146

3.5b5 Hihitiij Fault 147

3.5b6 Additional Normal Faults and Related Folds 148

3.5b7 Thrust Faults and Related Folds 150

3.6 YAWASSAG FAULT STUDY AREA 151

3.6a Stratigraphy and Geochronology 151

3.6a1 Basement Rocks 151

3.6a2 Middle Miocene Volcanic and Sedimentary Rocks 152

3.6a3 Late Miocene to Pliocene(?) Tecomate Basin 154

3.6a4 Quaternary Deposits 156

3.6b Faulting and Folding 156

3.6b1 Yawassag fault 157

3.6b2 Additional Strike-slip Faults 158

3.6b3 Kunkaak fault 159

3.6b4 Tecomate fault 159

3.6b5 Hinzime fault 160

3.6b6 Additional Normal Faults and Related Folds 160

3.7 DISCUSSION 161

3.7a Timing of Faulting and Basin Formation on Isla Tiburón 161

3.7a1 Middle to Late(?) Miocene Normal Faulting and Basin Formation 161

3.7a2 Late Miocene to Pliocene(?) Strike-slip Faulting and Basin Formation 163

3.7b New Constraints for Total Dextral Offset Along the La Cruz Fault 166

3.7c Synchronous Onset of Transform Faulting in the Gulf of California 170

3.7d Implications for Latest Miocene Rift Localization in Northwestern Mexico 176

3.8 CONCLUSIONS 180

BIBLIOGRAPHY 191

LIST OF TABLES

1.1 Summary of paleomagnetic data and rotation values. 26

2.1 Pre-Quaternary geologic map units of southwest Isla Tiburón. 100

2.2 U-Th-Pb analytical data for volcanic rocks on southwest Isla Tiburón. 104

2.3 $^{40}Ar/^{39}Ar$ total laser fusion data for volcanic rocks on southwest Isla Tiburón. 106

2.4 $^{40}Ar/^{39}Ar$ step-heating data for volcanic rocks on southwest Isla Tiburón. 107

3.1 $^{40}Ar/^{39}Ar$ step-heating data for volcanic rocks on Isla Tiburón. 184

3.2 $^{40}Ar/^{39}Ar$ total laser fusion data for volcanic rocks on Isla Tiburón. 185

3.3 U-Th-Pb analytical data for volcanic rocks on Isla Tiburón. 189

LIST OF FIGURES

1.1 Physiographic map of the northern Gulf of California oblique rift. 4

1.2 Geologic map of new paleomagnetic drill sites, north-central Baja California. 8

1.3 Field photographs of paleomagnetic sampling techniques. 9

1.4 Representative paleomagnetic demagnetization results. 10

1.5 Field panorama of the Tuff of San Felipe at Mesa El Cartabon. 13

1.6 Field panorama showing exposures of regional tuffs. 14

1.7 Field panorama of the Tuffs of Mesa Cuadrada at Mesa Nube. 16

1.8 Field panorama of the Tuffs of Mesa Cuadrada at Arroyo Derecho. 18

1.9 Paleomagnetic transect across the northern Gulf of California. 21

1.10 Palinspastic reconstruction of the Pacific-North America plate boundary ca. 6 Ma. 23

2.1 Regional tectonic map of western North America. 31

2.2 1:5,000-scale geologic map of southwest Isla Tiburón (SWIT). 38

2.3 Schematic stratigraphic column of geologic map units on southwest Isla Tiburón. 39

2.4 Field photographs of monolithologic volcanic breccia (*Tbxv*). 42

2.5 $^{206}Pb/^{238}U$ zircon ages for volcanic rocks on southwestern Isla Tiburón. 44

2.6 Field photograph of angular unconformity between pre-basin volcanic units and overlying marine and non-marine sediments and volcanic units. 47

2.7 $^{40}Ar/^{39}Ar$ ages for volcanic rocks on southwestern Isla Tiburón. 48

2.8 Breccia units observed at base of SWIT marine basin. 52

2.9 Panoramic and annotated view of the 'cove' outcrops. 54

2.10 Field photographs of marine deposits on southwest Isla Tiburón. 55

2.11 Field photographs of Upper Conglomerate (*Tcmu*) on southwest Isla Tiburón. 61

2.12 Field photographs of Non-marine Conglomerate and Sandstone (*Tcnm*) on southwest Isla Tiburón. 64

2.13 Field photographs of Hast Pitzcal (Cerro Starship) hill and Pliocene volcanic units that cap the SWIT marine basin. 67

2.14 Geologic cross-sections for southwest Isla Tiburón. 69

2.15 Enlarged cross-section of erosional window exposure in Arroyo 3. 76

2.16 Modern-day and restored late Miocene locations of key marine strata and fossil localities in the Gulf of California. 88

3.1 Physiographic map of the northern Gulf of California. 112

3.2 Simplified geologic map and structural domain map of Isla Tiburón. 118

3.3A 1:15,000-scale geologic map of southern Isla Tiburón. 121

3.3B 1:15,000-scale geologic map of northeastern Isla Tiburón. 122

3.4 Schematic stratigraphic columns of Isla Tiburón map units. 123

3.5 $^{40}Ar/^{39}Ar$ matrix ages for volcanic rocks on Isla Tiburón. 126

3.6 $^{40}Ar/^{39}Ar$ k-spar ages for volcanic rocks on Isla Tiburón. 127

3.7 $^{206}Pb/^{238}U$ zircon ages for volcanic rocks on Isla Tiburón. 130

3.8 Geologic cross-sections for southern and northeastern Isla Tiburón. 135

3.9 Present-day and restored distributions of correlative map units across the La Cruz strike-slip fault. 167

3.10 Paleotectonic map reconstruction of the northern Gulf of California, ~6-7 Ma. 172

Chapter 1

Paleomagnetic evidence of oblique rift localization in the Gulf of California

Chapter has been submitted for publication in the journal *Geology*. Author list is:

Scott E.K. Bennett and Michael E. Oskin

1.1 ABSTRACT

A paleomagnetic transect of Miocene ignimbrites across the Pacific-North America plate boundary in northwest Mexico reveals the timing and distribution of dextral shear associated with inception of the Gulf of California oblique rift. Using new high-precision paleomagnetic vectors (alpha-95 ≈ 1°) from tectonically stable sites in north-central Baja California, we determine relative clockwise vertical-axis block rotations up to 76° (mean of 28°) for previous sites within the rift, currently separated across its conjugate margins. Low reference site error now permits isolation of intra-rift block rotation during proto-Gulf time, prior to rift localization ca. 6 Ma (million years before present). We estimate 48% (locally 0% to 75%) of the net rotation occurred between 12.5 Ma and 6.4 Ma. Rotated sites define a newly-constrained ~50-100 kilometer-wide transtensional belt of strike-slip faulting and clockwise block rotation, which was embedded within the wider Mexican Basin and Range extensional province, and connected to the San Andreas fault in southern California. After a protracted history of non-localized extension, strike-slip faulting increased strain rates and connected areas of focused crustal thinning, catalyzing subsequent formation of the Gulf of California.

1.2 INTRODUCTION

Mechanisms of strain localization during continental rifting play a critical role in formation of ocean basins and the ultimate form of passive margins (Huismans and Beaumont, 2011) where large concentrations of human population and natural resources are found. Regional subsidence of mature rifted margins conceals the history of continental break-up beneath kilometers of water and sediment, obscuring the origins of rift architecture and processes that lead to rift localization. In highly oblique rifts, where the divergence direction is ≤30° from the

regional rift trend, deformation involves significant transform (strike-slip) motion (Withjack and Jamison, 1986). Because strike-slip faulting tends to remain localized and accumulate larger displacements (Chester, 1995), it may counter buoyancy and flexural forces that limit normal fault-slip and drive rift widening (Buck, 1991; Forsyth, 1992). Quantifying strike-slip deformation of geologic markers along submerged rift margins can be particularly difficult to document with geophysical techniques (e.g., Brothers et al., 2012; Sutherland et al., 2012). Observation of well-exposed incipient rift systems is thus key to understanding the timing, distribution, and three-dimensional aspects of deformation that lead to strain localization and successful continental rupture.

The nascent Gulf of California rift formed by oblique separation across the Pacific-North America plate boundary (Lonsdale, 1989). Due to support by warm, buoyant mantle (Wang et al., 2009), the majority of thinned continental crust on its margins remains above sea level, exposing the record of rift formation and localization (Fig. 1.1). Oblique plate motion across the Gulf of California is presently accommodated by a NW-trending system of right-stepping, *en echelon*, strike-slip and oblique-slip fault zones that transfer strain across shorter extensional pull-apart basins. The Gulf of California superseded diffuse, orthogonal extension across the Mexican Basin and Range province (Fig. 1.1 inset) that initiated in Oligocene time (Gans, 1997; Henry and Aranda Gomez, 1992) within the Sierra Madre Occidental, and expanded westward behind the subduction-related volcanic arc. At the onset of proto-Gulf time (12.5 Ma), with the southward jump of the Rivera triple junction, the plate tectonic setting evolved from subduction and back-arc extension to dextral transtension (Atwater and Stock, 1998). By the end of proto-Gulf time (6 Ma), rifting localized (Oskin et al., 2001) along the western edge of this asymmetric

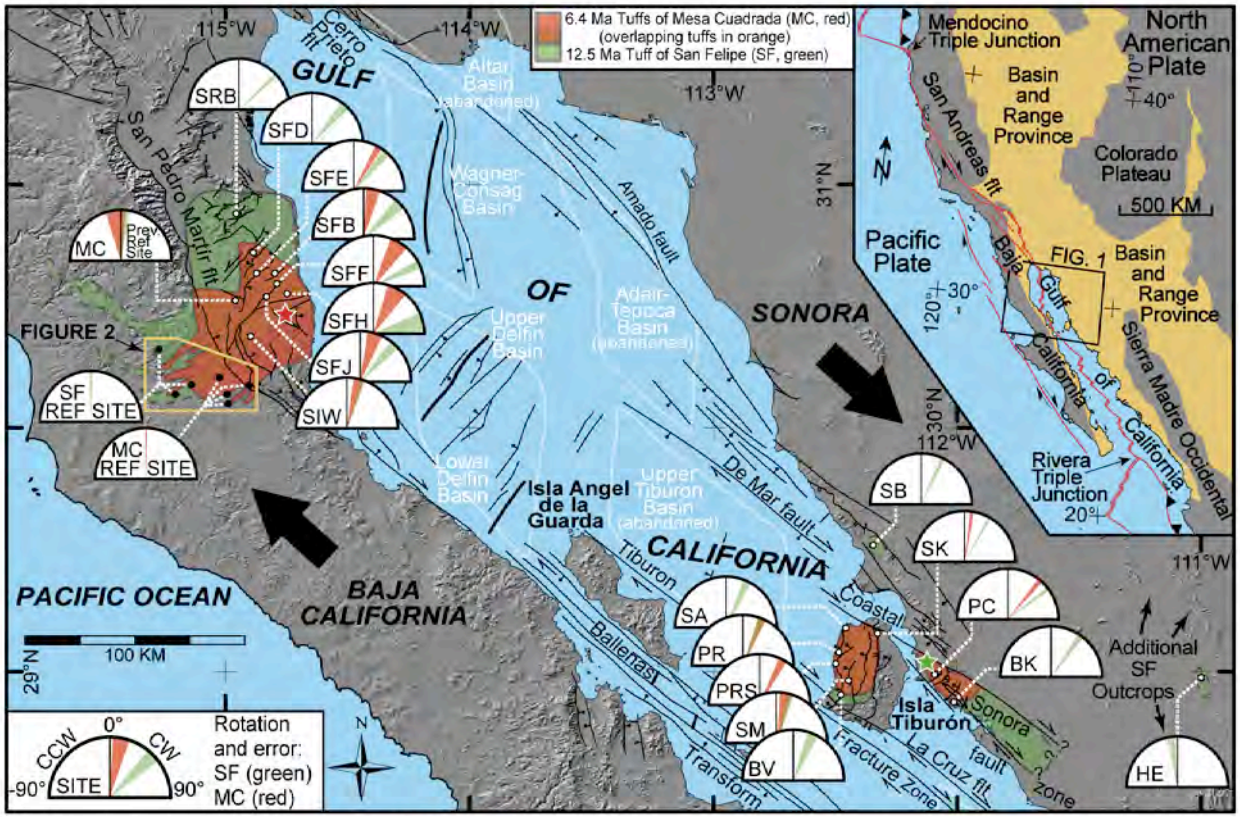

Figure 1.1 Physiographic map of the northern Gulf of California oblique rift, showing extent of Miocene ignimbrites. Pacific-North America relative plate motion (large black arrows) has translated Baja California and portions of these ignimbrites towards the northwest, relative to Sonora (North America). Hypothesized ignimbrite vents shown as colored stars (Oskin and Stock, 2003b). Rift-related strike-slip and normal faults shown as thin black lines. Rift segment axes shown as thick black lines. Sedimentary pull-apart basins created during the formation of the Gulf of California outlined in white. New paleomagnetic reference sites (black dots) located in distal tuff outcrops of central Baja California, beyond the western limit of rift-related faulting. Intra-rift paleomagnetic sites (white dots) are rotated clockwise with respect to these reference sites (pie plots) due to dextral shear-driven block rotation. 7 out of 11 sites show statistically significant larger magnitude rotation of older tuff. Inset map shows present-day tectonic setting of western North America and diffuse Pacific-North America plate boundary, modified from (Oskin and Stock, 2003b). Provinces of mid- to late-Cenozoic extension in tan.

extensional province, an event broadly synchronous with marine incursion and formation of a continuous Gulf of California seaway at ca. 6.5 - 6.3 Ma (Oskin and Stock, 2003a).

The divergent plate boundary in the Gulf of California connects northward with the San Andreas dextral transform (strike-slip) fault system. Propagation of dextral shear into the Mexican Basin and Range extensional province, in the form of clockwise block-rotation and strike-slip faulting, could have promoted rift localization (Umhoefer, 2011), a prerequisite for continental rupture and formation of oceanic crust. Dextral shear likely initiated with plate-boundary reorganization at the beginning of proto-Gulf time (~12.5 Ma), distributed widely across the western half of the extensional province (Fletcher et al., 2007; Gans, 1997). It is unclear whether focused dextral shear at the rift axis preceded or followed rift localization at the end of proto-Gulf time. Two widespread ignimbrite markers, the 12.5 Ma Tuff of San Felipe (SF) and 6.4 Ma Tuffs of Mesa Cuadrada (MC), are both offset by similar amounts across the northern Gulf of California (Oskin et al., 2001; Oskin and Stock, 2003b) (Fig. 1.1). However, dextral shear via clockwise block-rotation and strike-slip faulting did occur within the rifted margins (Bennett et al., 2013; Lewis and Stock, 1998a; Oskin and Stock, 2003b; Seiler et al., 2010), but its extent and magnitude prior to rift localization is unknown.

1.3 PALEOMAGNETISM OF REGIONAL IGNIMBRITES

In order to quantify the extent and magnitude of dextral shear prior to rift localization, we compile a transect of vertical-axis block rotation across the Pacific-North America plate boundary using paleomagnetism of the extensive SF and MC tuffs. Widespread ignimbrites form ideal markers from which to measure the distribution and timing of rotational deformation (Wells and Hillhouse, 1989). Dextral shear results in clockwise vertical-axis rotation, detectable

with high precision by comparing paleomagnetic reference vectors preserved by the alignment of magnetic minerals, primarily magnetite (Nagy, 2000), in the tuffs. These vectors indicate the apparent orientation of the geomagnetic dipole field at the time the tuff cooled below the Curie temperature (500 to 650 °C). The eruption that produced SF blanketed >4,000 km^2 of the western Mexican Basin and Range (Oskin and Stock, 2003b), and was likely sourced from a vent near Punta Chueca, Sonora (Fig. 1.1). Paleomagnetic remanence directions measured from SF have unusually shallow inclinations (~5°) up to the southwest associated with an apparent geomagnetic field excursion or reversal (Stock et al., 1999). MC is another regionally extensive (>2,100 km^2) ignimbrite deposit, which consists of two distinct and widespread cooling units, Tmr3 and Tmr4 (Oskin and Stock, 2003b). Thick, near-vent deposits of MC west of Puertecitos, Baja California grade into distal exposures that abruptly thin or pinch out at the San Pedro Martír fault in Baja California and the Tecomate fault on Isla Tiburón. Deposits of MC have a typical normal polarity paleomagnetic remanence direction (Lewis and Stock, 1998a).

Previous paleomagnetic studies of SF and MC in northeastern Baja California (Lewis and Stock, 1998a; Nagy, 2000; Stock et al., 1999), on Isla Tiburón (Oskin et al., 2001; Oskin and Stock, 2003b), and in coastal Sonora (Darin, 2011; Bennett et al., 2013) document clockwise vertical-axis rotations relative to the Mesa Cuadrada reference site in northeastern Baja California (Fig. 1.1). Both SF and MC are gently tilted toward the west at the Mesa Cuadrada site, which though relatively undeformed, lies east of the rift-bounding San Pedro Martír fault, within an accommodation zone between rift segments (Stock and Hodges, 1989). Due to the small number of collected cores ($n \leq 6$ per tuff), this reference site yields large uncertainty that propagates into all previous rotation calculations and prevents comparison of rotations between deposition of SF and MC.

1.4 PALEOMAGNETIC METHODS

In order to assess the proportion of rotation accumulated during proto-Gulf time, between eruption of the SF and MC tuffs, we drilled new high-precision paleomagnetic reference sites for both tuffs at seven, undeformed, mesa-top sites in north-central Baja California, west of the San Pedro Martír fault system (Fig. 1.2; Table 1). 188 samples (1”-diameter cores) were collected, consisting of 48 samples of SF, 92 samples of the Tmr3 unit of MC, and 48 samples of the Tmr4 unit of MC. At drill sites where n>10, multiple, randomly-oriented samples were collected via a gas-powered, water-cooled, portable paleomagnetic drill (Fig. 1.3). At drill sites where n<10, oriented block samples were collected in the field and randomly-oriented samples were drilled from these block samples in the laboratory. Core orientations in the field and the laboratory were obtained with a Pomeroy orienting fixture (Fig. 1.3B).

Samples were cut into 1-cm tall specimens for demagnetization experiments. All specimens were subjected to progressive alternating field (AF) demagnetization, typically including 13 steps to a magnetic field strength of 80 millitesla (mT) (Fig. 1.4). AF partial demagnetization steps gradually demagnetize the secondary low-stability component and isolate the primary high-stability component of natural remanent magnetization (NRM) of a specimen. This primary NRM, typically a thermoremanent magnetism, is representative of Earth’s magnetic field at the time the sampled rock cooled below the Curie temperature. Because ignimbrites cool much faster than significant changes in the secular variation of Earth’s magnetic field, the NRM directions determined from multiple specimens collected from the same ignimbrite cooling unit should agree within uncertainty (Lewis and Stock, 1998a). NRM and low-temperature measurement steps preceded all AF steps. All experiments were conducted using an automated 2G Enterprises superconducting rock magnetometer in a magnetically

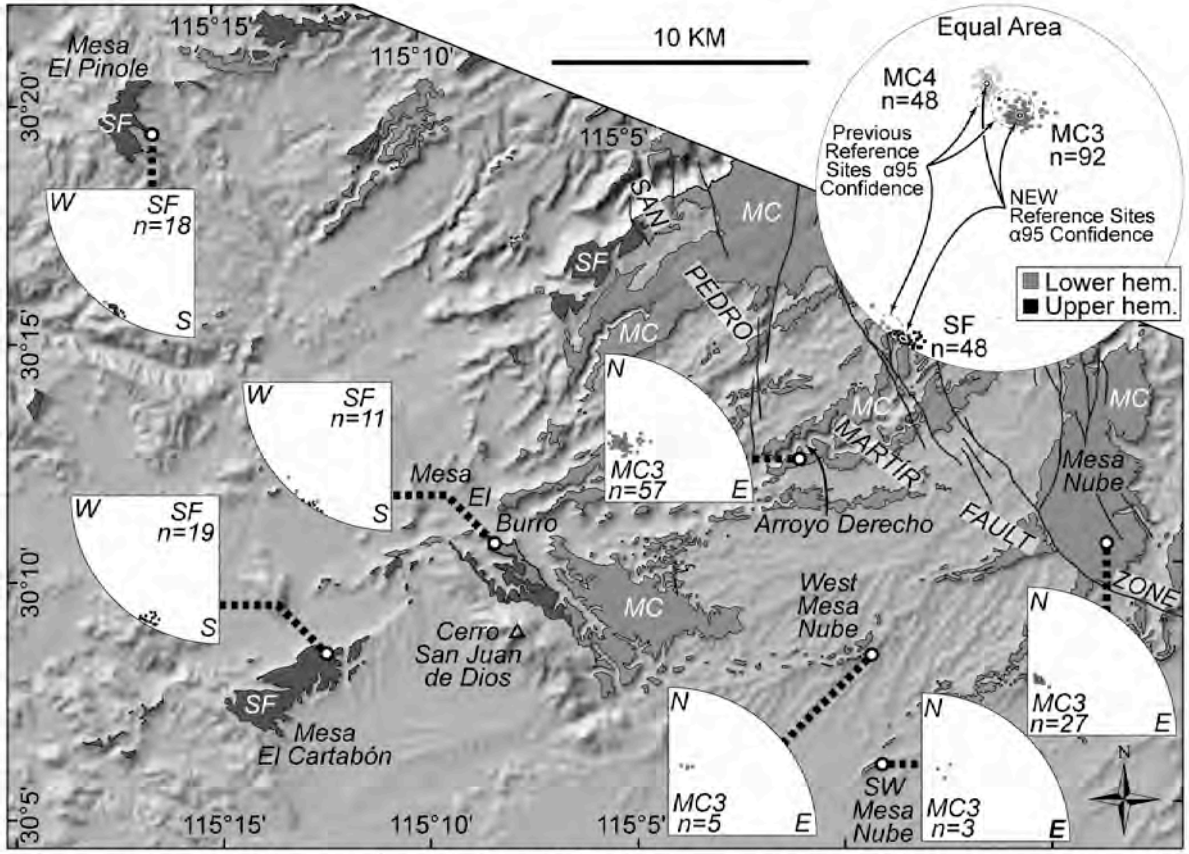

Figure 1.2 Geologic map of new paleomagnetic drill sites (white dots) amongst the distal, westernmost deposits of the Tuffs of Mesa Cuadrada (MC, medium gray) and the Tuff of San Felipe (SF, dark gray) in north-central Baja California. Primary natural remanent magnetization (NRM) vectors for cores of SF and unit Tmr3 of MC collected in this study are plotted in stereonet quadrants tied to each drill site. Rift-bounding San Pedro Martír normal fault zone are bold black lines. Upper right stereonet shows all cores for the SF tuff and both the Tmr3 (MC3) and Tmr4 (MC4) cooling units of the MC tuff collected in this study. α95 confidence cones from new paleomagnetic drill sites shown as small solid white or black ellipses near center of data clusters. Larger α95 confidence cones from the previous reference sites at Mesa Cuadrada (cores not shown) (Lewis and Stock, 1998a) shown as dashed gray ellipses. Modern-day geocentric axial dipole field location shown as black star. No tilt-corrections were performed. Examples of representative paleomagnetic demagnetization results shown in Figure 4.

Figure 1.3 Field photographs of paleomagnetic field techniques. (A) drilling cores with portable, gas-powered paleomagnetic drill and water cooling system, (B) recording the orientation of a drilled paleomagnetic core prior to collection from outcrop using Pomeroy core orienter and Brunton compass, (C) typical tuff outcrop after collection of paleomagnetic cores.

Figure 1.4 Representative paleomagnetic demagnetization results for the Tmr3 unit of the Tuffs of Mesa Cuadrada (A) and Tuff of San Felipe (B) in central Baja California. For each, vector-component Zijderveld diagram (left) and equal area stereonet (upper right) displays vector orientations for all NRM, LT, and AF partial demagnetization steps. J/J0 plot shown for each core (lower right).

A Tmr3 unit of Tuffs of Mesa Cuadrada @ Arroyo Derecho, central Baja California

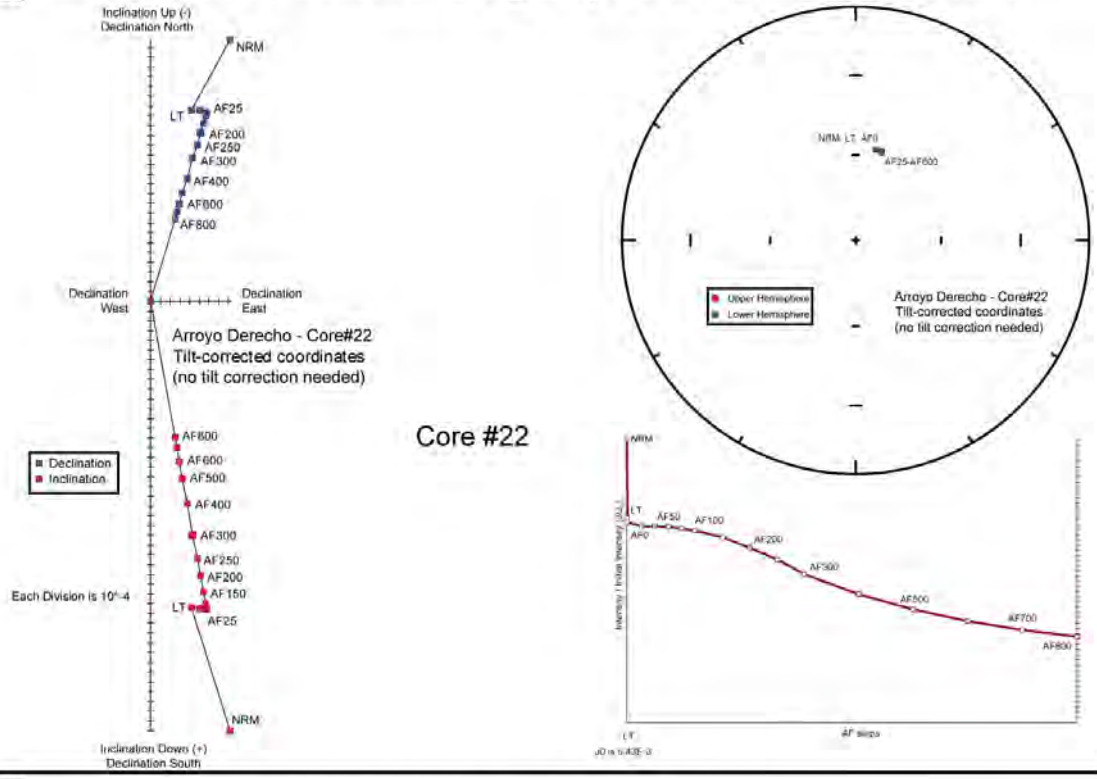

B Tuff of San Felipe @ Mesa El Pinole, central Baja California

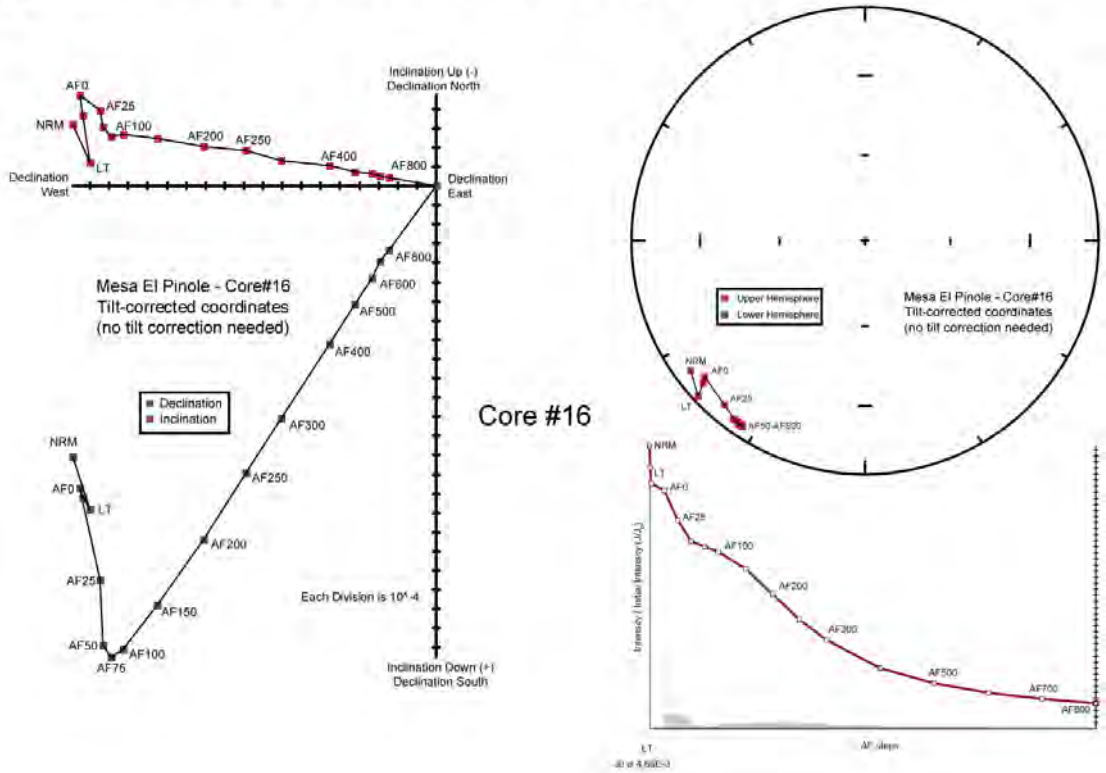

shielded μ-metal room at the Paleomagnetics Laboratory of the California Institute of Technology. No thermal demagnetization steps were performed, as thermal and AF demagnetization typically yield similar results for these tuffs (Nagy, 2000).

Best-fit of lines and planes for demagnetization paths were estimated for each specimen (Kirschvink, 1980). Typically, directions resolved from higher AF steps were utilized to obtain best-fit lines and planes, while NRM, low-temperature, and low AF steps revealed inconsistent vector directions, indicative of variable magnitudes of a secondary NRM component (Fig. 1.4).

At tectonically deformed sites within the rift, paleomagnetic remanence directions are corrected for the tilt (bedding dip) of the sampled outcrop (Bennett et al., 2013; Lewis and Stock, 1998a; Oskin et al., 2001; Oskin and Stock, 2003; Stock et al., 1999). Regionally, the basal tuff contacts in central Baja California are typically horizontal to ~1° southwest-dipping, which reflects the gently, southwest-draining landscape that these tuffs blanketed. All SF outcrops are horizontal (Figs. 1.5, 1.6). Many MC outcrops are also horizontal (Fig. 1.7), but some fill southwest- to west-draining paleo-channels carved into the post-12.5 Ma landscape (Figs. 1.6, 1.8). Basal contacts and internal eutaxitic foliation of flattened pumice in these paleo-channel fills locally dip 25° - 45° towards the center of paleo-canyons. Steeply-dipping paleo-channel fills were avoided during sample collection, as we targeted horizontal to gently dipping (≤5°) outcrops. We assume that the observed tuff inclinations in central Baja California are primary and formed prior to the ignimbrite cooling below the Curie temperature. Thus no tilt corrections are performed.

For each new drill site, mean paleomagnetic remanence directions (Declination, Inclination) and their α95 confidence cones and precision parameters (κ) were determined (Table 1). The paleomagnetic remanence directions from intra-rift drill sites were then compared to

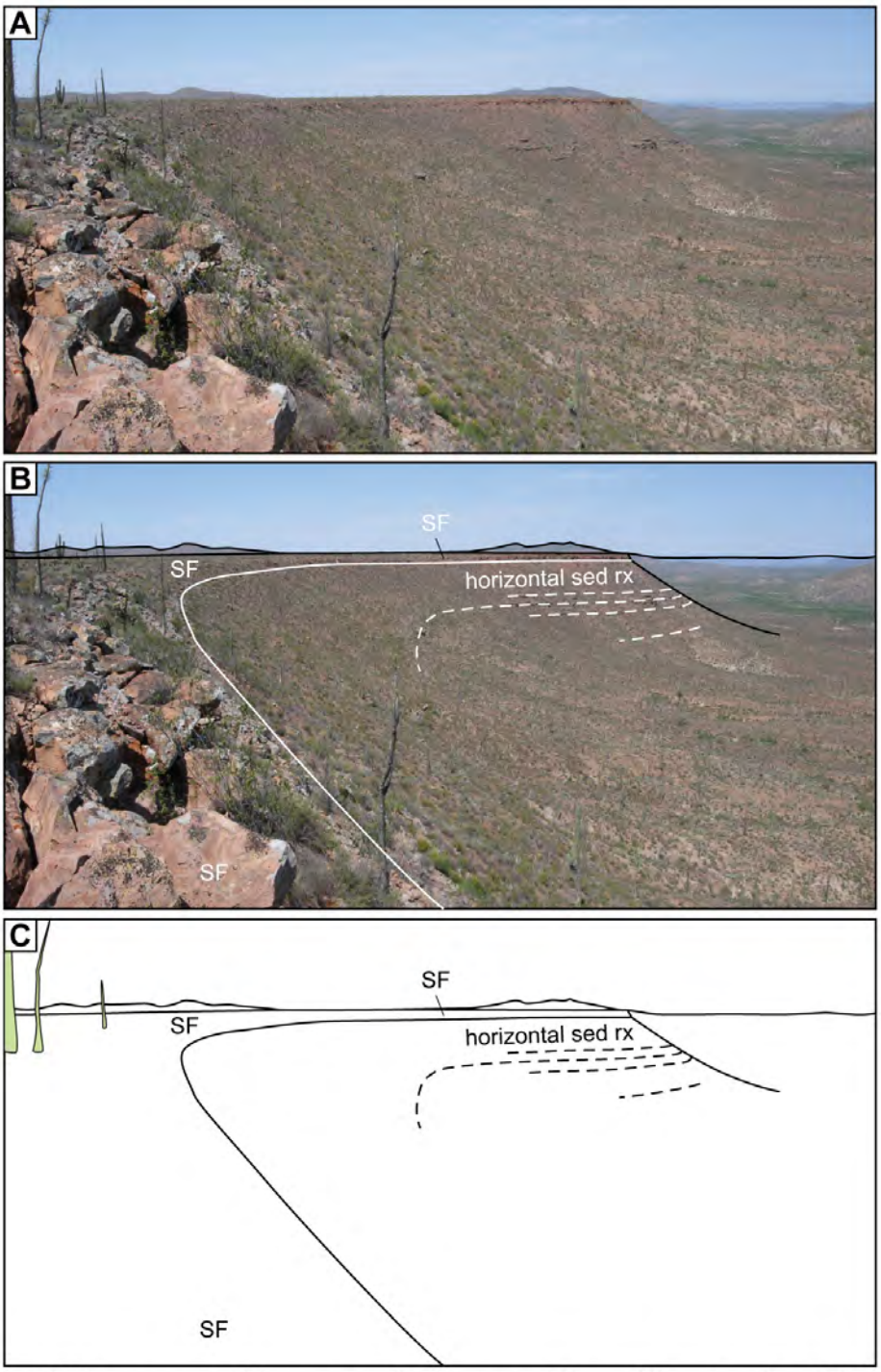

Figure 1.5 Field panorama (A), annotated panorama (B), and line drawing (C) of mesa-top outcrops of the 12.5 Ma Tuff of San Felipe (SF) at Mesa El Cartabon. See Figure 2 for location. Deposits of SF conformably overlie pre-12.5 Ma sub-horizontal sandstone and conglomerate deposits with no observed paleotopography between these units. Looking approximately west in center of panorama. Panorama photograph taken standing on SF, ~0.5 km east of the Mesa El Cartabon drill site (Fig. 2).

Figure 1.6 Field panorama (A), annotated panorama (B), and line drawing (C) of mesa-top outcrops of both the 6.4 Ma Tuffs of Mesa Cuadrada (MC) and the 12.5 Ma Tuff of San Felipe. Deposits of SF conformably overlie pre-12.5 Ma sub-horizontal sandstone and conglomerate deposits in the upper left half of this panorama view, with no observed paleotopography between these units. Deposits of the Tuffs of Mesa Cuadrada (MC3) fill in paleotopography carved down through the Tuff of San Felipe and into underlying, sub-horizontal sandstone and conglomerate deposits. The upper portion of Tmr3 is slightly vapor-phase altered and less resistant than its lower portion. In the right half of this panorama, MC3 fills a paleo-canyon carved into the post-12.5 Ma landscape, where inclined, perched MC3 outcrops dip up to ~40° towards the center of the paleo-canyon. Paleo-canyon flow direction is to the southwest (toward the viewer). The modern-day canyon (blue line) occupies the same approximate position as the paleo-canyon. The Tmr4 cooling unit of the Tuffs of Mesa Cuadrada (MC4) locally caps deposits of MC3. Looking approximately northeast in center of panorama. Panorama photograph taken standing on MC3, ~8 km east-southeast of the Mesa El Pinole drill site (Fig. 2).

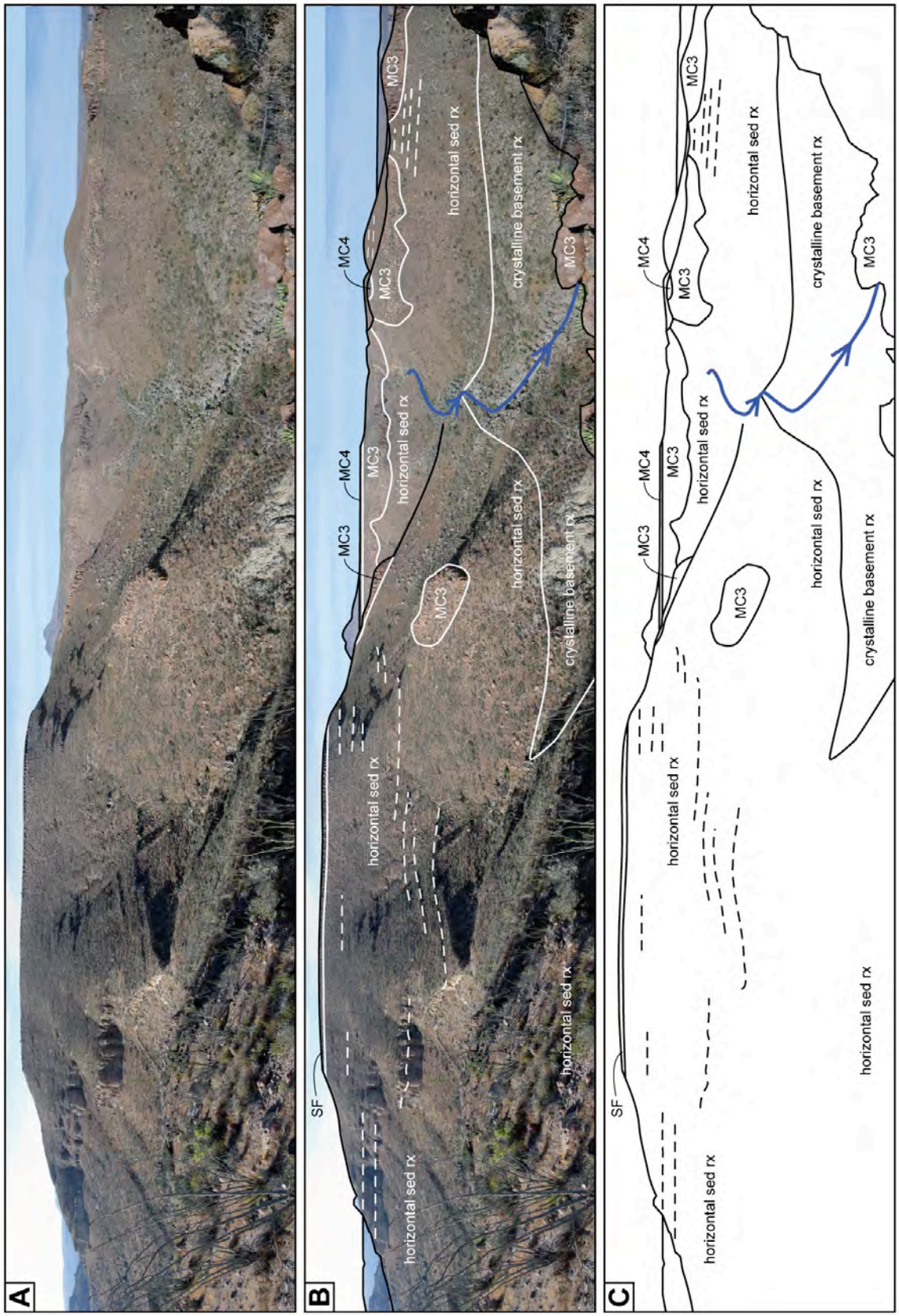
A
B
C
SF
MC3
MC4
horizontal sed rx
crystalline basement rx

Figure 1.7 Field panorama (A), annotated panorama (B), and line drawing (C) of mesa-top outcrops of the 6.4 Ma Tuffs of Mesa Cuadrada (MC) at Mesa Nube. See Figure 2 for location. A single cooling unit of the Tmr3 ignimbrite (MC3) fills in gentle paleotopography carved into pre-12.5 Ma sub-horizontal sandstone and conglomerate deposits. The upper portion of Tmr3 is slightly vapor-phase altered and less resistant than its lower portion. The Tmr4 cooling unit of the Tuffs of Mesa Cuadrada (MC4) caps Mesa Nube. Looking approximately east in center of panorama. Panorama photograph taken standing on MC4, ~1 km northeast of the Mesa Nube drill site (Fig. 2).

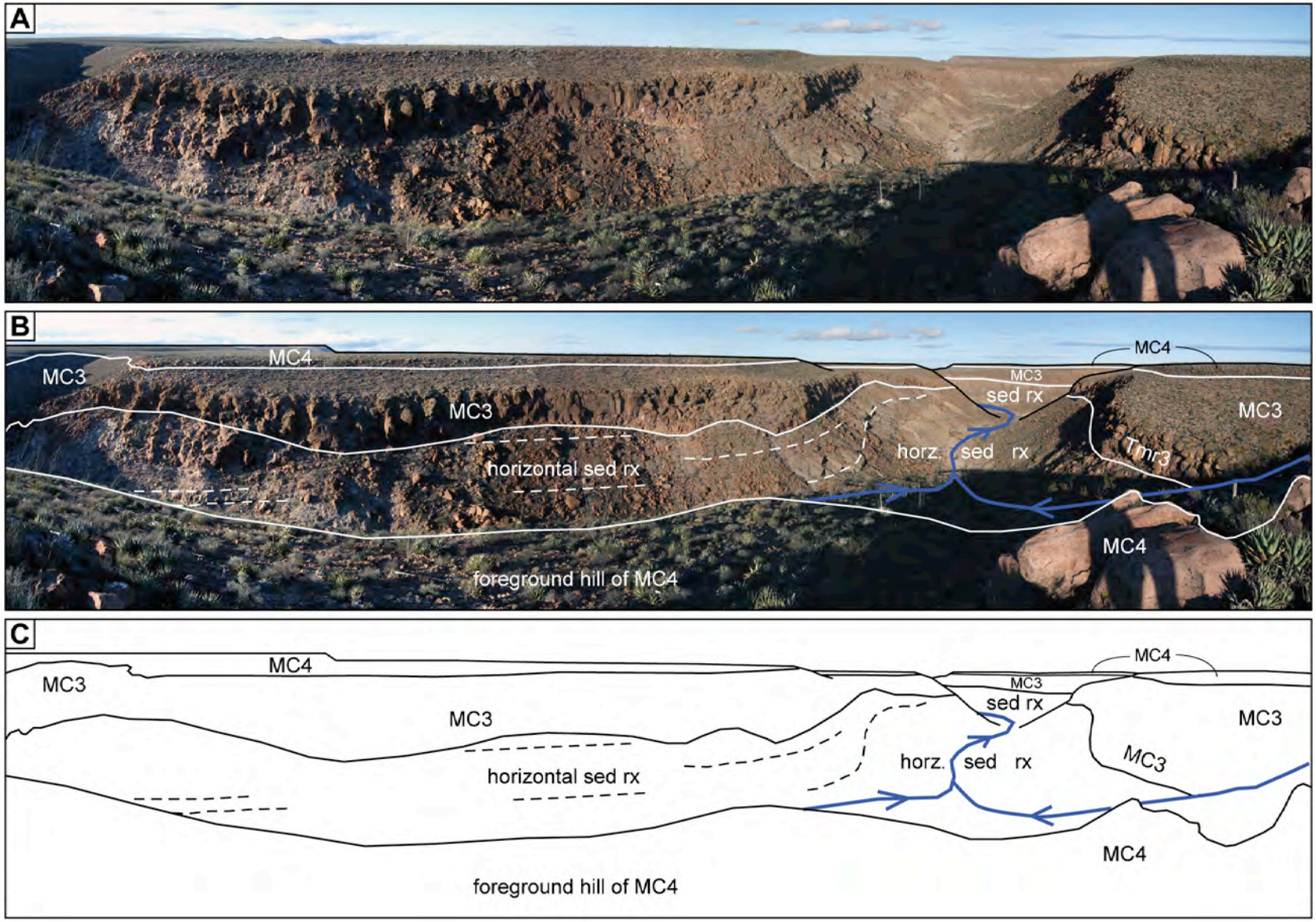
A
B
MC3
MC4
MC3
horizontal sed rx
MC3
sed rx
MC4
MC3
horz. sed rx
Tmr3
MC4
foreground hill of MC4
C
MC3
MC4
MC3
horizontal sed rx
MC3
sed rx
MC4
MC3
horz. sed rx
MC3
MC4
foreground hill of MC4

Figure 1.8 Field panorama (A), annotated panorama (B), and line drawing (C) of mesa-top outcrops of the 6.4 Ma Tuffs of Mesa Cuadrada (MC) in Arroyo Derecho. See Figure 2 for location. The lower cooling unit of the Tmr3 ignimbrite (MC3L) fills in paleotopography carved into pre-12.5 Ma sub-horizontal sandstone and conglomerate deposits. In the right half of this panorama, this basal cooling unit fills a paleo-canyon, where inclined MC3L outcrops dip up to ~40° towards the center of the paleo-canyon. Paleo-canyon flow direction is to the southwest (generally away from the viewer). The modern-day Arroyo Derecho canyon (blue line) occupies the same approximate position as the paleo-canyon.The basal contact of the upper Tmr3 cooling unit (MC3U) is sub-horizontal. The upper portions of both MC3L and MC3U are slightly vapor-phase altered and less resistant than their respective lower portions. The Tmr4 cooling unit of the Tuffs of Mesa Cuadrada (MC4) caps the landscape. Looking approximately southwest in center of panorama. Panorama photograph taken standing on MC4 cooling unit of MC, ~4.5 km east-northeast and up-canyon of the Arroyo Derecho drill site (Fig. 2).

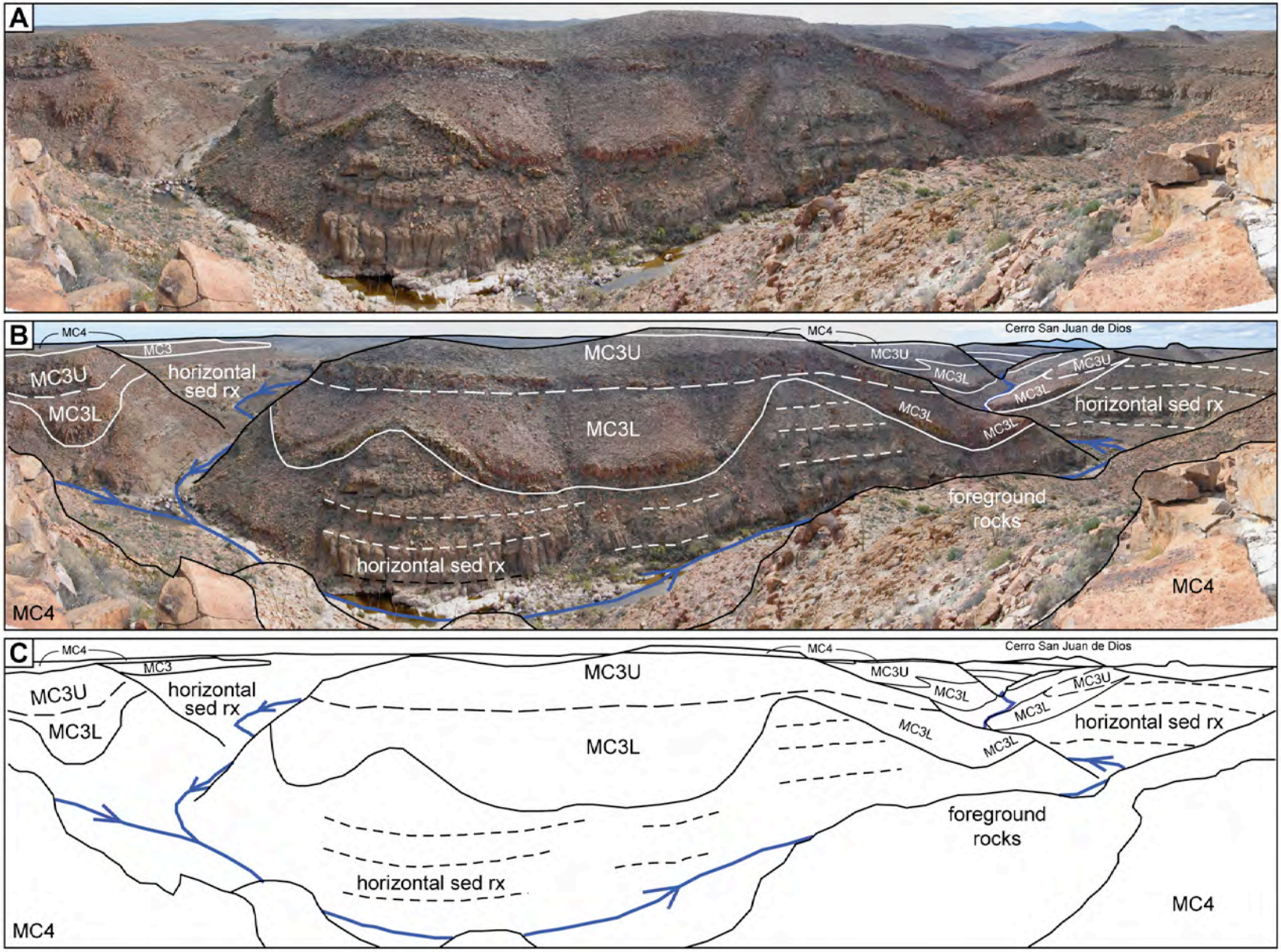
A
B
MC4
MC3
MC3U
MC3L
horizontal sed rx
MC3U
MC3L
MC4
Cerro San Juan de Dios
MC3U
MC3L
MC3U
MC3L
MC3L
MC3L
horizontal sed rx
foreground rocks
horizontal sed rx
MC4
MC4
C
MC4
MC3
MC3U
MC3L
horizontal sed rx
MC3U
MC3L
MC4
Cerro San Juan de Dios
MC3U
MC3L
MC3U
MC3L
MC3L
MC3L
horizontal sed rx
foreground rocks
horizontal sed rx
MC4
MC4

directions determined at the new reference sites in order to calculate the rotation (R), rotation error (ΔR), flattening (F), and flattening error (ΔF) of the intra-rift site (Demarest, 1983).

1.5 PALEOMAGNETIC TRANSECT ACROSS THE GULF OF CALIFORNIA

The paleomagnetic remanence directions determined at these tectonically stable sites (D_{SF} = 212.4°, I_{SF} = -3.0°; D_{MC} = 15.6°, I_{MC} = 56.2°) are consistent across tens of kilometers (Fig. 1.2) and are assumed to have experienced no vertical-axis block rotation. Here, magnitudes of the alpha-95 (α95) confidence cones for multiple cores (SF=1.3°, MC=1.0°) are smaller than the confidence cones at the previous Mesa Cuadrada reference sites (SF=4.1°, MC=8.9°) (Fig. 1.2 inset; Table 1). Comparisons of new paleomagnetic remanence directions from central Baja California with directions from 19 intra-rift sites (2 new, 17 previously published) indicate clockwise vertical-axis rotations for SF and MC up to 76 ± 11° and 40 ± 3°, respectively (Figs. 1.1, 1.9; Table 1). An important exception is the easternmost SF site ('HE') in central Sonora where no clockwise rotation has occurred since 12.5 Ma. Although SF is tilted gently to the west at this site, it appears to lie beyond the eastern limit of clockwise vertical-axis rotation related to oblique rifting (Fig. 1.9). The mean magnitudes of the rotation errors (ΔR_{SF} = 4.3°, ΔR_{MC} = 6.3°) using these new paleomagnetic sites are lower than the rotation errors using the previous reference sites at Mesa Cuadrada (ΔR_{SF} = 5.6°, ΔR_{MC} = 13.2°), owing to the larger number of cores (n_{SF} = 48, n_{MC} = 92) collected at the new reference sites (Table 1). At sites where both the Tmr3 and Tmr4 cooling units of the MC tuff were drilled, the magnitude of rotation is similar. However, due to higher rotation errors for Tmr4 sites (Table 1), we include only the results from Tmr3 in our analysis. At paired sites where both SF and MC are present in the same fault block, clockwise rotation that occurred prior to 6.4 Ma is detectable by differential rotation between SF

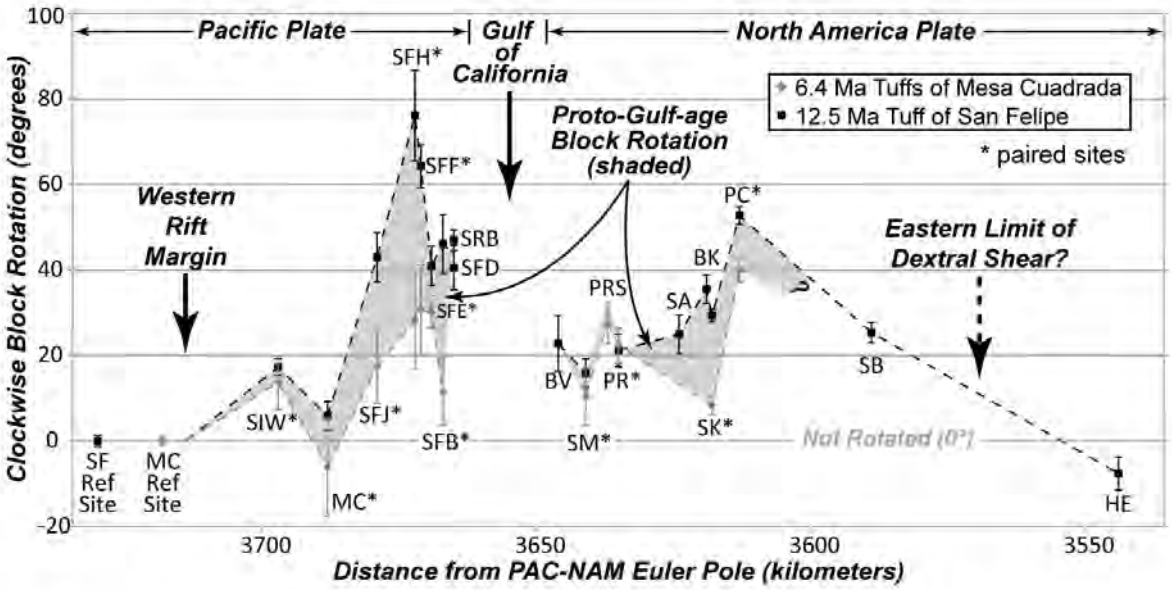

Figure 1.9 Paleomagnetic transect across the northern Gulf of California. Plot shows updated clockwise vertical-axis block rotation at previous and new paleomagnetic drill sites of the Tuff of San Felipe and the Tuffs of Mesa Cuadrada using the new paleomagnetic reference sites in central Baja California. Block rotation that occurred 12.5 - 6.4 Ma, during proto-Gulf time, is shaded gray. See Table 1.1 for paleomagnetic data and analysis.

and MC. At 10 of 11 paired sites across the northern Gulf of California, SF is rotated clockwise by a greater amount than MC (Fig. 1.9). 7 of these 10 sites are precise enough to statistically isolate differential rotation. At paired sites, up to 48° (weighted mean of 16°) of clockwise rotation occurred prior to 6.4 Ma (Table 1). By weighting all paired site results by the differential rotation error, we estimate that 48% (locally 0% to 75%) of the net rotation occurred during proto-Gulf time.

1.6 DISCUSSION AND CONCLUSIONS

The results of this regional paleomagnetic study show that a narrow belt of focused dextral shear, kinematically linked to the San Andreas fault system, was embedded within the western Mexican Basin and Range prior to 6.4 Ma and after 12.5 Ma, during proto-Gulf time. These data alone cannot further constrain the onset of dextral shearing. However, recent geologic studies from both margins of the northern Gulf of California document significant transtensional faulting and related formation of non-marine sedimentary basins after 9 Ma, during late-proto-Gulf time (Bennett et al., 2013; Seiler et al., 2010). The development of these new strike-slip faults may have been prompted by a ~15° clockwise shift in the direction of Pacific-North America relative plate motion at ~8 Ma (Atwater and Stock, 1998) that increased the obliquity of the rift.

After restoring the Baja California peninsula 245 km to its ~6 Ma position adjacent to Isla Tiburón (Fig. 1.10), these paleomagnetic results place new spatial constraints on a ~50-100 km-wide transtensional belt of dextral strike-slip faulting and clockwise vertical-axis block rotation that was broadly coincident, in both time and space, with rift localization (Oskin et al., 2001) and marine seaway incursion (Oskin and Stock, 2003a; Chapter 2 of this thesis) in the

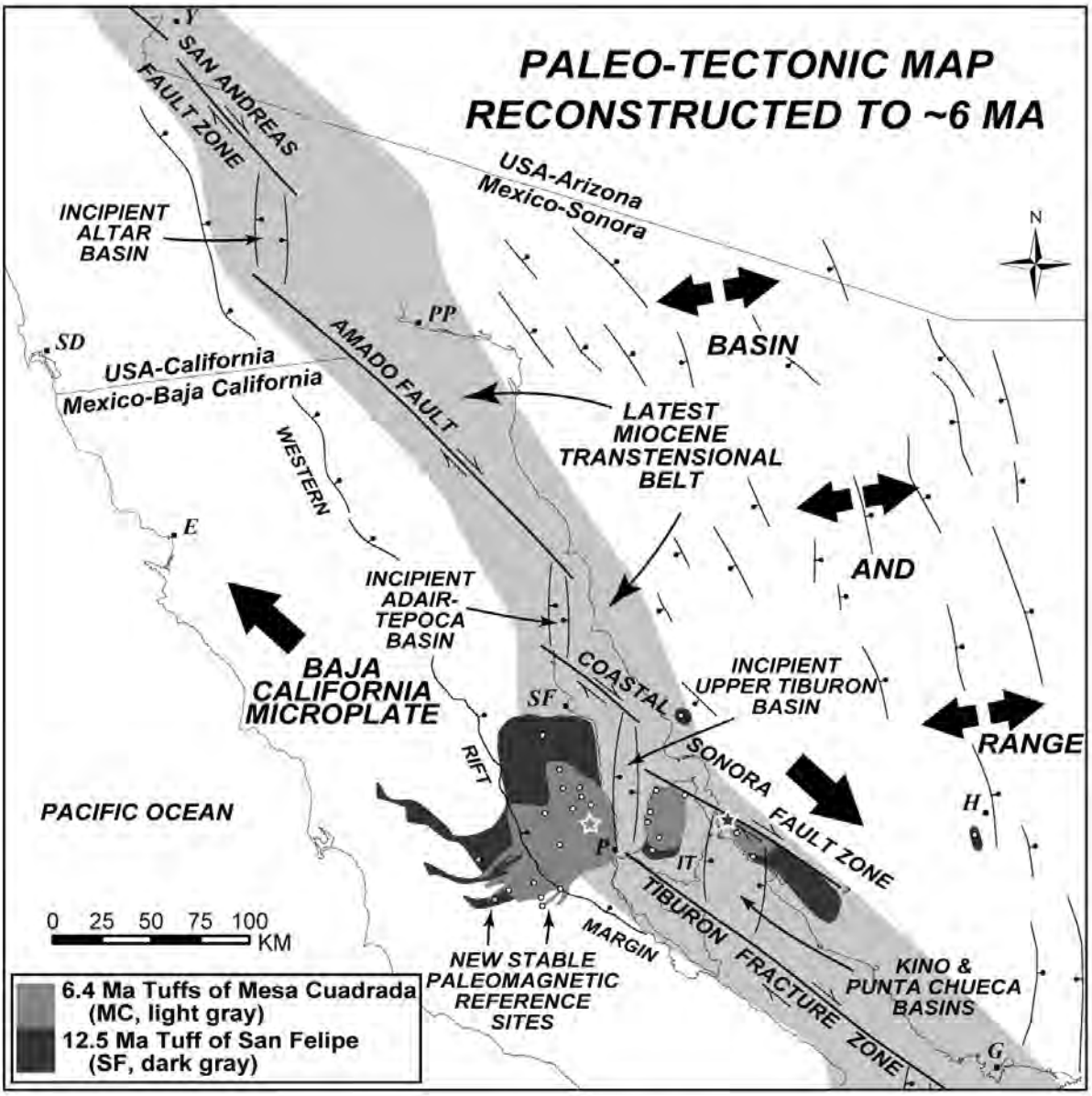

Figure 1.10 Palinspastic reconstruction of the Pacific-North America tectonic plate boundary ca. 6 Ma. Paleomagnetic sites across the northern Gulf of California (white dots) constrain a ~50-100 km-wide transtensional belt (light gray) of incipient pull-apart basin formation, en echelon dextral strike-slip faulting, and related clockwise vertical-axis block rotation. This transtensional belt likely continued northward to the San Andreas fault zone and was co-located and coeval with both localization of plate boundary strain and marine seaway incursion during latest Miocene time. Baja California peninsula is reconstructed ~245 km back to the southeast, the minimum estimate of (Oskin and Stock, 2003b). Shaded stars are restored vent locations for the MC and SF regional ignimbrite deposits. IT - Isla Tiburon, Y - Yuma, SD - San Diego, E - Ensenada, PP - Puerto Penasco, SF - San Felipe, P - Puertecitos, G - Guaymas, H - Hermosillo.

northern Gulf of California. We hypothesize that dextral deformation progressively became more focused within the rift near the end of the proto-Gulf period, likely along *en echelon* dextral strike-slip fault zones and nascent pull-apart basins embedded within a broader area of extension and bounded to the west by the stable Baja California microplate (Fig. 1.10). This late proto-Gulf of California configuration (Fig. 1.10) may be analogous to the Walker Lane transtensional belt of western Nevada and eastern California (Unruh et al., 2003), where modern-day continental strike-slip and extensional faulting, block rotation, and syn-rift volcanism are embedded along the western margin of the Basin and Range extensional province, adjacent to the stable Sierra Nevada-Great Valley microplate.

Where extension is hosted within a strike-slip-dominated setting (i.e. oblique rift), the overall higher strain rates along shear zones and across the intervening extensional regions could ultimately enhance the potential of a rift to localize (Al-Zoubi and ten Brink, 2002) and shorten the duration of time until continental rupture (Umhoefer, 2011). For the case of the Gulf of California rift, a transtensional shear zone likely hosted a majority of plate-boundary dextral slip by 6 Ma, and facilitated the transition to narrow rifting and subsequent ~250 km of NW-SE crustal stretching via kinematically linked, large-offset normal faults (González-Fernández et al., 2005). Extensional pull-apart basins bounded by large-offset strike-slip faults, as we infer were present prior to rift localization in the Gulf of California, may focus crustal thinning and facilitate crustal rupture more rapidly than orthogonal rifting, consistent with results from recent numerical models of oblique rifting (Brune et al., 2012; van Wijk et al., 2011). The ~20 Myr history of largely orthogonal extension of the Mexican Basin and Range, culminating in lithospheric-scale oblique rift localization, demonstrates how oblique, three dimensional strain

may catalyze the localization process, accelerate the evolution from a 'wide' to 'narrow' rift (Buck, 1991) and lead to the formation of strongly asymmetric rifted margins.

ACKNOWLEDGMENTS

This research was funded by grant EAR-0904373 from the US NSF Tectonics and MARGINS programs. Discussion with J. Stock assisted with outcrop reconnaissance. Conversations with A. Elliott, A. Forte, and N. Longinotti helped refine an early version of this manuscript. We thank J. Kirschvink, the Caltech Paleomagnetics Laboratory, and M. Darin for assistance with sample preparation and analysis. K. Bossenbroek and D. Hadley provided exceptional field assistance.

Table 1.1 Summary of paleomagnetic data and updated rotation values for the Tmr3 (MC3) and Tmr4 (MC4) cooling units of the Tuffs of Mesa Cuadrada and the Tuff of San Felipe (SF), northern Gulf of California, México.

		Location			Bedding		In Situ		Tilt-Corrected		Fisher Statistics		Bingham Statistics				USING MESA CUADRADA REFERENCE SITES (Lewis and Stock, 1998)				USING NEW REFERENCE SITES (This Study)						
Drill Site, Reference	Unit	Lat. (°N)	Long. (°W)	n/n_0	Strike	Dip	D	I	D	I	α_{95}	κ	κ_1	α_{95}	κ_2	α_{95}	R	ΔR	F	ΔF	R	ΔR	F	ΔF	Differential R (TSF-TMC)	Δ Differential R (TSF-TMC)	% of PRE-6.4 Ma Clockwise Rotation
BAJA CALIFORNIA																											
NEW REFERENCE SITES																											
Arroyo Derecho	MC4	30.21	115.01	28/28	-	0	352.2	42.7	352.2	42.7	1.4	364.2	-189.5	1.4	-0.1	1.4											
Mesa Nube	MC4	30.17	114.89	15/15	-	0	355.1	40.7	355.1	40.7	1.6	529.5	-364.5	1.3	-261.2	1.6											
Southwest Mesa Nube	MC4	30.10	114.98	5/5	-	0	352.9	44.9	352.9	44.9	2.7	3367.5	-1403.4	1.2	-337.7	40.5											
MC4 Mean	MC4			48/48	-	0	353.2	42.1	353.2	42.1	1.1	393.4	-198.5	1.0	-0.2	1.1					0	0	0	0			
Arroyo Derecho (a)	MC3	30.21	115.02	31/31	-	0	16.7	54.6	16.7	54.6	2.0	165.7	-195.3	1.3	-55.3	2.4											
Arroyo Derecho (b)	MC3	30.21	115.01	26/26	-	0	18.5	57.4	18.5	57.4	1.1	617.9	-579.0	0.8	-223.0	1.3											
Mesa Nube	MC3	30.18	114.89	27/27	-	0	11.8	58.6	11.8	58.6	0.7	1487.8	0.4	-457.1	0.9												
West Mesa Nube	MC3	30.14	114.99	5/5	-	0	12.7	51.1	12.7	51.1	4.8	208.6	-3370.3	0.8	-83.9	4.9											
Southwest Mesa Nube	MC3	30.10	114.98	3/3	-	0	17.6	48.5	17.6	48.5	7.9	164.9	-309.0	3.3	-132.8	5.0											
MC3 Mean	MC3			92/92	-	0	15.6	56.2	15.6	56.2	1.0	236.8	-172.5	0.8	-92.5	1.1					0	0	0	0			
Mesa El Cartabón	SF	30.14	115.21	19/19	-	0	209.6	-4.9	209.6	-4.9	1.6	458.1	-416.7	1.1	-170.7	1.8											
Mesa El Burro	SF	30.18	115.14	11/13	-	0	215.4	0.3	215.4	0.3	3.7	141.5	-258.8	1.9	-51.7	4.2											
Mesa El Pinole	SF	30.32	115.27	18/18	-	0	213.4	-2.9	213.4	-2.9	1.3	696.0	-535.7	1.0	-281.8	1.4											
SF Mean	SF			48/50	-	0	212.4	-3.0	212.4	-3.0	1.3	240.3	-319.9	0.8	-76.7	1.7					0	0	0	0			
MC - Mesa Cuadrada																											
Lewis and Stock (1998)	MC4	30.53	114.96	8/10	102	24	355.8	28.0	348.8	50.3	2.6	482.7	nr	nr	nr	nr	0	0	0	0	-4.4	3.4	-8.2	2.2	10.3	4.5	
Lewis and Stock (1998)	MC3	30.53	114.96	3/3	169	3	13.7	53.0	9.5	53.9	8.9	129.8	nr	nr	nr	nr	0	0	0	0	-6.1	11.5	2.3	6.7	12.0	11.9	
Lewis and Stock (1998) *	SF	30.53	114.96	5/6	169	7	221.7	-3.6	218.3	-6.9	4.1	442.5	-310.0	2.8	-0.6	3.3	0	0	0	0	5.9	3.4	3.9	3.3			
SIW - Santa Isabel Wash																											
site L of nrgy (2000)	MC3	30.38	114.92	8/8	-	0	29.3	52.1	29.3	52.1	4.8	135.0	nr	nr	nr	nr	19.8	12.9	-1.8	7.7	13.7	6.3	4.1	3.8	3.6	6.3	21%
Stock et al. (1999)	SF	30.38	114.92	11/11	-	0	229.7	-9.1	229.7	-9.1	2.0	497.7	-613.7	1.2	-200.0	2.1	11.4	4.0	2.2	3.6	17.3	1.9	6.1	1.9			
SFJ - San Fermin																											
Lewis and Stock (1998)	MC4	30.54	114.83	3/5	165	2	58.0	53.6	57.1	55.5	16.7	37.2	nr	nr	nr	nr	68.3	23.1	-5.2	12.7	63.9	22.9	-13.4	12.6	-20.9	23.6	0%
Lewis and Stock (1998)	MC3	30.54	114.83	5/6	165	2	34.7	50.8	33.1	52.4	6.7	105.5	nr	nr	nr	nr	23.6	14.2	1.5	8.4	17.5	8.6	3.8	5.2	25.5	10.2	59%
Lewis and Stock (1998) *	SF	30.54	114.83	6/6	179	27	255.0	5.0	255.4	-11.2	7.1	98.9	-62.1	5.2	-0.8	6.4	37.1	6.5	4.3	6.4	43.0	5.7	8.2	5.6			
SFH - San Fermin																											
Lewis and Stock (1998)	MC4	30.55	114.74	2/2	183	27	57.5	34.4	38.9	53.7	29.4	37.2	nr	nr	nr	nr	50.1	39.3	-3.4	20.7	45.7	39.2	-11.6	20.6	30.5	40.6	0%
Lewis and Stock (1998)	MC3	30.55	114.74	6/6	183	27	61.5	34.8	43.7	55.5	8.1	58.0	nr	nr	nr	nr	34.2	16.0	-1.6	9.2	28.1	11.3	0.7	6.4	48.1	15.4	63%
Lewis and Stock (1998) *	SF	30.55	114.74	4/5	183	27	292.1	36.2	288.6	10.6	13.6	46.8	-552.8	2.1	-19.5	11.6	70.3	11.0	-17.5	10.8	76.2	10.6	-13.6	10.4			
SFF - San Fermin																											
Lewis and Stock (1998)	MC4	30.60	114.79	5/5	65	6	37.8	34.6	41.8	37.4	15.3	17.9	nr	nr	nr	nr	53.0	15.3	12.9	12.0	48.6	15.0	4.7	11.8	15.7	15.7	24%
Lewis and Stock (1998)	MC3	30.60	114.79	6/6	228	24	77.5	49.6	46.2	55.8	7.5	67.9	nr	nr	nr	nr	36.7	15.5	-1.9	8.9	30.6	10.6	0.4	5.9	33.7	11.6	52%
Lewis and Stock (1998) *	SF	30.60	114.79	5/5	149	13	278.2	16.6	276.7	-3.0	6.4	116.1	-118.4	4.1	-73.8	5.2	58.4	5.9	-3.9	5.9	64.3	5.0	0.0	5.0			
SFB - San Fermin																											
Lewis and Stock (1998)	MC4	30.65	114.79	3/3	47	31	351.6	32.5	13.4	54.9	5.8	297.8	nr	nr	nr	nr	24.6	8.2	-4.6	4.8	20.2	7.7	-12.8	4.4	25.9	10.2	56%
Lewis and Stock (1998)	MC3	30.65	114.79	9/9	47	31	353.7	43.3	27.1	50.0	6.2	61.5	nr	nr	nr	nr	17.6	13.7	3.9	8.3	11.5	7.8	6.2	5.0	34.6	10.3	75%
Lewis and Stock (1998) *	SF	30.65	114.79														40.2	7.8	-3.8	7.8	46.1	6.9	0.1	6.9			
SFE - San Fermin																											
Lewis and Stock (1998)	MC3	30.66	114.83	7/7	211	5	50.1	41.1	45.8	42.6	3.4	275.5	nr	nr	nr	nr	36.3	12.0	11.3	7.2	30.2	3.9	13.6	2.8	10.8	5.7	26%
Lewis and Stock (1998) *	SF	30.66	114.83	7/7	47	20	251.8	-7.1	253.4	-2.8	5.7	93.3	-82.0	4.2	-1.5	6.2	35.1	5.5	-4.1	5.5	41.0	4.6	-0.2	4.6			
SFD - San Fermin																											
Lewis and Stock (1998) *	SF	30.73	114.85	8/8	10	56	239.2	-46.2	253.0	1.8	6.5	64.0	-671.1	1.4	-23.9	7.3	34.7	6.0	-8.7	6.0	40.6	5.2	-4.8	5.2			
SRB - Santa Rosa Basin																											
Stock et al. (1999)	SF	30.85	114.97	11/11	170	25	259.4	13.2	259.4	-11.5	2.7	261.6	-232.2	2.0	-120.4	2.7	41.1	3.9	-4.6	3.8	47.0	2.4	8.5	2.4			
ISLA TIBURON																											
SA - Tiburon																											
Oskin et al. (2001)	SF	29.18	112.46	6/7	12	38	219.7	-31.9	235.1	-15.8	5.4	128.6	-299.8	2.4	55.1	5.5	14.5	6.0	8.9	5.4	25.0	4.5	12.8	4.3			
PR - Tiburon																											
Oskin et al. (2001)	MC4	29.07	112.49	5/9	341	23	339.7	37.0	358.1	38.3	5.9	177.4	-114.4	4.2	-0.4	4.7	9.3	6.6	12.0	5.0	7.2	5.9	3.8	4.6	14.0	6.8	66%
Oskin et al. (2001)	MC3	29.07	112.49	13/13	341	23	0.1	64.4	35.6	53.7	2.9	188.4	-440.6	1.3	-63.5	3.5	26.1	12.1	0.2	7.1	22.3	4.1	2.5	2.4	-1.1	5.3	0%
Oskin et al. (2001)	SF	29.07	112.49	10/12	30	24	230.6	-1.7	231.3	-1.3	4.6	100.8	-109.2	3.0	-43.9	4.8	10.7	5.0	-5.6	4.9	21.2	3.8	-1.7	3.8			
PRS - Tiburon																											
Oskin et al. (2001)	MC4	29.05	112.49	8/9	25	10	16.3	32.2	22.7	35.1	3.3	292.2	-170.8	2.7	-0.4	3.0	31.6	5.0	14.6	3.3	31.8	3.4	7.0	2.7			
Oskin et al. (2001)	MC3	29.05	112.49	11/12	25	10	23.0	60.3	40.9	61.0	2.8	240.9	-1151.0	0.9	-78.0	3.4	31.4	12.3	-7.1	7.0	27.6	4.8	-4.8	2.3			
SM - Tiburon																											
Oskin et al. (2001)	MC4	28.98	112.46	9/11	112	12	7.1	34.0	2.6	44.7	3.5	217.0	-122.4	3.0	0.0	3.0	13.8	5.0	5.6	3.4	11.7	4.1	11.5	2.9	4.2	5.0	26%
Oskin et al. (2001)	MC3	28.98	112.46	11/12	195	16	46.0	53.0	23.8	55.6	4.7	96.0	-53.2	4.2	0.0	4.2	14.3	13.2	-1.7	7.6	10.5	6.7	0.6	3.8	5.4	7.3	34%
Oskin et al. (2001)	SF	28.98	112.46	11/13	330	15	225.4	-10.8	226.0	2.7	4.0	121.5	-181.4	2.2	-46.4	4.4	5.4	5.0	-9.6	4.6	15.9	3.3	-5.7	3.3			
BV - Tiburon																											
Oskin and Stock (2003)	SF	28.92	112.47	16/18	nr	nr	nr	nr	232.9	16.4	7.8	23.0	nr	nr	nr	nr	12.3	7.0	-23.3	7.0	22.8	6.5	-19.4	6.3			

Table 1.1 (cont.) Summary of paleomagnetic data and updated rotation values for the Tmr3 (MC3) and Tmr4 (MC4) cooling units of the Tuffs of Mesa Cuadrada and the Tuff of San Felipe (SF), northern Gulf of California, México.

		Location			Bedding		In Situ		Tilt-Corrected		Fisher Statistics		Bingham Statistics				USING MESA CUADRADA REFERENCE SITES (Lewis and Stock, 1998)				USING NEW REFERENCE SITES (This Study)						
Drill Site, Reference	Unit	Lat. (°N)	Long. (°W)	n/n_0	Strike	Dip	D	I	D	I	α_{95}	κ	κ_1	α_{95}	κ_2	α_{95}	R	ΔR	F	ΔF	R	ΔR	F	ΔF	Differential R (TSF-TMC)	Δ Differential R (TSF-TMC)	% of PRE-6.4 Ma Clockwise Rotation
SK - Tiburon**																											
This Study	MC4	29.17	112.35	13/13	339	33	334.1	31.1	355.3	32.7	2.6	231.2	-173.1	2.1	-112.1	2.6	8.8	4.0	17.6	2.9	4.4	2.7	9.4	2.2	25.0	2.7	85%
This Study	MC3	29.16	112.35	22/22	332	54	325.3	48.9	21.6	37.6	1.6	378.9	-507.2	0.9	-123.6	1.9	14.4	11.5	16.3	6.8	8.3	2.1	18.6	1.5	21.1	1.9	72%
This Study	SF	29.16	112.32	24/24	2	29	230.3	-33.5	239.5	-13.1	1.3	-547.5	-472.9	0.9	-205.1	1.4	23.5	3.3	6.2	3.3	29.4	1.5	10.1	1.5			
SONORA																											
Sierra Bacha																											
Darin (2011)	SF	29.55	112.37	19/19	359	55	nr	nr	235.5	4.7	2.6	181.3	nr	nr	nr	nr	19.5	3.8	-11.6	3.8	25.4	2.3	-7.7	2.3			
PC - Punta Chueca																											
Bennett et al. (in review)	MC3	28.99	112.08	11/11	342	37	331.6	71.9	53.3	56.3	1.8	596.5	-449.0	1.4	-302.2	1.7	46.1	11.7	-2.4	6.8	40.0	2.9	-0.1	1.8	12.8	5.0	24%
Oskin et al. (2001)	SF	29.02	112.08	13/13	13	73	210.1	-59.6	262.9	-11.6	2.2	323.9	-1150.0	0.8	-108.8	2.7	42.4	4.0	4.7	3.7	52.8	2.1	8.6	2.0			
BK - Bahia Kino																											
Oskin et al. (2001)	SF	28.88	112.01	10/11	10	71	199.7	-55.4	245.6	-10.4	3.9	138.2	-167.1	2.4	-57.6	4.2	25.0	5.0	3.5	4.5	35.5	3.3	7.4	3.3			
HE - Hermosillo**																											
This Study	SF	28.98	111.00	5/7	170	21	204.5	-1.1	202.5	-10.0	4.8	269.0	-173.5	3.4	-0.5	3.8	-13.4	5.1	3.1	5.0	-7.6	3.9	7.0	3.8			
																Average, both SF and MC3	**27.5**	**8.6**	**-1.5**	**6.3**	**29.9**	**5.1**	**2.2**	**4.1**			
																Average, SF only	**27.5**	**5.6**	**-3.5**	**5.4**	**35.1**	**4.3**	**0.9**	**4.3**			
																Average, MC3 only	**27.3**	**13.2**	**1.5**	**7.7**	**21.8**	**6.3**	**4.1**	**3.7**			
																Error Weighted Average									**16**		**48%**

n/n_0 . number of samples used to determine site mean vector/number of samples analyzed
D - Declination, in degrees
I - Inclination in degrees (positive is down, negative is up)
α95 - cone of 95% confidence about mean direction
κ - the precision parameter (Fisher, 1953)
R - Rotation, in degrees; for Isla Tiburón and Sonora sites, 2.3° has been added to R to account for finite rotation of reference locality due to Pacific-North America plate displacement
ΔR - Rotation error, in degrees
F - Flattening, in degrees
ΔF - Flattening error, in degrees
R, ΔR, F, ΔF, α95 all calculated according to Beck (1980) and Demarest (1983)
κ_1, κ_2, and corresponding α95 values calculated according to Onstott (1980)
nr - value not reported in published study
* Bingham statistics published in Stock et al. (1999)
** We report two new intra-rift paleomagnetic sites in this study.
Paleomagnetic data were analyzed using PaleoMag v3.1b1 (Jones, 2002) to estimate the best-fit of lines and planes for demagnetization paths for each specimen, as described in Kirschvink (1980).

Chapter 2

Stratigraphy and structural development of the late Miocene to Pliocene Southwest Isla Tiburón marine basin, and implications for the formation of the Gulf of California

Chapter is in preparation for submission to the journal *Geosphere*. Author list is:

Scott E.K. Bennett, Michael E. Oskin, Rebecca J. Dorsey, and Alexander Iriondo

2.1 ABSTRACT

Accurate timing information of earliest marine incursion in the Gulf of California is critical for models of paleogeography and for understanding the spatial and temporal evolution of strain accommodation across this obliquely divergent plate boundary. Marine strata exposed on Southwest Isla Tiburón (SWIT) have been cited as evidence for a middle Miocene marine incursion at least 7 million years (Myr) prior to localization of the Pacific-North America plate boundary. A middle Miocene interpretation for SWIT marine deposits has permeated the literature, playing a large role in subsequent interpretations of regional tectonics and rift evolution, the ages of fossil assemblages and marine basins along ~1,300 km of the plate boundary, and the timing of marine incursion into the Gulf of California. We report new detailed geologic mapping and geochronologic data from the marine and non-marine (up-dip) portions the SWIT basin, an elongate, fault-controlled sedimentary basin associated with transpressional and transtensional deformation along the dextral-oblique La Cruz fault. We synthesize these results with previously published biostratigraphic and geochronologic data from SWIT. We map and date the 6.44 ± 0.05 Ma Tuff of Hast Pitzcal, an ash-flow tuff stratigraphically below the marine rocks, and the 6.01 ± 0.20 Ma Tuff of Oyster Amphitheater, an ash-flow tuff interbedded amongst marine conglomerate, stratigraphically low in the SWIT basin. We also map and date a dike-fed rhyodacite lava flow that caps all marine strata and report ages of 3.51 ± 0.05 Ma and 4.13 ± 0.09 Ma from the base of the flow, consistent with previously reported ages of 4.16 ± 1.81 Ma from the flow top and 3.7 ± 0.9 Ma from the feeder dike. Our new mapping and geochronology results confirm a late Miocene to Pliocene age for the SWIT marine basin that is consistent with previously documented late Miocene to early Pliocene (ca. 6.2 - 4.3 Ma) planktonic and benthic foraminifera. In summary, results from microfossil biostratigraphy and

volcanic rock geochronology constrain the earliest marine conditions on southwest Isla Tiburón to ca. 6.4 - 6.0 Ma, coincident with a regional latest Miocene marine incursion in the northern proto-Gulf of California. This regional marine incursion likely flooded a narrow, incipient topographic depression along a ~650 km-long portion of the late Miocene Pacific-North America plate boundary and corresponds in time and space with focused strike-slip faulting and localization of transtensional plate boundary strain.

2.2 INTRODUCTION

Oblique rifting of the Baja California peninsula (Pacific plate) away from mainland Mexico (North America plate) has created a system of marine pull-apart basins, forming the Gulf of California-Salton Trough topographic depression (Fig. 2.1A; Lonsdale, 1989). Fragments of the earliest marine basins, now exposed along the margins of the modern Gulf of California and beneath Colorado River sediments in the Salton Trough, preserve an important record of the earliest marine conditions during localization of the plate boundary (e.g. McDougall et al., 1999; Dorsey et al., 2011; Martín-Barajas et al., 1997; Holt et al., 2000; Carreño, 1992; Oskin and Stock, 2003a). Marine seismic reflection data show that basin formation and subsidence has migrated westward as the Gulf of California opened (Aragón-Arreola and Martín-Barajas, 2007). Thus the earliest evidence of marine conditions should be preferentially preserved along the eastern (North America) rifted margin. Marine rocks located on the southwestern corner of Isla Tiburón (Fig. 2.1B; Gastil and Krummenacher, 1977a,b) represent the only exposed Miocene marine record along the eastern rift margin. This Southwest Isla Tiburón (SWIT) marine basin is located upon North American continental crust and is a small subaerial exposure of the larger offshore Upper Tiburón marine basin (Fig. 2.1). Because of its location and interstratified

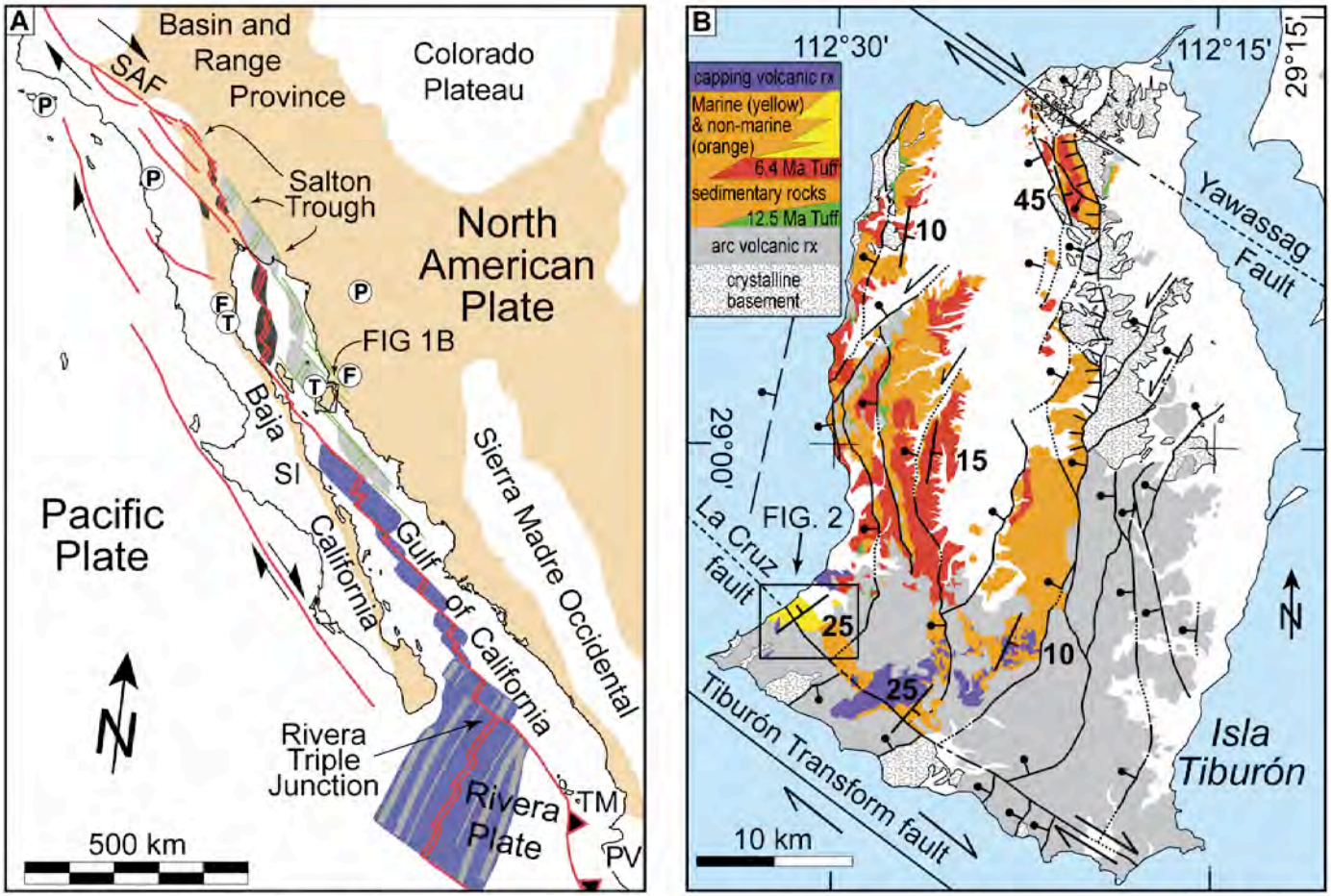

Figure 2.1 (A) Regional tectonic map of western North America showing the diffuse boundary between the Pacific-North American lithospheric plates (after Oskin and Stock, 2003b; Arregón-Arreola & Martín-Barajas, 2007; and Fletcher et al., 2007). Active faults and spreading centers in red; inactive in green. Active pull-apart basins in dark gray; inactive in light gray. Plio-Quaternary hybrid oceanic crust and sediments in solid purple. Basaltic ocean crust in purple with gray positive magnetic sea-floor anomalies. TM - Tres Marías Islands; SI - San Ignacio; PV - Puerto Vallarta. Cross-Gulf Tie Points: P - Poway conglomerate (Abbott and Smith, 1989); F - fusulinid-rich clast conglomerate (Gastil et al., 1973); T - Tuff sequence (Oskin et al., 2001; Oskin and Stock, 2003a).
(B) Geologic map of Isla Tiburón. Geology compiled from Gastil and Krummenacher (1977a); Oskin, (2002); this study.

volcanic rocks that provide age information, the SWIT marine basin is critical for understanding the timing and tectonic controls of earliest marine conditions in the Gulf of California.

Although the role of the SWIT marine basin in understanding the evolution of the Gulf of California has been the subject of decades of study (Gastil and Krummenacher, 1977a,b; Gastil et al., 1999; Oskin and Stock, 2003a), the timing of initial marine conditions on SWIT remains controversial. A group of studies interprets that SWIT marine deposits are middle Miocene in age, bracketed between ~15 - 12 Ma volcanic units (Gastil and Krummenacher, 1977a,b; Gastil et al., 1979; Smith et al., 1985; Smith, 1991; Gastil et al., 1999). Gastil et al. (1999) also document an assemblage of marine microfossils from the SWIT marine deposits that are late Miocene to Pliocene (6.2 - 4.3 Ma), but fail to integrate these biostratigraphic results into their interpretation that the basin is middle Miocene. A recent reexamination of the SWIT basin by Oskin and Stock (2003a) suggests that a middle Miocene age for SWIT marine deposits is derived from erroneous geochronologic (K-Ar) results and crosscutting field relationships that were interpreted inaccurately, in part due to poorly documented and complex structural and stratigraphic relationships. Oskin and Stock (2003a) reinterpret the timing of the SWIT marine basin to be late Miocene to Pliocene (6 - 4 Ma), consistent with the microfossil assemblage of Gastil et al. (1999). Most recently, Helenes et al. (2009) report thick middle Miocene (pre-11.2 Ma) marine deposits from deep exploration wells in the northern Gulf of California, including one well from the Upper Tiburón basin. These findings are at odds with the late Miocene to Pliocene interpretation for the age of the SWIT marine basin by Oskin and Stock (2003a) and with the age of earliest marine deposits elsewhere in the northern Gulf of California (e.g. Escalona-Alcázar et al., 2001) and Salton Trough (e.g. McDougall et al., 1999; Pacheco et al., 2006; Dorsey et al., 2011). The incomplete and controversial interpretations of the timing of the

Southwest Isla Tiburón marine basin inhibits understanding of the geodynamic conditions of oblique rifting that led to marine incursion in the Gulf of California.

In this paper we report the results of an integrated stratigraphic, structural, and geochronologic study of the Southwest Isla Tiburón marine basin. New constraints on timing and structural controls of basin formation, integrated with previously published results, yields a conclusive latest Miocene age (6.4 - 6.0 Ma) for the earliest marine deposits on southwest Isla Tiburón and an improved understanding of the role that oblique rifting played during basin development. A latest Miocene age for earliest marine conditions on Isla Tiburón is locally consistent with microfossil assemblages reported from the basin (Gastil et al., 1999) and regionally consistent with the well-constrained record of a latest Miocene (6.5 - 6.3 Ma) marine incursion into the northern Gulf of California and Salton Trough (Escalona-Alcázar et al., 2001; Oskin and Stock, 2003a; Pacheco et al., 2006; Dorsey et al., 2011). Results from the Southwest Isla Tiburón marine basin do not support an older, middle Miocene marine history in the northern Gulf of California. Rather, these results fit a regional tectonic model where a late Miocene marine incursion into the Gulf of California is coincident in both time and space with localization of strike-slip faulting and basin development along the transtensional Pacific-North America plate boundary.

2.3 PREVIOUS WORK AND CONTROVERSIAL RESULTS

Well-documented exposures of marine strata record late Miocene, south-to-north invasion of marine waters into the Gulf of California rift basin. At Punta Mita, Nayarit, located at the southernmost mouth of the Gulf near Puerto Vallarta (Fig. 2.1A), marine rocks are interstratified with 10 Ma basalt flows (Gastil and Krummenacher, 1978). Within the southern

half of the Gulf of California, to as far northward as Santa Rosalia, Baja California Sur, the earliest marine strata range in age from 8.2 to 7 Ma, based upon biostratigraphic (Carreño, 1985; McCloy et al., 1988; Molina-Cruz, 1994), and isotopic/paleomagnetic (Holt et al., 2000) age constraints. Earliest marine deposits exposed in Baja California Norte and southern California are distinctly younger, with biostratigraphic and isotopic/paleomagnetic age constraints between 6.0 and 6.5 Ma (Boehm, 1984; Dean, 1996; McDougall et al., 1999; Escalona-Alcázar et al., 2001; Pacheco et al., 2006; Dorsey et al., 2011).

Evidence for an earlier, middle Miocene (ca. 11-13 Ma) marine incursion into the central and northern Gulf of California is sparse, and controversial (Helenes and Carreño, 1999). In some localities, marine strata overlie middle Miocene volcanic rocks (e.g. Delgado-Argote et al., 2000; Eberly and Stanley, 1978 as cited in McDougall, 2008). However such a relationship provides only a maximum constraint on the age of marine incursion. Reworked microfossils reported both in outcrop samples (McDougall et al., 1999; McDougall, 2008) and borehole cuttings (Helenes and Carreño, 1999; Helenes et al., 2009) provide indirect biostratigraphic evidence of middle Miocene marine rocks, presumably eroded from elsewhere within the Gulf of California region. Helenes et al. (2009) also report microfossils from borehole cuttings from the northern Gulf of California, which they interpret as *in situ*. If correct, erosion of these strata could be the source of the reworked fossils. However the contention of Helenes et al. (2009) that almost half of the stratigraphic column sampled in the northern Gulf of California may be middle Miocene would, based on marine seismic reflection data (Aragón-Arreola and Martín-Barajas, 2007), require a wide marine seaway by ca. 11-13 Ma. Such a conclusion contradicts onshore constraints on the timing of rifting and opening of the Gulf of California (Oskin et al., 2001). Another issue is where to connect a middle Miocene seaway to the Pacific Ocean when basal

marine strata near the mouth of the Gulf of California are demonstrably younger. This has led to the hypothesis of a marine seaway across the central Baja California peninsula near San Ignacio (Helenes and Carreño, 1999), the existence of which has yet to be confirmed.

The only isotopic age constraints for middle Miocene marine rocks come from interstratified and capping volcanic rocks in the SWIT basin. The first complete geologic map of Isla Tiburón (Gastil and Krummenacher, 1977a) documents the fundamental geologic relationships of this basin (Fig. 2.1), including the underlying Cretaceous crystalline basement and early to middle Miocene volcanic rocks, and the inclined, fossiliferous, marine conglomerate beds. The marine strata are cut and modestly offset (~1 km) by a prominent dextral transform fault, the La Cruz fault (Gastil and Krummenacher, 1977a; Neuhaus, 1989) that parallels the southwestern coastline of the island. Gastil and Krummenacher (1977b) report an 11.2 ± 1.3 Ma (K-Ar) age for a subhorizontal rhyodacite lava flow that caps all marine deposits, interpreted as a minimum age constraint for the SWIT marine basin, and a 3.7 ± 0.9 Ma age for a nearby dike of similar lithology that crosscuts the marine strata. Smith et al. (1985) later revisited the island, and subsequently report a 12.9 ± 0.4 Ma (K-Ar) age for a clast from a monolithologic andesitic breccia deposit, interpreted to be interbedded amongst adjacent outcrops of marine conglomerate. This age corroborated the interpretation of Gastil and Krummenacher (1977b) of a middle Miocene age for SWIT marine deposits. Subsequent studies however failed to confirm these age constraints. Neuhaus (1989) examined the geochemistry of volcanic rocks across SWIT, reporting numerous K-Ar ages of ~21 - 15 Ma on arc-related volcanic rocks that underlie the SWIT basin and ages of ~6 - 4 Ma on tuffs and dikes interpreted to intrude and/or overlie the marine deposits. Gastil et al. (1999) summarize much of this earlier work and report additional geochronologic and paleontological data for SWIT, including a late Miocene to Pliocene (6.2 -

4.3 Ma) assemblage of marine microfossils. Gastil et al. (1999) conclude that marine conditions were present in the SWIT basin as early as 13 - 12 Ma, but do not provide an explanation for the discrepant late Miocene to Pliocene microfossils. Such a middle Miocene interpretation for SWIT marine deposits has played an important role in the age interpretation of other basins throughout the Gulf of California region. Smith (1991) correlates the molluscan assemblage from SWIT to assemblages observed elsewhere, using the SWIT assemblage as a megafossil standard for middle Miocene time. Helenes et al. (2009) prefer the middle Miocene interpretation for SWIT by Gastil et al. (1999) as it would allow a correlation between the SWIT marine deposits and the lowermost strata reported in the Upper Tiburón basin exploration well, which they interpret to be middle Miocene.

The middle Miocene age interpretation for the SWIT basin and the concept of a middle Miocene Gulf seaway was challenged by Oskin and Stock (2003a), who suggested this interpretation was based on a combination of incorrect dates and field interpretations. Geologic mapping by Oskin and Stock (2003a) demonstrates that a 5.7 ± 0.2 Ma age (K-Ar) reported by Neuhaus (1989) on what was interpreted as a dike-fed rhyolite flow that crosscuts and overlies all marine strata is instead from a pyroclastic ash-flow tuff that was emplaced at the base of fossiliferous marine conglomerate. Oskin and Stock (2003a) suggest that the 11.2 ± 1.3 Ma age for the capping rhyolite lava flow is erroneous and that a 4.16 ± 1.81 Ma age (K-Ar) (Neuhaus, 1989) and a 3.7 ± 0.9 Ma age (K-Ar) (Gastil and Krummenacher, 1977b), both interpreted to have been collected from a set of younger, crosscutting dikes, are more likely representative ages for the capping rhyodacite lava flow and its feeder dike. Oskin and Stock (2003a) also propose that the 12.9 ± 0.4 Ma andesitic breccia of Smith et al. (1985) is not interbedded amongst marine strata, and was unknowingly collected in an erosional window into underlying volcanic units,

possibly due to structural complexities. Oskin and Stock (2003a) conclude that the SWIT marine basin is late Miocene to Pliocene in age. However, they did not report any new age constraints and did not document structural and stratigraphic relationships in sufficient detail to fully understand the 12.9 ± 0.4 Ma age constraint from the base of the marine strata by Smith et al. (1985). Here we address these unresolved and controversial relationships from new structural, stratigraphic, and geochronologic results from the SWIT marine basin.

2.4 METHODS

2.4a Geologic, Structural, and Stratigraphic Mapping

We conducted detailed geologic, structural, and stratigraphic mapping during 27 days of fieldwork on SWIT, during March 2009 and March/April 2011 (Figs. 2.2, 2.3). Structural measurements include documentation of brittle fault orientations and kinematic indicators such as fault striae preserved on polished fault planes (Fig. 2.2). Mapping was conducted at 1:10,000-scale on Quickbird satellite imagery with topographic contours derived from the 90-m Shuttle Radar Topography Mission digital elevation model (Farr et al., 2007). Three visible and one infrared bands of Quickbird imagery were pan-sharpened to generate a 0.6 m-resolution false-color base map using spectral bands 4-2-1. 1:5,000-scale and 1:1,000-scale mapping was conducted in many portions of the study area that contain complex structural and stratigraphic relationships. Such high-resolution satellite imagery was not available during the previous mapping efforts on SWIT. To assist with location descriptions, we refer to and number the seven modern-day streams (Arroyos 0-6) that flow northwest through the study area into the Gulf of California, expanding on the Arroyo naming system of Gastil et al. (1999). Arroyo 0 lies west of a prominent peak, Hast Pitzcal (Fig. 2.2), held up by the rhyodacite flow that caps the marine

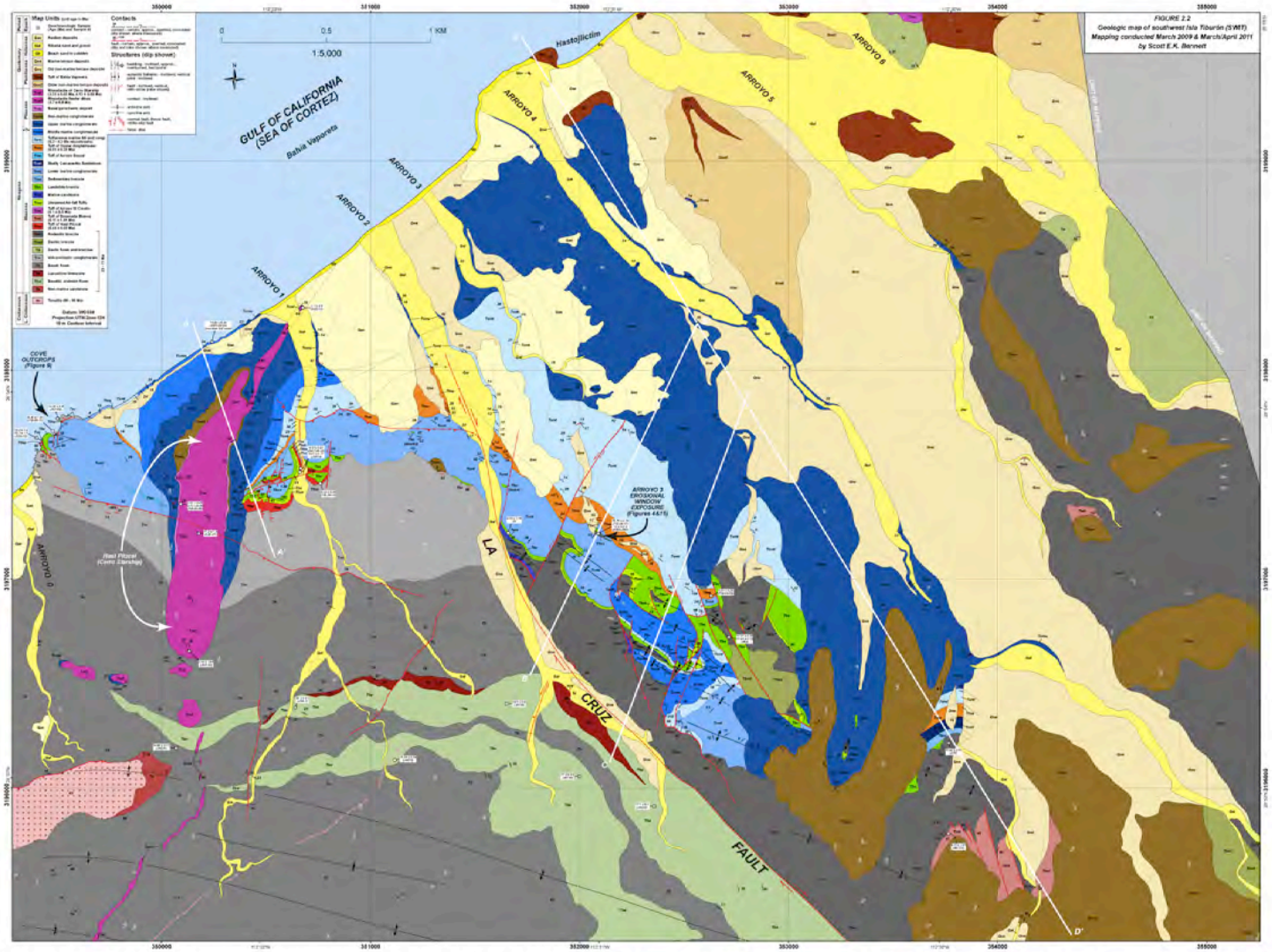

Figure 2.2 1:5,000-scale geologic map of southwest Isla Tiburón (SWIT). New and previously published geochronologic sample locations and isotopic ages shown on map.

Electronic copy of full-sized map is available on data disc in rear pocket. Printed map sheet is 36" tall, 48" wide.

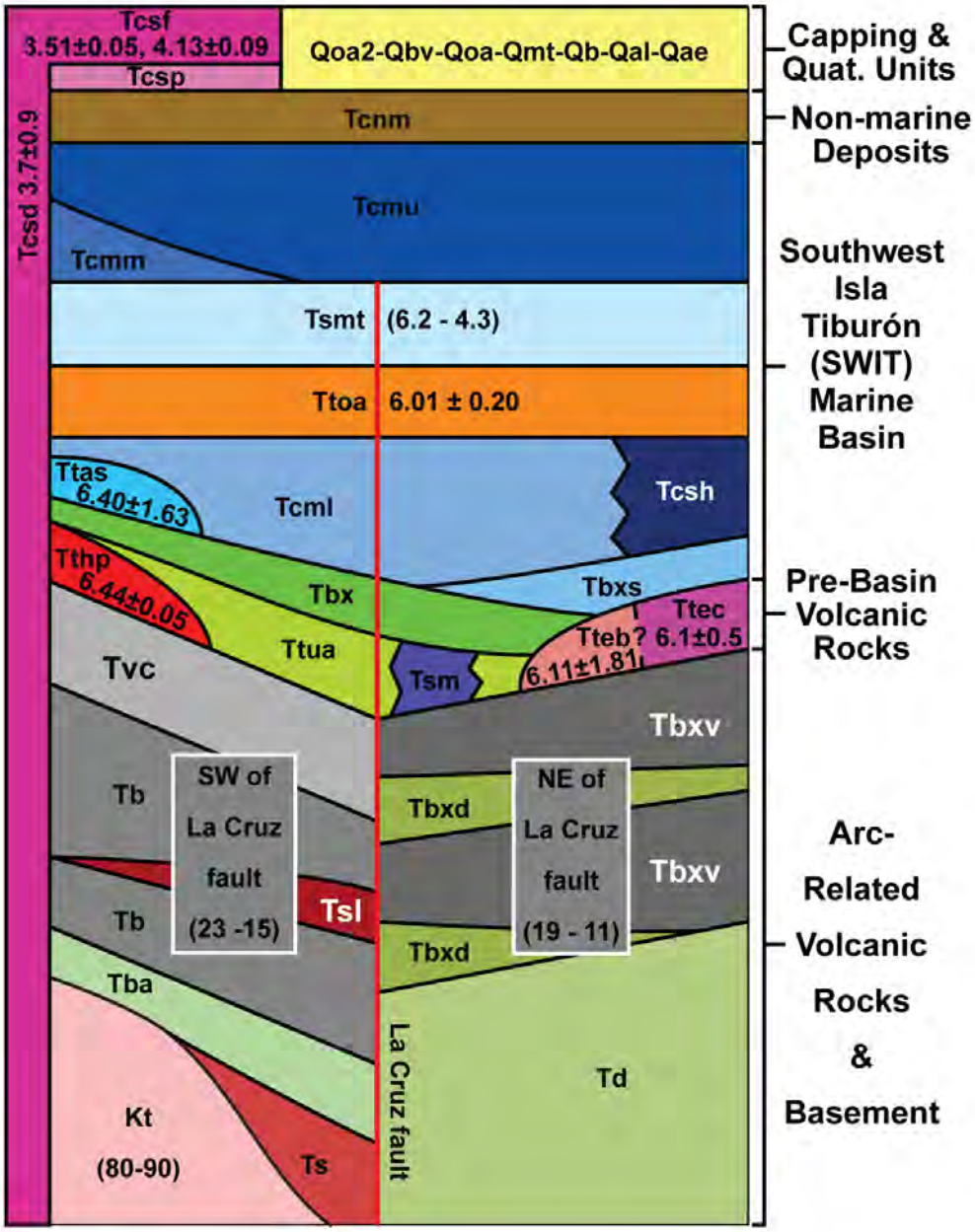

Figure 2.3 Schematic stratigraphic column of geologic map units on southwest Isla Tiburón, as mapped in Figure 2.2. Geochronologic and biostratigraphic ages shown in million years before present (Ma). See text for descriptions and isotopic ages of units.

strata (a peak referred to as Cerro Starship in previous publications). Arroyos 1-6 lie east of Hast Pitzcal and occur sequentially from southwest to northeast across the study area (Fig. 2.2).

2.4b Geochronology

To provide age constraints for marine deposits of the SWIT basin, we analyzed samples of volcanic units that underlie, are interbedded with, and overlie basin deposits. Samples typically consisted of 2 - 5 kg of fresh rock collected from representative, in-place outcrops. In the laboratory, samples were separated into their mineral constituents. Desired mineral phases for isotopic analysis were isolated via standard magnetic, density, and hand picking mineral separation techniques. U/Pb analysis of zircon crystals was conducted in the Stanford-USGS SHRIMP-RG laboratory at Stanford University. Zircon rims were targeted during multiple, single-crystal analyses to avoid older, inherited crystal cores. Typical sample spot beam locations varied between 23 - 32 microns in diameter. Cathodoluminescence (CL) images used in defining the zircon analytical spots will be presented in figures (currently being processed) when submitting manuscripts for publication. Ar/Ar analysis of k-feldspar crystals and volcanic matrix was conducted in the U.S. Geological Survey Thermochronology laboratory facility in Reston, VA. Multiple, single-crystal analyses were conducted to allow detection of older inherited sanidine crystal populations. For all geochronologic results, we report ages with small uncertainties of ≤3%. All geochronologic rock samples were sent to collaborator Alexander Iriondo (Universidad Nacional Autónoma de México, Juriquilla), who oversaw all mineral separation, laboratory analysis, and data interpretation for the ages reported in this manuscript.

2.5 STRATIGRAPHY AND GEOCHRONOLOGY

2.5a Basement Rocks

Basement rocks on SWIT consist entirely of tonalite similar to isotopically-dated outcrops of Late Cretaceous (~80 - 90 Ma) tonalite on northern Isla Tiburón (Gastil and Krummenacher, 1977a,b; Schaaf et al., 1999) and along the adjacent Sonora coastline near Bahía de Kino (Gastil and Krummenacher, 1977a,b; Ramos-Velázquez et al., 2008). Within the SWIT study area, tonalite outcrops are observed only southwest of the La Cruz fault, and are not exposed northeast of the fault (Fig. 2.2).

2.5b Arc-Related Volcanic Rocks

Variably thick packages of early to middle Miocene arc-related volcanic rocks nonconformably overlie crystalline basement rocks on Isla Tiburón. Locally, on SWIT, arc-related volcanic rocks southwest of the La Cruz fault are dissimilar in lithology and age range than the volcanic rocks observed northeast of the fault (Figs. 2.2, 2.3). Southwest of the fault, the succession consists of red volcaniclastic sandstone, basalt flows and breccias, and lacustrine limestone. These are conformably overlain by additional basaltic, rhyolitic, and dacitic-andesite lava flows and breccias. Previous workers report ages ranging from ~23 - 15 Ma for these volcanic units (Fig. 2.2, Table 2.1; Gastil and Krummenacher, 1977b; Neuhaus, 1989; Gastil et al., 1999). Northeast of the La Cruz fault, the volcanic succession consists of interbedded andesite and dacite flows and monolithologic breccias (Fig. 2.4A), as well as polylithologic, poorly stratified, andesitic ash-matrix-supported breccias. Previous workers report ages ranging from 18 - 11 Ma for these volcanic units (Table 2.1; Gastil and Krummenacher, 1977b; Smith et al., 1985; Gastil et al., 1999), including a 11.44 ± 2.61 Ma (Ar/Ar) plateau age on feldspars

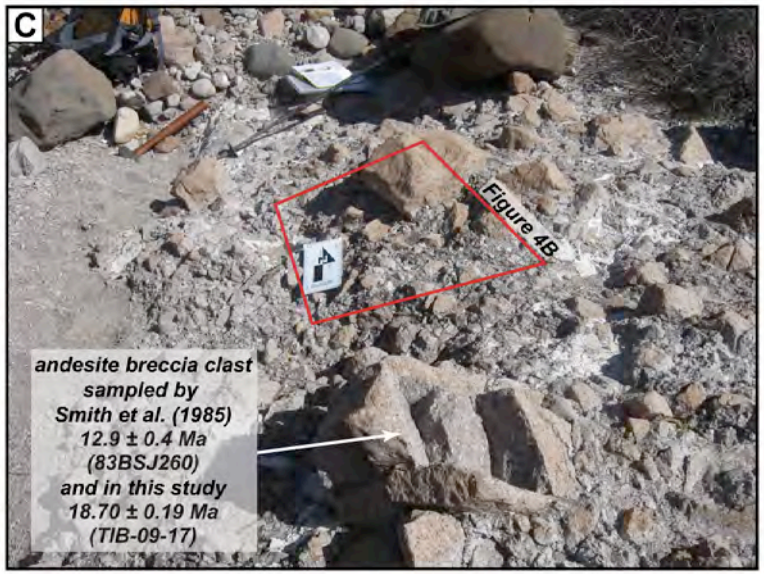

Figure 2.4

(A) Typical exposure of monolithologic volcanic breccia (Tbxv). Photo taken in the upper reaches of Arroyo 4. Hammer is 38 cm-long.

(B) Exposure of volcanic breccia (Tbxv) in erosional window in Arroyo 3, with print out of field photograph provided by J.T. Smith (Smith, personal communication). Photo also published in Carreño and Smith (2007). Matching clasts verify that this is the identical exposure visited by Smith et al. (1985). Note: matching caliche precipitate on vertical face of clast in upper left corner. Arrow on card is 10 cm-long. See geologic map (Fig. 2.2) for map location.

(C) View of andesitic breccia clast sampled by Smith et al. (1985), for which they report a 12.9 ± 0.4 Ma (K-Ar) age. Relatively fresh, angular surfaces of clast in foreground are from sample collection by Smith et al. (1985). After photograph was taken, a portion of this same breccia clast was sampled, for which we report a 18.70 ± 0.19 Ma (U/Pb) age. Area of Figure 4B is shown in red rectangle. Arrow on card is 10 cm-long.

separated from an andesite breccia near the top of this northeastern succession. The age spectrum for this sample was not published, however, and its large uncertainty (~23%) casts doubt on whether a plateau was achieved.

In the upper reaches of Arroyo 3 (Fig. 2.2), we mapped an outcrop of andesitic breccia exposed in an erosional window through younger marine deposits. Using a color copy of a field photo provided to us by J.T. Smith (Smith, personal communication), a photo published in black and white in Carreño and Smith (2007), we located the exact andesitic breccia outcrop (Fig. 2.4B) and previously sampled breccia clast (Fig. 2.4C) in this Arroyo for which Smith et al. (1985) report a 12.9 ± 0.4 Ma (K-Ar) age. Zircons separated from our sample of this same breccia clast yield an U/Pb age of 18.70 ± 0.19 Ma (Fig. 2.5A; Table 2.2), consistent with our interpretation that this deposit is part of the early to middle Miocene arc-related volcanic section that underlies the marine strata.

2.5c Pre-Basin, Syn-Rift Volcanic Rocks

An angular unconformity separates the middle Miocene arc-related volcanic rocks from syn-rift strata. On SWIT, three tuff units occur immediately above this unconformity. Due to the discontinuous nature of these outcrops, it is uncertain how these tuffs relate to the more stratigraphically contiguous overlying volcanic and sedimentary rocks of the SWIT basin. Unlike the SWIT basin strata, the pre-basin syn-rift volcanic rocks cannot be correlated across the La Cruz fault.

Figure 2.5 206Pb/238U zircon geochronologic ages calculated for volcanic rocks on southwestern Isla Tiburón. Tera-Wasserburg concordia diagram (left) and age spectrum diagram (right) for (A) andesite breccia (Tbxv) in Arroyo 3 erosional window that underlies the SWIT marine basin, (B) Tuff of Oyster Amphitheater (Ttoa) interbedded within the marine basin, and (C) the Rhyodacite of Cerro Starship (Tcsf) that caps the marine basin. Zircon crystals omitted from mean age calculation are gray squares with gray, dashed error ellipses. Relatively younger zircons have high uranium concentrations (Table 2.2) and are omitted from mean age due to possible lead loss. Relatively older zircons are omitted due to potential inheritance. See Table 2.2 for analysis data.

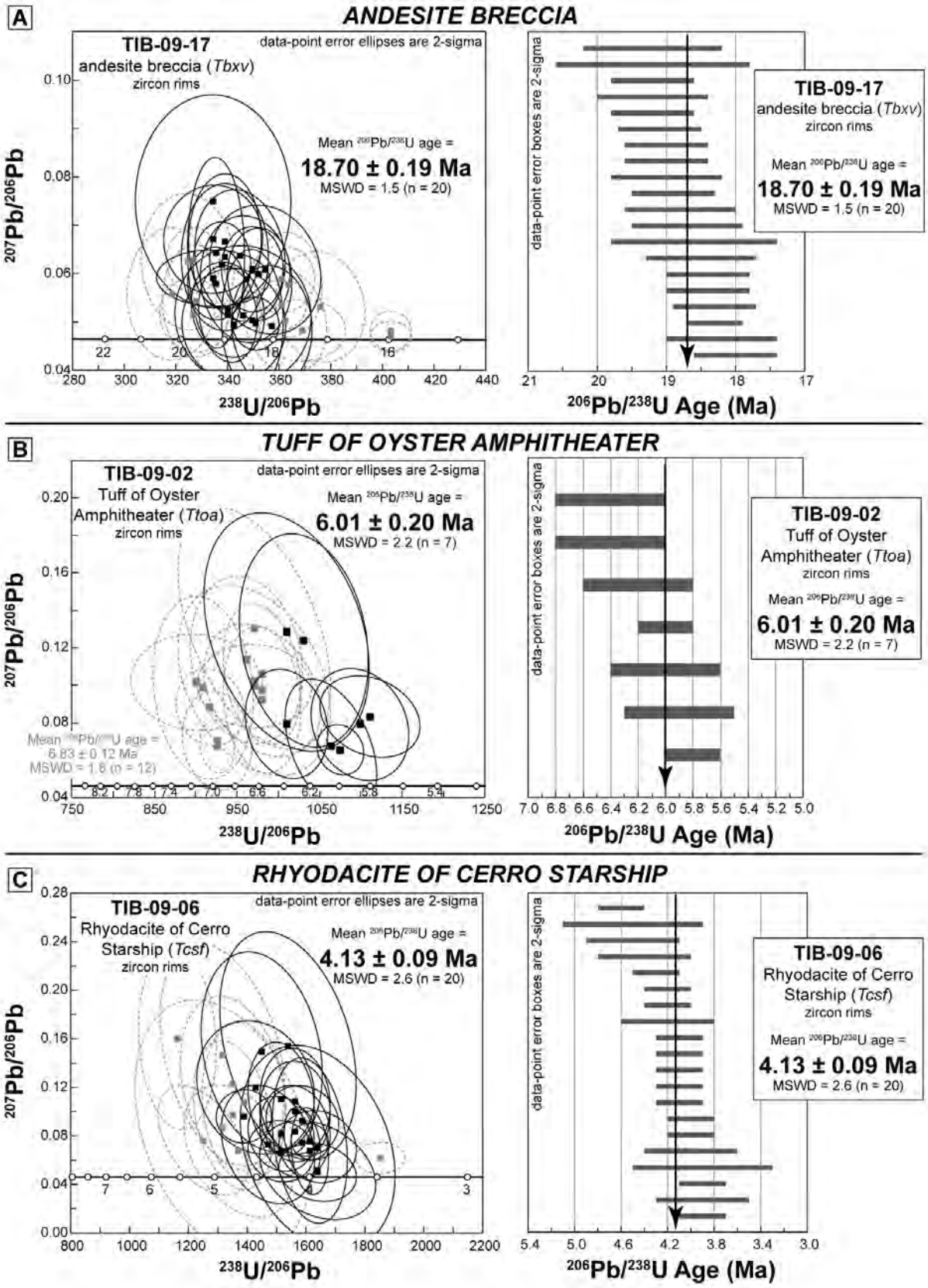
A
ANDESITE BRECCIA
TIB-09-17
andesite breccia (Tbxv)
zircon rims
data-point error ellipses are 2-sigma
Mean 206Pb/238U age =
18.70 ± 0.19 Ma
MSWD = 1.5 (n = 20)
207Pb/206Pb
238U/206Pb
data-point error boxes are 2-sigma
206Pb/238U Age (Ma)
B
TUFF OF OYSTER AMPHITHEATER
TIB-09-02
Tuff of Oyster
Amphitheater (Ttoa)
zircon rims
data-point error ellipses are 2-sigma
Mean 206Pb/238U age =
6.01 ± 0.20 Ma
MSWD = 2.2 (n = 7)
Mean 206Pb/238U age =
6.83 ± 0.12 Ma
MSWD = 1.8 (n = 12)
207Pb/206Pb
238U/206Pb
data-point error boxes are 2-sigma
206Pb/238U Age (Ma)
C
RHYODACITE OF CERRO STARSHIP
TIB-09-06
Rhyodacite of Cerro
Starship (Tcsf)
zircon rims
data-point error ellipses are 2-sigma
Mean 206Pb/238U age =
4.13 ± 0.09 Ma
MSWD = 2.6 (n = 20)
207Pb/206Pb
238U/206Pb
data-point error boxes are 2-sigma
206Pb/238U Age (Ma)

2.5c1 Tuff of Hast Pitzcal (Tthp)

The Tuff of Hast Pitzcal (*Tthp*), is a white, crystal-rich, rhyolitic, non-welded to slightly welded ash-flow tuff, up to 15 m-thick, with 5 - 10% phenocrysts of alkali feldspar > quartz, 2% white and orange pumice up to 2 cm long, and 2% angular andesite and dacite lithic fragments up to 2 cm long. Discontinuous outcrops of *Tthp* unconformably overlie arc-related volcanic rocks (Fig. 2.2) and are observed only southwest of the La Cruz fault on both sides of Arroyo 1 (Fig. 2.6) and just east of Arroyo 0, in a small cove along the shoreline (Fig. 2.2). Neuhaus (1989) reports a K-Ar age of 5.67 ± 0.17 Ma for a rhyolite observed on the western side of Arroyo 1 (his sample 'JN51a'), likely from *Tthp*. *Tthp* itself is nowhere in depositional contact with marine strata. We collected a sample of *Tthp* from outcrops on the eastern side of Arroyo 1. Sanidine crystals separated from this sample of *Tthp* yield an Ar/Ar age of 6.44 ± 0.05 Ma (Fig. 2.7A; Table 2.3). This new geochronologic age is consistent with an Ar/Ar age of 6.67 ± 0.83 Ma (Oskin, 2002) and similar to a K-Ar age of 5.67 ± 0.17 Ma (Neuhaus, 1989; Gastil et al., 1999) both from *Tthp* outcrops on the western side of Arroyo 1 (Fig. 2.2; Table 2.1). The isotopic age, lithology, and phenocrysts assemblage of this Tuff of Hast Pitzcal are strikingly similar to the Tmr3 cooling unit of the regionally-extensive 6.4 Ma Tuffs of Mesa Cuadrada (Oskin and Stock, 2003b). It is possible that the Tuff of Hast Pitzcal may be a distal, non-welded equivalent to this unit, which occurs as thick, densely welded tuff ~3 km northeast of Arroyo 6 (Fig. 2.1B; Oskin 2002).

2.5c2 Tuff of Ensenada Blanca (Tteb)

The Tuff of Ensenada Blanca (*Tteb*) is a ~15 - 20 m-thick, densely-welded ash-flow tuff that is commonly burgundy-colored, but locally may be purple- or orange-colored, depending on

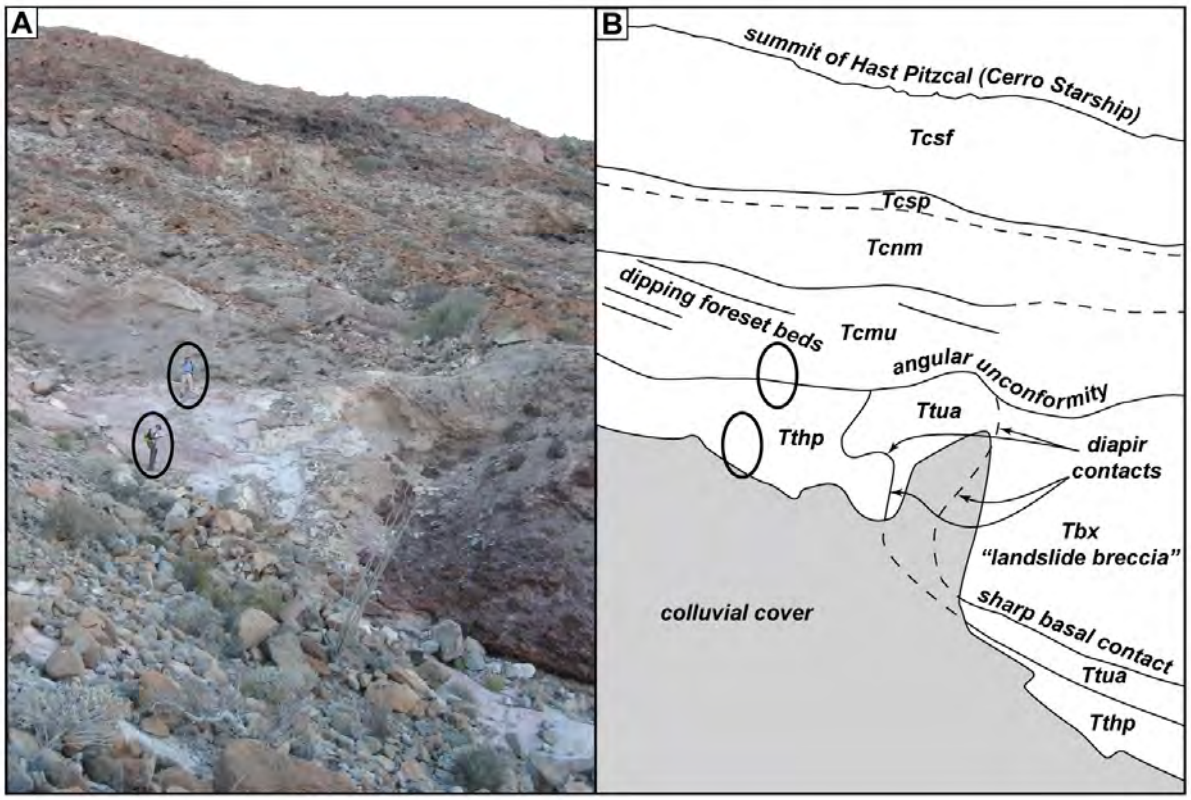

Figure 2.6 View of angular unconformity between pre-basin volcanic units (Tthp, Ttua, Tbx) and overlying marine deposits (Tcmu), non-marine sediments (Tcnm), and volcanic units (Tcsp, Tcsf). Photo taken looking northwest along eastern flank of Hast Pitzcal, west of Arroyo 1. Geologists for scale.

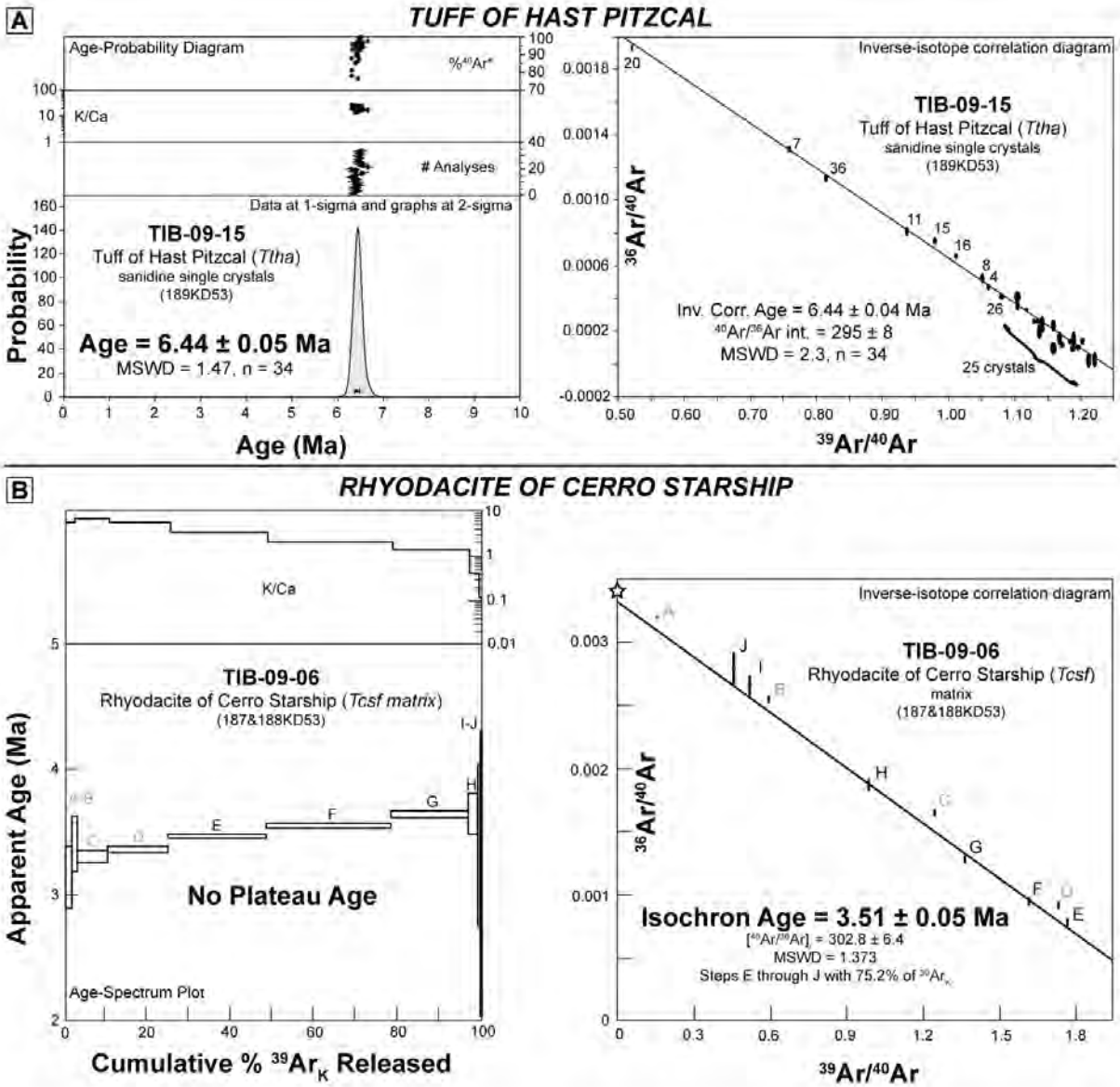

Figure 2.7 40Ar/39Ar geochronologic ages calculated for volcanic rocks on southwestern Isla Tiburón.

(A) %40Ar*, K/Ca ratios, and age probability diagram of multiple, single-grain, total fusion ages on potassium-feldspar crystals (left) and inverse-isotope correlation diagram (right) for the Tuff of Hast Pitzcal (Tthp) that immediately underlies the SWIT marine basin. See Table 2.3 for analysis data.

(B) K/Ca ratios and age spectrum plot (left) and inverse-isotope correlation diagram (right) for volcanic matrix of the Rhyodacite of Cerro Starship (Tcsf) that overlies the SWIT marine basin. Gray shaded letters indicate steps excluded from the isochron age determination. See Table 2.4 for analysis data.

the degree of welding and vapor-phase alteration. The lower section of *Tteb* displays a crystal-poor, 3 cm-thick, brown basal vitrophyre. Brown to black flattened pumice fiamme are oriented sub-parallel to its basal contact and increase in concentration above the vitrophyre, weathering out as elongate voids. *Tteb* is crystal-poor, with <1% phenocrysts of feldspar (plagioclase?) > pyroxene > quartz. *Tteb* unconformably overlies arc-related volcanic rocks and is observed only northeast of the La Cruz fault in Arroyos 4 and 5 (Fig. 2.2). Neuhaus (1989) reported a 6.11 ± 1.81 Ma (K-Ar) whole rock age from *Tteb* outcrops in Arroyo 4 (their sample 'MC275'). *Tteb* is nowhere in contact with marine strata. However, *Tteb* exposures in the upper reaches of Arroyos 4 and 5 underlie non-marine conglomerate deposits that we interpret to be coeval with marine deposits (see Section 5d).

2.5c3 Tuffs of Arroyo El Canelo (Ttec)

The Tuffs of Arroyo El Canelo (*Ttec*), a package of four to six distinctive cooling units (Oskin and Stock, 2003b), locally overlies arc-related volcanic rocks northeast of the La Cruz fault and northeast of Arroyo 6 (Fig. 2.2). This unit also overlies the 6.4 Ma Tuffs of Mesa Cuadrada north of the study area (Oskin and Stock, 2003b). Nagy et al. (1999) report a 6.1 ± 0.5 Ma (Ar/Ar) age for correlative *Ttec* outcrops in the Puertecitos Volcanic Province of northeastern Baja California. The outcrops mapped northeast of Arroyo 6 are the southernmost, distal exposures of the Tuffs of Arroyo El Canelo documented on the eastern side of the Gulf of California. *Ttec* is nowhere in contact with marine strata.

2.5d Southwest Isla Tiburón (SWIT) Marine Basin

2.5d1 Unnamed Air-Fall Tuffs (Ttua)

A sequence of tan, crystal-poor, ash and pumice lapilli air-fall tuff beds (*Ttua*) occurs at the base of the SWIT basin and is the oldest map unit observed on both sides of the La Cruz fault (Figs. 2.2 and 2.3). West of Arroyo 1, some of the thickest observed deposits of *Ttua* contain thin interbeds of angular welded tuff clast breccia, similar to an overlying, thicker landslide breccia deposit mapped as unit *Tbx*. Deposits of *Ttua* are discontinuous, 1 - 5 m thick, and nowhere in contact with marine strata. No published radiometric age exists for *Ttua*. However, the unit conformably overlies the 6.44 ± 0.05 Ma Tuff of Hast Pitzcal in outcrops adjacent to Arroyo 1 (Fig. 2.8A).

2.5d2 Marine Sandstone (Tsm)

The earliest marine deposits recognized in the SWIT basin are a <5 m-thick set of fossiliferous ash-rich sandstone beds (*Tsm*) that unconformably overlie arc-related volcanic rocks. These strata are observed only northeast of the La Cruz fault, on the northeast side of Arroyo 2. This unit consists of moderately stratified, light gray, coarse-grained sandstone with an ash-rich matrix and rare fragments of marine macrofossils (e.g. bivalves). Deposits of *Tsm* are discontinuous, but consistently observed at the same stratigraphic level as the unnamed air-fall tuffs (*Ttua*) elsewhere in the basin, though these units are nowhere observed in contact. The ash-rich matrix in *Tsm* could be sourced from the underlying *Tthp* and/or these air-fall tuffs.

2.5d3 Landslide Breccia (Tbx)

Landslide breccia deposits (*Tbx*) unconformably overlie arc-related volcanic rocks, the 6.44 ± 0.05 Ma Tuff of Hast Pitzcal (*Tthp*), marine sandstone (*Tsm*), and the unnamed air-fall tuffs (*Ttua*) and are observed on both sides of the La Cruz fault (Fig. 2.2). *Tbx* forms a distinctive marker at or ~5 m stratigraphically above the base of all marine rocks. *Tbx* outcrops are 2 - 15 m thick and are continuous across the study area except where locally absent at paleotopographic highs between Arroyos 1 and 2 and in Arroyo 4. Deposits of *Tbx* consist of distinctive, burgundy-colored, clast-supported, monolithologic breccia with angular clasts of densely-welded rhyolite tuff (Figs. 2.6 and 2.8A,B). The boundaries of breccia clasts truncate volcanic textures such as eutaxitic foliation of flattened pumice fiamme, indicating that this unit is sourced from an older ash-flow tuff that was fragmented after cooling and welding of the original deposit, and subsequently mobilized and emplaced as a breccia deposit. Breccia clasts in *Tbx* are identical to primary tuff outcrops of *Tteb* in Arroyo 4, suggesting it was the source of the landslide breccia (*Tbx*) and possibly also the source of thinner breccias interstratified with the unnamed air-fall tuffs. Gastil et al. (1999) report a 9.02 ± 1.18 Ma (Ar/Ar) plateau age on plagioclase crystals separated from a *Tbx* outcrop on the northeast side of Arroyo 2 (their sample 5). Although the error bounds for the reported ages for *Tteb* (6.11 ± 1.81 Ma) and *Tbx* barely overlap at 7.9 Ma, they are quite disparate overall. The spectra for the 9.02 ± 1.18 Ma (Ar/Ar) plateau age on *Tbx* was not published by Gastil et al. (1999), making it difficult to assess its reliability.

2.5d4 Sedimentary Breccia (Tbxs)

Sedimentary breccia deposits (*Tbxs*) overlie the landslide breccia (*Tbx*) and older arc-related volcanic rocks and are observed discontinuously on both sides of the La Cruz fault

Figure 2.8 Breccia units observed at base of SWIT marine basin.

(A) Distinctive landslide breccia (Tbx) in sharp contact above unnamed air-fall tuffs (Ttua). Hammer for scale. Photo from Neuhaus (1989).

(B) Typical outcrop texture of distinctive landslide breccia deposit (Tbx). Eutaxitic foliation of flattened pumice fiamme is visible in large breccia clasts, similar to intact source outcrops of the Tuff of Ensenada Blanca (Tteb). Hammer handle is ~3.5 cm-wide.

(C) Typical outcrop of polylithologic sedimentary breccia (Tbxs) that discontinuously underlies marine deposits in Arroyos 1 and 4. Photo taken in the upper reaches

adjacent to Arroyo 4 and Arroyo 1 (Fig. 2.2). *Tbxs* consists of clast-supported, very poorly sorted, angular to sub-angular sedimentary pebble-cobble-boulder breccia (Fig. 2.8C). The unit is massive to poorly-stratified and lacks fossils. Clasts are up to 1 m in length and include andesite, dacite, and rhyolite. *Tbxs* deposits are up to ~5 m thick and are interpreted to be the result of a debris flow or rock avalanche, likely in either a non-marine or marginal-marine setting (Keogh, 2010).

2.5d5 Lower Marine Conglomerate and Sandstone (Tcml)

Marine conglomerate and sandstone deposits (*Tcml*) conformably overlie older volcanic units (e.g. *Tbx*, and arc-related volcanic rocks; Fig. 2.9) and are observed on both sides of the La Cruz fault near the base of the SWIT basin (Fig. 2.2). *Tcml* deposits consist of poorly-sorted, conglomerate with sub-angular to sub-rounded clasts up to boulder size and matrix-supported conglomerate, sandy conglomerate, and medium- to coarse-grained sandstone (Fig. 2.10 A-C). *Tcml* clasts are arc-related volcanic rocks and welded tuff clasts derived from either *Tteb*, *Tbx*, or other units not present in the study area (Fig. 2.10D). Rare to common marine macrofossils include the remnants of barnacle bases on clasts (Fig. 2.10E) and rare large oysters (Fig. 2.10F). Coarse conglomerate deposits of *Tcml* in Arroyo 2 are estimated to be ~130 m thick (Keogh, 2010).

2.5d6 Shelly Calcarenitic Sandstone (Tcsh)

Shelly calcarenitic sandstone (*Tcsh*) deposits locally overlie sedimentary breccias deposits (*Tbxs*), observed only in the upper reaches of Arroyo 4 (Fig. 2.2) where they are ~12 m thick (Keogh, 2010). Deposits of *Tcsh* consist of massive, poorly-sorted, pebbly calcarenitic

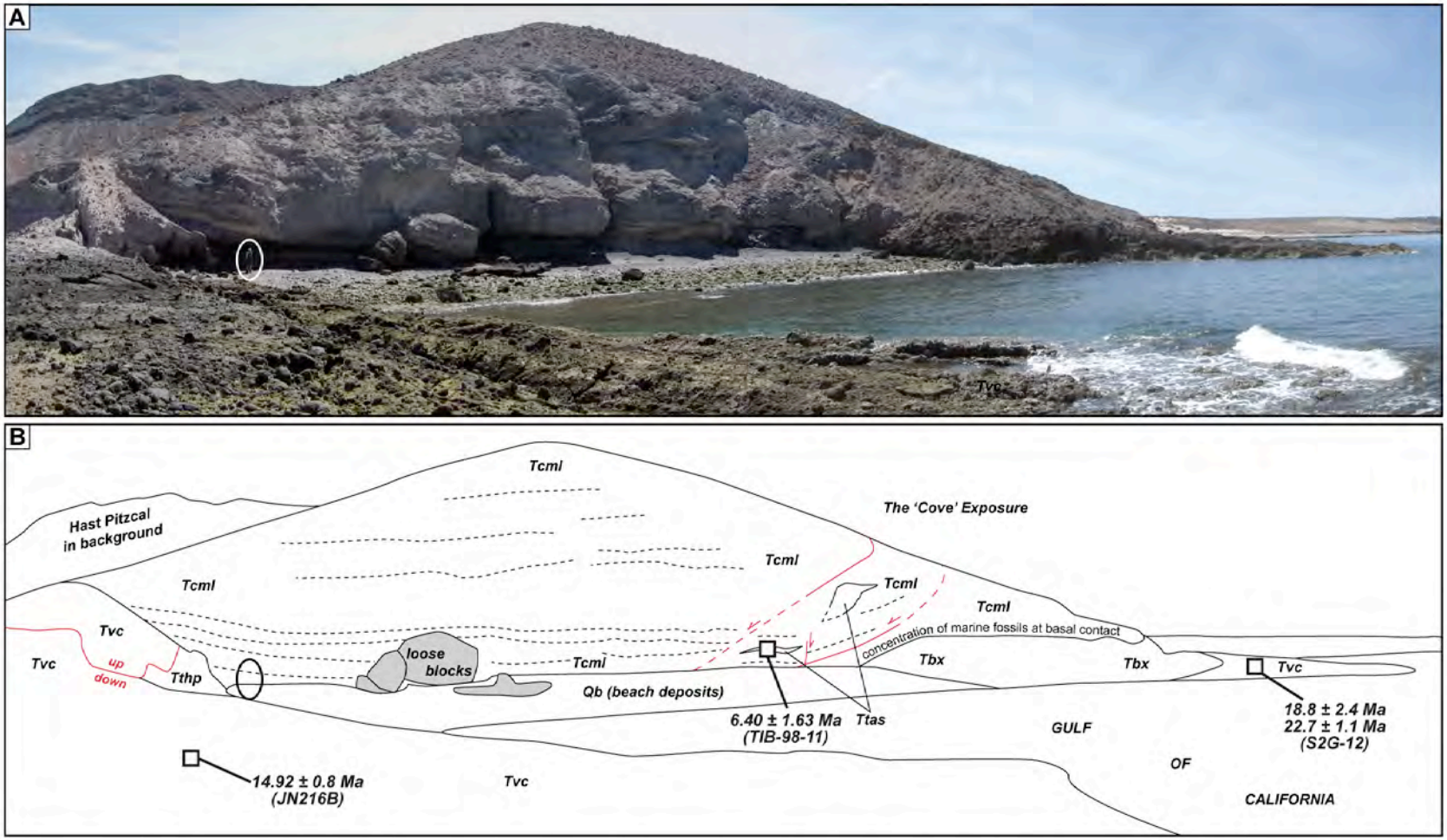

Figure 2.9 (A) Panoramic view of the 'cove' outcrops where the floor of the marine basin is well exposed. (B) Annotated interpretation of panorama in A. Marine conglomerate deposits (Tcml) containing discontinuous exposures of the Tuff of Arroyo Sauzal (Ttas) unconformably overlie the landslide breccia (Tbx) and pre-basin volcaniclastic conglomerate (Tvc). Three previously published geochron ologic ages have been reported from this 'cove' outcrop. Geologist for scale. See geologic map (Fig. 2.2) for map location and Table 2.1 for details of units and ages.

Figure 2.10 Field photographs of marine deposits on southwest Isla Tiburón. Hammer in each photo is 38 cm-long, with 12.5-cm wide hammer head.

(A) Moderately- to well-stratified Lower Conglomerate (Tcml) outcrops along coastline, northwest of Hast Pitzcal.

(B) Well-stratified Lower Conglomerate (Tcml) outcrops in the 'cove' (Fig. 2.9).

(C) Fossiliferous Lower Conglomerate (Tcml) outcrops on the western flank of Hast Pitzcal. Black rectangle shows enlargement in Figure 10F.

(D) Poorly-stratified Lower Conglomerate (Tcml) outcrops on the western bank of Arroyo 2. Clast composition is dominated by locally-derived arc-related volcanic rocks with occasional clasts of the distinctive landslide breccia deposit (Tbx).

(E) Boulder within Lower Conglomerate (Tcml) encrusted with remnants of late Miocene barnacles(?).

(F) Enlargement of rectangle area in Figure 10C showing pair of oyster fossils.

(G) Outcrop of tuffaceous marine sandstone (Tsmt) deposits on the eastern bank of Arroyo 2. Lower massive bed contains occasional layers of conglomerate stringers and marine fossils. Upper, well-stratified portion contains fossiliferous sandstone and sandy conglomerate beds. Circled hammer for scale.

(H) Large late Miocene gastropod fossil in Tsmt conglomerate bed.

(I) Sub-vertical burrow (arrows) within tectonically-inclined Tsmt sandstone and conglomerate beds.


A
Tcml
B
Tcml
C
Tcml
D
Tcml
Tbx
clast
E
F
G
Tsmt
Tsmt
H
Tsmt
I
Tsmt

sandstone with abundant shell fragments and clasts of andesite, dacite, and rhyolite (Keogh, 2010). *Tcsh* contains abundant burrows, which obscure most internal bedding structure. *Tcsh* deposits in Arroyo 4 are likely laterally equivalent to Lower Conglomerate deposits (*Tcml*), which are mapped at the same stratigraphic level, along strike to the WNW (Fig. 2.2).

2.5d7 Tuff of Arroyo Sauzal (Ttas)

The Tuff of Arroyo Sauzal (*Ttas*) overlies *Tbx* and forms discontinuous outcrops of non-welded ash-flow tuff just east of Arroyo 0, in a small cove at the shoreline and higher up on the western flank of Hast Pitzcal (Fig. 2.2). In the cove exposure (Fig. 2.9), *Ttas* consists of a 0.5 - 1 m-thick irregular zone of non-welded yellow pumice surrounding a discontinuous core of pink tuff with 20% phenocrysts (alkali feldspar >> clinopyroxene ≈ hornblende >> biotite ≈ plagioclase ≈ zircon) with <1% andesite and basement lithic fragments (Oskin and Stock, 2003a). Oskin (2002) reports an anorthoclase Ar/Ar total gas age of 6.40 ± 1.63 Ma for *Ttas* from this cove outcrop (Fig. 2.9). Oskin and Stock (2003a) interpret that *Ttas* was emplaced over an irregular paleotopographic surface formed by the underlying landslide breccia (*Tbx*) in a shoreline setting. *Ttas* also occurs higher on the steep slope above the cove as a lens-shaped exposure amongst marine conglomerate deposits. Oskin and Stock (2003a) also correlated the Tuff of Arroyo Sauzal to outcrops of the Tuff of Hast Pitzcal in Arroyo 1, which were dated at 5.67 ± 0.17 Ma by Gastil et al., (1999) and re-dated in this study at 6.44 ± 0.05 Ma (Fig. 2.7A; Table 2.3). Our detailed mapping of these outcrops shows this correlation to be incorrect, and that the landslide breccia actually overlies these Tuff of Hast Pitzcal outcrops in Arroyo 1, contrary to the interpretation of Oskin and Stock (2003a).

2.5d8 Tuff of Oyster Amphitheater (Ttoa)

The Tuff of Oyster Amphitheater (*Ttoa*) is a tan to yellowish-orange tuff that conformably overlies marine conglomerate (*Tcml*) and is observed on both sides of the La Cruz fault. Outcrops of *Ttoa* are up to ~30 m-thick in Arroyo 2. In most localities the tuff is non-welded and was probably emplaced within shallow marine water. Thicker tuff deposits display a central low-grade welded zone with black fiamme. *Ttoa* contains 2 - 5% lithic fragments of arc-related volcanic rocks and rare basement, and ~5% phenocrysts of quartz and green, iridescent sanidine. We collected a sample of *Ttoa* from outcrops atop the ridgeline between Arroyo 3 and Arroyo 4, adjacent to a topographic bowl that contains marine conglomerate with abundant oyster shell fossils. At this ridgeline, a ~20 - 30 m-thick outcrop of *Ttoa* exhibits a 5 - 10 m-thick core of slightly welded tuff. Zircons separated from a sample from this welded zone yielded an U/Pb age of 6.01 ± 0.20 Ma (Fig. 2.5B; Table 2.2).

2.5d9 Marine Tuffaceous Sandstone (Tsmt)

Marine tuffaceous sandstone deposits (*Tsmt*) conformably overlie the Tuff of Oyster Amphitheater (*Ttoa*) on both sides of the La Cruz fault. *Tsmt* consists of gray to tan, fossiliferous, ash-rich sandstone beds and occasional interbeds of stratified marine conglomerate (Fig. 2.10G). Ash-rich sedimentary deposits of *Tsmt* are likely reworked portions of the underlying Tuff of Oyster Amphitheater (*Ttoa*). Grains of green, iridescent sanidine are commonly observed in *Tsmt* matrix, similar to phenocrysts observed in *Ttoa*. *Tsmt* deposits are estimated to be 16.5 m thick in Arroyo 4 and laterally thicken to ~90 m in Arroyo 2 and along the coast northwest of Hast Pitzcal (Keogh, 2010). Previous workers report microfossil assemblages from *Tsmt* (unit 'Mss-Unit 4a' of Cassidy (1990); unit 'M8c' of Gastil et al. (1999))

that include benthic and planktonic foraminifera, calcareous nannoplankton, and ostracods that together restrict the age of *Tsmt* to 6.2 - 4.3 Ma (Gastil et al., 1999). Occasional macrofossils are also observed in *Tsmt*, including fragments of oyster, pecten, barnacle, gastropod, and echinoid spines and fragments (Fig. 2.10H; this study; Cassidy, 1990; Gastil et al., 1999). Trace fossils in the form of sub-vertical burrows are rare (Fig. 2.10I). The age range for these macrofossils is not known precisely enough to distinguish between middle or late Miocene (Gastil et al., 1999). However, Stump (1979) assigned a late Miocene age to the assemblage.

2.5d10 Middle Marine Conglomerate and Sandstone (Tcmm)

Marine conglomerate and sandstone deposits (*Tcmm*) conformably overlie the tuffaceous marine sandstone (*Tsmt*), or, less commonly, older units where *Tsmt* is absent. This unit is observed on both sides of the La Cruz fault. *Tcmm* deposits consist predominantly of poorly-sorted conglomerate and coarse-grained sandstone similar to *Tcml*, with a higher concentration of ash matrix. *Tcmm* deposits may appear similar to conglomeratic portions of *Tsmt*, but contain >50% conglomerate beds. Coarse conglomerate deposits of *Tcmm* along the coastline between Arroyos 0 and 1 are estimated to be at least 70 m thick (Keogh, 2010). Oskin (2002) reports an Ar/Ar age of 12.84 ± 0.40 Ma on a rounded clast of welded rhyolite tuff collected from *Tcmm* (location shown on Fig. 2.2). This clast is likely sourced from outcrops of the Tuff of San Felipe, a ~12.5 Ma regional ash-flow tuff (Oskin and Stock, 2003b) exposed just southeast of the SWIT marine basin (Chapter 3 of this thesis).

2.5d11 Upper Marine Conglomerate and Sandstone (Tcmu)

Marine conglomerate and sandstone deposits (*Tcmu*) are the most extensive unit of the SWIT basin, observed on both sides of the La Cruz fault (Fig. 2.2). In most locations, *Tcmu* overlies all aforementioned sedimentary and volcanic Miocene units (e.g. *Tsmt*, *Tbx*, *Ttua*, arc-related volcanic rocks) across a sub-horizontal angular unconformity. Locally, at the distal, northern extent of the exposed SWIT basin, the contact between *Tcmu* and underlying *Tsmt* and *Tcmm* appears conformable. Marine conglomerate deposits of *Tcmu* consist of inclined beds of fossiliferous, pebble to cobble conglomerate, with subrounded to rounded clasts of arc-related volcanic rocks and welded tuff clasts derived from either *Tteb* or *Tbx* (Fig. 2.11). Clasts of the 6.4 Ma Tuffs of Mesa Cuadrada ignimbrite, exposed ~3 km northeast of the study area (Oskin and Stock, 2003b), appear rarely within *Tcmu* (Oskin and Stock, 2003a). *Tcmu* is well-stratified with normal-graded and inverse-graded beds up to ~1 m thick (Fig. 2.11). *Tcmu* appears to have been deposited via subaqueous sediment gravity flows (Cassidy, 1990; Oskin and Stock, 2003a). The inclination of these beds ~15 - 30° (typically ~25°) to the north or northwest is interpreted to be primary dip acquired during deposition. These beds are interpreted to be foresets of a Gilbert-type fan delta system, which are typically constructed on relatively steep slopes via accumulation of coarse fan material into a body of water (Gilbert, 1885). Vertical burrows observed in inclined beds (Fig. 2.11 B,C) are consistent with this non-tectonic interpretation for *Tcmu* bed inclination. Previous workers found no microfossils from samples of *Tcmu* (Cassidy, 1990; Gastil et al., 1999). Common to abundant macrofossils are observed in *Tcmu*, including oyster, pecten, barnacle, gastropod, echinoid spines and fragments, and small corals (this study; Cassidy, 1990; Gastil et al., 1999). The age range for these macrofossils is not known precisely enough to distinguish between middle or late Miocene (Gastil et al., 1999).

Figure 2.11 Field photographs of Upper Conglomerate (Tcmu) on southwest Isla Tiburón.
(A) An inverse graded Tcmu conglomerate bed on the western bank of Arroyo 4. Bed inclination is primary depositional dip.
(B) Inclined Tcmu conglomerate beds on the western bank of Arroyo 4 containing multiple trace fossils. Black rectangle shows enlargement in Figure 11C. Circled hammer is 38 cm-long.
(C) Enlargement of rectangle area in Figure 11B showing multiple burrows in Tcmu sandy conglomerate bed. Sub-vertical burrows (black arrows) are oriented orthogonal to modern-day horizontal, not orthogonal to bedding. This supports that the ~25° inclination in Tcmu beds is due to primary depositional dip not due to tectonic tilting. Circled hammer is 38 cm-long.
(D) Panoramic view of Tcnm and Tcmu outcrops in Arroyo 4. Looking west at exposure where sub-horizontal, non-marine topset beds (Tcnm) laterally grade into inclined, marine foreset beds (Tcmu).
(E) Annotated interpretation of panorama in D.

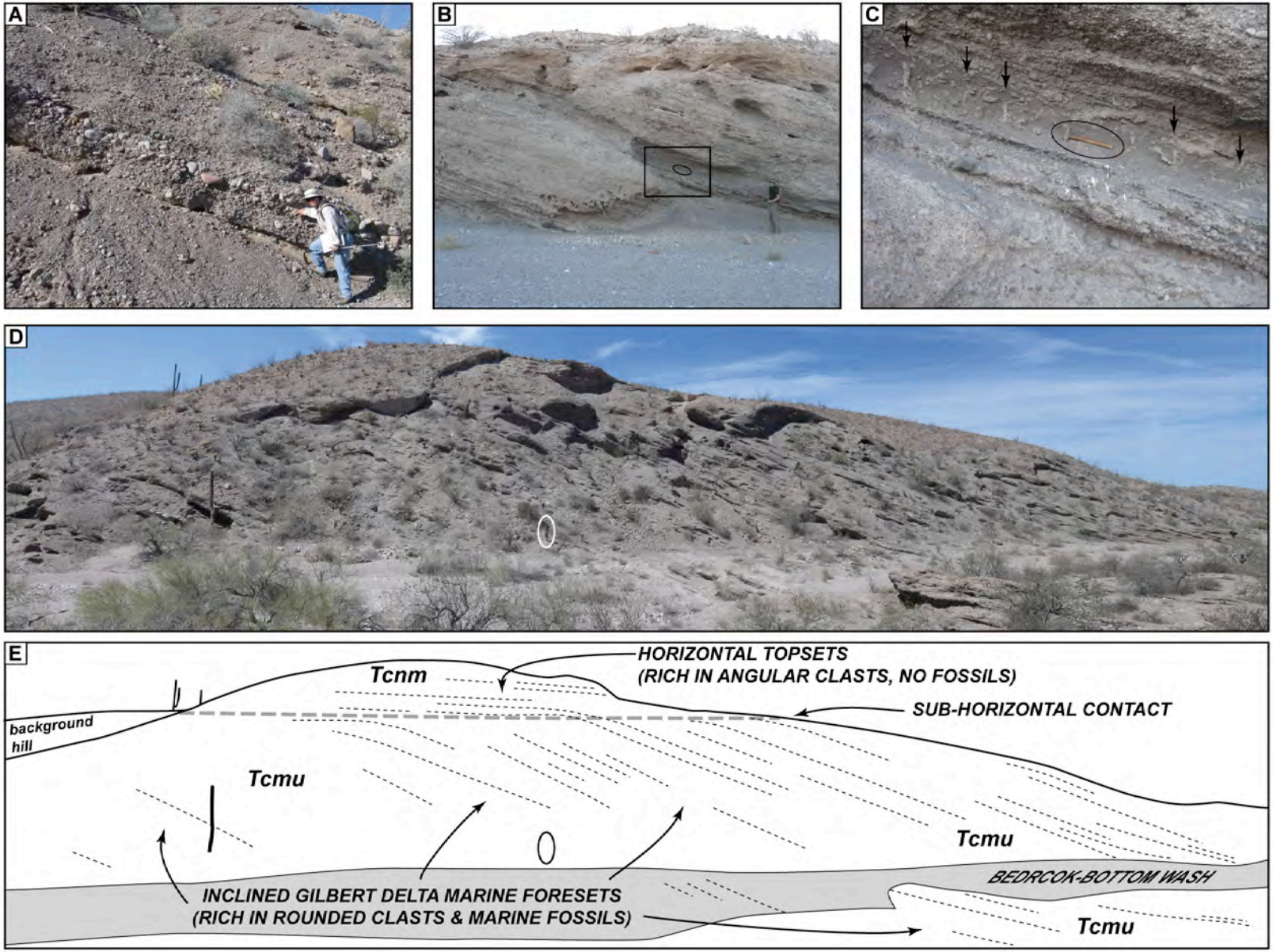
A
B
C
D
E
Tcnm
HORIZONTAL TOPSETS
(RICH IN ANGULAR CLASTS, NO FOSSILS)
SUB-HORIZONTAL CONTACT
background
hill
Tcmu
Tcmu
BEDRCOK-BOTTOM WASH
INCLINED GILBERT DELTA MARINE FORESETS
(RICH IN ROUNDED CLASTS & MARINE FOSSILS)
Tcmu

Thickness of *Tcmu* was greatly exaggerated by Gastil et al. (1999) due to misinterpretation of the inclination of the foresets as structural dip. Here we cite thicknesses measured vertically through the undeformed foreset sequence. *Tcmu* deposits are ~26 m thick in Arroyo 4 (Keogh, 2010) near the southeastern edge of the marine portion of the SWIT basin and are likely of similar thickness along strike to the west-northwest. However, *Tcmu* may be thicker further out in the SWIT basin towards the north. The thickness of *Tcmu* deposits at the modern-day shoreline is difficult to assess because its basal contact with *Tsmt* is below modern-day sea-level and not exposed, and its upper contact with *Tcnm* is not exposed due to erosion. Though, near the shoreline, a ~40 m-high hill between Arroyo 3 and Arroyo 4 is mapped entirely as *Tcmu*, which suggests that *Tcmu* likely exceeds 40 m in thickness at the northernmost exposure of marine deposits.

2.5d12 Non-marine Conglomerate and Sandstone (Tcnm)

Non-marine conglomerate and sandstone deposits (*Tcnm*) overlie all aforementioned sedimentary and volcanic Miocene units, and is observed on both sides of the La Cruz fault (Fig. 2.2). *Tcnm* consists of moderately stratified, sub-horizontal beds of pebble to cobble conglomerate, with angular to subangular clasts of arc-related volcanic rocks and welded tuffs and no fossils (Fig. 2.12A,B). *Tcnm* exposures are mapped at higher elevation relative to marine deposits, located at the tops of many topographic hills near Arroyos 2, 3, and 4. A 5 - 15 m-thick outcrop of *Tcnm* is observed near the top of Hast Pitzcal, stratigraphically beneath a capping lava flow (Fig. 2.2). In the upper reaches of Arroyo 4, *Tcnm* deposits are ~30 m-thick. The northeastern margin of the SWIT basin is mapped on the northeast side of Arroyo 5, where *Tcnm* deposits are perched upon a buttress unconformity in contact against higher elevation hills of arc-

Figure 2.12 Field photographs of Non-marine Conglomerate and Sandstone (Tcnm) on southwest Isla Tiburón.
(A) Moderately stratified exposure of Tcnm. Hammer is 38 cm-long.
(B) Tcnm contains subrounded to angular clasts of locally-derived, middle Miocene arc-related volcanic rocks and late Miocene welded tuffs. Hammer is 38 cm-long.
(C) Panoramic view of northeastern portion of study area. Looking northeast at Arroyo 5 where Tcnm deposits are perched upon and banked up against paleo-topographic highs of pre-basin, arc-related volcanic rocks. These exposures of Tcnm and Tcmu are along the northeastern margin of the SWIT basin. The top of the basin is visible as a sub-horizontal geomorphic bench that dips gently towards the Gulf of California.
(D) Annotated interpretation of panorama in C.

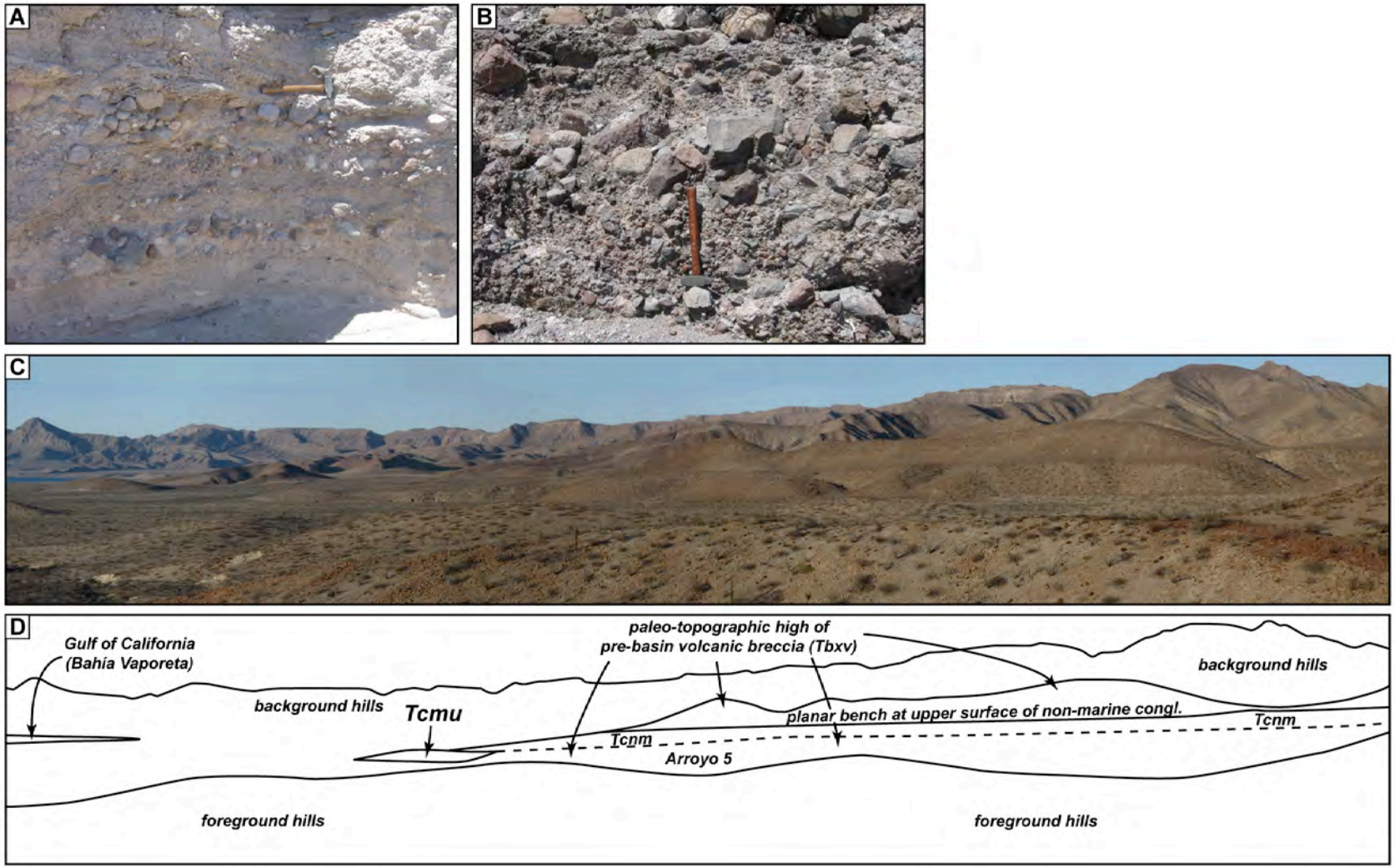
A
B
C
D
Gulf of California
(Bahía Vaporeta)
paleo-topographic high of
pre-basin volcanic breccia (Tbxv)
background hills
background hills
Tcmu
planar bench at upper surface of non-marine congl.
Tcnm
Tcnm
Arroyo 5
foreground hills
foreground hills

related volcanic rocks (Fig. 2.12C,D). Nearby, two small paleo-tributaries of the SWIT basin, carved into older arc-related volcanic rocks, are filled with *Tcnm* deposits (Fig. 2.2). Further inland to the southeast, deposits of *Tcnm* at least 50 m thick are observed almost continuously, in angular unconformable contact with underlying arc-related volcanic rocks.

2.5e Capping Rhyodacite of Cerro Starship (*Tcsf*) and Related Volcanic Units (*Tcsp*, *Tcsd*)

Our observations confirm that the Rhyodacite of Cerro Starship (*Tcsf*) is a 10 - 40 m-thick lava flow that was emplaced subaerially and caps all marine and non-marine strata of the SWIT basin. The lava flow forms a topographically prominent, NNE-trending, elongate hill, Hast Pitzcal (Cerro Starship) (Figs. 2.13A, 2.14A). The base of *Tcsf* is a 1 - 3 m-thick, banded, black glassy vitrophyre, underlain by a discontinuous 1 - 3 m-thick pumice-rich, pyroclastic unit (*Tcsp*) (Fig. 2.13B). *Tcsf* and *Tcsp* overlie all sedimentary units of the SWIT basin as well as older arc-related volcanic rocks. Along the elongate Hast Pitzcal exposure, the lower *Tcsf* contact dips gently northward, towards the Gulf of California (Fig. 2.13A), similar to the underlying sub-horizontal non-marine deposits. The top of the flow is a continuous, weathered, undulatory surface that also dips gently northward (Fig. 2.13C). *Tcsf* consists of 10 - 30% phenocrysts of plagioclase > hornblende > alkali feldspar > opaque minerals > biotite > zircon within a gray to purple aphanitic groundmass that displays macroscopic flow foliation and trachytic alignment of plagioclase phenocrysts. At the outcrop scale, the flow deposit exhibits irregular cm-scale foliation (Fig. 2.13D) that rolls over from sub-horizontal to sub-vertical across 5 - 10 m (Fig. 2.13E), indicating viscous flow prior to cooling.

We collected a sample from the basal vitrophyre of the main flow deposit (Fig. 2.2). Zircons separated from this sample yield an U/Pb age of 4.13 ± 0.09 Ma (Fig. 2.5C; Table 2.2).

Figure 2.13 Field photographs of Hast Pitzcal (Cerro Starship) hill and Pliocene volcanic units that cap and cut through the marine basin on southwest Isla Tiburón.

(A) Looking northwest at Hast Pitzcal. Resistant hilltop is ~1 km in length.

(B) Ash- and pumice-rich pyroclastic deposits (Tcsp) locally underlie the capping Rhyodacite of Cerro Starship (Tcsf) lava flow. Hammer is 38 cm-long.

(C) Looking north along undulatory upper surface of Hast Pitzcal. No crosscutting dikes are observed along crest of hilltop. Circled geologist for scale.

(D) Cm-scale flow banding within porphyritic rhyodacite. Maroon object in center of photo is loose clast. Hammer is 38 cm-long.

(E) Flow banding within rhyodacite outcrops (Tcsf) have highly variable patterns of foliation suggesting viscous flow prior to cooling.

(F) Looking southwest on the eastern flank of Hast Pitzcal at sub-vertical foliation within feeder dikes (Tcsd). Foliation in Tcsd is parallel to outcrop pattern of dike outcrops. Dike leads directly to base of capping Rhyodacite of Cerro Starship (Tcsf) lava flow.

(G) Looking north from southwestern corner of study area. Discontinuous, en echelon rhyodacite dikes (Tcsd) lead to capping Rhyodacite of Cerro Starship (Tcsf) atop Hast Pitzcal.

(H) Looking north at southernmost tip of main flow body of Rhyodacite of Cerro Starship (Tcsf). Base of rhyodacite flow consists of 2 - 4 m-thick black glassy vitrophyre. Geologist standing on middle Miocene arc-related basalt flows. Basal contact of Tcsf is continuous and sharp. No crosscutting dikes are observed. White region in upper left portion of photo is recent landslide scar.

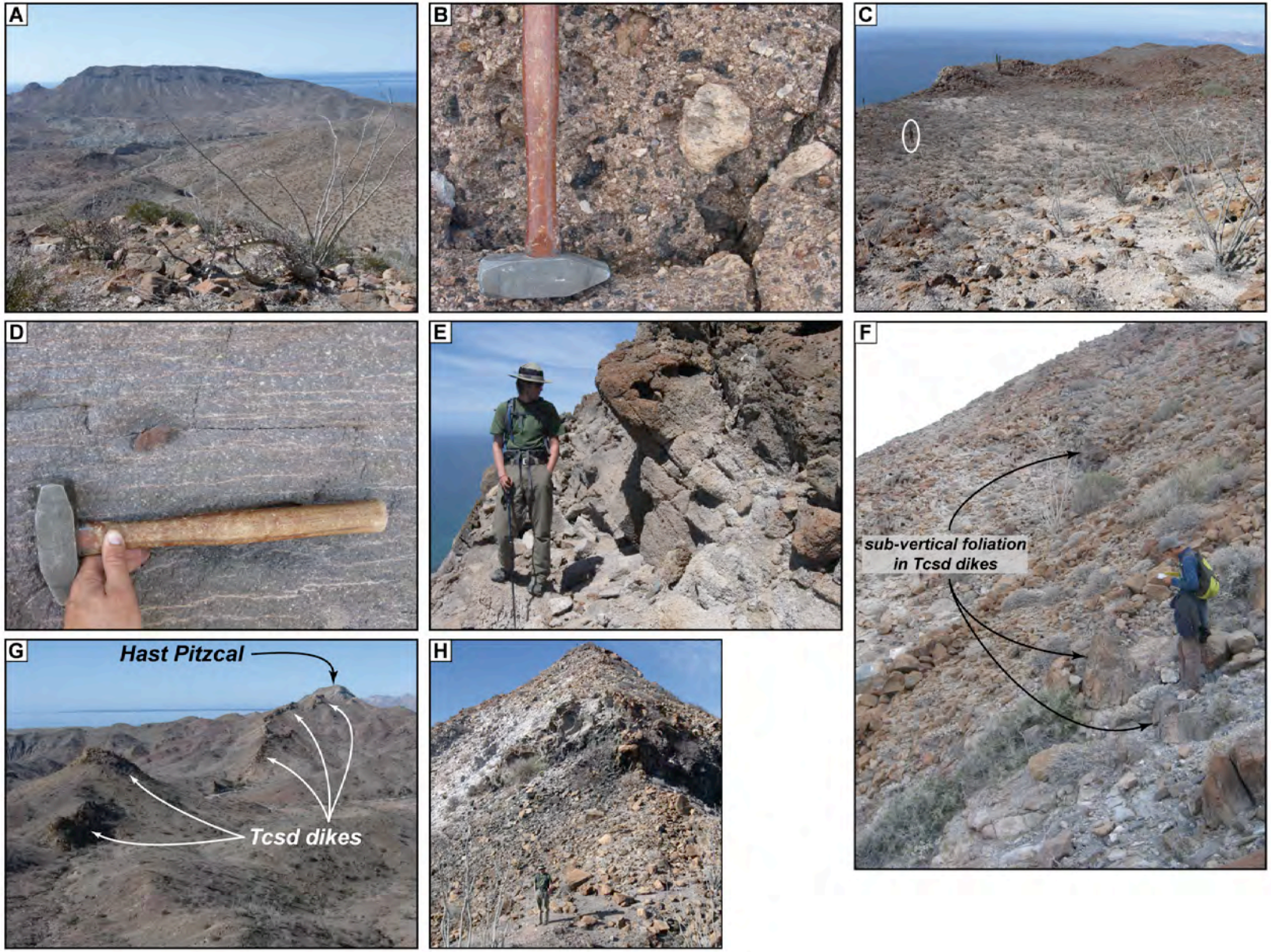
A
B
C
D
E
F
sub-vertical foliation
in Tcsd dikes
G
Hast Pitzcal
Tcsd dikes
H

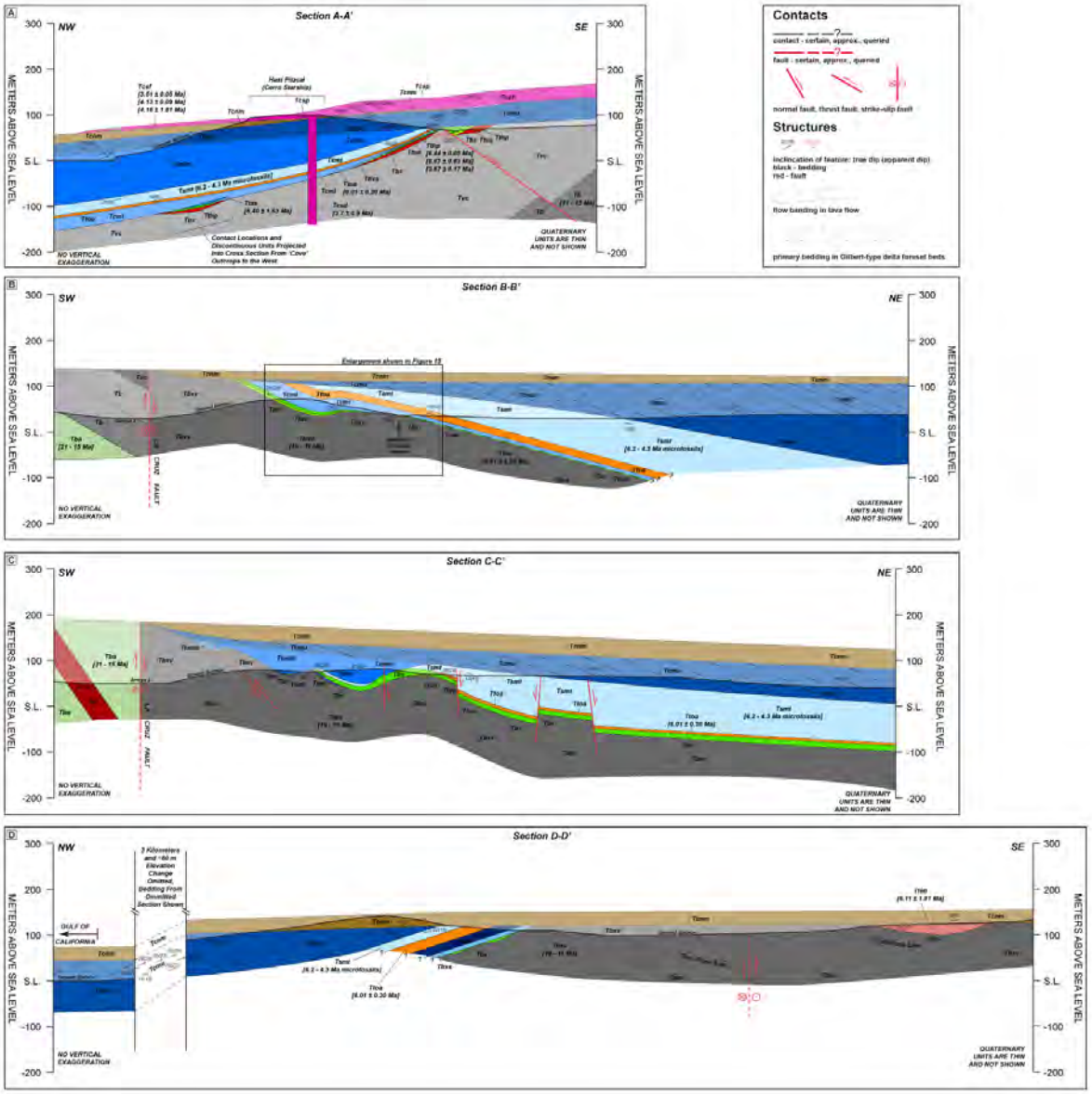

Figure 2.14 (A-D) Geologic cross-sections for southwest Isla Tiburón. Map unit colors and other symbology as in Figure 2.2. Dip values from structural measurements used to construct cross-sections shown near ground surface. Apparent dip values shown in parentheses. See geologic map (Fig. 2.2) for cross-section line locations.

Electronic copy of full-sized cross-section sheet is available on data disc in rear pocket. Printed cross-section sheet is 19" tall, 19" wide.

Analysis of the glass matrix from the same sample yields an Ar/Ar isochron age of 3.51 ± 0.05 Ma (Fig. 2.7B; Table 2.4). We prefer the Ar/Ar isochron age of 3.51 ± 0.05 Ma for this sample, because the Ar/Ar technique provides a better estimate of a true eruption age than the U/Pb technique (Simon et al., 2008). Both of these ages are consistent with a 4.16 ± 1.81 Ma (K-Ar) age that Neuhaus (1989) reported for a sample from the top of this flow (his sample 'JNS-10'). Gastil and Krummenacher (1977b) report an 11.2 ± 1.3 Ma (K-Ar) age from this rhyodacite flow (their sample 'S2B-27'). This age is incongruent with other ages for *Tcsf*, and the stratigraphic position of this flow above in-place late Miocene ash-flow tuffs (*Tthp, Ttas, and Ttoa*).

Mapped outcrops of *Tcsf* on the southwestern flank of Hast Pitzcal overlie a thin patch of inclined marine(?) conglomerate and are unusual because they are at much lower elevation and are not co-planar with the major *Tcsf* flow body (Fig. 2.2). Rather, these outcrops are approximately co-planar with the modern-day colluvial slopes of Hast Pitzcal and are likely the eroded remnants of a relatively intact landslide block, sourced from outcrops at the summit of Hast Pitzcal.

Parallel to and beneath the flow deposits of the Rhyodacite of Cerro Starship (*Tcsf*) and its basal pyroclastic unit (*Tcsp*) is a system of sub-vertical, discontinuous dikes that extend beyond the NNE and SSW ends of Hast Pitzcal (Fig. 2.2). These dikes (*Tcsd*) are rhyodacite in composition and display a pervasive sub-vertical foliation. On the northeastern flank of Hast Pitzcal, a *Tcsd* dike up to ~40 m thick is exposed continuously down into Arroyo 1 (Fig. 2.13F). Gastil and Krummenacher (1977b) report a 3.7 ± 0.9 Ma (K-Ar) age from an exposure of this dike on the east side of Arroyo 1 (their sample 'S2G-13'). South of the mapped *Tcsf* flow, discontinuous, NNE-striking, steeply ESE-dipping *en echelon Tcsd* dikes up to 15 m-thick continue to the southern shoreline of Isla Tiburón (Figs. 2.2, 2.13G).

2.5f Quaternary Sediments and Volcanic Rocks

Multiple Quaternary-age sedimentary and volcanic units post-date the SWIT marine basin. Two generations of older, non-marine, alluvial to fluvial conglomerate and sandstone deposits are found on the flat, low-lying terraces up to 110 m above modern sea-level (Fig. 2.2). The basal contact of these terraces is sub-horizontal, and dips gently towards the Gulf of California, similar to its dissected upper geomorphic surfaces. Remnants of an older generation of alluvial terraces (*Qoa2*) are preserved within 1 - 2 km of the coastline, near the mouths of Arroyos 4 - 6. The Tuffs of Bahía Vaporeta (*Qbv*) are flat-lying welded tuffs observed either interbedded amongst or capping terraces of *Qoa2* deposits. *Qbv* is lithic-rich, with abundant light and dark pumice and 1% anorthoclase phenocrysts (Oskin and Stock, 2003a). A more extensive, younger generation of alluvial terraces (*Qoa*) are observed in arroyos throughout the study area, perched up to ~10 m above the active channels (Fig. 2.2). Thin benches of recent marine terraces are perched ~5 - 10 m above modern sea-level. Between Arroyos 2 - 5, subtle geomorphic evidence exists for a recent wave-cut bench at ~8 m elevation, ~150 m inland from the modern shoreline. These marine deposits are likely coeval with the more extensive non-marine alluvial deposits (Qoa/Qoa2) and could be related to a global sea-level high stand during a Pleistocene interglacial period (MIS 5e) (Ortlieb, 1991). It is feasible that in some places the marine--non-marine transition between *Qmt* and Qoa/Qoa2 is well inland, and some of the mapped Qoa/Qoa2 deposits near the modern-day shoreline are actually *Qmt*. Younger fluvial sand and cobble deposits (*Qal*) are found within active channels (Arroyos 0 - 6). A strip of unconsolidated beach sand and cobble deposits (*Qb*) is found along the modern shoreline, and a veneer of unconsolidated, aeolian sand deposits (*Qae*) are found inland up to 1.5 km from the modern shoreline.

2.6 FAULTING AND FOLDING

Multiple structures associated with the La Cruz fault system deform rocks on SWIT. The intensity of deformation is greatest within the older marine units and underlying early to middle Miocene volcanic rocks. The uppermost marine rocks (*Tcmu*) and adjacent non-marine rocks (*Tcnm*) display very little deformation and overlie older strata across an angular unconformity. The capping Pliocene-age volcanic units and Quaternary sedimentary and volcanic units appear undeformed.

The La Cruz fault is a first-order, NW-striking, dextral strike-slip fault that deforms most late Miocene and older map units on SWIT (Figs. 2.2, 2.14B,C). Although the La Cruz fault is primarily a sub-vertical strike-slip structure, it has a history of vertical motion, with evidence for both transpressional and transtensional deformation. Overall displacement across the fault in the study area is dextral oblique-normal, with down-to-the-northeast vertical motion. Crystalline basement rocks in the study area are sporadically exposed southwest of the fault and nowhere exposed northeast of the fault (Fig. 2.2). The La Cruz fault juxtaposes 21 - 15 Ma arc-related volcanic rocks to the southwest, against 18 - 11 Ma arc-related volcanic rocks of different composition to the northeast (Gastil and Krummenacher, 1977b; Neuhaus, 1989; Gastil et al., 1999; this study). Locally, early Miocene arc-related volcanic rocks are juxtaposed against late Miocene marine rocks. The La Cruz fault cuts unit *Tsmt* and all older marine and non-marine units (Fig. 2.2). Adjacent faults and folds do not appear to deform the La Cruz fault. From this it may be surmised that slip on these second-order structures was contemporaneous with slip on the La Cruz fault as part of a wrench zone. Total dextral offset for the La Cruz fault is not well constrained as no known correlative units match across its 28 km length across southern Isla Tiburón (Oskin and Stock, 2003a), indicating it may have experienced tens of kilometers of total

dextral displacement. However, less dextral slip may be required if down-to-the-northeast displacement across the fault has obscured correlative units. Younger arc-related volcanic rocks northeast of the fault may conceal older units that are correlative to those now exposed southwest of the fault.

Many map units are deformed by second-order folds and thrust faults. Mapped folds are gentle, with ~120 - 155° interlimb angles (Fig. 2.14). The traces of fold axial planes are oriented approximately NW-SE and slightly more westerly than the NW-striking La Cruz fault (Fig. 2.2). Thrust faults are oriented between NW-SE and E-W, typically inclined 20 - 80° to the south to southwest. Displacement along these faults is minor, with tens to hundreds of meters of total slip (Fig. 2.14). Both folds and thrust faults deform unit *Tsmt* and older units.

In addition to the tilting related to gentle folding and faulting, the entire SWIT study area is regionally tilted, broadly down-to-the-north (Figs. 2.2, 2.14). Generally, map units on both sides of the La Cruz fault dip northward, except locally within ~south-dipping limbs of folds. This tilting pattern is best demonstrated on the geologic map (Fig. 2.2), where older arc-related volcanic rocks are exposed in the southern study area and map units are progressively younger towards the northern portions of the study area.

Map units are also deformed by second-order normal faults (Figs. 2.2, 2.14). Mapped normal faults are oriented approximately NNW-SSE to NNE-SSW with moderate to steep dips. Displacement across these normal faults is minor, with tens of meters of total displacement. Normal faults deform unit *Tsmt* and older units, and cut folds and thrust faults. The dike system (*Tcsd*) that fed the Rhyodacite flow of Cerro Starship (*Tcsf*) is oriented approximately NNE-SSW across SWIT, subparallel to the strike of many mapped normal faults in the study area (Fig. 2.2) and southeast of the study area across southern Isla Tiburón (Chapter 3 of this thesis). This

orientation is similar to the expected orientation of extensional structures (e.g. fractures and faults) in the transtensional Gulf of California (Withjack and Jamison, 1986), and the *Tcsd* dike system is likely a reflection of the transtensional strain field at the time of its emplacement.

2.7 DISCUSSION

The results of our new detailed geologic mapping and geochronology support the interpretation of Oskin and Stock (2003a) that marine rocks on southwest Isla Tiburón (SWIT) were deposited during the latest Miocene to Pliocene. Here we compare previously published and our new timing constraints for the SWIT marine basin. This is followed by discussion of the implications of this age for the formation of the Gulf of California seaway and its geodynamic setting.

2.7a Timing of Marine Deposition on Isla Tiburón

Complex stratigraphic, structural, and intrusive relationships on Southwest Isla Tiburón underlie the long-standing debate on the age of the marine deposits here, as well as generating confusing and conflicting interpretations of the volcanic and sedimentary processes that occurred therein. Here, we use our detailed structural, stratigraphic, and geochronologic results to address and clarify controversies regarding (1) the age of the base of the SWIT basin, (2) the age and emplacement mechanism of the lava flow that caps the marine basin, (3) the relative age relationships of late Miocene igneous units, and (4) the thickness and depositional setting of the youngest marine strata.

2.7a1 Age of the Base of Marine Strata

Smith et al. (1985) published a 12.9 ± 0.4 Ma age for a monolithologic andesite breccia (their sample '83BSJ260') they interpreted to be interstratified near the base of the SWIT marine section, within deposits of the white tuffaceous marine sandstone unit (*Tsmt*) (Smith, 1991). Though Oskin and Stock (2003a) suggested that this outcrop was instead within an erosional window into volcaniclastic strata beneath the marine basin, their mapping was insufficient to prove this case. Our geologic mapping, constructed with the advantage of color satellite imagery of the area (Fig. 2.2), relocated the exact outcrop that was sampled by Smith et al. (1985) (Fig. 2.4B; Smith, personal communication) and clearly delineates its structural and stratigraphic relationships to nearby marine strata, as illustrated in an enlargement of our Cross-Section B-B' (Fig. 2.15). The andesite breccias sample locality (Fig. 2.4C) is located within the floor of Arroyo 3, surrounded by higher topography (Fig. 2.2). On the hill south of the arroyo exposure, *Tcml*, *Tbx* and older units are all deformed by gentle folds (Fig. 2.15). A gently north-dipping fold limb is mapped on the north-facing slope of this hill, dipping towards the arroyo exposure. The sharp, ~15° northwest-dipping, basal contact of marine conglomerate (*Tcml*) is exposed 1 - 2 m above the arroyo bottom on both the northeastern and southwestern sides of the ~20 m-wide bedrock-bottom arroyo (Fig. 2.15). Within the arroyo floor, the distinctive landslide breccia (*Tbx*) is in contact stratigraphically above the andesitic breccia (*Tbxv*), and nearby, is stratigraphically below the marine conglomerate. Thus, as first suggested by Oskin and Stock (2003a), the andesite breccia exposure occurs within an erosional window carved down through the gently-dipping marine conglomerate and the underlying landslide breccia (Fig. 2.15). In fact, multiple erosional windows such as this exist within 0.5 km of this key outcrop (Fig. 2.2). These relationships clearly show that the isotopically-dated andesitic breccia is beneath, rather than

Figure 2.15 Cross-section of erosional window exposure in Arroyo 3 where Smith et al. (1985) collected and dated (12.9 ± 0.4 Ma; K-Ar) a sample of andesitic breccia, thought to be interbedded in marine strata. This figure is an enlargement of a portion of cross-section B-B' (Fig. 2.14B). Inset shows cross-section B-B' by Gastil et al. (1999), drawn along same line as our cross-section B-B' (note different scale). Extent of main enlargement indicated by blue rectangle. Gastil et al. (1999) shows unit 'M8b', the unit that Smith et al. (1985) dated (black arrow) and we map as Tbxv, as a discontinuous, fault-bounded wedge of andesite interbedded within marine strata (e.g. 'M8a', 'M8c', 'M8d'). The floor of the marine basin is highlighted by a red dashed line. We reject this interpretation, as our detailed mapping demonstrates that Arroyo 3 exposes an erosional window through the base of the marine strata (Tcml) and into older arc-related volcanic rocks (Tbxv) and the landslide breccia (Tbx). Our interpretation of the floor of the marine basin is also shown as red dashed line. 'M1'-'M7' of Gastil et al. (1999) is equivalent to our arc-related volcanic rocks (e.g. Tbxv, Tbxd). 'M10' is equivalent to our landslide breccia (Tbx), interpreted by Gastil et al. (1999) as a younger, cross-cutting rhyolite dike.

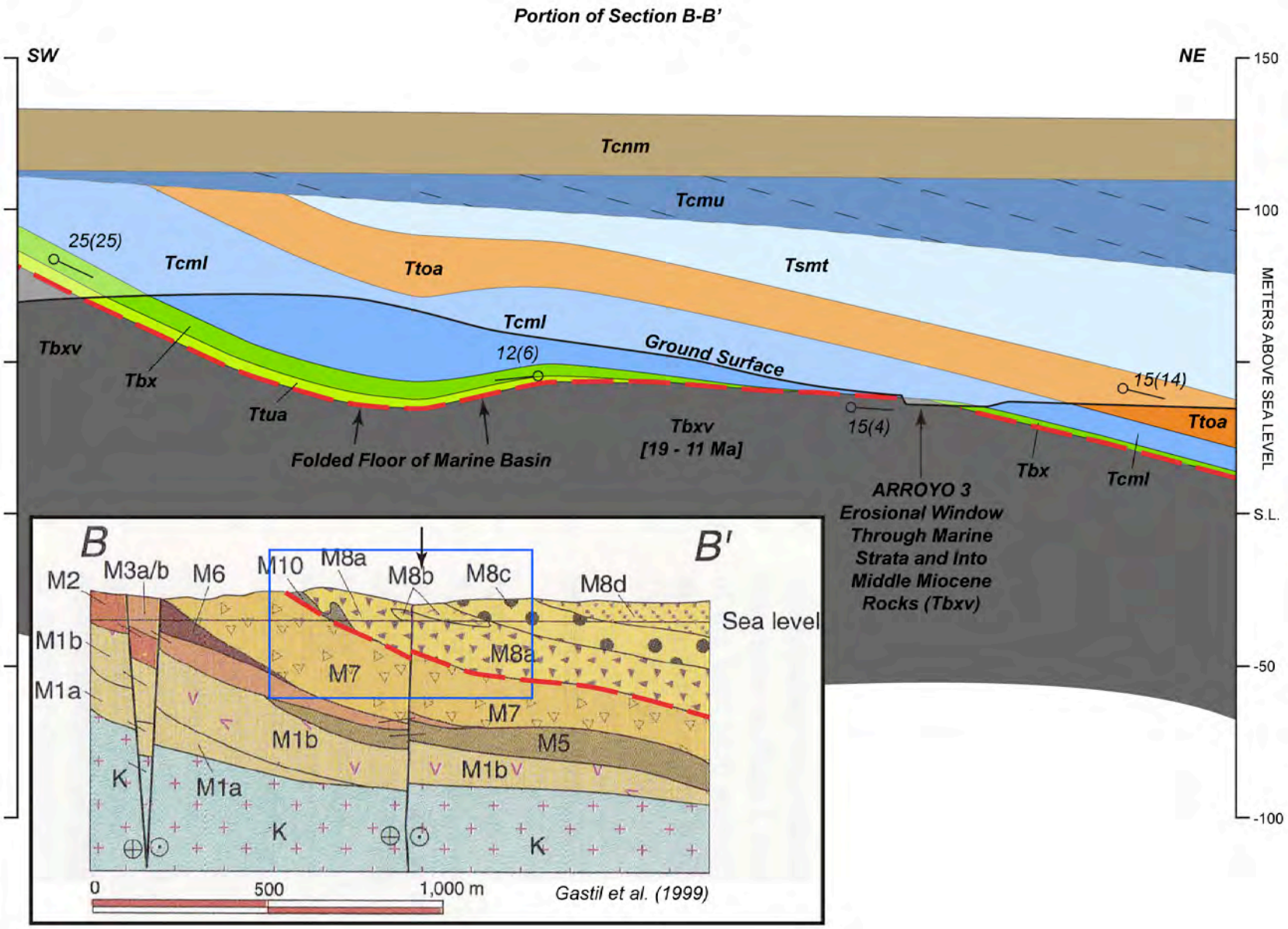
Portion of Section B-B'
SW
NE
150
100
S.L.
-50
-100
METERS ABOVE SEA LEVEL
Tcnm
Tcmu
Tcml
Ttoa
Tsmt
25(25)
Tcml
Ground Surface
12(6)
Tbxv
Tbx
Ttua
Folded Floor of Marine Basin
Tbxv
[19 - 11 Ma]
15(4)
15(14)
Ttoa
Tbx
Tcml
ARROYO 3
Erosional Window
Through Marine
Strata and Into
Middle Miocene
Rocks (Tbxv)
B
B'
M2
M3a/b
M6
M10
M8a
M8b
M8c
M8d
Sea level
M1b
M1a
M7
M8a
M7
M1b
M5
M1b
M1a
K
K
K
0
500
1,000 m
Gastil et al. (1999)

within, the marine strata and is part of the older, arc-related volcanic rocks (*Tbxv*). We report an U/Pb age of 18.70 ± 0.19 Ma from the same andesite breccia clast sampled by Smith et al. (1985) (Fig. 2.4C). This age should supersede the 12.9 ± 0.4 Ma (K-Ar) age by Smith et al. (1985). Neither age should be used as more than a loose maximum pre-dating marine sedimentation on SWIT.

We propose a new constraint on the age of the floor of the SWIT marine basin based on the widespread, lithologically distinctive landslide breccia marker (*Tbx*). This unit is exposed almost continuously at the base of the SWIT basin, either resting directly on the angular unconformity with the early to middle Miocene arc-related volcanic rocks, or upon a thin (< 5 m), discontinuous set of marine sandstone beds (*Tsm*). The age of the floor of the SWIT marine basin and this distinctive marker are bracketed between the 6.44 ± 0.05 Ma the Tuff of Hast Pitzcal that underlies marine strata and the 6.01 ± 0.20 Ma Tuff of Oyster Amphitheater interbedded within the earliest marine deposits.

That the age of the base of the SWIT marine basin is latest Miocene, rather than middle Miocene as previously claimed (Smith et al., 1985; Gastil et al., 1999), was presaged by the 6.2 - 4.3 Ma marine microfossils described in Gastil et al. (1999). This microfossil dataset is all but ignored from their conclusions and from the conclusions of subsequent paleontological studies in the Gulf of California (e.g. Carreño and Smith, 2007; Helenes et al., 2009). Both Carreño and Smith (2007) and Helenes et al., (2009) indicate that the SWIT marine basin is middle Miocene in age, calling upon the 12.9 ± 0.4 Ma age by Smith et al. (1985) and the 11.2 ± 1.3 Ma age by Gastil and Krummenacher (1977b) for the rhyodacite flow that caps the entire marine basin, despite the doubts raised about these constraints by Oskin and Stock (2003a). Helenes et al. (2009) also cite the late Miocene microfossils from SWIT when discussing the extent of the late

Miocene Gulf of California, despite that these data are inconsistent with the isotopic age constraints as interpreted by Gastil et al. (1999). The results from our study resolve this controversy, demonstrating that both isotopic ages and microfossils are consistent with a SWIT marine basin that is latest Miocene to early Pliocene in age.

Of more regional concern, paleontological studies of molluscan assemblages (e.g. Smith et al., 1985; Smith, 1991; Carreño and Smith, 2007) use the fossil assemblage from SWIT as a standard for middle Miocene time in the Gulf of California, affecting the age interpretation of other marine basins. These paleontological studies incorrectly assign a middle Miocene age to correlative fossil assemblages over a significant length of the Gulf of California and Salton Trough, including the Imperial Formation >650 km northwest of Isla Tiburón, the basal Boleo Formation >150 km south of Isla Tiburón, and the basal Trinidad Formation >650 km southeast of Isla Tiburón (Gastil et al., 1999). Marine rocks at some of these locations have subsequently been shown to be late Miocene in age (e.g. McDougall et al. 1999). Future Gulf of California paleontological studies should not continue to propagate the erroneous middle Miocene interpretation for the age of marine strata and fossil assemblages on SWIT.

2.7a2 Age and Emplacement of the Rhyodacite of Cerro Starship

Conflicting interpretations (Gastil and Krummenacher, 1977b; Gastil et al., 1999; Oskin and Stock, 2003a) have been put forth for the age and emplacement mechanism of the Rhyodacite of Cerro Starship (*Tcsf*) that caps all marine deposits (Fig. 2.13). The basis for this conflict lies in disparity between the original K-Ar ages obtained by Gastil and Krummenacher (1977b) for the flow, 11.2 ± 1.3 Ma, versus a nearby dike of similar lithology, 3.7 ± 0.9 Ma, leading to the interpretation of these features as separate igneous events. A younger K-Ar age of

4.16 ± 1.81 Ma from a sample of top of the flow obtained by Neuhaus (1989) and reported in Gastil et al., (1999) was interpreted to have been accidentally collected from a dike instead. Oskin and Stock (2003a) rejected this interpretation, and instead propose that the K-Ar age of 11.2 ± 1.3 Ma from the rhyodacite flow (*Tcsf*) is erroneous, inconsistent with its stratigraphic position, and that the younger K-Ar ages of 4.16 ± 1.81 Ma and 3.7 ± 0.9 Ma, previously interpreted to crosscut this flow, were actually collected from the primary lava flow and its coeval feeder dike, respectively.

We revisited this capping rhyodacite flow and nearby dikes to assess their relative age and emplacement mechanisms. The 3.7 ± 0.9 Ma dike outcrop on the eastern bank of Arroyo 1 (*Tcsd*) is at least 5 m wide and exhibits a strong NE-SW-striking, vertical foliation (Fig. 2.2). Southwest of this outcrop, across Arroyo 1, the same dike reappears and continues up the eastern flank of Hast Pitzcal. Here the dike thickens up to 20 - 40 m across, crosscuts marine and non-marine conglomerate beds, and outcrops continuously up to the base of the rhyodacite flow (Figs. 2.2, 2.13F). The dike does not cut through the rhyodacite flow. Instead, we observe the sub-horizontal rhyodacite flow as continuous and intact across this dike. In some exposures the dike rocks exhibit continuous foliation with the overlying flow. Gastil et al. (1999) interpreted the flow as an ash-flow tuff that consists of a basal pumice bed, overlain by a breccia flow, overlain by a vitrophyric welded tuff, overlain by a crystal-rich effusive rhyolite. Our observations confirm that the base of the flow is underlain by pyroclastic material (unit *Tcsp*). However, this unit is thin and discontinuous. The majority of the Rhyodacite of Cerro Starship consists of a lava flow. This is supported by the observation that the matrix of both the basal vitrophyre and the main flow deposit do not consist of ash or other pyroclastic material (e.g. pumice, lithic fragments) and instead exhibits irregular flow foliation (Figs. 2.2, 2.13E, 2.14A)

typical of felsic lava flows (Cas and Wright, 1987). We also revisited the southern end of the main, elongate flow body (Fig. 2.2) where Gastil et al. (1999) interpret the 4.16 ± 1.81 Ma (K-Ar) age from it to be from a crosscutting dike. We do not observe dikes exposed along the continuous, undulatory upper flow surface (Fig. 2.13C) and also none were observed where the sub-horizontal, basal contact of the flow is well exposed in a vertical, cliff exposure (Fig. 2.13H). In summary, our observations concur with the interpretation of Oskin and Stock (2003a) that the dike (*Tcsd*) is the feeder for the capping rhyodacite flow (*Tcsf*). The main rhyodacite flow body was likely sourced from a dike that was continuous with that exposed at its northern end. As additional support of this hypothesis, we find that the thickest pyroclastic deposits are observed nearby and immediately south of the point where this dike intersects the flow (Fig. 2.2).

To resolve disparate interpretations of the age of the rhyodacite, we dated a sample from basal *Tcsf*, away from any mapped dikes, and where its sharp, sub-horizontal basal contact is clearly exposed (Fig. 2.2). Our ages of 3.51 ± 0.05 Ma (Ar/Ar) and 4.13 ± 0.09 Ma (U/Pb) are consistent with previously published K-Ar ages of 3.7 ± 0.9 Ma on the Arroyo 1 feeder dike (Gastil and Krummenacher, 1977b) and 4.16 ± 1.81 Ma from the top of the flow (Neuhaus, 1989). Altogether, these data confirm that the K-Ar age of 11.2 ± 1.3 Ma by Gastil and Krummenacher (1977b) does not represent the age of the flow and should not be used as a minimum age constraint on marine sedimentation on SWIT. This capping rhyodacite flow (*Tcsf*) is Pliocene in age.

2.7a3 Reinterpretation of Late Miocene Igneous Units

Neuhaus (1989) and Gastil et al. (1999) mapped and dated three late Miocene igneous units interpreted as dikes or pods of rhyolite flows that crosscut and/or overlie all SWIT marine

deposits (Fig. 2.2; Table 2.1). Our observations indicate that none of these igneous units crosscut or overlie marine strata, but rather, these are within the stratigraphic section where they are faulted and folded similar to underlying and overlying map units.

A rhyolite from Arroyo 1 was interpreted as either a flow that overlies SWIT marine conglomerate (Neuhaus, 1989; unit 'Mr') or as a crosscutting dike (Gastil et al., 1999; unit 'M10'). Their petrographic description and age (5.67 ± 0.17 Ma) is very similar to the description and age (6.44 ± 0.05 Ma) of the Tuff of Hast Pitzcal (*Tthp*), which outcrops at their sample location on our geologic map (Fig. 2.2). Here, *Tthp* is tilted and faulted and unequivocally within the stratigraphic section, unconformably beneath marine deposits (Figs. 2.2, 2.14A). Locally, in a side canyon on the western side of Arroyo 1, the upper contact of *Tthp* diapirically intrudes into overlying stratified ash and pumice beds of unit *Ttua* and up against the basal contact of *Tbx* (Fig. 2.6). We observe similar diapiric relationships in outcrops just west of a coastal cove, between Arroyo 0 and Hast Pitzcal (Fig. 2.2). This contact relationship may have occurred as a result of the rapid deposition and overburden pressure of these breccia deposits onto older, unconsolidated deposits of water-saturated tuffs. Such diapric flow contact relationships may have led previous authors to the incorrect interpretation that the emplacement of the Tuff of Hast Pitzcal occurred as an intrusion.

Neuhaus (1989) also maps another local rhyolite unit (Mry) from an outcrop in Arroyo 4, in the southeastern corner of the study area (Fig. 2.2) and reports a 6.11 ± 1.81 Ma (K-Ar) age for this unit (Table 2.1). Neuhaus (1989) interprets this unit as a rhyolite flow that overlies SWIT marine conglomerate. Gastil et al. (1999) reports this age, but places this volcanic sample amongst outcrops of fluvial conglomerate (M11) on their geologic map. The sample location and petrographic description of Neuhaus (1989) are both similar to the Tuff of Ensenada Blanca

(*Tteb*) on our geologic map (Fig. 2.2). Here, *Tteb* is deposited upon older arc-related volcanic breccia deposits (*Tbxv*) and nowhere in contact with marine strata. Because *Tteb* is overlain by non-marine conglomerate (*Tcnm*), a unit coeval with the youngest SWIT marine deposits (*Tcmu*), *Tteb* must either pre-date or be coeval with marine conditions on SWIT.

Gastil et al. (1999) map a discontinuous rhyolite unit (M10) in the vicinity of Arroyos 1 - 3, from which a 9.02 ± 1.18 Ma (Ar/Ar) age was obtained. They interpret this unit as a rhyolite dike crosscutting marine conglomerate. Our mapping indicates that these outcrops are moderately-dipping deposits of the distinctive landslide breccias (*Tbx*) (Fig. 2.2), which consists predominantly of welded rhyolite tuff clasts (Fig. 2.8A,B), and was emplaced near the base of the marine rocks (Fig. 2.14B). We also observe angular to subrounded cobbles and boulders of cemented *Tbx* reworked into overlying *Tcml* marine conglomerate beds (Figs. 2.2, 2.10D) that further confirm that it pre-dates most marine sediments. Across the study area, breccia clasts of *Tbx* are identical to primary tuff outcrops of Tuff of Ensenada Blanca, which we interpret as the source of the landslide breccias deposit. We did not undertake re-dating of *Tteb*, nor its clasts within *Tbx*. If we take the ages from these units reported by Gastil et al. (1999) at face value, these data suggest that the Tuff of Ensenada Blanca was likely emplaced prior to marine conditions on SWIT, ca. 7 - 9 Ma. *Tteb* outcrops were subsequently destabilized and deposited the *Tbx* landslide breccia amongst the earliest marine deposits sometime prior to the emplacement of the 6.01 ± 0.20 Ma Tuff of Oyster Amphitheater.

2.7a4 Tectonic-Sedimentary Setting and Thickness of Marine Strata on Southwest Isla Tiburón

Our detailed structural and stratigraphic results require a reinterpretation of SWIT basin geometry, the controls on basin formation and subsidence, and estimates of total basin thickness.

We interpret that the majority of tectonic accommodation that formed the SWIT basin was produced northeast of the La Cruz fault in response to dextral oblique-normal motion (down-to-the-northeast). The exposed marine portion of the basin fills an elongate, 1.5 - 2.5 km-wide trough for 4 km parallel to the fault trace (Fig. 2.2). This trough continues to the southeast for at least an additional 5 km, filled by non-marine strata (Fig. 2.1B). For most of its length, the basin is restricted to the northeast side of the La Cruz fault, supporting the idea that it formed above the down-dropped, northeastern side of this dextral oblique structure. Within ~1 km of the modern shoreline the basin widens to >4 km and deposits are preserved on both sides of the La Cruz fault. Additional accommodation here was produced from the more regional pattern of down-to-the-north tilting. This tilting, which affects rocks on both sides of the La Cruz fault, may be due to a restraining geometry as strain is transferred from the La Cruz fault westward, onto the parallel dextral Tiburon Transform fault (Fig. 2.1B). Alternatively, sagging toward the axis of the Gulf of California may be a response to crustal thinning (Gastil and Fenby, 1991; González-Fernández, 2005).

Slip along the La Cruz fault and deformation on adjacent faults and folds occurred simultaneously with filling of the SWIT marine basin. The oldest marine units, *Tsm, Tcml,* and *Tcsh,* are faulted and folded similar to underlying arc-related volcanic rocks. Intermediate units *Ttoa*, *Tsmt*, and *Tcmm* are the youngest map units folded or cut by these faults. Deformation was mostly complete prior to deposition of the youngest marine conglomerate (*Tcmu*) and adjacent non-marine conglomerate (*Tcnm*), as these units are relatively undeformed and cap most faults. Thus, deformation associated with the La Cruz fault likely ceased sometime after emplacement of the 6.01 ± 0.20 Ma Tuff of Oyster Amphitheater and prior to the emplacement of the 3.51 ± 0.05 Ma to 4.13 ± 0.09 Ma Rhyodacite of Cerro Starship.

We interpret deposits of *Tsmt*, *Tcmm*, *Tcmu*, and *Tcnm* to represent a linked fluvial-marine Gilbert-type fan delta system fed by a northwest-flowing fluvial system that drained watersheds across much of southern Isla Tiburón into the marine waters of the late Miocene Gulf of California seaway. This Gilbert-type fan delta system became organized by the latest stages of deformation, and only the lower units of the system (e.g. *Tsmt*, *Tcmm*) are folded or faulted. Non-marine topset deposits (*Tcnm*) both truncate (Figs. 2.11 D, E; see also Fig. 1D of Oskin and Stock, 2003a) and grade laterally into inclined marine foreset deposits (*Tcmu*), where individual beds of horizontal non-marine conglomerate roll over into beds of inclined fossiliferous marine conglomerate (Fig. 2.11 D,E). Where observed, this non-marine to marine transition represents the approximate position of the paleoshoreline. Gently-dipping marine tuffaceous sandstone deposits (*Tsmt*) are interpreted to be distal marine bottomset turbidite deposits. In places, coarser marine conglomerate and sandstone deposits (*Tcmm*) overlie *Tsmt*. *Tcmm* may represent a period of relatively lower sea level, when coarser sediments were delivered further out into the basin and overlie finer-grained bottomset deposits. *Tsmt* and *Tcmm* are both overlain by marine conglomerate deposits (*Tcmu*), which we interpret as a prograding set of marine foresets. Foreset sediments were sourced from an up-dip fluvial system and prograded across older, deformed marine units (e.g. *Tsm*, *Tcml*), filling the basin in a roughly southeast to northwest direction. The delta-fan appears to have infilled an embayment formed along the La Cruz fault that had previously hosted a more heterogeneous, isolated set of marine depositional systems. In the northwest, a thick, fossil-poor sedimentary breccia (*Tbxs*) was deposited at indeterminate paleo-depths. Contemporaneously, in the southeast, there was an isolated, sediment-starved region that was dominated by limestone deposition and rich in fossils (*Tcsh*).

Maximum thickness of the SWIT marine basin is estimated to be ~300 m in the study area (Fig. 2.14), from a combination of our detailed geologic mapping and from detailed measured sections by Keogh (2010). This estimate utilizes maximum thickness measurements of ~10 m of *Tsm*, *Ttua*, and *Tbx*, ~130 m of *Tbxs*, *Tcml*, and *Tcsh*, ~30 m of *Ttoa*, ~90 m of *Tsmt*, ~100 m of *Tcmm*, ~40 m of *Tcmu*, and ~50 m of *Tcnm*. However, marine units are of variable thickness across the study area and in no single section are all observed at their maximum thickness. This basin thickness estimate is drastically less than the ~1,500 m estimate by Cassidy (1990) and Gastil et al. (1999), an estimate based only on the thickness of *Tcmu*. This discrepancy is rooted in the different interpretations for the origin of *Tcmu* bedding inclination. Cassidy (1990) and Gastil et al. (1999) interpreted that *Tcmu* beds were deposited sub-horizontally in a subaqueous delta-fan system and subsequently tilted ~15 - 30° by extension-related normal faults located beyond the SWIT study area. These previous authors calculate basin thickness by traditional measured section techniques, summing bed thicknesses orthogonal to bedding planes. In contrast, we estimate basin thickness via a combination of two techniques. First, for units that are folded and faulted and bed inclination is thus clearly tectonic (e.g. *Tcml*, *Tsmt*), we rely on the thicknesses determined in the study area by Keogh (2010) who used traditional measured section techniques and sums bed thickness orthogonal to bedding planes. Second, for *Tcmu*, for which bed inclination is non-tectonic, we determine its thickness by measuring the height of the marine foreset package between the bottomsets (e.g. *Tsmt*) and topsets (*Tcnm*). Gilbert-type fan delta systems of comparable thickness have been documented in a similar manner elsewhere in the Gulf of California (e.g. Dorsey et al., 1995).

2.7b Implications for Gulf of California Marine Incursion

A conclusive latest Miocene to Pliocene age for the SWIT marine basin supports synchronous late Miocene marine incursion into the northern half of the proto-Gulf of California, and does not support the existence of an earlier, middle Miocene seaway. Here, we integrate paleontologic, geologic, and plate tectonic information to present a paleo-geographic reconstruction of the seaway during the earliest oblique opening of the northern Gulf of California rift. This integrated analysis illustrates the relationship between marine basin formation and the geodynamic evolution of this portion of the Pacific-North America plate boundary. We also explore the implications of this reconstruction for the interpretation of Helenes et al. (2009) of middle Miocene marine strata in offshore boreholes.

2.7b1 Synchronous Marine Incursion Into the Northern Proto-Gulf of California

A latest Miocene age for the earliest marine deposits on Isla Tiburón is consistent with a regionally synchronous marine incursion, no earlier than 6.5 Ma, into basins of the northern Gulf of California and basins now buried by continental deposits in the Salton Trough and Altar desert. Throughout this region (Fig. 2.16A), all timing information for marine incursion established through clear crosscutting relationships and/or microfossil assemblages indicates marine conditions first existed here sometime between 6.5 - 6.0 Ma (e.g. Carreño, 1992; Martín-Barajas et al., 1997; McDougall et al 1999; Holt et al., 2000; Oskin and Stock, 2003a; McDougall, 2008; Dorsey et al., 2011; this study). This late Miocene marine incursion (Fig. 2.16B) likely occurred along a relatively narrow set of *en echelon* basins formed within a ~600 km-long transtensional segment of the Pacific-North America plate boundary (Oskin et al., 2001; Chapter 1 of this thesis). Marine incursion in the northern Gulf of California appears to have

Figure 2.16 (A) Modern-day location of key marine strata and fossil localities. Exposures of late Miocene (6.5 - 6.0 Ma) marine rocks with isotopic age constraints in the northern Gulf of California and Salton Trough (light blue squares). Slightly older, late Miocene (~7 Ma) marine rocks, or poorly-constrained localities (locale '7') of the central Gulf of California (dark blue squares). Basins or wells containing middle Miocene microfossils that are either reworked (orange squares) or considered in situ by the original authors (green squares). Pull-apart basins (thin black lines) after Aragón-Arreola & Martín-Barajas (2007) and Miller and Lizarralde (2013). Physiographic basemap from GeoMapApp (www.geomapapp.org). Cities abbreviated in italics: LA - Los Angeles, SD - San Diego, E - Ensenada, Y - Yuma, T - Tucson, SF - San Felipe, P - Puertecitos, BLA - Bahía de Los Angeles, H - Hermosillo, G - Guaymas, L - Loreto. (B) Earliest Gulf of California seaway (blue) during late Miocene time (~6.3 Ma). Same features as in A are restored to their ~6.3 Ma position. This reconstruction restores the Baja California peninsula 235 km to the southeast, matching correlative outcrops of the 12.5 Ma Tuff of San Felipe and the 6.4 Ma Tuffs of Mesa Cuadrada (Oskin et al., 2001; Oskin and Stock 2003b), while honoring minimal overlap of the relatively thick continental crust and shallow basement geophysically imaged offshore Isla Tiburón and northeastern Baja California (Aragón-Arreola and Martín-Barajas, 2007; Mar-Hernández et al., 2012). Tens of kilometers of dextral deformation in northeastern Baja California (Lewis and Stock, 1998a) and tens of kilometers of pre-6 Ma dextral faulting in coastal Sonora (Bennett et al., 2013) are not accounted for in this reconstruction. These onshore displacements play little to no role in the ~6.3 Ma position of the offshore and coastal features tracked in this reconstruction.

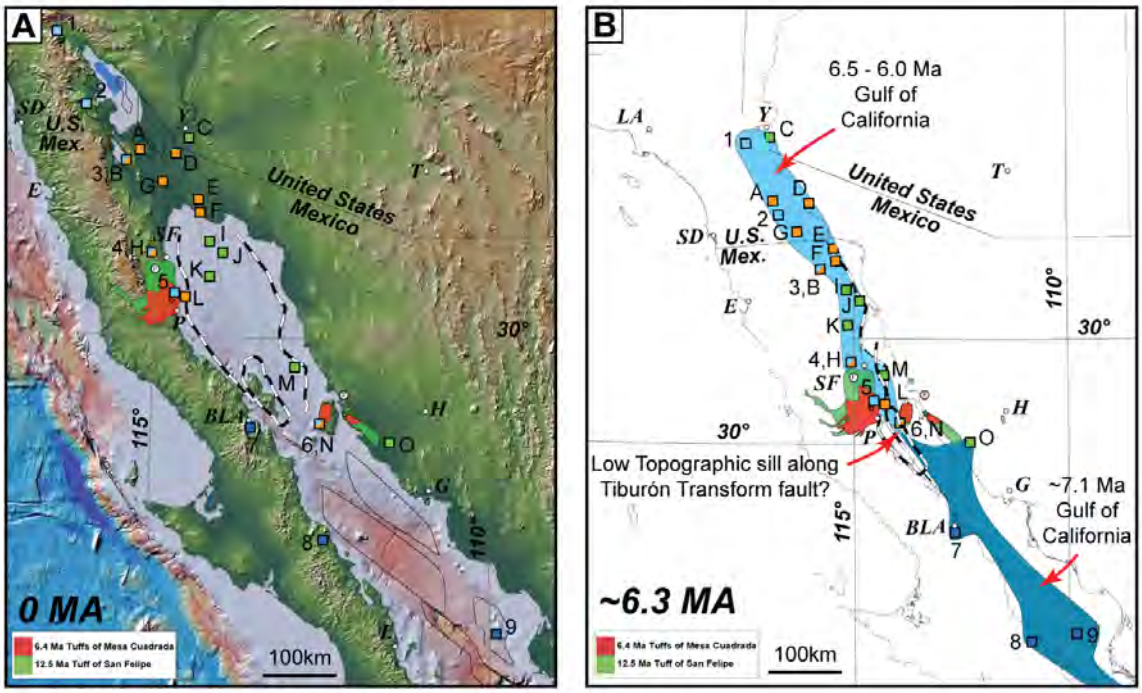

- middle Miocene microfossils, considered *in situ* by author
- middle Miocene microfossils, reworked
- earliest marine deposits of central Gulf, ca. 7 Ma
- earliest marine deposits of northern Gulf & Salton Trough, ca. 6.5 - 6.0 Ma
- earliest marine deposits ca. 6.5 - 6.0 Ma containing reworked middle Miocene microfossils
- (F) correlative fusilinid-rich clast conglomerate (Gastil et al., 1973)
- approximate ignimbrite vent location
- ○ city
- approximate edge of thick continental crust (after Aragón-Arreola and Martín-Barajas, 2007; Mar-Hernández et al., 2012)
- rift-related pull-apart basins (after Aragón-Arreola and Martín-Barajas, 2007; Miller and Lizarralde, 2013)

EARLIEST MARINE ROCKS

(1) Imperial Fm, San Gorgonio Pass [6.5 - 6.3 Ma], McDougall et al. (1999)
(2) Fish Creek Gypsum, Split Mtn. Gorge [6.3 Ma], Dean (1996); Dorsey et al. (2007, 2011)
(3) Cerro Colorado basin (Laguna Salada) [8 - 6 Ma], Martin-Barajas et al. (2001)
(4) San Felipe Marine Sequence [6.0 Ma], Boehm (1984); Stock (1997)
(5) Puertecitos Fm [<6.1 Ma], Martin-Barajas et al. (1997)
(6) Southwest Isla Tiburon [6.4 - 6.0 Ma], Gastil et al. (1999); Oskin & Stock (2003a); This Study
(7) Bahia de los Angeles [<12.1 Ma], Delgado-Argote et al. (2000)
(8) Boleo Fm, Santa Rosalia [~7 Ma], Holt et al. (2000)
(9) Marine Evaporite, East Guaymas embayment [~7 Ma], Miller and Lizarralde (2013)

MIDDLE MIOCENE MICROFOSSILS

(A) Cerro Prieto geothermal wells, Cotton & Van der Haar (1980)
(B) Cerro Colorado basin (Laguna Salada), Martin-Barajas et al. (2001)
(C) Yuma wells, McDougall (2008)
(D) Well A-1 (Altar basin), Helenes et al. (2009)
(E) Well A-2, Altar basin), Helenes et al. (2009)
(F) Well A-3 (Altar basin), Helenes et al. (2009)
(G) Well D (Colorado River delta), Helenes et al. (2009)
(H) San Felipe marine sequence, Boehm (1984)
(I) Well W-1 (Wagner basin), Helenes et al. (2009)
(J) Well W-2 (Wagner basin), Helenes et al. (2009)
(K) Well C (Consag basin), Helenes et al. (2009)
(L) Well P (Puertecitos shelf), Helenes et al. (2009)
(M) Well T (Tiburon basin), Helenes et al. (2009)
(N) Southwest Isla Tiburon basin, Gastil et al. (1999)
(O) Water wells (coastal Sonora plain), Gomez-Ponce (1971)

shortly followed the ca. 7 Ma marine incursion documented in the central Gulf of California (Holt et al., 2000; Miller and Lizarralde, 2013).

Whether latest Miocene marine incursion was preceded by an earlier, middle Miocene marine seaway, remains controversial. Middle Miocene microfossils are reported from the northern Salton Trough (McDougall et al., 1999), Cerro Prieto (Cotton and Vonder Haar, 1980), Laguna Salada (Martín-Barajas et al., 2001), near San Felipe (Boehm, 1984), from wells in the northern Gulf of California and southern Salton Trough (Helenes et al., 2009), in the coastal Sonora plains southeast of Bahía de Kino (Gómez-Ponce, 1971), and on Tres Marías Islands at the mouth of the Gulf of California (Figs. 2.1A, 2.15A; Carreño, 1985) (see regional summary in Carreño and Smith, 2007). At most of these locales, the original authors consider the middle Miocene microfossils to be reworked and not *in situ* specimens. One exception that may be *in situ* is the lower Miocene specimens documented ~250 - 750 m deep in water wells in coastal southern Sonora (Fig. 2.16A; Gómez-Ponce, 1971). However, McDougall (2008) reports that Winker (1987) discounts the *in situ* status of these specimens due to the unavailability of samples and additional documentation. Additionally, Gastil and Krummenacher (1977b) reports personal communication with James Ingle in 1973 who believed the recognition of lower Miocene strata in these Sonora water wells was not reliable and the strata could be post-10 Ma. No such marine rocks occur in mountain ranges that flank the modern-day Sonora coastline, despite evidence of significant faulting, tilting, and basin formation ca. 6 to 9 Ma (Herman and Gans, 2006; Seiler et al., 2010; Darin, 2011; Bennett et al., 2013).

A second, more substantive report of in situ middle Miocene microfossils comes from cuttings from four PEMEX exploration wells (PEMEX, 1985) analyzed by Helenes et al. (2009) (Fig. 2.16A). These authors report *in situ* dinoflagellates and calcareous nannofossils that

indicate up to 3,750 m of early to middle Miocene (pre-11.6 Ma) marine deposits are present in the Wagner, Consag, and Upper Tiburón marine basins of the northern Gulf of California. Within the Upper Tiburón basin offshore SWIT, Helenes et al. (2009) conclude that the lower 1,833 m of strata within a 4,813 m-deep well (Fig. 2.16) are middle Miocene, with geophysical evidence for ~1,000 m of additional sediments below the bottom of the well. This lower interval correlates to the laterally extensive (~50 km-wide) sedimentary unit 'A' of Aragón-Arreola and Martín-Barajas (2007) observed on geophysical profiles across the Upper Tiburón basin. This interpretation of a substantial, pre-11.6 Ma marine basin is at odds with onshore evidence that rift-related faulting began only after 11 - 12.5 Ma (Stock and Hodges, 1990; Lee et al., 1996; Lewis and Stock, 1998a) and that transtensional marine basins in the western Gulf of California (e.g. Wagner, Consag) began opening ca. 3.3 - 2.0 Ma, not during middle Miocene time (Nagy and Stock, 2000; Stock, 2000; Aragón-Arreola and Martín-Barajas, 2007). Additionally, two extensive late Miocene ash-flow tuffs that blanketed both rift margins of the proto-Gulf restore to close proximity across the Upper Tiburón basin (Fig. 2.16B; Oskin and Stock, 2003b). No major intervals of ash deposits are described from the Upper Tiburón well, despite the presence of up to several hundred meters of these late Miocene tuffs on the basin margins.

To reconcile the paleontological results with onshore geologic constraints, we suggest that the specimens documented as *in situ* by Helenes et al. (2009) must instead be reworked. Reworked specimens are observed at a higher interval within the Upper Tiburón well, and a late Miocene calcareous nannofossil (*S. neoabies*) is reported at depth 3,470 m, amongst deposits interpreted to be early to middle Miocene in age. PEMEX (1985) considers *S. neoabies* to be latest Miocene to Pliocene in age (6 - 3 Ma), an age applied to basal marine deposits (unit 'A') that contain this species in the Altar basin (Pacheco et al., 2006) and would correlate to the lower

interval in the Upper Tiburón basin. Additionally, Dorsey (2010) highlights that unit 'A' where documented by Pacheco et al. (2006) in the Altar basin contains clinoforms of Colorado River delta sands and thus must post-date 5.3 Ma. Though the first appearance of *S. neoabies* may lie within the middle Miocene at 11.8 Ma (Perch-Nielsen, 1985) the lower part of this range is speculative (McDougall, 2008).

Alternatively, Helenes et al. (2009) question the validity of the cross-Gulf tie point by Oskin et al. (2001) and Oskin and Stock (2003b), suggesting that the correlation of these once-proximal volcanic deposits could be erroneous because paleomagnetic results would not detect longitudinal (east-west) motion of Baja California during subsequent rifting. Helenes et al. (2009) seem to have misconstrued the paleomagnetic data presented in Oskin et al. (2001) as a direct measure of paleolatitude through its relationship to paleomagnetic inclination (Butler, 1992). This is a misunderstanding of the evidence for correlation of these tuffs, which is based on their unique paleomagnetic remanence vector directions (Lewis and Stock, 1998a; Stock et al., 1999; Chapter 1 of this thesis), among other evidence such as the tuff lithology, cooling-unit stratigraphy, and whole-rock and phenocryst geochemistry (Oskin and Stock, 2003b). To this list we also add that the geochronology of these tuffs also matches across the Gulf of California (Bennett et al., 2013). The original proximity of the tuff deposits now separated across the Gulf of California was not based on paleomagnetic data, but rather the thickness and outcrop distribution of multiple tuff markers and internal cooling units (Oskin and Stock, 2003b). This cross-Gulf tuff correlation is robust and must be considered in any discussion regarding the tectonic evolution of, or marine seaway incursion into, the northern Gulf of California.

Honoring the constraints from correlative tuffs (Oskin et al., 2001; Oskin and Stock, 2003b) and geophysical data available on the extent of thick continental crust submerged beneath

the northern Gulf of California (Aragón-Arreola and Martín-Barajas, 2007; Mar-Hernández et al., 2012), we present a revised reconstruction of the northern Gulf of California at latest Miocene time with the reconstructed locations of observed Miocene marine strata (Fig. 2.16B). In order to avoid substantial overlap of relatively thick continental crust (i.e. shallow depth to basement), this reconstruction restores Baja California 235 km towards the southeast, 10 km less than the minimum distance estimated by Oskin and Stock (2003b) (255 ± 10 km). This matches the western edge of a ~25 km-wide submerged continental shelf offshore western Isla Tiburón with the eastern edge of a ~10 - 15 km-wide shelf offshore Puertecitos, Baja California (distances here measured NW-SE, parallel to the rifting direction). Thus, in latest Miocene time coincident with marine deposition on SWIT, the maximum possible distance between the Isla Tiburón and Baja California coastlines was ~35 - 40 km (Fig. 2.16B).

A ~35 - 40 km-wide combined Puertecitos-Isla Tiburón shelf does not require a marine basin of the same width, as portions of the shelf may have subsided and become submerged at a later stage. In fact, an exploration well drilled on the outboard edge of the Puertecitos shelf (location 'L' in Fig. 2.16) report only late Miocene strata that overlie an 8 ± 1 Ma andesite directly overlying crystalline basement (PEMEX, 1985). If the history for the conjugate Isla Tiburón shelf is similar, this leaves little or no space for a middle Miocene marine basin. Alternatively, if the Isla Tiburón shelf is different, and hosted a middle Miocene seaway between Isla Tiburón and Baja California, it could not have been wider than ~25 km in the NW-SE dimension, the restored distance between the Puertecitos well and the western Isla Tiburón shoreline. Such a limited lateral extent is inconsistent with the greater extent (~50 km; SW-NE direction) of unit 'A' deposits documented in the Upper Tiburón basin on line '2D' of Aragón-Arreola and Martín-Barajas (2007). Thus, we conclude that the more extensive deposits of unit

‘A’ in the Upper Tiburón basin (Aragón-Arreola and Martín-Barajas, 2007), that correlate to the middle Miocene interval of Helenes et al. (2009), are unlikely to be middle Miocene in age. Instead, these lowermost Upper Tiburón basin deposits probably began to accumulate during late Miocene time (ca. 6.5 - 6.0 Ma), similar to marine deposits on SWIT, when the Upper Tiburón basin began to rapidly widen due to localized oblique divergence (Oskin et al., 2001).

2.7b2 Speculative Origins of Reworked Middle Miocene Microfossils

Though concrete evidence of *in situ* middle Miocene marine strata within or adjacent to the Gulf of California has yet to be found, the presence of reworked middle Miocene marine microfossils across the Gulf of California region (McDougall, 2008) suggests that marine water did exist somewhere in the region during middle Miocene time and deposits from this could have contributed the reworked fossils. Here we speculate for three potential origins of these reworked microfossils, from middle Miocene strata both within and beyond the Gulf of California rift.

One possible source is a middle Miocene seaway that was broadly coincident with the late Miocene Gulf of California axis (Helenes et al., 2009). Such a seaway is required to be smaller and potentially more discontinuous than the well-documented extent of the late Miocene seaway (blue squares on Fig. 2.16B). Portions of these basins containing middle Miocene microfossils could have been exposed and eroded during subsequent rift-related faulting, contributing specimens to late Miocene basins. However, geologic constraints that tie the margins of the Gulf of California into close proximity at late Miocene time (Oskin et al., 2001) make it difficult to argue for such a seaway at the current location of the Gulf of California.

Another possible location could be a shallow seaway within an area of middle Miocene back-arc extension that existed NE of and parallel to the modern-day Gulf of California, within

Sonora and Sinaloa. Such a middle Miocene back-arc basin would have existed northeast of a NW-SE chain of middle Miocene volcanic centers, in the wake of the southwestward migrating volcanic arc (Karig and Jensky, 1972; Hausback, 1984; Dorsey and Burns, 1994; Ferrari et al., 1999; Umhoefer et al, 2001) and has been speculated previously (Smith, 1991; Fenby and Gastil, 1991; Helenes and Carreño, 1999). Subsequent uplift and exposure of these marine deposits could have provided the middle Miocene microfossils to the latest Miocene marine basins in the northern Gulf of California via roughly southwest-directed drainages. Critically, however, no outcrops of middle Miocene marine strata, or reworked material from now buried outcrops, exist in western Mexico, despite the documented presence of non-marine strata of the appropriate age (Herman and Gans, 2006; Darin, 2011; Bennett et al., 2013). Regionally extensive outcrops of the 12.5 Ma Tuff of San Felipe (Fig. 2.16; Stock et al., 2006) have not been reported to overlie marine sedimentary rocks, as would be expected if extensive marine basins existed during middle Miocene time. If microfossils observed beneath the coastal Sonora plain (Gómez-Ponce, 1971) are in fact *in situ* specimens, and the strata in the subsurface beneath Yuma, Arizona (McDougall, 2008) are in fact middle Miocene, these locales (Fig. 2.16) may be the only potential examples of this older back-arc basin seaway, distinctive from the late Miocene to present Gulf of California, in both time and space.

A third speculative source for older, reworked microfossils is from the continental shelf on the Pacific side of the southernmost Baja California peninsula, adjacent to the mouth of the Gulf of California. Here middle Miocene marine strata were exposed to wave-base erosion during late Miocene time (Brothers et al., 2012) and could have contributed middle Miocene specimens into late Miocene basins 700 - 900 km away, as marine waters progressively spilled northwestward, into intra-rift transtensional basins of the proto-Gulf of California. Erosion, long

distance transport, and redeposition of microfossils, such as foraminifera, have been documented elsewhere that supports 800 km and >2,000 km of transport via wind (Goudie and Sperling, 1977) and suspended load currents (Otvos and Bock, 1976), respectively.

2.7b3 Tectonic Evolution of Gulf of California

A synchronous, late Miocene marine incursion along the Pacific-North America plate boundary is a critical event in the evolution of the Gulf of California rift. A considerable geodynamic change must have occurred for this region to evolve from a high-standing volcanic arc at the end of middle Miocene time (Hausback, 1984; Dorsey and Burns, 1994; Umhoefer et al., 2001) to a system of pull-apart basins at or below sea level sometime before the end of the Miocene epoch. Such a significant modification of topography implies rapid crustal thinning and related subsidence. The majority of timing information from near San Gorgonio Pass in the north (McDougall et al 1999; McDougall, 2008) to Isla Tiburón in the south (Gastil et al., 1999; this study) supports a widespread and broadly synchronous occurrence of earliest marine deposits, ca. 6.5 - 6.0 Ma, coeval with the onset of strong transtensional plate motion across the northern Gulf of California (Oskin et al., 2001). This marine incursion is likely the consequence of crustal thinning and subsidence related to oblique rifting. The incipient late Miocene seaway was spatially coincident with, and occurred immediately following the development of, a ~50 - 100 km-wide belt of localized strike-slip faulting and related clockwise vertical-axis block rotations (Fig. 2.16B; Chapter 1 of this thesis), including formation of related non-marine transtensional basins ca. 6 - 9 Ma (Seiler et al., 2010; Bennett et al., 2013). South of Isla Tiburón, marine incursion had reached the Guaymas basin in the central Gulf of California ca. 7.1 Ma (Holt et al., 2000; Miller and Lizarralde, 2013). Flooding of marine waters into the northern Gulf of

California may have been delayed by a topographic barrier formed along the Tiburón transform fault, which separated areas of crustal thinning and subsidence in the Upper Tiburón basin, to the northwest, from the Lower Tiburón and Guaymas basins, to the southeast. As the Baja California Peninsula translated northward along the Tiburón Transform fault, a low topographic spill point likely formed between these areas, allowing seawater to enter the sub-sea level basin of the northern Gulf of California and Salton Trough. The formation of a proto-Gulf of California seaway was thus likely to have been intimately linked, in both time and space, to the onset of focused oblique rifting, which became established toward the end of Miocene time (Oskin et al., 2001; Bennett et al., 2013).

2.8 CONCLUSIONS

Isotopic and biostratigraphic data from the southwest Isla Tiburón (SWIT) marine basin conclusively show that earliest marine conditions there occurred during late Miocene time, and marine sedimentation ceased by early Pliocene time. Earliest marine conditions are constrained by the 6.44 ± 0.05 Ma Tuff of Hast Pitzcal that underlies the marine basin and the 6.01 ± 0.20 Ma Tuff of Oyster Amphitheater that is interbedded near the base of the earliest exposed marine deposits. Marine sedimentation in the study area ceased prior to the subaerial eruption of the 3.51 ± 0.05 Ma to 4.13 ± 0.09 Ma Rhyodacite of Cerro Starship. These timing constraints are all remarkably consistent with microfossils assemblages collected from SWIT marine deposits, independently constrained to 6.2 - 4.3 Ma (Gastil et al., 1999).

New, detailed geologic mapping and modern geochronologic results demonstrate that previous interpretations of timing of the marine basin on SWIT were based on incorrect K-Ar results and misinterpreted field relationships in part due to the structural complexity of the area.

The upper age constraint of 11.2 ± 1.3 Ma from the capping Rhyodacite of Cerro Starship (Gastil and Krummenacher, 1977b) is an erroneous age inconsistent with other ages and clear crosscutting relationships. The 12.9 ± 0.4 Ma age by Smith et al. (1985) is from an underlying, rather than interstratified deposit, redated here to 18.70 ± 0.19 Ma. The SWIT marine rocks do not reinforce middle Miocene strata proposed in offshore marine basins (Helenes et al. 2009), nor do they serve as a reference section for middle Miocene macrofauna (Smith, 1991).

A late Miocene age for the SWIT marine basin is consistent with a regional marine incursion into the proto-Gulf of California, no earlier than 6.5 Ma (Oskin and Stock, 2003a; McDougall, 2008). This regional marine incursion occurred from at least Isla Tiburón in the south to near San Gorgonio pass in the north, a distance of ~650 km, and is regionally constrained to between 6.5 and 6.0 Ma. This relatively narrow, incipient seaway was co-located with an active portion of the transtensional Pacific-North America plate boundary.

Middle Miocene microfossils documented at some locations in the Gulf of California-Salton Trough region are unlikely to be *in situ*. Rather, these specimens are likely reworked into late Miocene strata, as documented in several onshore exposures (McDougall, 2008), contributed from erosion of middle Miocene deposits, the location of which is unclear. Speculative sources for these reworked specimens include a seaway that may have occupied a back-arc extensional basin in the western Mexican Basin and Range province, for which outcrops have not been discovered, or from middle Miocene marine deposits along the western continental shelf of southernmost Baja California that were exposed to wave-base erosion during late Miocene time (Brothers et al., 2012).

Late Miocene marine incursion into the northern Gulf of California is likely the consequence of crustal thinning and tectonic subsidence related to focused oblique rifting. The

incipient late Miocene seaway was spatially coincident with, and flooded immediately following the development of, a narrow belt of localized strike-slip faulting and formation of non-marine transtensional basins (Chapter 1 of this thesis). Improved timing information for the SWIT marine basin helps address a long-standing debate over the age of marine incursion in the northern Gulf of California and its association with focused crustal deformation related to localization of the Pacific-North America transtensional plate boundary.

ACKNOWLEDGMENTS

Funding from the National Science Foundation Tectonics and MARGINS programs, awards #0739017 and #0904337, made this research possible. Permission to enter Isla Tiburón was granted by the Secretaría de Medio Ambiente y Recursos Naturales-Comisión Nacional de Areas Naturales Protegidas and the native Cumcaác (Seri) tribe. We thank A. Martín-Barajas for assistance with permit acquisition. Discussions with R. Dorsey, A. Forte, and A. Elliott helped to improve this manuscript. We thank M. Kunk and J. Wooden for assistance with our Ar/Ar and U/Pb geochronology data, respectively. M. Tappa, J. Ford, N. Buckmaster, and M. Keogh all provided great company, safety, and support while conducting fieldwork on Isla Tiburón. T. Donovan and the Prescott College Kino Bay Center for Cultural and Ecological Studies staff provided incredible logistical support and comfortable accommodations while conducting fieldwork. We thank Ernesto Molina Villa-Lobos of the native Cumcaác (Seri) tribe for his superb boatmanship and safekeeping during our field research.

TABLE 2.1 Pre-Quaternary map units of the Soutwest Isla Tiburón study area, including correlation to previously published mapping efforts. Geochronologic and biostratigraphic ages shown for this and previous studies.

Rock Unit	This Study				Oskin and Stock (2003a), Oskin (2002)			
	Unit Name	**Age (Ma)**	**Technicque & Material**	**Sample #**	**Unit Name**	**Age (Ma)**	**Technicque & Material**	**Sample #**
Crystalline Basement (Tonalite)	*Kt*				Mzg			
Arc-Related Volcanic Rocks	*Tb* *Tb* *Tvc @ cove* *Tvc @ cove* *Tbxv* *Tbxv* *Tba* *Tba* *Tba* *Tb* *Tvc @ cove* *Tbxv* *Tbxv*	18.70 ± 0.19	U/Pb zircon	TIB-09-17	Tvc,Tb,Ta(SW of LCF = Tmvlc) Tbxv(NE of LCF) = Tma1 Tvc(NE of LCF) = Tmvs			
Pre-basin, Syn-rift Volcanic Rocks								
Tuff of Hast Pitzcal	*Tthp*	6.44 ± 0.05	Ar/Ar sanidine	TIB-09-15	Tmprsz1	6.67 ± 0.83	Ar/Ar	SWT-99-28
Tuff of Ensenada Blanca	*Tteb*				Tmrec			
Tuffs of Arroyo El Canelo	*Ttec*				Tmrec correlated from Baja; Nagy et al. (1999)	6.1 ± 0.5	Ar/Ar	
Southwest Isla Tiburón Marine Basin								
Unnamed Air-fall Tuffs	*Ttua*				n/m			
Marine Sandstone	*Tsm*				n/m			
Landslide Breccia	*Tbx*				Tmbr			
Sedimentary Breccia	*Tbxs*				n/m			
Tuff of Arroyo Sauzal	*Ttas*				Tmprsz1	6.40 ± 1.63	Ar/Ar	TIB-98-11
Lower Marine Conglomerate and Sandstone	*Tcml*				Tmpm clast (rounded welded rhyolite tuff)	12.84 ± 0.40	Ar/Ar	SWT-99-25
Tuff of Oyster Amphitheater	*Ttoa*	6.01 ± 0.20	U/Pb zircon	TIB-09-02				
Marine Tuffaceous Sandstone	*Tsmt*				Tmpm			
Middle Marine Conglomerate and Sandstone	*Tcmm*							
Upper Marine Conglomerate and Sandstone	*Tcmu*				Tmpm			
Non-marine Conglomerate and Sandstone	*Tcnm*				Tmpal			
Capping & Crosscutting Volcanic Units								
Rhyodacite of Cerro Starship	*Tcsf, Tcsp*	3.51 ± 0.05 4.13 ± 0.09	Ar/Ar matrix U/Pb zircon	TIB-09-06 TIB-09-06	Tprcs			
(Flow, Basal Pyroclastic, Feeder Dike)	*Tcsd*							

n/m = unit not mapped by previous study

TABLE 2.1 (cont.) Pre-Quaternary map units of the Soutwest Isla Tiburón study area, including correlation to previously published mapping efforts. Geochronologic and biostratigraphic ages shown for this and previous studies.

Rock Unit	Gastil et al. (1999)				Cassidy (1990)			
	Unit Name	Age (Ma)	Technicque & Material	Sample #	Unit Name	Age (Ma)	Technicque & Material	Sample #
Crystalline Basement (Tonalite)	M1-M7							
Arc-Related Volcanic Rocks	M1-M7							
	M1-M7							
	M1-M7							
	M1-M7							
	M1-M7							
	M1-M7							
	M1-M7							
	M5	17.91 ± 0.36	Ar/Ar;horn-	284				
	M5	17.68 ± 0.15	blende plateau	284				
	M1-M7							
	M1-M7							
	M1-M7							
	M1-M7							
	M1-M7							
	M1-M7							
	M1-M7							
	M1-M7				Mvm - Unit 4b			
	M7	11.44 ± 2.61	Ar/Ar; feldspar-plateau	276				
Pre-basin, Syn-rift Volcanic Rocks								
Tuff of Hast Pitzcal	M10							
Tuff of Ensenada Blanca	M11							
Tuffs of Arroyo El Canelo								
Southwest Isla Tiburón Marine Basin								
Unnamed Air-fall Tuffs	n/m				n/m			
Marine Sandstone	n/m				n/m			
Landslide Breccia	"dike" cutting Unit	9.02 ± 1.18	Ar/Ar;plagio-clase-plateau	5	Mr - Unit 4c			
Sedimentary Breccia								
Tuff of Arroyo Sauzal	M10							
Lower Marine Conglomerate and Sandstone	M8a							
Tuff of Oyster Amphitheater								
Marine Tuffaceous Sandstone	M8c				Mss-Unit 4a	6.2 - 4.3	microfossils	
Middle Marine Conglomerate and Sandstone								
Upper Marine Conglomerate and Sandstone	M8d				Mcgl - Unit 5, Unit 6; Mss - Unit 7			
Non-marine Conglomerate and Sandstone	M11							
Capping & Crosscutting Volcanic Units								
Rhyodacite of Cerro Starship (Flow, Basal Pyroclastic, Feeder Dike)	M9 M10							

n/m = unit not mapped by previous study

TABLE 2.1 (cont.) Pre-Quaternary map units of the Soutwest Isla Tiburón study area, including correlation to previously published mapping efforts. Geochronologic and biostratigraphic ages shown for this and previous studies.

Rock Unit	Neuhaus (1989)				Gastil & Krummenacher, (1977a,b)			
	Unit Name	Age (Ma)	Technicque & Material	Sample #	Unit Name	Age (Ma)	Technicque & Material	Sample #
Crystalline Basement (Tonalite)					gd			
	Mb - Unit 3	21.0 ± 0.5	K-Ar; feldspar	JN4-15(274a)	T1/T2			
Arc-Related Volcanic Rocks	Ma - Unit 2	20.5 ± 0.5	K-Ar; hornblende	JNA-1	T1/T2			
	Ma - Unit 2	19.1 ± 0.6	K-Ar; whole rock	JN150	T1/T2			
	Mb - Unit 4	19.0 ± 0.4	K-Ar; feldspar	JN223	T1/T2			
	Mb - Unit 4	17.67 ± 1.4	K-Ar; whole rock	JN223	T1/T2			
					T1/T2	18.8 ± 2.4	K-Ar; hornblende	S2G-12
					T1/T2	22.7 ± 1.1	K-Ar; plagioclase	S2G-12
	Mb - Unit 4	18.52 ± 0.68	K-Ar; whole rock	JN274	T1/T2			
					T1/T2			
					T1/T2			
	Mb - Unit 4	17.8 ± 0.6	K-Ar; whole rock	JN145	T1/T2			
	Mb - Unit 4	17.7 ± 0.5	K-Ar; feldspar	JN252	T1/T2			
	Mad - Unit 5	17.4 ± 0.4	K-Ar; feldspar	JN237	T1/T2			
	Mb - Unit 4	15.3 ± 1.3	K-Ar; whole rock	JN106	T1/T2			
	Mba - Unit 6	15.24 ± 0.54	K-Ar; whole rock	JN272	T1/T2			
	Mad - Unit 5	14.96 ± 2.17	K-Ar; whole rock	JN219	T1/T2			
	Mry - Unit 7a	14.92 ± 0.8	K-Ar; whole rock	JN216B	T1/T2			
					T1/T2			
					T1/T2			
Pre-basin, Syn-rift Volcanic Rocks								
Tuff of Hast Pitzcal	Mr - Unit 9	5.67 ± 0.17	K-Ar; feldspar	JN51a	n/m			
Tuff of Ensenada Blanca	Mry - Unit 9	6.11 ± 1.81	K-Ar; whole rock	MC275	n/m			
Tuffs of Arroyo El Canelo					n/m			
Southwest Isla Tiburón Marine Basin								
Unnamed Air-fall Tuffs	n/m				n/m			
Marine Sandstone	n/m				n/m			
Landslide Breccia	Mr - Unit 9				n/m			
Sedimentary Breccia					n/m			
Tuff of Arroyo Sauzal					n/m			
Lower Marine Conglomerate and Sandstone					T3m			
Tuff of Oyster Amphitheater					n/m			
Marine Tuffaceous Sandstone					T3m			
Middle Marine Conglomerate and Sandstone								
Upper Marine Conglomerate and Sandstone					T3m			
Non-marine Conglomerate and Sandstone	Unit 11				T3			
Capping & Crosscutting Volcanic Units								
Rhyodacite of Cerro Starship	Unit 8				T4	11.2 ± 1.3	K-Ar; plagioclase	S2B-27
(Flow, Basal Pyroclastic, Feeder Dike)	rhyolite "dike" - Unit 10	4.16 ± 1.81	K-Ar whole rock	JNS-10	T5	3.7 ± 0.9	K-Ar; plagioclase	S2G-13

n/m = unit not mapped by previous study

TABLE 2.1 (cont.) Pre-Quaternary map units of the Soutwest Isla Tiburón study area, including correlation to previously published mapping efforts. Geochronologic and biostratigraphic ages shown for this and previous studies.

Rock Unit	Smith et al. (1985)			
	Unit Name	**Age (Ma)**	**Technicque & Material**	**Sample #**
Crystalline Basement (Tonalite)				
Arc-Related Volcanic Rocks				
	non-marine andesitic volcani-clastic debris flow	12.9 ± 0.4	K-Ar; plagioclase	83BSJ260
Pre-basin, Syn-rift Volcanic Rocks				
Tuff of Hast Pitzcal				
Tuff of Ensenada Blanca				
Tuffs of Arroyo El Canelo				
Southwest Isla Tiburón Marine Basin				
Unnamed Air-fall Tuffs				
Marine Sandstone				
Landslide Breccia				
Sedimentary Breccia				
Tuff of Arroyo Sauzal				
Lower Marine Conglomerate and Sandstone				
Tuff of Oyster Amphitheater				
Marine Tuffaceous Sandstone				
Middle Marine Conglomerate and Sandstone				
Upper Marine Conglomerate and Sandstone				
Non-marine Conglomerate and Sandstone				
Capping & Crosscutting Volcanic Units				
Rhyodacite of Cerro Starship (Flow, Basal Pyroclastic, Feeder Dike)				

n/m = unit not mapped by previous study

Table 2.2 U-Th-Pb analytical data for LA-ICPMS spot analyses on zircon grains for volcanic rocks from Southwest Isla Tiburón, México.

				CORRECTED RATIOS										CORRECTED AGES (Ma)									
	U# (ppm)	Th# (ppm)	Th/U	$^{207}Pb/^{206}Pb^{\dagger}$	±1s*	$^{207}Pb/^{235}U^{\dagger}$	±1s*	$^{206}Pb/^{238}U^{\dagger}$	±1s*	$^{208}Pb/^{232}Th^{\dagger}$	±1s*	Rho	% disc**	$^{206}Pb/^{238}U$	±1s*	$^{207}Pb/^{235}U$	±1s*	$^{207}Pb/^{206}Pb$	±1s*	$^{208}Pb/^{232}Th$	±1s*	Best age (Ma)	1s
Sample **TIB-09-17**	andesite breccia (*Tbxv*)			Mount ICGEO-7 (October 2009)																			
TIB17-**11**	1273	487	0.36	0.0469	0.0012	0.0161	0.0005	0.0025	0.00002	0.0008	0.00002	0.280	1	16.0	0.1	16.2	0.5	43	57	16.0	0.4	16.0	± 0.1
TIB17-**19**	1400	485	0.32	0.0481	0.0016	0.0165	0.0006	0.0025	0.00002	0.0008	0.00001	0.240	4	16.0	0.1	16.6	0.6	106	69	15.9	0.3	16.0	± 0.1
TIB17-**1**	272	163	0.56	0.0531	0.0044	0.0195	0.0018	0.0027	0.00005	0.0008	0.00002	0.300	15	17.1	0.3	20.0	2.0	332	192	16.8	0.4	17.1	± 0.3
TIB17-**12**	373	127	0.32	0.0483	0.0025	0.0180	0.0010	0.0027	0.00005	0.0009	0.00003	0.320	3	17.4	0.3	18.0	1.0	114	104	17.3	0.6	17.4	± 0.3
TIB17-**2**	328	201	0.57	0.0577	0.0042	0.0219	0.0017	0.0028	0.00004	0.0009	0.00001	0.240	20	17.7	0.3	22.0	2.0	519	149	17.2	0.3	17.7	± 0.3
TIB17-**18**	342	289	0.79	0.0503	0.0042	0.0191	0.0018	0.0028	0.00005	0.0009	0.00002	0.350	6	17.8	0.3	19.0	2.0	209	173	17.6	0.5	17.8	± 0.3
TIB17-**23**	574	499	0.81	0.0537	0.0022	0.0205	0.0009	0.0028	0.00003	0.0008	0.00002	0.260	14	17.8	0.2	20.6	0.8	360	84	16.8	0.4	17.8	± 0.2
TIB17-**7**	468	278	0.55	0.0592	0.0028	0.0225	0.0011	0.0028	0.00004	0.0009	0.00003	0.270	23	17.8	0.3	23.0	1.0	573	97	18.6	0.6	17.8	± 0.3
TIB17-**22**	309	165	0.50	0.0492	0.0049	0.0190	0.0020	0.0028	0.00005	0.0009	0.00006	0.230	5	18.0	0.3	19.0	2.0	157	195	18.0	1.0	**18.0**	**± 0.3**
TIB17-**17**	170	74	0.40	0.0608	0.0051	0.0237	0.0023	0.0028	0.00007	0.0009	0.00002	0.380	24	18.2	0.4	24.0	2.0	632	171	17.6	0.4	**18.2**	**± 0.4**
TIB17-**32**	621	356	0.53	0.0497	0.0022	0.0195	0.0009	0.0029	0.00003	0.0009	0.00002	0.260	7	18.3	0.2	19.6	0.9	182	96	17.4	0.4	**18.3**	**± 0.2**
TIB17-**4**	302	116	0.36	0.0602	0.0039	0.0235	0.0016	0.0028	0.00004	0.0010	0.00004	0.210	24	18.3	0.3	24.0	2.0	610	131	19.2	0.8	**18.3**	**± 0.3**
TIB17-**34**	429	279	0.61	0.0612	0.0036	0.0240	0.0015	0.0029	0.00004	0.0009	0.00003	0.240	23	18.4	0.3	24.0	1.0	647	118	18.6	0.6	**18.4**	**± 0.3**
TIB17-**3**	144	56	0.36	0.0504	0.0058	0.0199	0.0024	0.0029	0.00004	0.0009	0.00008	0.150	8	18.4	0.3	20.0	2.0	213	231	18.0	2.0	**18.4**	**± 0.3**
TIB17-**8**	125	60	0.45	0.0589	0.0051	0.0234	0.0022	0.0029	0.00006	0.0009	0.00002	0.280	20	18.5	0.4	23.0	2.0	563	178	18.0	0.4	**18.5**	**± 0.4**
TIB17-**24**	83	40	0.45	0.0514	0.0055	0.0205	0.0025	0.0029	0.00009	0.0009	0.00006	0.290	11	18.6	0.6	21.0	2.0	258	215	18.0	1.0	**18.6**	**± 0.6**
TIB17-**33**	175	86	0.46	0.0638	0.0053	0.0255	0.0024	0.0029	0.00006	0.0009	0.00002	0.340	28	18.7	0.4	26.0	2.0	733	166	18.0	0.3	**18.7**	**± 0.4**
TIB17-**13**	315	165	0.49	0.0495	0.0045	0.0199	0.0020	0.0029	0.00007	0.0009	0.00005	0.270	6	18.8	0.4	20.0	2.0	172	181	19.0	1.0	**18.8**	**± 0.4**
TIB17-**10**	232	107	0.43	0.0525	0.0038	0.0213	0.0017	0.0029	0.00005	0.0009	0.00002	0.350	10	18.9	0.3	21.0	2.0	307	153	18.6	0.4	**18.9**	**± 0.3**
TIB17-**14**	138	60	0.40	0.0653	0.0064	0.0258	0.0026	0.0030	0.00006	0.0010	0.00006	0.200	27	19.0	0.4	26.0	3.0	785	195	19.0	1.0	**19.0**	**± 0.4**
TIB17-**15**	350	202	0.54	0.0516	0.0039	0.0209	0.0017	0.0029	0.00004	0.0009	0.00002	0.300	10	19.0	0.3	21.0	2.0	266	158	18.7	0.4	**19.0**	**± 0.3**
TIB17-**27**	151	65	0.40	0.0672	0.0058	0.0271	0.0024	0.0030	0.00005	0.0010	0.00006	0.180	30	19.0	0.3	27.0	2.0	843	169	20.0	1.0	**19.0**	**± 0.3**
TIB17-**30**	287	102	0.33	0.0622	0.0036	0.0253	0.0015	0.0030	0.00004	0.0009	0.00004	0.240	24	19.1	0.3	25.0	1.0	681	115	18.8	0.8	**19.1**	**± 0.3**
TIB17-**16**	221	114	0.48	0.0642	0.0080	0.0264	0.0033	0.0030	0.00004	0.0009	0.00002	0.140	26	19.2	0.3	26.0	3.0	750	252	18.5	0.4	**19.2**	**± 0.3**
TIB17-**29**	134	51	0.36	0.0685	0.0047	0.0277	0.0020	0.0030	0.00007	0.0010	0.00005	0.310	31	19.2	0.4	28.0	2.0	883	132	20.0	1.0	**19.2**	**± 0.4**
TIB17-**36**	348	228	0.61	0.0583	0.0031	0.0238	0.0013	0.0030	0.00004	0.0010	0.00005	0.270	20	19.2	0.3	24.0	1.0	540	108	20.0	1.0	**19.2**	**± 0.3**
TIB17-**5**	59	51	0.80	0.0765	0.0092	0.0309	0.0039	0.0030	0.00011	0.0010	0.00009	0.300	38	19.2	0.7	31.0	4.0	1108	231	21.0	2.0	**19.2**	**± 0.7**
TIB17-**6**	226	176	0.73	0.0590	0.0024	0.0244	0.0012	0.0030	0.00008	0.0009	0.00005	0.570	20	19.2	0.5	24.0	1.0	565	81	18.0	1.0	**19.2**	**± 0.5**
TIB17-**37**	261	140	0.50	0.0548	0.0048	0.0229	0.0020	0.0031	0.00005	0.0010	0.00004	0.200	15	19.6	0.3	23.0	2.0	406	183	19.4	0.8	19.6	± 0.3
TIB17-**25**	241	97	0.37	0.0624	0.0027	0.0265	0.0012	0.0031	0.00004	0.0009	0.00004	0.300	27	19.7	0.3	27.0	1.0	687	87	18.4	0.8	19.7	± 0.3
TIB17-**38**	293	134	0.42	0.0514	0.0029	0.0217	0.0014	0.0031	0.00005	0.0010	0.00002	0.320	10	19.7	0.3	22.0	1.0	258	121	19.4	0.4	19.7	± 0.3
TIB17-**40**	170	61	0.33	0.0625	0.0055	0.0265	0.0025	0.0031	0.00007	0.0010	0.00002	0.280	27	19.8	0.4	27.0	3.0	690	179	19.1	0.4	19.8	± 0.4
TIB17-**35**	110	41	0.35	0.0577	0.0058	0.0241	0.0025	0.0031	0.00007	0.0011	0.00006	0.210	16	20.2	0.4	24.0	2.0	517	208	22.0	1.0	20.2	± 0.4
n = 33																		**Weighted $^{206}Pb/^{238}U$ mean age =**				**18.70**	**± 0.19**
																						MSWD =1.5; n = 20	
Sample **TIB-09-02**	Tuff of Oyster Amphitheater (*Ttoa*)			Mount ICGEO-17 (January 2011)																			
TIB02-**27**	468	522	1.01	0.0830	0.0083	0.0103	0.0012	0.0009	0.00002	0.0003	0.00001	0.420	42	5.8	0.1	10	1.0	1268	196	5.4	0.1	**5.8**	**± 0.1**
TIB02-**1**	486	515	0.96	0.0786	0.0113	0.0099	0.0016	0.0009	0.00002	0.0003	0.00001	0.320	41	5.9	0.2	10	2.0	1162	282	5.5	0.1	**5.9**	**± 0.2**
TIB02-**15**	739	447	0.55	0.0674	0.0140	0.0087	0.0020	0.0009	0.00002	0.0003	0.00002	0.500	33	6.0	0.2	9	2.0	850	428	5.8	0.3	**6.0**	**± 0.2**
TIB02-**25**	449	361	0.72	0.0652	0.0053	0.0084	0.0007	0.0009	0.00001	0.0003	0.00002	0.250	29	6.0	0.1	8.5	0.7	780	171	5.8	0.1	**6.0**	**± 0.1**
TIB02-**5**	324	205	0.57	0.1244	0.0213	0.0166	0.0033	0.0010	0.00003	0.0003	0.00001	0.340	64	6.2	0.2	17	3.0	2021	312	5.6	0.2	**6.2**	**± 0.2**
TIB02-**14**	442	487	0.99	0.0797	0.0111	0.0108	0.0017	0.0010	0.00002	0.0003	0.00001	0.290	42	6.4	0.2	11	2.0	1189	272	6.0	0.1	**6.4**	**± 0.2**
TIB02-**8**	326	205	0.57	0.1281	0.0247	0.0175	0.0038	0.0010	0.00004	0.0003	0.00002	0.470	64	6.4	0.2	18	4.0	2072	352	5.7	0.4	**6.4**	**± 0.2**
TIB02-**13**	224	161	0.65	0.0971	0.0134	0.0137	0.0022	0.0010	0.00003	0.0003	0.00001	0.460	53	6.6	0.2	14	2.0	1570	253	6.0	0.2	6.6	± 0.2
TIB02-**17**	234	146	0.56	0.0923	0.0155	0.0130	0.0023	0.0010	0.00002	0.0003	0.00001	0.240	49	6.6	0.1	13	2.0	1473	319	6.1	0.2	6.6	± 0.1
TIB02-**2**	293	226	0.70	0.1028	0.0198	0.0146	0.0032	0.0010	0.00004	0.0003	0.00001	0.490	56	6.6	0.2	15	3.0	1674	362	6.0	0.2	6.6	± 0.2
TIB02-**22**	225	137	0.55	0.0995	0.0084	0.0141	0.0014	0.0010	0.00003	0.0003	0.00001	0.340	53	6.6	0.2	14	1.0	1615	158	6.1	0.2	6.6	± 0.2
TIB02-**30**	227	133	0.53	0.1056	0.0146	0.0149	0.0022	0.0010	0.00002	0.0003	0.00001	0.360	56	6.6	0.2	15	2.0	1725	258	6.0	0.2	6.6	± 0.2
TIB02-**26**	234	173	0.66	0.1129	0.0172	0.0163	0.0027	0.0010	0.00003	0.0003	0.00001	0.330	58	6.7	0.2	16	3.0	1846	281	6.1	0.2	6.7	± 0.2
TIB02-**4**	526	699	1.20	0.1301	0.0246	0.0185	0.0042	0.0010	0.00004	0.0003	0.00001	0.610	65	6.7	0.3	19	4.0	2099	344	5.9	0.3	6.7	± 0.3
TIB02-**23**	521	333	0.58	0.0675	0.0055	0.0100	0.0009	0.0011	0.00001	0.0003	0.00001	0.240	32	6.9	0.1	10.1	0.9	853	171	6.6	0.1	6.9	± 0.1
TIB02-**18**	170	79	0.42	0.0701	0.0103	0.0105	0.0016	0.0011	0.00002	0.0003	0.00001	0.240	36	7.0	0.1	11	2.0	931	300	6.6	0.2	7.0	± 0.1
TIB02-**28**	382	186	0.44	0.0881	0.0080	0.0133	0.0013	0.0011	0.00002	0.0003	0.00001	0.290	46	7.0	0.1	13	1.0	1385	175	6.5	0.1	7.0	± 0.1
TIB02-**11**	371	155	0.38	0.0986	0.0191	0.0150	0.0031	0.0011	0.00003	0.0003	0.00001	0.270	53	7.1	0.2	15	3.0	1598	368	6.5	0.3	7.1	± 0.2

CONT.

Table 2.2 CONT. U-Th-Pb analytical data for LA-ICPMS spot analyses on zircon grains for volcanic rocks from Southwest Isla Tiburón, México.

				CORRECTED RATIOS										CORRECTED AGES (Ma)									
	U# (ppm)	Th# (ppm)	Th/U	$^{207}Pb/^{206}Pb$†	±1s*	$^{207}Pb/^{235}U$†	±1s*	$^{206}Pb/^{238}U$†	±1s*	$^{208}Pb/^{232}Th$†	±1s*	Rho	% disc**	$^{206}Pb/^{238}U$	±1s*	$^{207}Pb/^{235}U$	±1s*	$^{207}Pb/^{206}Pb$	±1s*	$^{208}Pb/^{232}Th$	±1s*	Best age (Ma)	1s
Sample **TIB-09-02**	Tuff of Oyster Amphitheater (*Ttoa*)			Mount ICGEO-17 (January 2011) **(CONT.)**																			
TIB02-**24**	130	63	0.43	0.1017	0.0098	0.0155	0.0017	0.0011	0.00004	0.0003	0.00001	0.370	56	7.1	0.3	16	2.0	1656	179	6.5	0.2	7.1	± 0.3
TIB02-**12**	374	231	0.56	0.0812	0.0141	0.0239	0.0046	0.0021	0.00006	0.0006	0.00002	0.510	43	13.8	0.4	24	5.0	1227	343	12.9	0.5	13.8	± 0.4
TIB02-**10**	297	290	0.88	0.0558	0.0040	0.0792	0.0063	0.0103	0.00013	0.0032	0.00004	0.290	14	66.0	0.8	77	6.0	446	154	64.6	0.7	66.0	± 0.8
TIB02-**21**	855	389	0.41	0.0493	0.0014	0.0761	0.0024	0.0112	0.00007	0.0035	0.00002	0.280	3	71.7	0.5	74	2.0	163	67	71.4	0.5	71.7	± 0.5
TIB02-**20**	387	220	0.51	0.0535	0.0019	0.1103	0.0042	0.0149	0.00011	0.0047	0.00003	0.270	10	95.6	0.7	106	4.0	352	79	94.3	0.6	95.6	± 0.7
TIB02-**9**	762	351	0.42	0.0551	0.0008	0.1141	0.0019	0.0150	0.00010	0.0048	0.00006	0.400	13	96.0	0.6	110	2.0	417	34	96.0	1.0	96.0	± 0.6
n = 24																		**Weighted $^{206}Pb/^{238}U$ mean age =**				**6.01**	**± 0.20**
																						MSWD = 2.2; n = 7	
Sample **TIB-09-06**	Rhyodacite of Cerro Starship (*Tcsf*)			Mount ICGEO-7 (October 2009)																			
TIB06-**32**	864	1041	1.11	0.0630	0.0054	0.0046	0.0004	0.0005	0.00001	0.0002	0.00001	0.200	26	3.5	0.1	4.7	0.4	709	167	3.4	0.2	3.5	± 0.1
TIB06-**13**	556	548	0.91	0.0499	0.0091	0.0042	0.0009	0.0006	0.00002	0.0002	0.00002	0.320	9	3.9	0.1	4.3	0.9	191	350	3.9	0.3	**3.9**	**± 0.1**
TIB06-**35**	357	278	0.72	0.0521	0.0154	0.0044	0.0015	0.0006	0.00003	0.0002	0.00003	0.430	3	3.9	0.2	4.0	1.0	288	481	3.9	0.6	**3.9**	**± 0.2**
TIB06-**5**	606	389	0.59	0.0711	0.0115	0.0060	0.0011	0.0006	0.00002	0.0002	0.00001	0.280	35	3.9	0.1	6.0	1.0	959	315	3.7	0.1	**3.9**	**± 0.1**
TIB06-**29**	190	95	0.46	0.0700	0.0329	0.0059	0.0030	0.0006	0.00004	0.0002	0.00007	0.390	35	3.9	0.3	6.0	3.0	928	807	4.0	1.0	**3.9**	**± 0.3**
TIB06-**11**	293	154	0.48	0.0760	0.0268	0.0065	0.0024	0.0006	0.00002	0.0002	0.00004	0.320	43	4.0	0.2	7.0	2.0	1095	735	3.8	0.8	**4.0**	**± 0.2**
TIB06-**28**	393	275	0.64	0.0775	0.0063	0.0065	0.0005	0.0006	0.00001	0.0002	0.00001	0.260	39	4.0	0.1	6.5	0.5	1134	148	4.0	0.2	**4.0**	**± 0.1**
TIB06-**34**	346	338	0.90	0.0673	0.0140	0.0058	0.0013	0.0006	0.00001	0.0002	0.00001	0.250	33	4.0	0.1	6.0	1.0	847	402	3.8	0.2	**4.0**	**± 0.1**
TIB06-**2**	237	167	0.65	0.1007	0.0165	0.0088	0.0015	0.0006	0.00002	0.0002	0.00001	0.220	54	4.1	0.1	9.0	2.0	1637	315	3.8	0.1	**4.1**	**± 0.1**
TIB06-**20**	353	354	0.92	0.0925	0.0111	0.0080	0.0011	0.0006	0.00002	0.0002	0.00001	0.320	49	4.1	0.1	8.0	1.0	1478	229	3.7	0.1	**4.1**	**± 0.1**
TIB06-**27**	322	199	0.57	0.0838	0.0146	0.0074	0.0014	0.0006	0.00002	0.0002	0.00001	0.270	41	4.1	0.1	7.0	1.0	1287	334	3.8	0.1	**4.1**	**± 0.1**
TIB06-**31**	330	313	0.87	0.0744	0.0111	0.0065	0.0011	0.0006	0.00001	0.0002	0.00001	0.370	41	4.1	0.1	7.0	1.0	1052	289	3.8	0.1	**4.1**	**± 0.1**
TIB06-**6**	241	199	0.76	0.1083	0.0168	0.0096	0.0016	0.0006	0.00002	0.0002	0.00001	0.260	59	4.1	0.1	10.0	2.0	1772	272	3.8	0.1	**4.1**	**± 0.1**
TIB06-**1**	269	202	0.69	0.1535	0.0378	0.0138	0.0038	0.0007	0.00004	0.0002	0.00001	0.520	70	4.2	0.2	14.0	4.0	2385	457	3.7	0.3	**4.2**	**± 0.2**
TIB06-**10**	277	200	0.67	0.0823	0.0122	0.0074	0.0012	0.0007	0.00002	0.0002	0.00001	0.320	48	4.2	0.1	8.0	1.0	1252	296	4.0	0.1	**4.2**	**± 0.1**
TIB06-**30**	287	160	0.51	0.0678	0.0099	0.0061	0.0010	0.0007	0.00002	0.0002	0.00001	0.270	32	4.2	0.1	6.2	1.0	863	288	4.0	0.1	**4.2**	**± 0.1**
TIB06-**9**	355	248	0.64	0.1104	0.0181	0.0101	0.0018	0.0007	0.00002	0.0002	0.00001	0.320	57	4.3	0.1	10.0	2.0	1806	289	3.9	0.1	**4.3**	**± 0.1**
TIB06-**16**	256	156	0.56	0.0728	0.0192	0.0069	0.0020	0.0007	0.00003	0.0002	0.00002	0.390	37	4.4	0.2	7.0	2.0	1007	552	4.2	0.4	**4.4**	**± 0.2**
TIB06-**19**	113	63	0.52	0.1485	0.0326	0.0142	0.0035	0.0007	0.00004	0.0002	0.00001	0.440	68	4.5	0.2	14.0	3.0	2328	401	3.9	0.2	**4.5**	**± 0.2**
TIB06-**3**	149	82	0.51	0.1208	0.0211	0.0116	0.0024	0.0007	0.00004	0.0002	0.00001	0.410	63	4.5	0.3	12.0	2.0	1968	305	4.0	0.2	**4.5**	**± 0.3**
TIB06-**15**	300	185	0.57	0.0993	0.0092	0.0096	0.0009	0.0007	0.00002	0.0002	0.00002	0.260	53	4.6	0.1	9.7	0.9	1610	174	4.9	0.4	**4.6**	**± 0.1**
TIB06-**4**	145	79	0.50	0.1078	0.0251	0.0107	0.0028	0.0007	0.00003	0.0002	0.00001	0.270	58	4.6	0.2	11.0	3.0	1763	439	4.2	0.2	4.6	± 0.2
TIB06-**25**	225	149	0.61	0.0672	0.0211	0.0068	0.0024	0.0007	0.00004	0.0002	0.00004	0.510	33	4.7	0.3	7.0	2.0	845	641	4.5	0.7	4.7	± 0.3
TIB06-**24**	161	121	0.69	0.0977	0.0236	0.0099	0.0027	0.0007	0.00003	0.0002	0.00001	0.420	53	4.7	0.2	10.0	3.0	1580	458	4.3	0.2	4.7	± 0.2
TIB06-**18**	168	114	0.62	0.1224	0.0283	0.0126	0.0032	0.0007	0.00004	0.0002	0.00001	0.450	63	4.8	0.3	13.0	3.0	1992	445	4.3	0.3	4.8	± 0.3
TIB06-**12**	141	83	0.54	0.1474	0.0367	0.0154	0.0044	0.0008	0.00005	0.0002	0.00001	0.540	67	4.9	0.3	15.0	4.0	2316	466	4.3	0.3	4.9	± 0.3
TIB06-**22**	212	138	0.60	0.0864	0.0402	0.0091	0.0048	0.0008	0.00007	0.0002	0.00006	0.470	46	4.9	0.5	9.0	5.0	1348	856	5.0	1.0	4.9	± 0.5
TIB06-**17**	343	227	0.61	0.0759	0.0177	0.0084	0.0023	0.0008	0.00004	0.0002	0.00002	0.620	42	5.2	0.3	9.0	2.0	1091	495	4.9	0.3	5.2	± 0.3
TIB06-**26**	82	35	0.39	0.1606	0.0296	0.0190	0.0038	0.0009	0.00004	0.0002	0.00001	0.340	71	5.5	0.2	19.0	4.0	2462	323	4.8	0.2	5.5	± 0.2
TIB06-**14**	4354	248	0.05	0.0473	0.0006	0.0801	0.0011	0.0123	0.00009	0.0039	0.00007	0.530	-1	78.7	0.6	78.0	1.0	66	29	79.0	1.0	78.7	± 0.6
n = 30																		**Weighted $^{206}Pb/^{238}U$ mean age =**				**4.13**	**± 0.09**
																						MSWD =2.6; n = 20	

#U and Th concentrations (ppm) are calculated relative to analyses of trace-element glass standard NIST 612.
†Isotopic ratios ratios are corrected relative to PLE standard zircon for mass bias and down-hole fractionation (PLE, Plešovice = ~337 Ma; Sláma *et al*., 2008). Common Pb corrections were made using the Andersen Method (Andersen, 2002).
*All errors in isotopic ratios and ages are absolute and given at the 1-sigma level except for the Weighted Mean $^{206}Pb/^{238}U$ age that is reported at the 2-sigma level.
**Percentage discordance obtained using the following equation (100*[(age $^{207}Pb/^{235}U$)-(age $^{206}Pb/^{238}U$)]/age $^{207}Pb/^{235}U$). Positive and negative values indicate normal and inverse discordance, respectively.
Individual zircon ages in bold were used to calculate the weighted mean $^{206}Pb/^{238}U$ age and MSWD (Mean Square of Weighted Deviates) using the computational program Isoplot (Ludwig , 2003).

Table 2.3 $^{40}Ar/^{39}Ar$ laser total fusion data of single-crystal sanidine crystals from the Tuff of Hast Pitzcal, Southwest Isla Tiburón, México.

Hole number	$^{39}Ar_k$ (Moles)	Radiogenic Yield (%)	$^{40}Ar^*/^{39}Ar_k$	K/Ca	K/Cl	Age (Ma)	Error (Ma)
sample TIB-09-15	Tuff of Hast Pitzcal *(Ttha)*		***sanidine***	*J = 0.004411 ± 0.25%*		*#189KD53*	
15	6.27E-15	77.9	0.795	19.1	25000	6.32	± 0.05
23	4.22E-15	88.0	0.796	19.4	3125	6.32	± 0.07
16	5.96E-15	80.6	0.796	26.1	25000	6.33	± 0.04
1	8.74E-15	95.9	0.797	17.3	8333	6.33	± 0.04
21	6.08E-15	92.5	0.798	19.8	14286	6.34	± 0.03
12	4.11E-15	95.5	0.803	22.6	4545	6.38	± 0.09
5	4.56E-15	93.2	0.804	21.5	9091	6.39	± 0.08
8	5.59E-15	84.5	0.804	21.4	5882	6.39	± 0.07
13	6.19E-15	95.8	0.805	14.1	14286	6.39	± 0.03
17	5.26E-15	96.1	0.807	13.3	6667	6.41	± 0.04
7	5.90E-15	61.3	0.807	15.0	9091	6.41	± 0.08
22	8.93E-15	90.3	0.808	20.7	6667	6.41	± 0.03
2	6.70E-15	89.3	0.808	23.6	4545	6.42	± 0.05
10	4.85E-15	92.6	0.811	23.9	7692	6.44	± 0.08
30	5.11E-15	96.1	0.811	17.9	3448	6.44	± 0.04
32	4.85E-15	97.1	0.811	15.7	4348	6.45	± 0.04
4	8.16E-15	86.1	0.812	14.8	5556	6.45	± 0.05
28	4.88E-15	89.8	0.813	17.0	2381	6.46	± 0.04
11	5.67E-15	76.2	0.813	17.7	4545	6.46	± 0.07
14	5.00E-15	92.4	0.813	17.1	20000	6.46	± 0.04
9	3.59E-15	99.4	0.814	22.3	***	6.46	± 0.10
26	3.77E-15	88.0	0.814	16.6	11111	6.46	± 0.05
29	6.24E-15	98.7	0.814	14.2	8333	6.47	± 0.03
33	2.77E-15	95.2	0.815	15.7	7692	6.47	± 0.06
36	3.17E-15	66.5	0.816	18.2	10000	6.48	± 0.08
35	5.96E-15	92.3	0.817	16.5	2128	6.49	± 0.04
31	3.76E-15	97.3	0.818	19.2	3448	6.50	± 0.05
37	2.07E-15	99.5	0.821	21.5	5882	6.52	± 0.09
19	5.55E-15	93.9	0.822	24.6	3571	6.53	± 0.05
34	3.80E-15	96.0	0.822	17.1	9091	6.53	± 0.05
25	5.13E-15	96.6	0.824	17.4	3333	6.55	± 0.04
20	3.73E-15	43.0	0.825	20.2	4348	6.55	± 0.10
27	1.99E-15	94.2	0.828	16.4	2778	6.58	± 0.09
24	2.57E-15	97.3	0.839	16.9	2222	6.67	± 0.08
		MSWD = 1.47		**Weighted Mean Age =**		**6.44**	**± 0.05**

Table 2.4 $^{40}Ar/^{39}Ar$ step-heating data of volcanic matrix from the Rhyodacite of Cerro Starship, Southwest Isla Tiburón, México.

Step	Temp. °C	%^{39}Ar of total	Radiogenic Yield (%)	$^{39}Ar_k$ (moles x 10^{-12})	$^{40}Ar^*/^{39}Ar_k$	Apparent K/Ca	Apparent K/Cl	Apparent Age (Ma)	Error (Ma)
TIB-09-06	***dacite matrix***	*J = 0.004439 ± 0.30%*		*wt = 356.1 mg*	*#187&188KD53*				
A	550	1.9	5.5	0.0007	0.393	4.95	71	3.14	± 0.12
B	600	1.3	24.6	0.0131	0.426	5.88	99	3.41	± 0.11
C	700	7.2	51.0	0.0176	0.413	6.03	109	3.31	± 0.02
D	800	14.5	72.6	0.0281	0.421	5.00	108	3.36	± 0.01
E	900	23.6	76.4	0.0338	0.434	3.14	105	3.47	± 0.01
F	1000	29.9	71.6	0.0227	0.445	1.87	105	3.56	± 0.01
G	1100	18.5	62.0	0.0044	0.457	1.31	107	3.65	± 0.01
H	1200	2.3	44.5	0.0007	0.457	0.39	100	3.65	± 0.08
I	1300	0.5	21.4	0.0003	0.426	0.11	28	3.41	± 0.33
J	1450	0.4	17.4	0.0003	0.396	0.07	59	3.17	± 0.57
Total Gas		100	66.7	0.1216	0.438	3.09	105	3.5	

Ages calculated assuming an initial $^{40}Ar/^{36}Ar = 295.5 \pm 0$
All precision estimates are at the one sigma level of precision.
Ages of individual steps do not include error in the irradiation parameter J.
No error is calculated for the total gas age.

Chapter 3

Onset of transform faulting in the northern Gulf of California: Implications for oblique rifting and late Miocene localization of the Pacific-North America plate boundary

Chapter is in preparation for submission to the journal *Geosphere*. Author list is:

Scott E.K. Bennett, Michael E. Oskin, and Alexander Iriondo

3.1 ABSTRACT

The Gulf of California rift has accommodated oblique divergence of the Pacific and North America tectonic plates in northwestern Mexico since Miocene time. Due to its infancy, the rifted margins of the Gulf of California preserve a rare onshore record of early continental break-up processes from which to investigate the role of rift obliquity in strain localization. We document and map rift-related structures and syn-tectonic basins on Isla Tiburón, a proximal onshore exposure of the rifted North America margin, adjacent the axis of the Gulf of California. We integrate basin analysis of syn-tectonic sedimentary basins and mapped cross-cutting relationships with geochronology of pre-rift and syn-rift volcanic units to estimate the timing of fault activity and basin formation. On southern Isla Tiburón, an early phase of east-west extension initiated sometime after ~19 Ma and was ongoing by ~12.2 Ma. Extensional faults and basins were subsequently buried by younger, less-deformed deposits of the La Cruz basin, which formed due to 5 ± 2 km of dextral motion on the La Cruz fault ca. ~7 - 4 Ma. On northeastern Isla Tiburón, extension commenced later, recorded by ~7.1 - <6.4 Ma syn-tectonic deposits in the Tecomate basin. Strike-slip faulting along the Yawassag fault subsequently cut and truncated Tecomate basin-fill and related normal faults via ≥8 km of post-6.4 Ma dextral strike-slip. Latest Miocene onset of strike-slip faulting on Isla Tiburón was synchronous with the onset of transform faulting along a significant length of the Pacific-North America plate boundary ca. 9 – 6 Ma. This transition coincides with a clockwise azimuthal shift in Pacific-North America relative motion that increased the obliquity of the rift. The record from the proto-Gulf of California illustrates how highly oblique rift geometries, where transform faults are kinematically linked to large-offset normal faults in adjacent pull-apart basins, enhance the

ability of continental lithosphere to rupture and, ultimately, hasten the formation of new oceanic rift basins.

3.2 INTRODUCTION

Continental rifts require focused strain to successfully rupture and form a new ocean basin (Buck, 1991). Rift localization may occur via a variety of processes, such as lithospheric necking (Buck, 1991, Lavier and Manatschal, 2006) heating and magmatism from asthenospheric upwelling (Kusznir and Park, 1987; Hopper and Buck, 1996; Buck et al., 1999), formation of large-offset, translithospheric detachment faults (Tucholke et al., 1998; Lavier and Manatschal, 2006), thermal weakening beneath thick rift sedimentation (Lavier and Steckler, 1997; Bialas and Buck, 2009), or an increase in extensional strain rate (England, 1983; Kusznir and Park, 1987; Bassi, 1995; Huismans and Beaumont, 2003). Fully three-dimensional numerical modeling of rifting indicates the degree of rift obliquity may also enhance localization (van Wijk, 2007; Brune et al., 2012). Highly oblique rifts accommodate a significant component of deformation on transform (strike-slip) structures (Withjack and Jamison, 1986), which tend to remain more localized (Chester, 1995) than normal faults (Buck, 1991, Forsyth, 1992), and may catalyze continental rupture along linked pull-apart basins (van Wijk, 2007; Bennett et al., 2013). Testing the role of obliquity in rift localization requires knowledge of the spatio-temporal history of deformation, and particularly the timing of transform fault formation and activity. Such records are readily accessible in sedimentary basins formed adjacent to strike-slip faults that preserve a signature of fault activity in their architecture, subsidence history, sediment provenance, and facies relationships (Christie-Blick and Biddle, 1985; Ingersoll, 1988; Xie and Heller, 2009).

The nascent Gulf of California rift is an active oblique rift (Lonsdale, 1989) where strain localization (Oskin et al., 2001; Oskin and Stock, 2003b), marine basin formation (Oskin and Stock, 2003a), and continental rupture (Lizarralde et al., 2007; Martín-Barajas et al., 2010) have each recently occurred, preserving a fresh record from which to investigate the role of obliquity in rift localization. The Gulf of California rift is located within the western portion of the Mexican Basin and Range, a diffuse continental extensional province that initiated within the Sierra Madre Occidental (Fig. 3.1 inset) during Oligocene time (Gans, 1997; Henry and Aranda-Gomez, 1992; González-León et al., 2010) and expanded westward behind the subduction-related volcanic arc. By ~12.3 Ma (chron 5a of Atwater and Stock, 1998), the plate tectonic setting evolved from subduction and back-arc extension to a broad region of integrated transtensional dextral shearing between the Pacific and North America plates both east and west of the stable Baja California microplate (Gans, 1997; Fletcher et al., 2007). This transtensional strain was accommodated across a heterogeneous, incompletely documented system of dextral, normal, and oblique-slip faults kinematically linked to the southern San Andreas fault in southern California. Following a relatively brief duration of oblique motion, this diffuse region of deformation coalesced within the NNW-trending axis of an early to middle Miocene volcanic arc (Umhoefer, 2011), and by latest Miocene time (ca. 6 Ma) Pacific-North America (PAC-NAM) plate motion localized into the Gulf of California (Oskin et al., 2001; Oskin and Stock, 2003b).

Regional models for the post-12.3 Ma tectonic evolution of the PAC-NAM plate boundary provide variable estimates for the onset, magnitude, and location of earliest dextral deformation. Early geologic and global plate circuit models (Stock and Hodges, 1989; Atwater and Stock, 1998) invoke little to no dextral faulting within the Gulf of California region east of

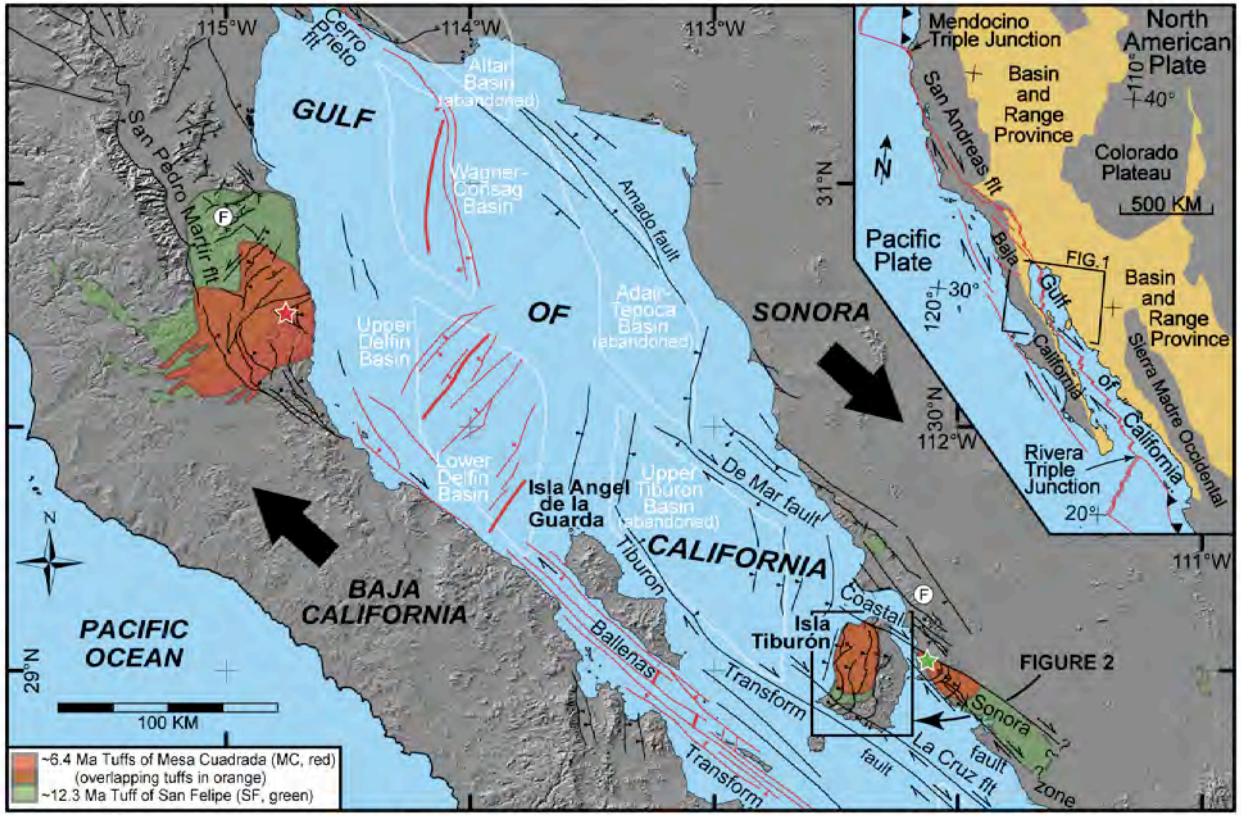

Figure 3.1 Physiographic map of the northern Gulf of California. Structures related to oblique rifting shown from Fenby and Gastil (1991), Oskin (2002), Aragón-Arreola & Martín-Barajas (2007), Aragón-Arreola et al. (2005), Darin (2011), Seiler et al. (2010), Pacheco et al. (2006), Mar-Hernández et al. (2012); Bennett et al. (2013), this study. Active Pacific-North America plate boundary structures colored in red. Inactive structures colored black. Rhombochasm-shaped transtensional basins (white lines) from Aragón-Arreola and Martín-Barajas (2007). Cross-Gulf Tie Points include 'F' - fusulinid-rich clast conglomerate (Gastil et al., 1973), and Tuff sequence in red and green (Oskin et al., 2001; Oskin and Stock, 2003b).

(INSET MAP) Simplified regional tectonic map of Western North America showing the diffuse boundary between the Pacific-North American lithospheric plates (after Oskin and Stock, 2003b). Active faults and spreading centers in red. Stable continental blocks in gray. Extensional provinces in tan.

the Baja California microplate (Fig. 3.1 inset) prior to the ~6 Ma localization event, a period loosely referred to as the proto-Gulf of California (Karig and Jensky, 1972). In contrast, other tectonic models (e.g. Gans, 1997; Fletcher et al., 2007; Seiler et al., 2010) invoke significant magnitudes (150 - 250 km) of dextral deformation here during the proto-Gulf time period. Importantly, because restorations of correlative cross-Gulf Miocene ignimbrites (Fig. 3.1; Oskin et al., 2001; Oskin and Stock, 2003b), suggest that the ~250 km of NW-SE dextral-oblique divergence across the northern Gulf of California occurred largely after ~6.4 - 6.1 Ma, any substantial earlier dextral deformation must be preserved on the fringes of the modern Gulf basin, within the rifted continental margins of eastern Baja California or western Sonora and Sinaloa.

Recent studies of the rifted continental margins of the Gulf of California (Fig. 3.1) document evidence of significant dextral deformation (up to tens of kilometers) during proto-Gulf time (Herman and Gans, 2006; Seiler et al., 2010; Bennett et al. 2013; Chapter 1 of this thesis). Timing constraints from these flanking regions suggest this deformation and related basin formation post-dates ~9 Ma, a few million years after the ~12.3 Ma plate tectonic reorganization that formed the dextral-oblique PAC-NAM plate boundary at the latitude of the Gulf of California (Stock and Molnar, 1988). It is not currently well understood if this delay indicates an evolution to a more oblique rifting phase, perhaps due to a change in PAC-NAM plate motion ca. 8 Ma (Atwater and Stock, 1998), or alternatively, if earlier dextral deformation was unevenly distributed in time and space across the Mexican Basin and Range extensional province and thus not well preserved. Consequently, it is unclear what role this dextral faulting may have played in focusing a broad region of continental extension into a localized rift and led to the formation of the Gulf of California ocean basin.

In this paper, we report the results of an integrated stratigraphic, structural, and geochronologic study of transform faults and related basins exposed on Isla Tiburón, a large (1,200 km^2) island in the Gulf of California that constitutes the outboard, exposed edge of the Sonora (North America) rifted margin. We incorporate our results with previous findings from coastal Sonora and the northeastern Baja California conjugate margin to synthesize the tectonic evolution of the northern Gulf of California, and draw connections to similar activity previously documented in the Salton Trough and southern Gulf of California. We document an early phase of normal faulting, block tilting, and related extensional basin formation on southern Isla Tiburón that initiated sometime after ~19 Ma and was active by ~12.2 Ma. From constraining the timing of tectonically related basins, we find that two dextral transform faults, the La Cruz fault and Yawassag fault, became active ~8 - 7 Ma. These faults crosscut older normal faults and their basin deposits. Strike-slip faulting and basin sediment accumulation ceased by ~4 Ma along the La Cruz fault; termination of activity is poorly constrained for the Yawassag fault. The late Miocene onset of dextral-oblique strike-slip faulting and related basin formation on Isla Tiburón is regionally consistent with findings from adjacent coastal Sonora to the east (Herman and Gans, 2006; Bennett et al., 2013), on the conjugate rift margin in northeastern Baja California (Lewis and Stock, 1998a; Seiler et al., 2010), and at great distances to the north and south along plate boundary strike (e.g. Dorsey et al., 2011). This regional onset supports the contention that increasing obliquity of PAC-NAM plate motion triggered a reorganization of faulting within the proto-Gulf of California, leading to formation of major transform faults in coastal Sonora and Isla Tiburón, and development of a belt of transrotational deformation and basin formation within the western portion of the Mexican Basin and Range province (Seiler et al, 2010; Chapter

1 of this thesis). We propose that the development of this zone of focused transtensional strain facilitated subsequent rift localization and formation of the Gulf of California ocean basin.

3.3 TECTONIC SETTING

3.3a Gulf of California

Formation of the Gulf of California occurred due to oblique-divergent separation of the Pacific and North America plates (Hamilton, 1961; Larson et al., 1968; Lonsdale, 1989; Fenby and Gastil, 1991), which initiated along the length of the Baja California peninsula ca. 12.3 Ma (Atwater and Stock, 1998). Evidence for the earliest dextral-oblique deformation east of Baja California is documented onshore, across a broad zone of transtensional deformation (Chapter 1 of this thesis), preserved within the continental margins of Baja California (Lewis and Stock, 1998a; Seiler et al., 2010) and Sonora (Bennett et al., 2013). This proto-Gulf dextral deformation was commonly associated with formation of non-marine tectonic basins.

Rifting became localized within the core of this early-formed transtensional belt by ~6.4 - 6.1 Ma (Oskin et al., 2001; Oskin and Stock, 2003b). By ~6.3 Ma, coeval with localization of the plate boundary, a permanent continuous marine seaway was established (Oskin and Stock, 2003a; Chapter 2 of this thesis), connecting slightly older (~8.5 - 7.0 Ma) marine basins in the southern Gulf of California (e.g. Carreño, 1992; Molina-Cruz, 1994; Holt et al., 2000) with marine basins in the northern Gulf of California and the Salton Trough (e.g. Escalona-Alcázar et al., 2001; Pacheco et al., 2006; Dorsey et al., 2011; Chapter 2 of this thesis). Large marine depocenters, which contain thick (>4 km) sequences of marine sediments (González-Fernández et al., 2005; Pacheco et al., 2006), developed within a NNW-trending belt of *en echelon* pull-

apart basins, now located in the eastern part of the modern-day Gulf of California (Fig. 3.1; Aragón-Arreola and Martín-Barajas, 2007).

By late Pliocene time, transtensional strain in the northern Gulf of California migrated (Aragón-Arreola and Martín-Barajas, 2007), abandoning the eastern marine basins and initiating new marine pull-apart basins to the west (see also Lonsdale, 1989). This westernmost system of faults remains the primary PAC-NAM plate boundary, with oblique plate motion accommodated along a system of long, NW-striking, right-stepping, *en echelon*, transform faults connected by short (≤50 km-wide), NW-SE-extending, pull-apart basins. Many of these basins have proceeded to seafloor spreading in the southern half of the Gulf of California, where the plate boundary eventually connects with the East Pacific Rise at the mouth of the Gulf of California (Fig. 3.1 inset; Larson et al., 1968; Lonsdale, 1989; Fenby and Gastil, 1991; Aragón-Arreola and Martín-Barajas, 2007; Kluesner, 2011).

3.3b Sonoran Margin

In the northern Gulf of California, the largely submerged Sonoran continental margin serves as the western, rifted edge of North America continental crust (Fig. 3.1). Here, a detailed offshore seismic reflection study (Mar-Hernández et al., 2012) demonstrates that the irregular edge of the margin is structurally controlled by a system of NW-striking *en echelon* dextral-oblique faults kinematically linked to major N-striking normal faults (Fig. 3.1). These first-order structures define the eastern edges of deep rhomb-shaped marine pull-apart basins, which have accommodated NW-SE extension related and parallel to the NW-striking dextral-oblique faults. Together, these structures and basins form a series of NW-SE-elongate structural rift segments:

Wagner-Consag--Adair-Tepoca, Upper Delfín-Upper Tiburón, and Lower Delfín-Lower Tiburón-Yaqui rift segments (Fig. 3.1).

The southeastern reaches of these offshore transform faults bound the eastern, now-abandoned marine pull-apart basins that were the site of rapid divergence immediately following rift localization ca. 6.4 - 6.1 Ma (Oskin and Stock, 2003b; Aragón-Arreola and Martín-Barajas, 2007). At the latitude of Isla Tiburón, NW-striking dextral-oblique faults that bound the Upper Delfín-Upper Tiburón rift segment appear to continue to the southeast within the Sonoran continental margin (Gastil and Krummenacher, 1977a, b). Here, the total length of these transform fault zones each exceeds multiple tens of kilometers, suggesting they were significant, plate boundary-scale structures prior to rift localization.

The southwestern edge of the Upper Delfín-Upper Tiburón rift segment is bound by the Tiburón transform fault offshore southern Isla Tiburón (Figs. 3.1 and 3.2A; Lonsdale, 1989; Fenby and Gastil, 1991). Approximately 9 km to the northeast, the dextral La Cruz fault runs parallel to the Tiburón transform fault across southern Isla Tiburón (Gastil and Krummenacher, 1977a; Oskin, 2002; Oskin and Stock, 2003a,b; Chapter 2 of this thesis), both continuing offshore ~150 km southeast of the island (Aragón-Arreola et al., 2005). Although the Tiburón transform fault is the primary transform structure along the southwestern edge of this rift segment, the La Cruz fault is considered to be a less-significant, but related dextral fault (Oskin and Stock, 2003a,b). Thick sequences of middle Miocene arc-related volcanic deposits exposed on both sides of the La Cruz fault (Fig. 3.2A) do not match, suggesting large amounts of dextral and/or normal displacement (Oskin and Stock, 2003b). Reconstructions by Oskin and Stock (2003b) suggest minimum total dextral offset of ~28 km, based on the total onshore distance of these mismatched volcanic rocks along the La Cruz fault. The oldest rocks known to directly

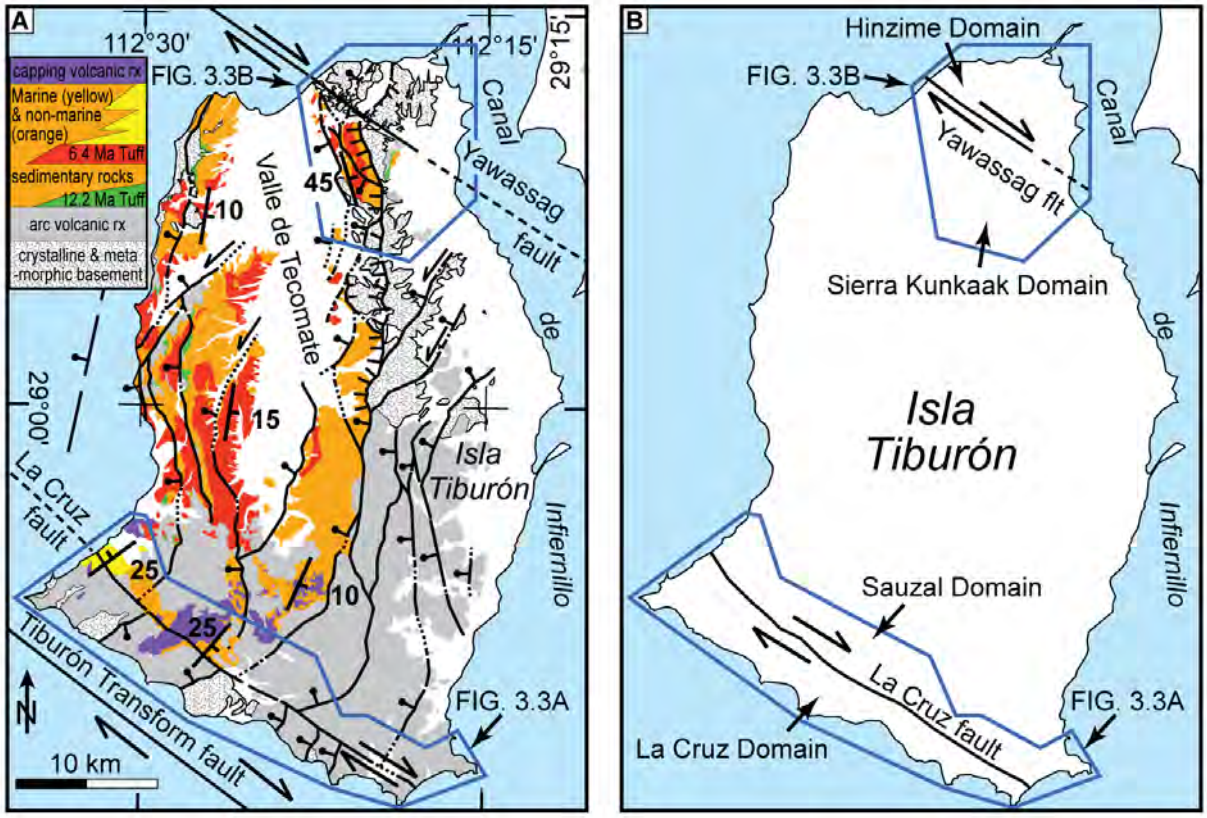

Figure 3.2 (A) Simplified geologic map of Isla Tiburón. Geology compiled from Gastil and Krummenacher (1977a); Oskin, (2002); this study.

(B) Map showing structural domains discussed in text.

correlate across the La Cruz fault are late Miocene (6.4 - 6.0 Ma) marine deposits (Fig. 3.2A), which display no more than 1 km of dextral displacement (Oskin and Stock, 2003a; Chapter 2 of this thesis). This correlation suggests that most of the significant fault activity on the La Cruz fault occurred prior to rift localization. Thus the La Cruz fault preserves a relatively intact record of how strike-slip faulting evolved within the rift during proto-Gulf time.

The northeastern edge of the Upper Delfín-Upper Tiburón rift segment is bound offshore by the De Mar transform fault (Fig. 3.1; Aragón-Arreola and Martín-Barajas, 2007; Mar-Hernández et al., 2012). This transform fault likely connects via a right step to the Coastal Sonora Fault Zone, exposed on northeastern Isla Tiburón and the Sonoran mainland (Fig. 3.1). On northeastern Isla Tiburón, the only onshore exposure of the Coastal Sonora Fault Zone consists of the Yawassag fault (Fig. 3.2A; Gastil and Krummenacher, 1977a). Along the ~8 km-long exposed portion of the fault, basement units do not directly correlate and Miocene volcanic rocks do not match, suggesting at least 8 km of dextral displacement. Additional, sub-parallel branches of the Coastal Sonora Fault Zone may be present offshore northeastern Isla Tiburón, beneath the northern end of the Canal de Infiernillo (Fig. 3.2). On mainland Sonora to the southeast, the Coastal Sonora Fault Zone consists of the Sacrificio, Bahía Kino, and Infiernillo faults (Fig. 3.1; Oskin, 2002; Bennett et al., 2013). Previous regional tectonic models, informed by geologic results along the PAC-NAM plate boundary and knowledge of total PAC-NAM post-12.3 Ma dextral offset, postulate that dextral faults in coastal Sonora have accommodated significant displacement (150 - 250 km) since 12.3 Ma (Nicholson et al, 1994; Gans, 1997; Wilson et al, 2005; Fletcher et al., 2007; Seiler et al., 2010). However, detailed mapping suggests a more modest amount. Along the Sonoran coast directly east of Isla Tiburón, Bennett et al. (2013) report a minimum of 41 ± 11 km of displacement across the Coastal Sonora Fault Zone,

with the majority of deformation and basin formation initiating ca. 7 Ma. This minimum estimate is close to the maximum of 60 ± 30 km of displacement permitted from matching pre-15 Ma distinctive conglomerate exposures across the Gulf of California (Fig. 3.1; Gastil et al., 1973) after restoration of post-6.1 Ma divergence (Oskin et al., 2001; Oskin and Stock, 2003b).

3.4 METHODS

3.4a Geologic, Structural, and Stratigraphic Mapping

Building upon the reconnaissance work by Gastil and Krummenacher (1977a) and Oskin (2002) (Fig. 3.2A), we present geologic mapping and analysis of the La Cruz and Yawassag dextral faults where these first-order structures are exposed across southern and northeastern Isla Tiburón, respectively. These first-order structures divide each study area into two structural domains (Fig. 3.2B). We also document well-exposed sedimentary basins that are adjacent and intimately related to these structures. These syn-tectonic basins contain rift-related rocks and second-order structures that preserve a record of fault-related subsidence and deformation.

We conducted detailed geologic, structural, and stratigraphic mapping along 5 - 10 km-wide swaths straddling the La Cruz and Yawassag faults (Figs. 3.3 and 3.4). Structural measurements include documentation of brittle fault orientations and kinematic indicators such as fault striae preserved on polished fault planes (Fig. 3.3). Mapping was conducted at 1:10,000-scale on Quickbird satellite imagery with topographic contours derived from the 90-m Shuttle Radar Topography Mission digital elevation model (Farr et al., 2007). Three visible and one infrared bands of Quickbird imagery were pan-sharpened to generate a 0.6 m-resolution false-color base map using spectral bands 4-2-1.

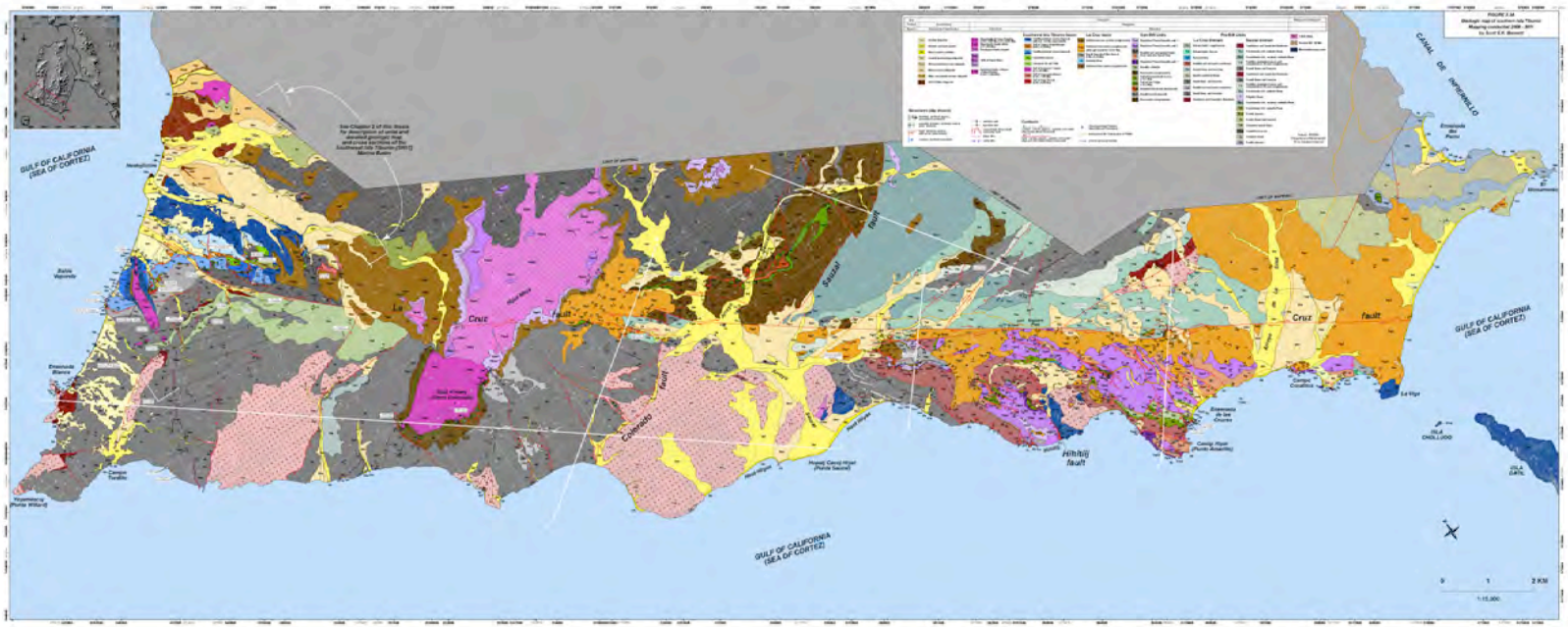

Figure 3.3A (A) 1: 15,000-scale geologic map of southern Isla Tiburón. New and previously published geochronologic sample locations and isotopic ages shown on map.

Electronic copy of full-sized map is available on data disc in rear pocket. Printed map sheet is 36” tall, 90” wide.

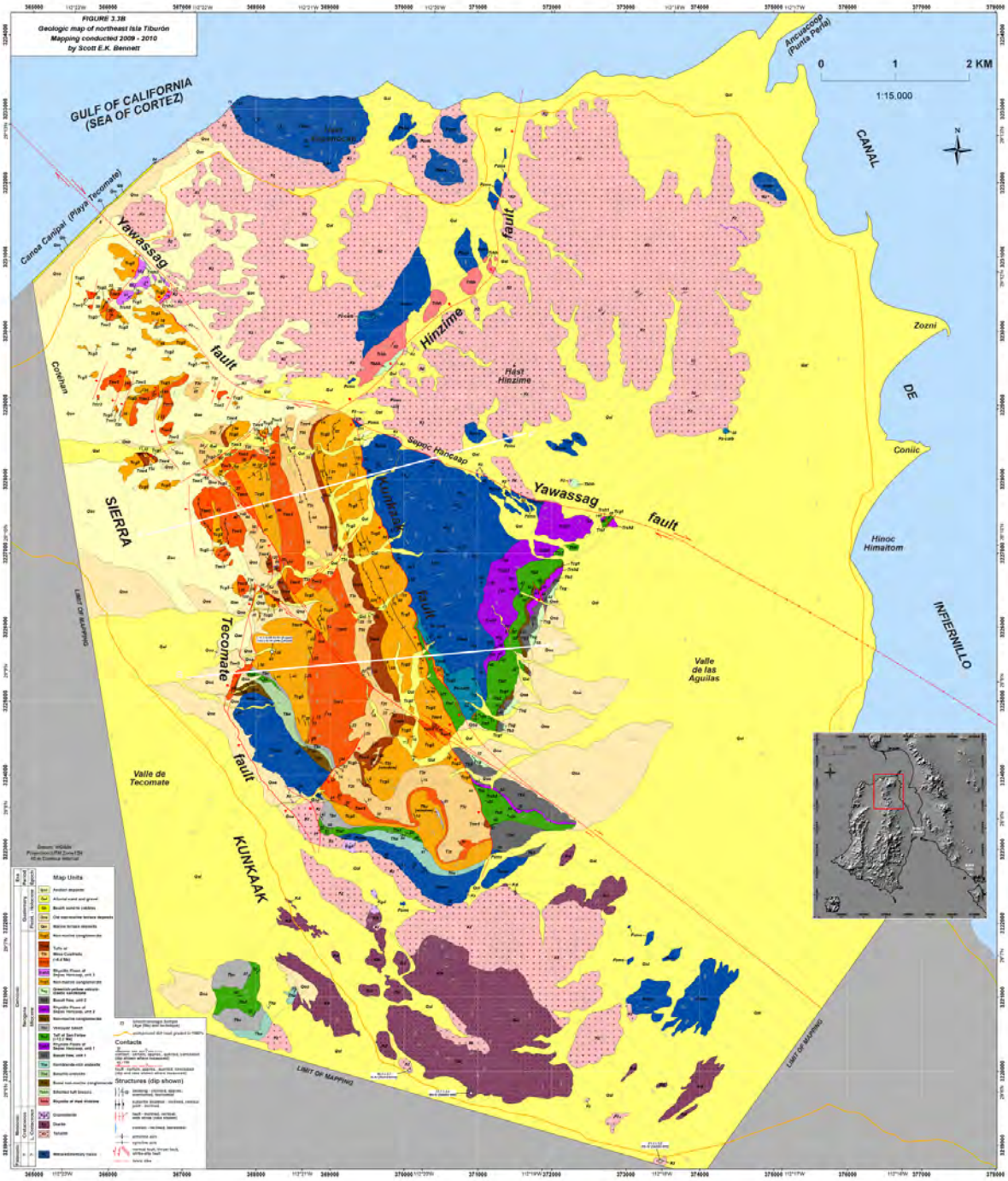

Figure 3.3B (B) 1: 15,000-scale geologic map of northeastern Isla Tiburón. New and previously published geochronologic sample locations and isotopic ages shown on map.

Electronic copy of full-sized map is available on data disc in rear pocket. Printed map sheet is 42” tall, 36” wide.

Figure 3.4 Schematic stratigraphic columns of geologic map units for (A) southern and (B) northeastern Isla Tiburón. Lithologic unit indicators and colors correspond to units on geologic maps (Fig. 3.3) and geologic cross sections (Fig. 3.8). Isotopic ages for units (if known) are shown in million years (Ma). See text for descriptions of map units and details of isotopic ages.

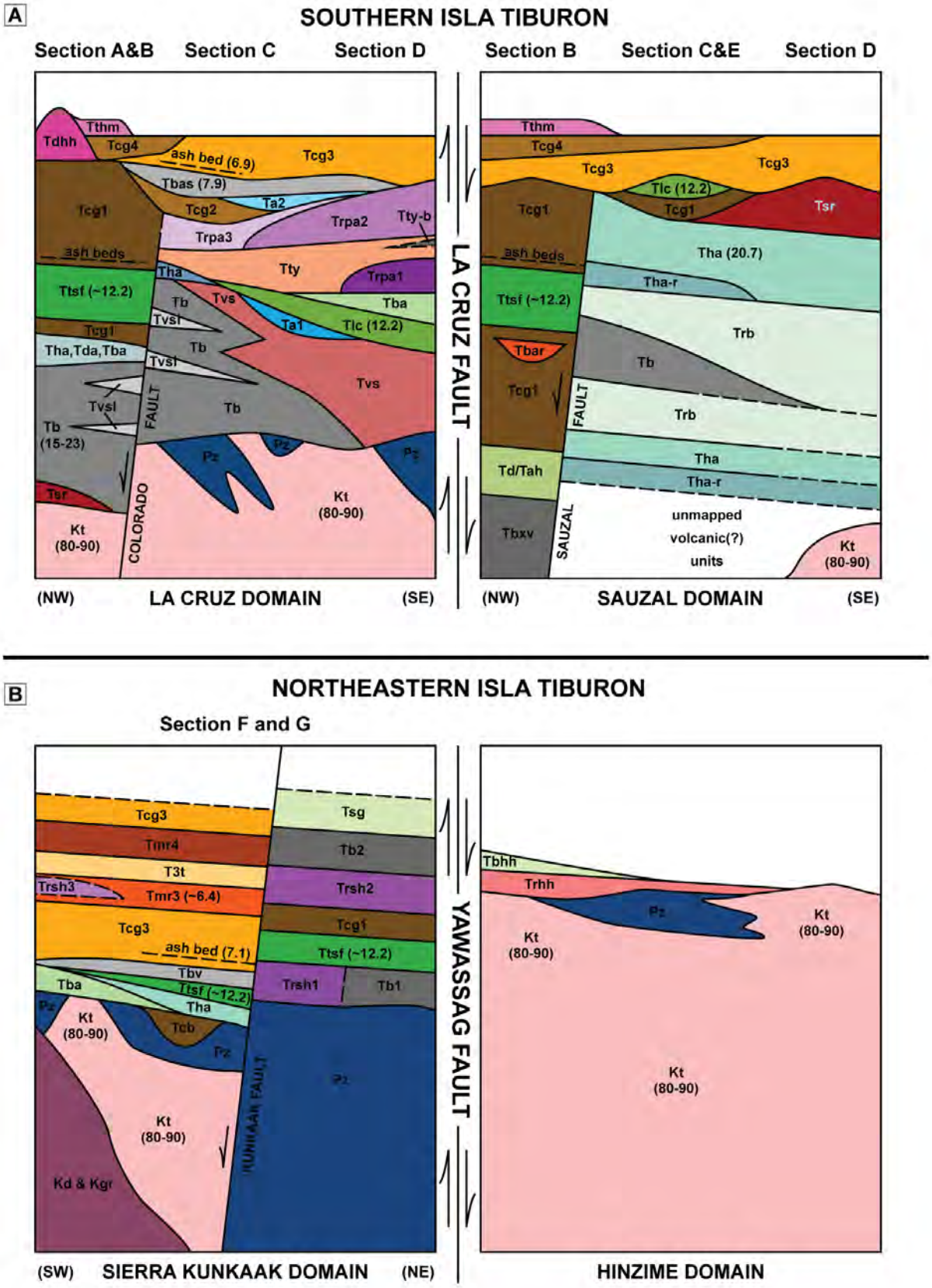
A
SOUTHERN ISLA TIBURON
Section A&B
Section C
Section D
Section B
Section C&E
Section D
Tthm
Tdhh
Tcg4
ash bed (6.9)
Tcg3
Tbas (7.9)
Tcg2
Ta2
Tcg1
Trpa2
Tty-b
Trpa3
ash beds
Tty
Tha
Trpa1
Ttsf (~12.2)
Tb
Tvs
Tba
Tvsl
Ta1
Tlc (12.2)
Tcg1
Tha,Tda,Tba
Tb
Tvsl
Tvs
FAULT
Tb
Tvsl
Tb
(15-23)
Pz
Pz
Pz
Tsr
COLORADO
Kt
(80-90)
Kt
(80-90)
LA CRUZ FAULT
Tthm
Tcg4
Tcg3
Tcg3
Tlc (12.2)
Tcg1
Tcg1
Tsr
ash beds
Tha (20.7)
Tha-r
Ttsf (~12.2)
Trb
Tbar
Tb
Tcg1
FAULT
Trb
Tha
Td/Tah
Tha-r
unmapped
volcanic(?)
units
Tbxv
SAUZAL
Kt
(80-90)
(NW)
LA CRUZ DOMAIN
(SE)
(NW)
SAUZAL DOMAIN
(SE)
B
NORTHEASTERN ISLA TIBURON
Section F and G
Tcg3
Tsg
Tmr4
Tb2
T3t
Trsh3
Tmr3 (~6.4)
Trsh2
Tcg3
Tcg1
ash bed (7.1)
Ttsf (~12.2)
Tbv
Tba
Ttsf (~12.2)
Trsh1
Tb1
Tha
Pz
Kt
(80-90)
Tcb
Pz
Pz
KUNKAAK FAULT
Kt
(80-90)
Kd & Kgr
YAWASSAG FAULT
Tbhh
Trhh
Pz
Kt
(80-90)
Kt
(80-90)
Kt
(80-90)
(SW)
SIERRA KUNKAAK DOMAIN
(NE)
HINZIME DOMAIN

3.4b Geochronology

To provide age constraints for faulting and basin formation along the La Cruz and Yawassag faults, we analyzed samples of volcanic units that underlie and are interbedded within basin deposits (Figs. 3.5, 3.6, and 3.7). Samples consisted of 2 - 5 kg of fresh rock collected from representative, in-place outcrops. In the laboratory, samples were separated into their mineral constituents. Desired mineral phases for isotopic analysis were isolated via standard magnetic, density, and hand picking mineral separation techniques. U/Pb analysis of zircon crystals was conducted in the Stanford-USGS SHRIMP-RG laboratory at Stanford University. Zircon rims were targeted during multiple, single-crystal analyses to avoid older, inherited crystal cores. Typical sample spot beam locations varied between 23 - 32 microns in diameter. Cathodoluminescence (CL) images used in defining the zircon analytical spots will be presented in figures (currently being processed) when submitting manuscripts for publication. Ar/Ar analysis of k-feldspar crystals and volcanic matrix was conducted in the U.S. Geological Survey Thermochronology laboratory facility in Reston, VA. Multiple, single-crystal analyses were conducted to allow detection of older inherited sanidine crystal populations. For all geochronologic results, we report ages with small uncertainties of ≤3%. All geochronologic rock samples were sent to collaborator Alexander Iriondo (Universidad Nacional Autónoma de México, Juriquilla), who oversaw all mineral separation, laboratory analysis, and data interpretation for the ages reported in this manuscript.

3.5 LA CRUZ FAULT STUDY AREA

The La Cruz fault study area encompasses southern Isla Tiburón (Fig. 3.3A). Here, the NW-striking La Cruz fault separates the La Cruz and Sauzal structural domains (Fig. 3.2B).

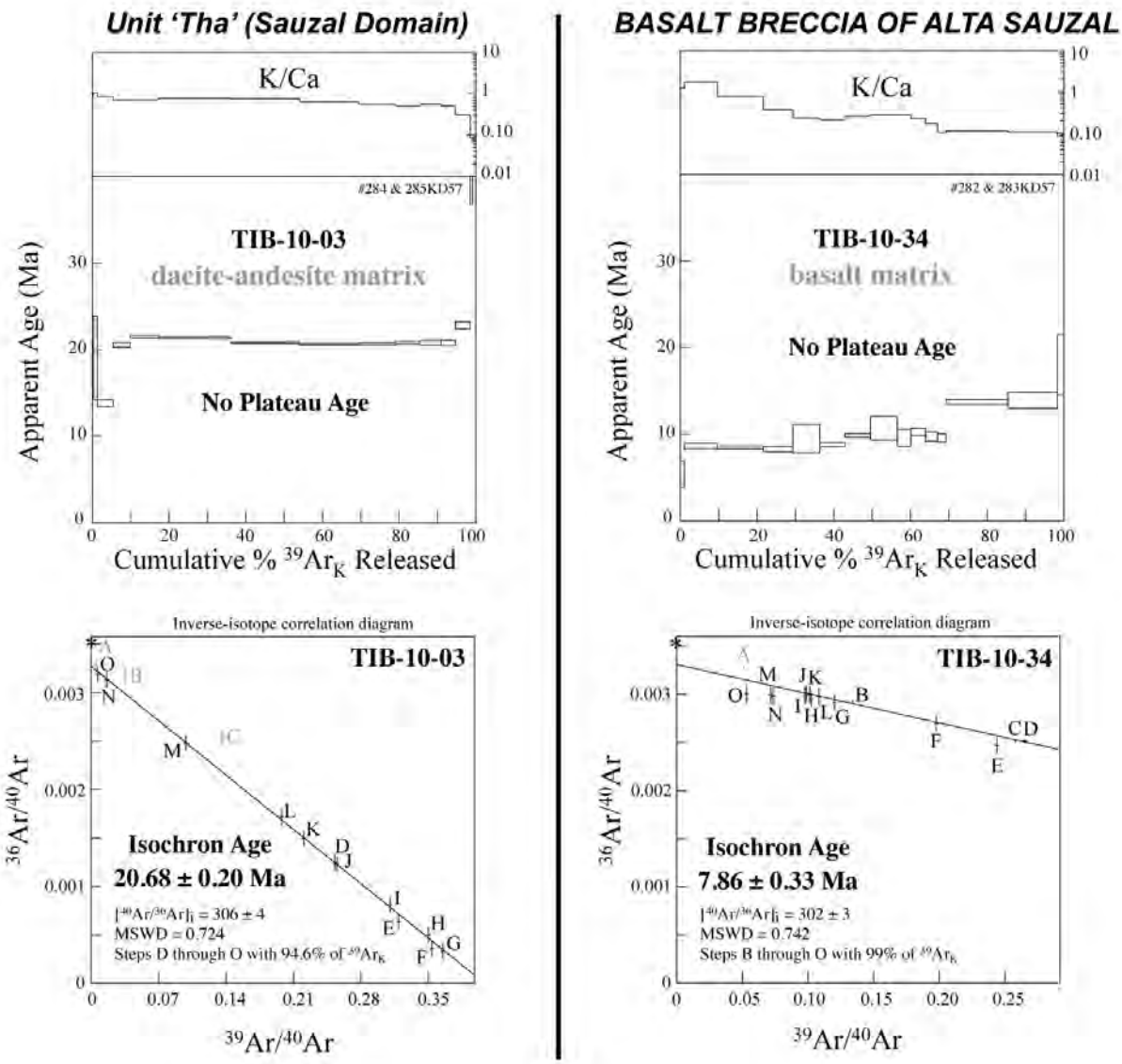

Figure 3.5 K/Ca ratios and 40Ar/39Ar age spectrum plot (top) and inverse-isotope correlation diagram (bottom) for volcanic matrix from samples of (A) unit 'Tha' in the Sauzal domain, and (B) the Basalt Breccia of Alta Sauzal. Gray shaded letters indicate steps excluded from the isochron age determination. See Table 3.1 for analysis data.

Figure 3.6 40Ar/39Ar geochronologic ages calculated for volcanic rocks on southwestern Isla Tiburón. %40Ar*, K/Ca ratios, and age probability diagram of multiple, single-grain, total fusion ages on potassium-feldspar crystals (left) and inverse-isotope correlation diagram (right) for samples of (A and C) the Tuff of San Felipe (Ttsf), (B, D, and E) the Tuff of Ensenada de La Cruz (Tlc), and (F) an ash bed interbedded near the base of Tecomate basin conglomerate (Tcg3). Crystals omitted from mean age calculation are gray hollow circles (left) and gray shaded ellipses and crystal numbers (right). See Table 3.2 for analysis data.

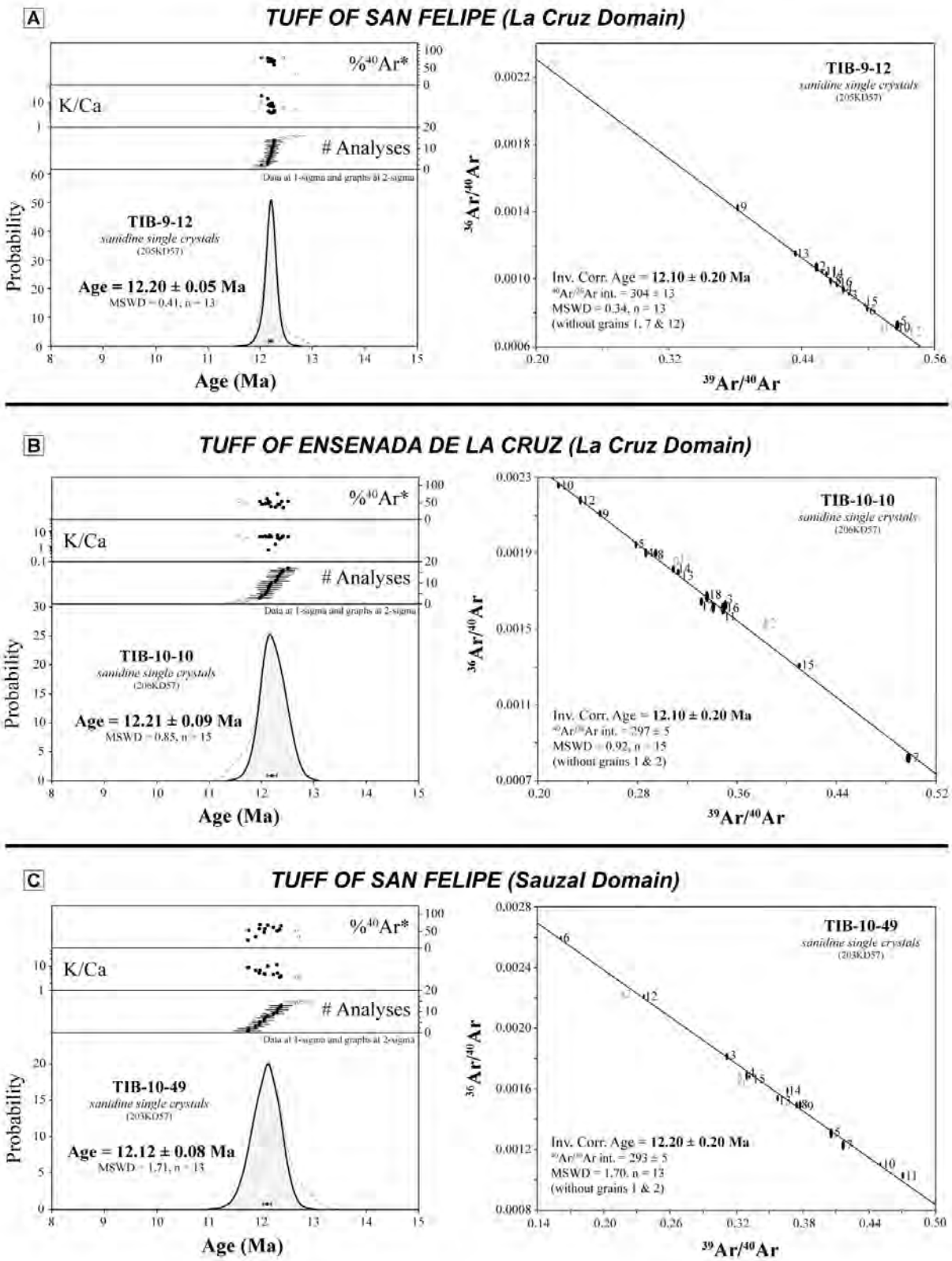
A
TUFF OF SAN FELIPE (La Cruz Domain)
%40Ar*
K/Ca
Analyses
Data at 1-sigma and graphs at 2-sigma
Probability
TIB-9-12
sanidine single crystals
(205KD57)
Age = 12.20 ± 0.05 Ma
MSWD = 0.41, n = 13
Age (Ma)
TIB-9-12
sanidine single crystals
(205KD57)
Inv. Corr. Age = 12.10 ± 0.20 Ma
40Ar/36Ar int. = 304 ± 13
MSWD = 0.34, n = 13
(without grains 1, 7 & 12)
36Ar/40Ar
39Ar/40Ar
B
TUFF OF ENSENADA DE LA CRUZ (La Cruz Domain)
%40Ar*
K/Ca
Analyses
Data at 1-sigma and graphs at 2-sigma
Probability
TIB-10-10
sanidine single crystals
(206KD57)
Age = 12.21 ± 0.09 Ma
MSWD = 0.85, n = 15
Age (Ma)
TIB-10-10
sanidine single crystals
(206KD57)
Inv. Corr. Age = 12.10 ± 0.20 Ma
40Ar/36Ar int. = 297 ± 5
MSWD = 0.92, n = 15
(without grains 1 & 2)
36Ar/40Ar
39Ar/40Ar
C
TUFF OF SAN FELIPE (Sauzal Domain)
%40Ar*
K/Ca
Analyses
Data at 1-sigma and graphs at 2-sigma
Probability
TIB-10-49
sanidine single crystals
(203KD57)
Age = 12.12 ± 0.08 Ma
MSWD = 1.71, n = 13
Age (Ma)
TIB-10-49
sanidine single crystals
(203KD57)
Inv. Corr. Age = 12.20 ± 0.20 Ma
40Ar/36Ar int. = 293 ± 5
MSWD = 1.70, n = 13
(without grains 1 & 2)
36Ar/40Ar
39Ar/40Ar

D

TUFF OF ENSENADA DE LA CRUZ (Sauzal Domain)

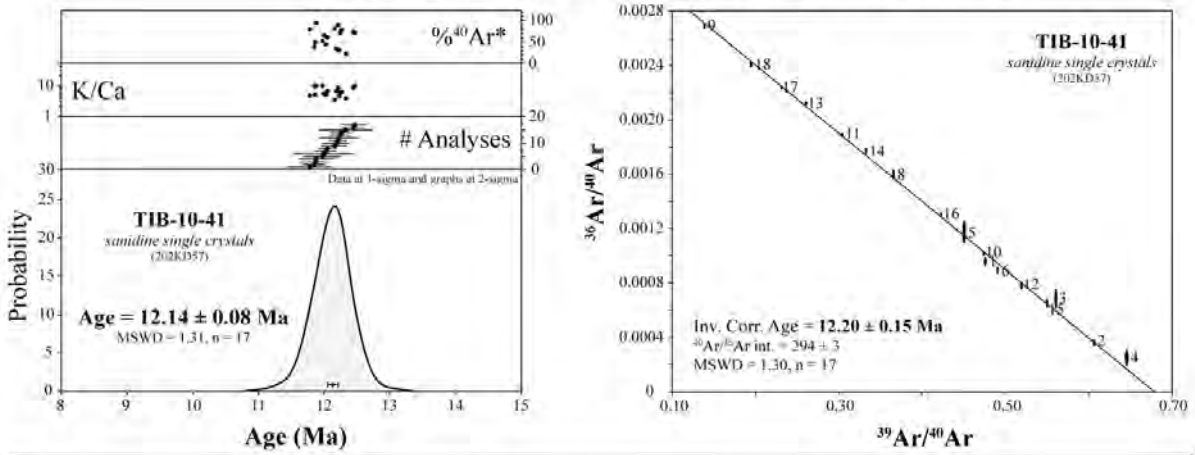

E

TUFF OF ENSENADA DE LA CRUZ (La Cruz fault zone)

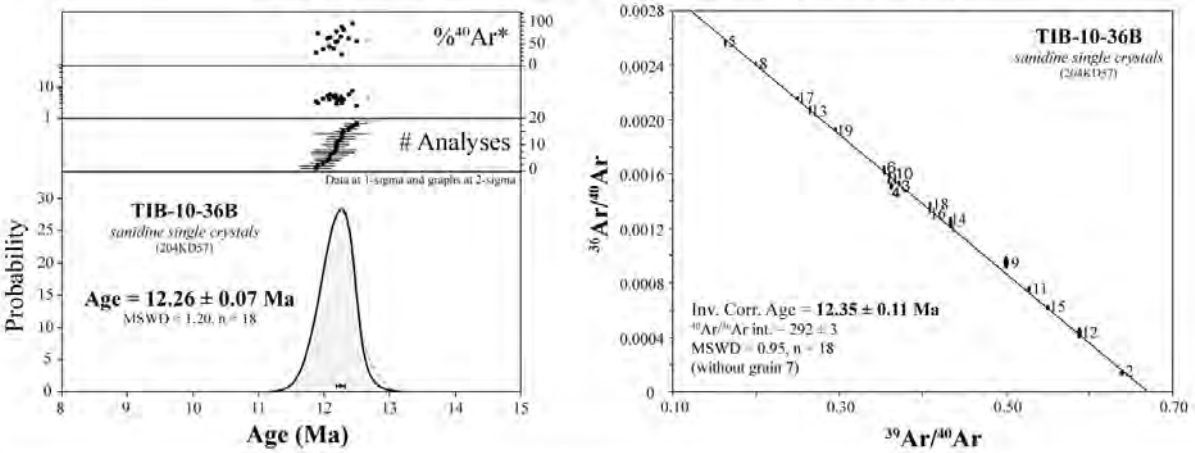

F

Ash Bed in 'Tcg3' (Tecomate Basin)

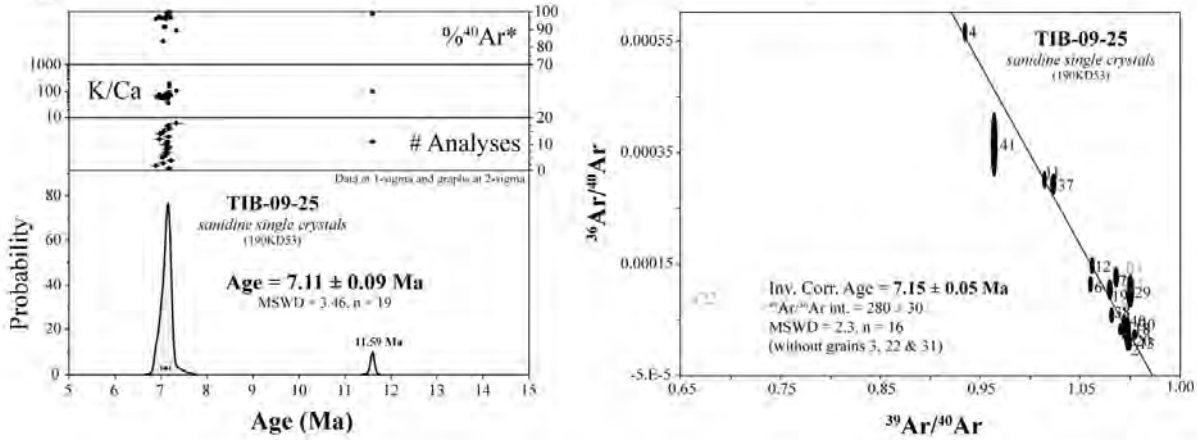

Figure 3.7 206Pb/238U Tera-Wasserburg concordia diagram (left) and age spectrum diagram (right) for multiple zircon crystals from samples of (A) an ash bed interbedded near the base of the La Cruz basin conglomerate (Tcg3), and (B) an ash bed interbedded near the base of Tecomate basin conglomerate (Tcg3). Sample shown in panel B is same sample dated with 40Ar/39Ar techniques shown in Figure 6F. Zircon crystals omitted from mean age calculation are gray squares with gray, dashed error ellipses. Relatively younger zircons have high uranium concentrations (Table 3.3) and are omitted from mean age due to possible lead loss. Relatively older zircons are omitted due to potential inheritance. See Table 3.3 for analysis data.

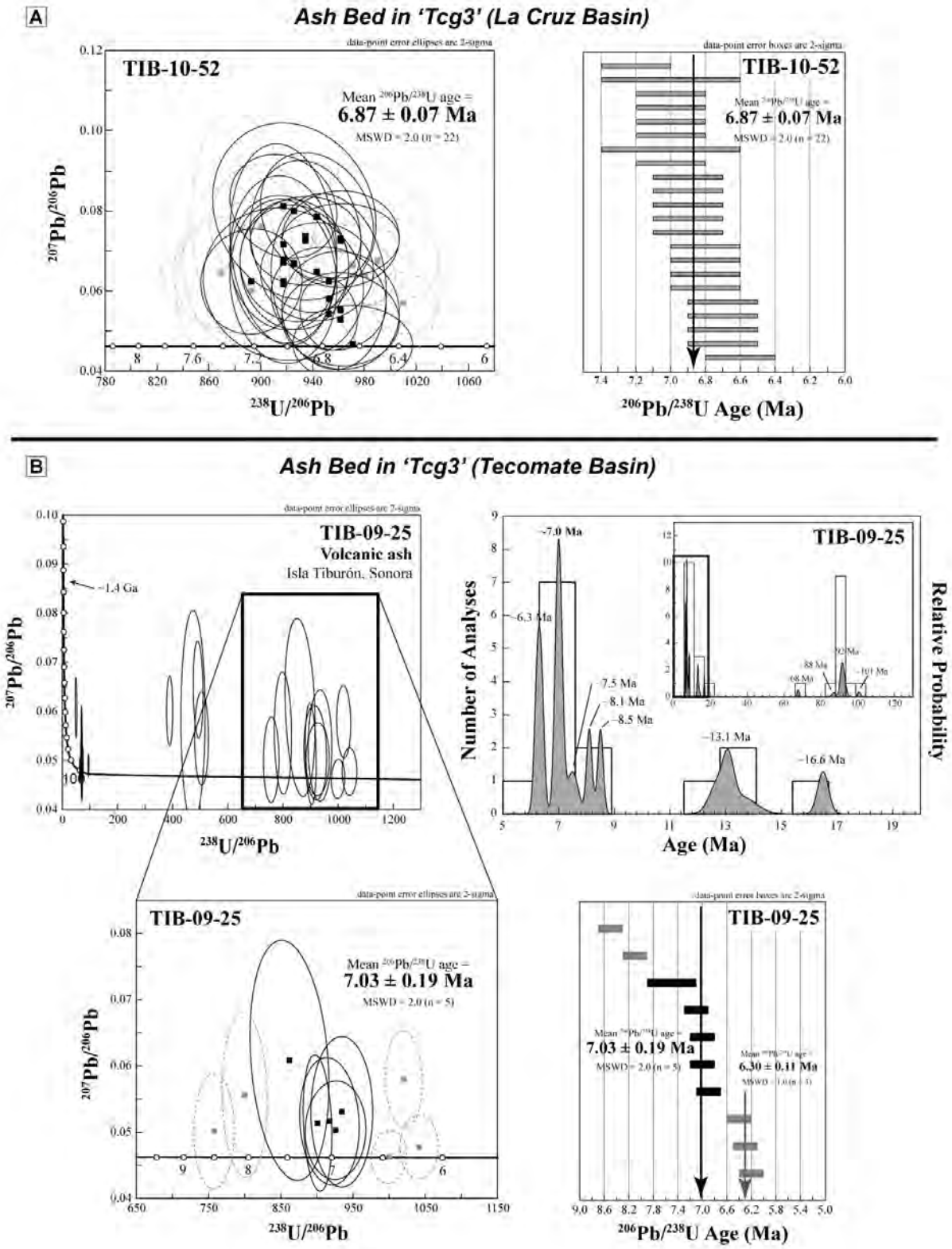
A
Ash Bed in 'Tcg3' (La Cruz Basin)
data-point error ellipses are 2-sigma
TIB-10-52
Mean 206Pb/238U age =
6.87 ± 0.07 Ma
MSWD = 2.0 (n = 22)
207Pb/206Pb
238U/206Pb
data-point error boxes are 2-sigma
TIB-10-52
Mean 206Pb/238U age =
6.87 ± 0.07 Ma
MSWD = 2.0 (n = 22)
206Pb/238U Age (Ma)
B
Ash Bed in 'Tcg3' (Tecomate Basin)
data-point error ellipses are 2-sigma
TIB-09-25
Volcanic ash
Isla Tiburón, Sonora
~1.4 Ga
207Pb/206Pb
238U/206Pb
~7.0 Ma
~6.3 Ma
7.5 Ma
~8.1 Ma
~8.5 Ma
~13.1 Ma
~16.6 Ma
TIB-09-25
Number of Analyses
Relative Probability
Age (Ma)
data-point error ellipses are 2-sigma
TIB-09-25
Mean 206Pb/238U age =
7.03 ± 0.19 Ma
MSWD = 2.0 (n = 5)
207Pb/206Pb
238U/206Pb
data-point error boxes are 2-sigma
TIB-09-25
Mean 206Pb/238U age =
7.03 ± 0.19 Ma
MSWD = 2.0 (n = 5)
Mean 206Pb/238U age =
6.30 ± 0.11 Ma
206Pb/238U Age (Ma)

These domains consist of arc-related volcanic rocks of broadly similar age (~21 - 12 Ma) (Gastil and Krummenacher, 1977b; Neuhaus, 1989; Gastil et al., 1999; this study), though in detail, the arc-related volcanic rocks immediately juxtaposed along the La Cruz fault trace are dissimilar. We correlate deposits of early to middle Miocene arc-related rocks and two latest middle Miocene ash-flow tuffs across the La Cruz fault. Younger, late Miocene sedimentary and volcanic units also correlate across the La Cruz fault and were emplaced syn-tectonically with dextral-oblique faulting.

3.5a Stratigraphy and Geochronology

3.5a1 Basement Rocks

Basement rocks exposed adjacent to the La Cruz fault on southern Isla Tiburón consist of metamorphic units that serve as the host rock for younger plutonic bodies (Fig. 3.4A). Metamorphic basement rocks consist of slate, quartzite, and phyllite and are observed only southwest of the La Cruz fault, east of Arroyo Sauzal (Fig. 3.3A), including the adjacent small islands of Isla Dátil and Isla Cholludo (Gastil and Krummenacher, 1977a). These host rocks are thought to be pre-Cambrian to Cambrian in age (Gastil and Krummenacher, 1977b). Plutonic basement rocks in the La Cruz fault study area consist entirely of tonalite and related, typically felsic, dikes. These plutonic rocks have not been dated, but are similar to isotopically-dated outcrops of Late Cretaceous (~80 - 90 Ma) crystalline basement units on northern Isla Tiburón (Gastil and Krummenacher, 1977b; Schaaf et al., 1999) and along the adjacent Sonora coastline (Gastil and Krummenacher, 1977b; Valencia-Moreno, 2003; Ramos-Velázquez et al., 2008). In our mapping we also discovered an exposure of tonalite approximately one kilometer northeast

of the La Cruz fault (Fig. 3.3A) that was not known to previous studies (Gastil and Krummenacher, 1977a; Gastil et al., 1999; Oskin, 2002; Oskin and Stock, 2003a).

3.5a2 Early to Middle Miocene Volcanic and Sedimentary Rocks

A thick sequence of volcanic and sedimentary rocks of early to middle Miocene age nonconformably overlies basement rocks on southern Isla Tiburón (Figs. 3.3A and 3.4A). These units are heterogeneous along strike and appear to be concentrated into three, compositionally diverse volcanic centers. We observe concentrations of basaltic units in the west, andesitic and dacitic units to the north, and rhyolitic units to the southeast (Fig. 3.3A). Deposits of these volcanic centers appear to be interstratified over large, along strike distances. Previous studies that focused on the southwestern corner of Isla Tiburón document early to middle Miocene volcanic and sedimentary units of different lithology and age juxtaposed across the La Cruz fault (Gastil and Krummenacher, 1977a; Neuhaus, 1989; Gastil et al., 1999; Oskin, 2002; Oskin and Stock, 2003a; Chapter 2 of this thesis), a pattern that persists along the entire fault trace (Fig. 3.3A; Gastil and Krummenacher, 1977a; this study). Here, we summarize this volcanic and sedimentary sequence, spatially from west to east, within both the La Cruz and Sauzal domains.

From the western tip of the island to Hast Hinamj (sometimes referred to as Cerro Colorado), the early to middle Miocene sequence in the La Cruz domain consists of red volcaniclastic sandstone (*Tvsl*), basalt flows and breccias (*Tb*), and lacustrine limestone (*Tsr*) (Neuhaus, 1989; Gastil et al., 1999; Chapter 2 of this thesis). These are conformably overlain by additional basaltic- and dacitic-andesite lava flows and breccias (*Tba and Tda*) (Fig. 3.3A and 8A). Several of these volcanic units have been isotopically dated in previous studies, and range in age from 23 - 15 Ma (Fig. 3.3A; Gastil and Krummenacher, 1977b; Neuhaus, 1989; Gastil et

al., 1999). Beneath Hast Hinamj and east towards the Arroyo Sauzal drainage, equivalent La Cruz domain units consist of basalt flows and breccias (*Tb*) with occasional interbedded red volcaniclastic sandstone (*Tvsl*) conformably overlain by an andesite lava flow (*Tha*) (Figs. 3.3A and 3.8B). East of the Arroyo Sauzal drainage in the La Cruz domain, the interbedded basalt (*Tb*) and red volcaniclastic sandstone (*Tvsl*) persist at the base of the Miocene section. Gastil and Krummenacher (1977b) report a K-Ar (whole rock) age of 7.0 ± 0.3 Ma from a basalt just east of Arroyo Sauzal (Fig. 3.3A). This sample location is amongst moderately inclined basalt flows (*Tb*) that we confidently map immediately overlying the regional basement nonconformity and 100's of meters stratigraphically below an extensive latest middle Miocene tuff marker discussed below (Fig. 3.3A and 3.8C). Thus, this reported K-Ar age is either erroneously young, or the sample was mislocated on their map. It is possible that a younger basalt flow, located ~1 km to the east of their locality, was sampled instead. The basal basalt flows (*Tb*) and volcaniclastic sandstone and conglomerate (*Tvsl*) units gradually thin to the east where they are conformably overlain by thick deposits of red volcaniclastic sandstone (*Tvs*). Further to the east, in the footwall of the Hihitiij fault, the basal basalt flows (*Tb*) are no longer present and this relatively younger red volcaniclastic sandstone (*Tvs*) rests directly upon basement rocks (Figs. 3.3A and 3.8D). *Tvs* is conformably overlain by another andesite flow (*Ta1*), distinct in lithology and location from andesite units mapped to the west. East of Arroyo de La Cruz, La Cruz domain units of this early to middle Miocene sequence include a volcaniclastic breccia (*Tvb*) and volcaniclastic conglomerate (*Tvc*) locally mapped near the southeastern corner of Isla Tiburón (Fig. 3.3A). We assign these two units to the early to middle Miocene sequence, but these units are mapped only in fault contact with more widespread units and thus their relative age is unknown.

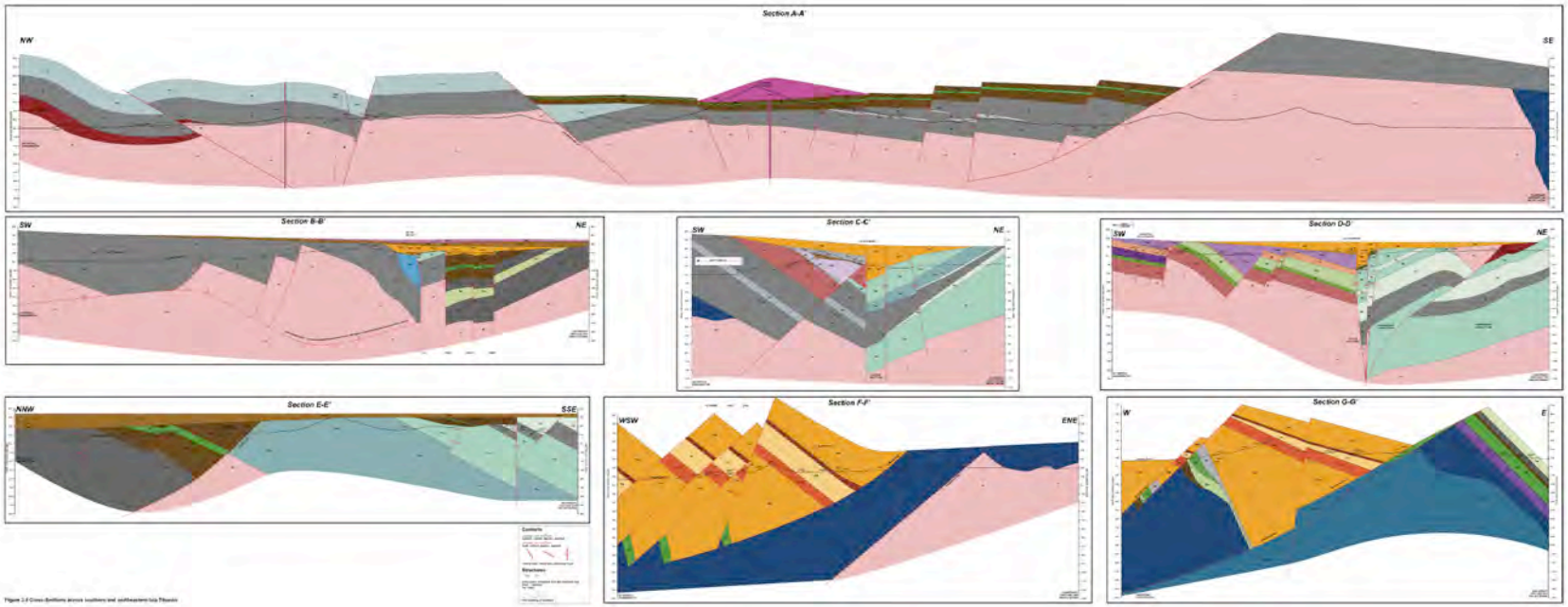

Figure 3.8 (A-G) Geologic cross-sections for southern and northeastern Isla Tiburón. Map unit lithologic indicators, colors, and other symbology as in Figures 3 and 4. Dip values from structural measurements used to construct cross-sections shown near ground surface. Apparent dip values shown in parentheses. See geologic map (Fig. 3.3) for cross-section line locations.

Electronic copy of full-sized cross-section sheet is available on data disc in rear pocket. Printed cross-section sheet is 28" tall, 72" wide.

In the Sauzal domain, northeast of the La Cruz fault, units from this early to middle Miocene sequence exposed west of Hipat Mesa consist of interbedded monolithologic volcaniclastic breccia (*Tbxv*), dacite flows (*Td*), and dacitic breccia (*Tbxd*) (Neuhaus, 1989; Gastil et al., 1999; Oskin and Stock, 2003a; Chapter 2 of this thesis). Many volcanic units here have been isotopically dated and range in age from 19 - 11 Ma (Fig. 3.3A; Smith et al., 1985; Neuhaus, 1989; Gastil et al., 1999; Chapter 2 of this thesis). Units from this sequence continue beneath and are again exposed east of Hipat Mesa, where they are undated and have only been mapped in reconnaissance (Gastil and Krummenacher, 1977a; Oskin, 2002). Between Hipat Mesa and the Sauzal fault, the oldest units in this sequence consist of monolithologic volcaniclastic breccia (*Tbxv*) conformably overlain by laterally discontinuous dacite (*Td*) and andesite flows (*Tah*) (Figs. 3.3A, 3.8B, and 3.8E). East of the Sauzal fault and towards Arroyo de La Cruz, Sauzal domain units of this early to middle Miocene sequence are notably distinct from those west of this structure. East of the Sauzal fault, the oldest units in this sequence consist of a thick stack of andesite flows (*Tha-r*, *Tha*) with subordinate rhyolite flows (*Tr*). These flows are conformably overlain by interbedded deposits of red-gray, andesitic breccia and volcaniclastic sandstone and conglomerate (*Trb*), basalt flows (*Tb*), additional andesite flows (*Tha-r*, *Tha*), and stratified deposits of red volcaniclastic sandstone and white lacustrine limestone (*Tsr*) (Figs. 3.3A, 3.8C, 3.8D, and 3.8E). We report a new $^{40}Ar/^{39}Ar$ (volcanic matrix, isochron) age of 20.68 ± 0.20 Ma from exposures of *Tha* <1 km northeast of the La Cruz fault (Fig. 3.5A; Table 3.1). East of Arroyo de La Cruz, Sauzal domain units of this sequence consist of interbedded dacite breccia (*Tdb*), andesite flows (*Ta*), and andesitic basalt flows (*Tab*) (Fig. 3.3A). The relative age of these units with units of this sequence to the west is unknown due to younger conglomerate and alluvial deposits that conceal this relationship.

3.5a3 Latest(?) Middle Miocene Syn-Rift Rocks

A sequence of syn-rift volcanic and sedimentary rocks of latest(?) middle Miocene age overlies the early to middle Miocene arc-related volcanic and sedimentary rocks on southern Isla Tiburón (Figs. 3.3A and 3.4A). These syn-rift units consist of non-marine sandstone and conglomerate, interstratified ash-flow tuffs, and a sequence of effusive and pyroclastic volcanic rocks. These syn-rift rocks are observed either conformably above the older early to middle Miocene sequence, or above an angular unconformity that separates these sequences. Here, we summarize this syn-rift volcanic and sedimentary sequence, spatially from west to east, within both the La Cruz and Sauzal domains.

In the La Cruz domain, beneath Hast Hinamj, syn-rift rocks overlie older early Miocene basalt (*Tb*) and volcaniclastic sandstone (*Tvsl*) above an angular unconformity (Figs. 3.3A and 3.8A). Here, syn-rift rocks consist of non-marine conglomerate (*Tcg1*) with up to ~45 m of an interbedded ash-flow tuff (*Ttsf*). Oskin (2002) reports an $^{40}Ar/^{39}Ar$ (K-feldspar, total gas) age of 9.58 ± 2.66 Ma from the lower of two cooling units in this tuff, a densely welded, crystal- and pumice-rich, ash-flow tuff, which he names the Tuffs of Cerro Colorado. We report a new $^{40}Ar/^{39}Ar$ (K-feldspar, multiple crystals) age of 12.20 ± 0.05 Ma from the basal vitrophyre of this same ash-flow tuff, ~1.5 km along strike to the northwest (Fig. 3.6A; Table 3.2). Based on its broadly similar lithology and age, we tentatively correlate this tuff with the Tuff of San Felipe (Stock et al., 1999), a regionally extensive tuff that blanketed >4,000 km^2 of the Mexican Basin and Range and is now observed in Baja California (Lewis and Stock, 1998a; Stock et al., 1999; Stock et al., 2008; Olguín-Villa, 2010; Chapter 1 of this thesis), on Isla Angel de la Guarda (Stock et al., 2008; Skinner et al., 2012), across western and northern Isla Tiburón (Oskin et al., 2001; Oskin, 2002; Oskin and Stock, 2003b; this study), in coastal Sonora (Oskin, 2002; Darin,

2011; Bennett et al., 2013), and in central Sonora (Oskin, 2002; Vidal-Solano et al., 2005; Stock et al., 2006; Hernández-Méndez et al., 2008; Gómez-Valencia and Vidal-Solano, 2010; Vidal-Solano et al., 2010; Chapter 1 of this thesis).

From Arroyo Sauzal to the southeastern corner of Isla Tiburón, coeval syn-rift rocks appear to conformably overlie older early to middle Miocene volcaniclastic sandstone (*Tvs*) and an andesite flow (*Ta1*) (Figs. 3.3A, 3.8C, and 3.8D). The oldest syn-rift unit here is the Tuff of Ensenada de La Cruz (*Tlc*), an extensive, densely welded, crystal-rich, ash-flow tuff. Oskin (2002) reports an $^{40}Ar/^{39}Ar$ (K-feldspar, total gas) age of 11.25 ± 1.98 Ma for *Tlc* exposures immediately west of Ensenada de la Cruz (Fig. 3.3A). We report a new $^{40}Ar/^{39}Ar$ (K-feldspar, multiple crystals) age of 12.21 ± 0.09 Ma (Fig. 3.6B; Table3) from the same strike-ridge of *Tlc*, ~150 m to the northwest (Fig. 3.3A). *Tlc* is conformably overlain by a diverse volcanic sequence that consists of the >400 m-thick Rhyolite Flows of Punta Amarillo (*Trpa1, Trpa2, Trpa3*), a basaltic andesite flow up to 100 m-thick (*Tba*), and up to ~80 m of bedded ash and pumice deposits (*Tty*) and a local vesicular basalt flow (*Tty-b*) (Figs. 3.8C and 3.8D).

In the Sauzal domain, between Hipat Mesa and the Sauzal fault, syn-rift rocks overlie gently tilted older volcanic units (e.g. *Tbxv*, *Td*, *Tah*) (Figs. 3.3A, 3.8B, and 3.8E). These syn-rift rocks consist of volcaniclastic conglomerate (*Tcg1*) and several intercalated, discontinuous volcanic units, including a resistant, brick-red, andesitic block and ash deposit (*Tbar*), basalt breccias (*Tbxb*), a welded tuff we correlate to the Tuff of San Felipe (*Ttsf*), and undated, thin airfall ash beds (Fig. 3.3A). Here, northeast of the La Cruz fault, we report a new $^{40}Ar/^{39}Ar$ (K-feldspar, multiple crystals) age of 12.12 ± 0.08 Ma from exposures of *Ttsf* (Fig. 3.6C; Table 3.2). This age is ~400 ka younger than ages obtained from coastal Sonora (Bennett et al., 2013) and central Sonora (Vidal-Solano et al., 2005), but is consistent with our isotopic age for *Ttsf*

southwest of the La Cruz fault and with the range of reported ages (12.0 - 12.7 Ma) for *Ttsf* in northeastern Baja California (Stock, et al., 2008). The true age of the Tuff of San Felipe is not settled, and may be biased by contamination from older xenocrystic material liberated from rhyolite inclusions that were partially molten at the time of eruption. Stock et al. (2008) suggest that ~12.3 Ma may represent the most probable age for the Tuff of San Felipe. For the purpose of this study, we will use an age of ~12.2 Ma when referring to the Tuff of San Felipe, an age consistent with our two $^{40}Ar/^{39}Ar$ ages.

In the Sauzal domain, east of the Sauzal fault and towards Arroyo de La Cruz, syn-rift rocks are only locally exposed and overlie older early Miocene volcanic units (e.g. *Thf-r*, *Thf*, *Trb*, *Tb*, *Tha*) above an angular unconformity (Figs. 3.3A and 3.8E). These syn-rift units consist of non-marine conglomerate (*Tcg1*) interstratified with deposits of the Tuff of Ensenada de la Cruz (*Tlc*). In this area, we report two new $^{40}Ar/^{39}Ar$ (K-feldspar, multiple crystals) ages for *Tlc*, 12.14 ± 0.08 Ma (Fig. 3.6D; Table 3.2) from *Tlc* exposures ~1.5 km northeast of the La Cruz fault (Fig. 3.3A) and 12.26 ± 0.07 Ma (Fig. 3.6E; Table 3.2) from steeply titled *Tlc* exposures within the La Cruz fault zone (Fig. 3.3A), consistent with isotopic ages for *Tlc* southwest of the La Cruz fault. East of Arroyo de La Cruz, syn-rift deposits are only exposed at a small, isolated mesa-top of non-marine conglomerate (*Tcg1*), capped by 10 - 15 m-thick densely welded tuff (Fig. 3.3A). From its lithology and stratigraphic position, we tentatively correlate this isolated tuff exposure to the Tuff of San Felipe (*Ttsf*).

3.5a4 Late Miocene to Pliocene(?) La Cruz Basin

Across southern Isla Tiburón, a sequence of volcanic and sedimentary units of the La Cruz sedimentary basin discontinuously overlie the early to middle Miocene sequence in angular

unconformable contact. These La Cruz basin deposits are typically located immediately adjacent to the La Cruz fault (Fig. 3.3A) and consist of non-marine coarse conglomerate and sandstone with intercalated volcanic rocks. We subdivide the conglomeratic infill of the La Cruz basin into three units: *Tcg2*, *Tcg3*, and *Tcg4*, which are progressively less deformed up-section. These deposits, and the volcanic rocks and angular unconformities that separate them, record the history of deformation along the La Cruz fault. The overall geometry of the La Cruz basin appears to be controlled by an elongate structural depression formed by both vertical fault motion and block tilting down towards the fault (Figs. 3.8B, 3.8C, and 3.8D). In contrast to the older units, La Cruz basin rocks are commonly exposed continuously across the La Cruz fault (Fig. 3.3A).

The lowest preserved portion of the La Cruz basin is exposed east of the Arroyo Sauzal delta, and west of the Hihitiij fault (Fig. 3.3A). Here, up to ~40 m of non-marine conglomerate (*Tcg2*) and an andesite flow up to 25 m-thick (*Ta2*), discontinuously overlie deposits of the ~12.2 Ma Tuff of Ensenada de La Cruz (*Tlc*) and the upper flow unit of the Rhyolite Flows of Punta Amarillo (*Trpa3*). The lowermost *Tcg2* beds are conformable with the underlying units, both inclined 31 - 34° (Fig. 3.8C). Conglomerate and sandstone beds within *Tcg2* are gradually less inclined up-section, with the uppermost *Tcg2* beds inclined 13 - 17°, similar to the basal contact of the overlying Basalt Breccia of Alta Sauzal (*Tbas*), a vesicular basalt breccia deposit (Fig. 3.8C). *Tbas* deposits are at least ~90 m-thick, but appear to dramatically thin to <10 m-thick across a north-striking normal fault (Fig. 3.3A). The extent of *Tbas* deposits appears to be restricted to ~1- 2 km along strike, similar to and coincident with *Tcg2* sediments. We report a new $^{40}Ar/^{39}Ar$ (volcanic matrix, isochron) age of 7.86 ± 0.33 Ma on a breccia clast sample collected from this exposure of *Tbas* (Fig. 3.5B; Table 3.1). *Tbas* is interpreted to be a breccia

deposit, possibly of landslide origin, and not a primary volcanic deposit, and thus this age is considered to be a maximum age for its emplacement.

The intermediate generation of non-marine conglomerate and sandstone (*Tcg3*) is much more widespread on southern Isla Tiburón than *Tcg2* (Fig. 3.3A). Deposits of *Tcg3* overlie an angular unconformity, where *Tcg3* strata are inclined up to 25° less steep than underlying units, including *Tcg2* and *Tbas* (Figs. 3.3A, 3.8B, 3.8C, and 3.8D). Southeast of Hipat Mesa, within the La Cruz fault zone, a white airfall tuff, up to 5 m-thick, is intercalated with *Tcg3* deposits just above its basal angular unconformity (Figs. 3.3A and 3.8B). We report a new U/Pb (zircon, multiple crystals) age of 6.87 ± 0.07 Ma from a sample of this tuff (Fig. 3.7A; Table 3.3).

Northwest of Hipat Mesa, younger La Cruz basin deposits (*Tcg3*) correspond to and are coeval with the extensively studied marine strata of the Southwest Isla Tiburón basin (Gastil and Krummenacher, 1977a,b; Smith et al., 1985; Cassidy, 1990; Gastil et al., 1999; Oskin and Stock, 2003a; Chapter 2 of this thesis), which locally preserve a record of regional marine incursion into the northern Gulf of California, ca. 6.4 - 6.0 Ma (Chapter 2 of this thesis). Similar to the La Cruz basin, all isotopically dated deposits within the Southwest Isla Tiburón basin are latest Miocene in age (Neuhaus, 1989; Gastil et al., 1999; Chapter 2 of this thesis). Based upon the architecture of marine and non-marine strata on southwest Isla Tiburón (Chapter 2 of this thesis), it appears that these marine rocks were sourced from a stream system that flowed along the axis of La Cruz basin.

The La Cruz basin is capped by a sequence of relatively undeformed volcanic and sedimentary units. Exposures of these capping deposits are concentrated in the central and western portions of southern Isla Tiburón (Fig. 3.3A). An andesitic-dacite volcano complex (*Tdhh*) forms the topographically prominent peak, Hast Hinamj (sometimes referred to as Cerro

Colorado) (Fig. 3.8A). The basal flows of *Tdhh* directly overlie deposits of *Tcg1* and *Ttsf* and pinch out abruptly to the east and northeast beneath younger, sub-horizontal non-marine conglomerate and sandstone deposits (*Tcg4*) (Figs. 3.3A and 3.4A). *Tcg4* deposits straddle the La Cruz fault beneath Hipat Mesa and are in buttress unconformable contact against deposits of *Tcg1*, *Ttsf*, and *Tdhh* along the northeastern edge of Hast Hinamj (Figs. 3.3A and 3.4A). Non-marine deposits of *Tcg4* continue to the north and northeast beyond the map area, towards the Valle de Tecomate (Fig. 3.2A; Gastil and Krummenacher, 1977a; Oskin, 2002). These *Tcg4* deposits also continue northwest of Hipat Mesa, where they laterally grade (down-dip) into a system of Gilbert-delta marine foreset and bottom set deposits that represent the youngest, undeformed marine strata in the Southwest Isla Tiburón basin (Fig. 3.3A; Chapter 2 of this thesis).

Stratigraphically above *Tcg4* and capping Hipat Mesa are sub-horizontal deposits of the Tuffs of Hipat Mesa (*Tthm*) (Fig. 3.3A). Deposits of *Tthm* consist of three, distinct, crystal-poor, ash and pumice units (*Tthm1*, *Tthm2*, *Tthm3*). Though *Tthm* is undated, isotopically dated flat-lying volcanic rocks are observed at a similar stratigraphic position and topographic elevation at Hast Pitzcal (Cerro Starship), ~7 km northwest of Hipat Mesa (Gastil and Krummenacher, 1977a; Gastil et al., 1999). At Hast Pitzcal, the Southwest Isla Tiburón basin is capped by the Rhyodacite of Cerro Starship, a late Pliocene (~4 Ma) dike-fed lava flow (Gastil and Krummenacher, 1977a,b; Neuhaus, 1989; Chapter 2 of this thesis). The precise age of the youngest La Cruz basin deposits across southern Isla Tiburón is unknown and could be latest Miocene to early Pliocene, similar to the adjacent and related Southwest Isla Tiburón basin.

3.5a5 Quaternary Deposits

Many young, likely Quaternary age deposits are observed across southern Isla Tiburón (Fig. 3.3A). The oldest Quaternary deposits consist of non-marine alluvium (*Qoa*) and fossiliferous marine terrace deposits (Qm). Thin marine terrace deposits (<5 m-thick) are located along the coastline, perched up to ~10 m above modern sea-level, above a sub-horizontal wave-cut bedrock platform. Perched *Qm* deposits are probably related to a global sea-level high stand during a Pleistocene interglacial period (MIS 5e or earlier) (Ortlieb, 1991). Deposits of *Qoa* are more abundant than *Qm*, and observed inland from the coastline filling valley bottoms with alluvium and capped by topographically smooth, inactive terrace tread surfaces. Deposition of *Qoa* may have been coeval with *Qm*, during a significant increase in base level (sea-level) that allowed sediment accumulation to occur. Modern, active channels ubiquitously incise into these *Qoa* deposits. Younger fluvial sand and cobble deposits (*Qal*) are commonly found within active channels. A discontinuous strip of unconsolidated beach sand and cobble deposits (*Qb*) is found along the modern shoreline. Patches of coastal areas seasonally flooded by marine water contain marine playa deposits (*Qpl*) just inland of beach-deposit berms.

3.5b Faulting and Folding

Numerous Late Cenozoic structures deform rocks on southern Isla Tiburón. The intensity of deformation is greatest within the early to middle Miocene volcanic and sedimentary sequence, which is deformed by thrust faults and folds, normal faults, and strike-slip faults. La Cruz basin deposits (e.g. *Tcg3*), which overlie older strata across a significant, widespread angular unconformity, display relatively less deformation, bury older structures, and are cut by

structures related to strike-slip faulting. Capping sedimentary and volcanic units (e.g. *Tcg4*, *Tthm*) display very little to no deformation.

3.5b1 La Cruz fault

The La Cruz fault is a first-order, NW-striking, vertical, dextral strike-slip fault that transects the southern part of Isla Tiburón, parallel to the offshore dextral Tiburón transform fault (Figs. 3.1 and 3.2A). All sub-parallel splays of the La Cruz fault deform late Miocene and older map units, commonly juxtaposing early to middle Miocene volcanic and sedimentary units (e.g. *Tha*) against latest Miocene non-marine conglomerate (*Tcg3*) (Fig. 3.3A). Small-offset brittle faults with sub-horizontal (strike-slip) slickenlines oriented parallel to strands of the La Cruz fault are observed in all pre-Quaternary units, including the capping Tuffs of Hipat Mesa (*Tthm*). Northwest of Hipat Mesa, internal tuff stratigraphy within *Tthm* is offset vertically ~2 - 4 meters across the primary northwest-striking branch of the La Cruz fault and the basal contact of the *Tthm* is offset a few tens of meters across a nearby northwest-dipping normal fault. Adjacent faults and folds do not appear to deform the La Cruz fault. From this it may be surmised that slip on these second-order structures was contemporaneous with slip on the La Cruz fault as part of a wrench zone.

Although the La Cruz fault is primarily a sub-vertical dextral fault, evidence suggests the fault has accommodated significant down-to-the-northeast dip slip. Relatively deeper structural levels are exposed southwest of the fault where outcrops of crystalline basement rocks are common. In contrast, in the Sauzal domain northeast of the fault, basement rocks are exposed only in an isolated, fault-bounded block in the southeastern portion of the island (Fig. 3.3A). Fault juxtaposition of disparate early to middle Miocene units across the La Cruz fault is thus

likely a result of both dextral strike-slip and normal dip-slip motion. This vertical motion likely caused the tectonic subsidence necessary for formation of syn-tectonic sedimentary basins along the La Cruz fault. The La Cruz fault is co-located with the Southwest Isla Tiburón basin on the southwestern portion of the island (Cassidy, 1990; Gastil et al., 1999; Oskin and Stock, 2003a; Chapter 2 of this thesis), and with the La Cruz basin across the south-central (Oskin, 2002; this study), and southeastern (this study) portions of the island (Fig. 3.3A).

3.5b2 Additional Strike-slip Faults

Additional strike-slip faults, both dextral and sinistral, deform rocks on southern Isla Tiburón. One notable such fault is a NW-striking, sub-vertical (81°) dextral fault that cuts across the Punta Amarillo headland (Fig. 3.3A). This fault does not continue much more than 1 km to the northwest, as it is not observed in the prominent Hihitiij sea cliff ~2 km to the northwest. Middle Miocene volcanic units generally correlate across this structure. Total dextral offset on this fault likely does not exceed its 1 km exposed length and it may have also accommodated ~300 m of down-to-the-southwest dip-slip displacement (Fig. 3.8D). Sinistral strike-slip faults are uncommon overall. Where observed northeast of the La Cruz fault, sinistral faults are ENE-striking, and cut the early to middle Miocene sequence of rocks at high angle to their undulatory contacts. Here, one well-exposed sinistral fault dips moderately to the north-northwest (62°) and displays a strong set of sub-horizontal slickenlines (rake of 013°). Displacement on this sinistral-oblique normal fault is minor, with ~160 m of apparent sinistral offset of the *Trb-Tb* contact (Fig. 3.3A).

3.5b3 Sauzal Fault

The Sauzal fault is a significant normal fault (Oskin, 2002; this study) in the Sauzal domain with a structurally related half-graben in its hanging wall (Figs. 3.3A and 3.8E). It strikes NE-SW and dips moderately to gently (~30 - 40°) to the northwest. North of the study area, the strike of this fault turns to more N-S (Fig. 3.2A; Oskin, 2002). Across the Sauzal fault, hanging wall units of syn-tectonic middle Miocene non-marine conglomerate (*Tcg1*) and the ~12.2 Ma Tuff of San Felipe (*Ttsf*) are juxtaposed against footwall units of mostly andesitic (*Thf-r*, *Thf*, *Tha-r*) and mafic (*Tb*) lava flows. We estimate that the Sauzal fault here has accommodated ~1.7 km of dip-slip displacement by measuring the positions of coeval, but not correlative, tuff deposits: the ~12.2 Ma Tuff of San Felipe in its hanging wall and the ~12.2 Ma Tuff of Ensenada de La Cruz in its foot wall (Fig. 3.8E). However these units may not have been emplaced at the same elevation, and the offset could be less than 1.7 km as a result. In this area, exposures of younger, La Cruz basin deposits (e.g. *Tcg3*) are not preserved along the Sauzal fault, and thus the timing of cessation of its activity is poorly known, but must post-date middle Miocene time. However, this fault may cut younger, late Miocene(?) units north of this study area (Oskin, 2002). The Sauzal fault appears to be truncated by the dextral La Cruz fault.

3.5b4 Colorado Fault

The Colorado fault is a significant, previously unmapped normal fault in the La Cruz domain (Fig. 3.3A). It strikes NE-SW and dips moderately to gently (~30 - 40°) to the northwest. Immediately along the mapped trace of the Colorado fault, hanging wall units of early Miocene basalt (*Tb*) and Cretaceous tonalite (*Kt*) are juxtaposed against Cretaceous tonalite (*Kt*) in the foot wall (Fig. 3.8A). Similar to the Sauzal fault, middle Miocene non-marine conglomerate

(*Tcg1*) and the ~12.2 Ma Tuff of San Felipe (*Ttsf*) are exposed in the hanging wall of the Colorado fault, ~3 - 4 km northwest of its mapped trace. Preservation of these units is limited to just beneath the overlying, resistant dacitic volcano (*Tdhh*) (Fig. 3.8A). These hanging wall units are likely syn-tectonic and accumulated due to motion on the Colorado fault. We estimate that the Colorado fault here has accommodated ~1.5 km of dip-slip displacement of the basement nonconformity (Fig. 3.8A). However, this estimate is only loosely constrained due to limited exposure of the basement nonconformity in the foot wall block, where bedding attitudes in the overlying basalt flows and volcaniclastic sediments indicate folding along a SE-plunging axis. The hanging wall block is cut by several NNE- to NNW-striking normal faults that structurally duplicate the basement nonconformity. These faults do not cut the Colorado fault and likely merge with the Colorado fault at depth (Fig. 3.8A). The timing of activity on the Colorado fault is poorly known, but must post-date middle Miocene time. Similar to the Sauzal fault, the Colorado fault appears to be truncated by the dextral La Cruz fault.

3.5b5 Hihitiij Fault

The Hihitiij fault is a significant, previously unmapped normal fault in the La Cruz domain (Fig. 3.3A). It strikes N-S and dips steeply (~70°) to the west. Along the Hihitiij fault, early to middle Miocene units of volcaniclastic sediments (*Tvs*), the Tuff of Ensenada de La Cruz (*Tlc*), and the Rhyolite Flows of Punta Amarillo (*Trpa2,3*) in the hanging wall are juxtaposed against metasedimentary rocks (*Pzms*) and Miocene volcaniclastic sediments (*Tvs*) in the foot wall. At the shoreline, we map three splays of the fault that bound wedges of *Tvs* and *Kt*. We estimate that the Hihitiij fault at the shoreline has accommodated at least 1 km of dip-slip from displacement of the basement nonconformity. Total fault slip likely diminishes northward, where

the Hihitiij fault juxtaposes the same rock unit (*Tvs*) (Fig. 3.3A). Along strike to north, the Hihitiij fault may either end at a fault tip or bend to the northwest where it may accommodate minor dextral displacement. The Hihitiij fault is cut and offset by a younger, NW-striking dextral-oblique normal fault with ~100 m of apparent dextral displacement. The timing of activity on the Hihitiij fault is poorly known, but must post-date middle Miocene time and pre-date this younger fault.

3.5b6 Additional Normal Faults and Related Folds

Additional, less significant normal faults deform rocks throughout southern Isla Tiburón, but are most abundant in the La Cruz domain, between the La Cruz fault and the offshore Tiburón transform fault (Fig. 3.3A). Here, N- to NNW-striking normal faults structurally duplicate tilted blocks of early to middle Miocene volcanic and sedimentary units (e.g. *Tb*, *Tvs*, *Tlc*, *Trpa*) and underlying basement (e.g. *Pzms*, *Kt*). These faults are typically inclined moderately to steeply towards the west, although a few east-dipping, antithetic(?) faults are also observed. This style of faulting is most common southeast of Arroyo Sauzal (Fig. 3.3A). Displacement across these normal faults ranges up to ~500 m (Fig. 3.8). Late Miocene non-marine conglomerate deposits of the La Cruz basin (*Tcg3*) bury these normal faults. Another common style of normal faulting within the La Cruz domain is NE-SW-striking normal faults. This is the predominant style of faulting west of Arroyo Sauzal, where these faults juxtapose early middle Miocene volcanic units (e.g. *Tb*) against crystalline basement (*Kt*). Nowhere are exposures of younger, La Cruz basin deposits (e.g. *Tcg3*) preserved along these faults, and thus the timing of activity on these faults is poorly known, but must post-date early middle Miocene time. NE-SW-striking, NW-dipping normal faults are less common southeast of Arroyo Sauzal,

but where such faults are observed, these deform and offset deposits of late Miocene non-marine conglomerate (*Tcg3*) within the La Cruz basin (Fig. 3.3A). Locally, some NE-SW-striking, NW-dipping normal faults appear to kinematically link with NW-striking dextral-oblique splays of the La Cruz fault.

Normal faults are less abundant in the Sauzal domain, northeast of the La Cruz fault (Fig. 3.3A). Where observed, these faults are typically NE- to ENE-striking and inclined moderately to steeply to the northwest. One SE-dipping, antithetic normal fault is observed near the Arroyo Sauzal drainage, just northeast of the La Cruz fault. One N-striking, west-dipping normal fault is observed just east of Sauzal Spring. Displacement across the majority of normal faults mapped northeast of the La Cruz fault is minimal (a few tens of meters each).

Extension-related folds also deform rocks on southern Isla Tiburón. In the La Cruz domain, a gentle syncline with an interlimb angle of ~130° is observed in the hanging wall of the Hihitiij fault, immediately west of and parallel to the fault trace (Fig. 3.3A). This syncline deforms middle Miocene volcanic and sedimentary units (e.g. *Tvs*, *Tlc*, *Trpa*). The axial plane trace of this syncline displays ~100 m of apparent dextral displacement along a NW-striking dextral-oblique normal fault. Additional folds are observed in the Sauzal domain, just southeast of Sauzal Spring. Here, a gentle to open syncline and anticline are observed in the hanging wall and foot wall, respectively, of a west-dipping normal fault (Fig. 3.8E). This fault and related folds deform middle Miocene units (e.g. *Tcg1*, *Ttsf*) and displays a few tens of meters of total displacement.

3.5b7 Thrust Faults and Related Folds

Second-order thrust faults deform rocks on southern Isla Tiburón adjacent to the La Cruz fault (Fig. 3.3A). Northeast of the La Cruz fault, a pair of E-W-striking, oppositely-dipping thrust faults bound the only known basement exposure in the Sauzal domain (Figs. 3.3A and 3.8D). Another thrust fault is observed southwest of the La Cruz fault adjacent to a subtle left fault bend (Fig. 3.3A). This thrust fault strikes NW-SE, sub-parallel to the La Cruz fault, and dips gently (30°) to the northeast, juxtaposing latest middle Miocene Rhyolite Flows of Punta Amarillo (*Trpa2*) structurally above younger, late Miocene non-marine conglomerate (*Tcg3*) of the La Cruz basin. Additional thrust faults are present on both sides of the La Cruz fault on southwest Isla Tiburon (Chapter 2 of this thesis).

Second-order folds also deform rocks on southern Isla Tiburón. South and west of Hast Hinamj, axial plane traces of gentle folds (~140 - 160° interlimb angles) are oriented approximately NE-SW and E-W (Figs. 3.3A and 3.8A). These folds appear to be basement-cored, and involve the entire early to middle Miocene stratigraphic section: early Miocene basalt (*Tb*), non-marine conglomerate (*Tcg1*), and the ~12.2 Ma Tuff of San Felipe (*Ttsf*). On the southwest flank of Hast Hinamj, one of these folds may be cut by a younger, east-dipping normal fault. It is unclear if this fold deforms the undulatory, sub-horizontal basal contact of the Dacite of Hast Hinamj (*Tdhh*). This set of folds marks a key structural transition in the La Cruz domain, where to the northwest units are typically inclined down to the north and northwest, and southeast of here units are typically inclined down to the northeast (Figs. 3.3A and 3.8A). Folds are also observed northeast of the La Cruz fault, in the Sauzal domain, where red volcaniclastic sandstone and lacustrine limestone strata (*Tsr*) are folded across ~E-W-striking axial planes (Figs. 3.3A and 3.8D). One fold pair appears to be parallel and likely related to an adjacent

south-dipping thrust fault. Additional folds are observed within the La Cruz fault zone just west of the Arroyo Sauzal drainage (Fig. 3.3A). These folds deform middle Miocene non-marine conglomerate (*Tcg1*) and the ~12.2 Ma Tuff of San Felipe (*Ttsf*) within a zone of left-steps between several dextral splays of the La Cruz fault.

3.6 YAWASSAG FAULT STUDY AREA

The Yawassag fault study area encompasses northeastern Isla Tiburón (Fig. 3.3B). Here, the NW-striking Yawassag fault separates the Sierra Kunkaak and Hinzime structural domains (Fig. 3.2B) and juxtaposes all pre-Quaternary map units southwest of the fault against predominantly crystalline basement northeast of the fault. Within each domain is a significant west-dipping normal or dextral-normal fault (Fig. 3.3B). The Sierra Kunkaak domain preserves an uplifted and eroded portion of the northeasternmost Tecomate basin in the hanging wall of the Kunkaak fault (Oskin and Stock, 2003b). These late Miocene sedimentary and volcanic units do not appear to correlate across the Yawassag fault.

3.6a Stratigraphy and Geochronology

3.6a1 Basement Rocks

Similar to southern Isla Tiburón, basement rocks on northeastern Isla Tiburón consist of plutonic and metamorphic rocks (Fig. 3.4B) and are observed on both sides of the Yawassag fault (Fig. 3.3B). Metamorphic rocks consist of meta-carbonate (*Pz-carb*) and other meta-sedimentary units (*Pzms*), including slate, quartzite, and phyllite. These metamorphic host rocks are thought to be pre-Cambrian to Cambrian in age, though a Mesozoic age for carbonate units is also possible (Gastil and Krummenacher, 1977b). Plutonic basement rocks in the Yawassag fault

study area consist predominantly of tonalite and related, typically felsic, dikes, similar to the basement rocks on northwest Isla Tiburón and an adjacent small island, Isla Patos (Gastil and Krummenacher, 1977a). Subordinate exposures of granodiorite and diorite composition are observed in the southernmost portion of the study area, southwest of the Yawassag fault (Fig. 3.3B). Gastil and Krummenacher (1977b) report a K-Ar (hornblende) age of 90.4 ± 2.7 Ma from a tonalite exposure in the southernmost portion of the study area (Fig. 3.3B). Schaaf et al. (1999) report two Rb-Sr (biotite-whole rock) cooling ages of 81.4 ± 3.2 Ma on tonalite and 77.7 ± 3.1 Ma on granodiorite from nearby basement exposures in the southern portion of this study area (Fig. 3.3B). These isotopic results are similar to a K-Ar (hornblende) age of 84.5 ± 7.9 Ma from tonalite on northwestern Isla Tiburón (Gastil and Krummenacher, 1977b) and to Late Cretaceous tonalite ages reported along the adjacent Sonora coastline (Gastil and Krummenacher, 1977b; Valencia-Moreno, 2003; Ramos-Velázquez et al., 2008).

3.6a2 Middle Miocene Volcanic and Sedimentary Rocks

A sequence of volcanic and sedimentary rocks of middle Miocene age nonconformably overlies basement rocks on northeastern Isla Tiburón. Overall this sequence is thinner than that present adjacent to the La Cruz fault on southern Isla Tiburón (Fig. 3.4) and likely consists of only middle Miocene units. Previous studies correlate Miocene volcanic and sedimentary units in the Sierra Kunkaak domain, southwest of the Yawassag fault, to units in the Hinzime domain, northeast of the fault (Gastil and Krummenacher, 1977a; Oskin, 2002). Here, we summarize this volcanic and sedimentary sequence in both domains and demonstrate that these units only broadly correlate across the Kunkaak dextral-normal fault within the Sierra Kunkaak domain, and do not correlate across the Yawassag dextral fault.

In the Sierra Kunkaak domain, southwest of the Yawassag fault, early to middle Miocene volcanic and sedimentary rocks largely differ across the Kunkaak fault (Fig. 3.3B). West of the Kunkaak fault, the lowest observed unit from this sequence is a basal non-marine conglomerate and sandstone unit (*Tcb*), observed discontinuously in angular and buttress unconformably contact with basement rocks (Figs. 3.3B and 3.8G). This unit likely correlates to unit 'Tcg' in the Sierra Menor of northwestern Isla Tiburón (Oskin, 2002) and unit 'Tcb' in coastal Sonora immediately east of Isla Tiburón (Bennett, 2009), both observed at a similar stratigraphic position. A basaltic andesite flow (*Tba*) conformably(?) overlies *Tcb*. Along strike to the southeast, an andesite flow (*Tha*) is observed at the same stratigraphic position as *Tcb* and *Tba*, in nonconformable contact with basement rocks. We tentatively assign a middle Miocene age to *Tcb*, *Tba*, and *Tha*. However, these units are not isotopically dated and could possibly be early Miocene in age. Discontinuous deposits of the ~12.2 Ma Tuff of San Felipe (*Ttsf*) overlie these units and are locally in nonconformable contact with basement rocks as well (Fig. 3.3B). Outcrop quality is insufficient to determine whether these contact relationships are the result of an angular unconformity between *Ttsf* and underlying units or due to paleotopography of basement rocks and discontinuous emplacement of *Tba* and *Tha*. The uppermost unit of this sequence is a discontinuous vesicular basalt flow (*Tbv*). East of the Kunkaak fault, the lowest observed units from this sequence are a basalt flow (*Tb1*) and the lower flow of the Rhyolite Flows of Sepoc Hancaap (*Trsh1*), a purplish-red aphanitic rhyolite with 1 - 2 cm-spaced foliation (Figs. 3.3B and 3.8G). We tentatively assign a middle Miocene age to *Tb1* and *Trsh1*, but these units are undated and could possibly be early Miocene in age. These units are overlain by the ~12.2 Ma Tuff of San Felipe (*Ttsf*), non-marine conglomerate and sandstone (*Tcg1*), another,

similar flow of the Rhyolite Flows of Sepoc Hancaap (*Trsh2*), another basalt flow (*Tb2*), and ash- and pumice-rich, greenish-yellow volcaniclastic sandstone (*Tsg*).

In the Hinzime domain, northeast of the Yawassag fault, two undated volcanic units are mapped (Fig. 3.3B). We tentatively assign these rocks to the middle Miocene sequence. These units are sparsely exposed due to the relatively deep exhumation northeast of the Yawassag fault, where basement rocks are the predominant surface lithology (Fig. 3.3B). These volcanic units include the Rhyolite of Hast Hinzime (*Trhh*) and an overlying silicified rhyolite tuff and breccia (*Tbhh*) that may be the top of the underlying flow. Gastil and Krummenacher (1977a) and Oskin (2002) mapped the Hinzime domain in reconnaissance, incorrectly correlating the exposures of these two volcanic units with younger volcanic and sedimentary deposits of the Tecomate basin discussed below.

3.6a3 Late Miocene to Pliocene(?) Tecomate Basin

In the Sierra Kunkaak domain, a thick sequence of late Miocene to Pliocene(?) volcanic and sedimentary units are exposed within the Tecomate basin and overlie the early to middle Miocene sequence (Figs. 3.3B and 3.4B) above an angular unconformity with up to ~20° difference in dip. These Tecomate basin deposits accumulated in a structurally related half-graben in the hanging walls of the Kunkaak fault and Tecomate fault (Figs. 3.8F and 3.8G).

The lowest portion of the Tecomate basin is exposed just east of the Tecomate fault where deposits of non-marine coarse conglomerate and sandstone (*Tcg3*) overlie volcanic units of the middle Miocene sequence that are more steeply inclined (Fig. 3.3B). Deposits within the Tecomate basin display a fanning-dip geometry, where the structural tilt of basin fill shallows up-section from >50° near its base to 15 - 20° near its top (Figs. 3.8F and 3.8G). The uppermost

Tcg3 deposits of the Tecomate basin are observed immediately west of the Kunkaak fault, in fault contact with basement rocks and older volcanic units in the foot wall. Within this study area, at least 2.0 km of non-marine conglomerate (*Tcg3*) and volcanic deposits (*Tmr3*, *T3t*, *Tmr4*) accumulated in the hanging wall, above the Kunkaak fault (Figs. 3.8F and 3.8G).

Three distinct volcanic units are interbedded amongst *Tcg3* sedimentary deposits of the Tecomate basin. A 2 m-thick, white, reworked ash deposit is mapped interbedded within *Tcg3*, ~ 60 - 70 m above the basal angular unconformity (Figs. 3.3B and 3.8G). We report a new $^{40}Ar/^{39}Ar$ (K-feldspar, multiple crystals) age of 7.11 ± 0.09 Ma (Fig. 3.6F; Table 3.2) and a similar U/Pb (zircon, multiple crystals) age of 7.03 ± 0.19 Ma (Fig. 3.7B; Table 3.3) for this ash deposit. We prefer the $^{40}Ar/^{39}Ar$ age of 7.11 ± 0.09 Ma for this sample, because the Ar/Ar technique provides a better estimate of a true eruption age than the U/Pb technique (Simon et al., 2008). Further up-section a thick sequence of pyroclastic deposits is observed interbedded amongst *Tcg3* deposits (Fig. 3.3B). The base of this sequence is a 110 - 120 m-thick, crystal- and lithic-rich, orangish, moderately- to densely-welded ash-flow tuff (*Tmr3*). Above this is 100 - 240 m of primary and reworked air-fall and volcaniclastic debris-flow deposits (*T3t*), capped by 25 - 40 m of a crystal- and lithic-poor, maroon, densely-welded ash-flow tuff (*Tmr4*). Following earlier reconnaissance mapping by Oskin and Stock (2003b), we correlate this volcanic sequence with the ~6.4 Ma Tuffs of Mesa Cuadrada, a regionally extensive tuff sequence that blanketed >2,100 km^2 of present-day northeastern Baja California (Stock, 1989; Lewis, 1996; Nagy et al., 1999), western and northern Isla Tiburón (Oskin et al., 2001; Oskin, 2002; Oskin and Stock, 2003b; this study), and coastal Sonora (Oskin and Martín-Barajas, 2003; Bennett et al., 2013). An additional, 2 m-thick interval of white, cross-bedded, crystal-poor, reworked ash beds occur amongst *Tcg3* conglomerate beds ~30 m stratigraphically above *Tmr4* (Figs. 3.3B and 3.8F).

Neither conglomerate nor pyroclastic rocks of the Tecomate basin-fill are observed east of the Kunkaak fault. However, these deposits may exist here in the subsurface, obscured beneath Quaternary deposits (Fig. 3.3B).

3.6a4 Quaternary Deposits

Similar to southern Isla Tiburón, many young, likely Quaternary age deposits are observed across northeastern Isla Tiburón (Fig. 3.3B). The oldest Quaternary deposits consist of non-marine alluvium (*Qoa*) and fossiliferous marine deposits (*Qm*). Thin deposits of *Qm* are observed along the lower 2 - 3 m of the 10 - 25 m-high sea cliff along Playa Tecomate. The upper portion of this sea cliff consists of stratified non-marine alluvial deposits (*Qoa*), which include capping cross-stratified dune deposits. Inland, deposits of *Qoa* fill valley bottoms and are widespread across alluvial plains with inactive upper terrace tread surfaces. Younger fluvial sand and cobble deposits (*Qal*) are commonly found within active channels. A discontinuous strip of unconsolidated beach sand and cobble deposits (*Qb*) is found along the modern shoreline, and a veneer of unconsolidated, aeolian sand deposits (*Qae*) are found inland up to 5.5 km from the modern northwestern shoreline.

3.6b Faulting and Folding

Several Late Cenozoic structures deform rocks on northeastern Isla Tiburón. Tecomate basin deposits (e.g. *Tcg3*) accumulated in a structurally related half-graben in the hanging wall of the Kunkaak fault and Tecomate fault (Figs. 3.8F and 3.8G). These basin deposits overlie older strata across an angular unconformity and are cut by structures related to strike-slip faulting. The onset of slip on the Kunkaak fault is best constrained from tilting relationships preserved within

this basin, though slip may have initiated prior to the accumulation of the oldest exposed sediments. The Yawassag fault appears to have initiated later, because it cross-cuts the Kunkaak fault and the Tecomate basin. The termination of activity on these faults cannot be determined because no undeformed, capping units are observed.

3.6b1 Yawassag fault

The Yawassag fault is a first-order, NW-striking, SW-dipping, dextral strike-slip fault that transects the northeastern part of Isla Tiburón (Fig. 3.3B). The trace of the Yawassag fault is slightly undulatory owing to its moderate (~50°) southwest dip. At one exposure, the fault dips 53° to the southwest with sub-horizontal slickenlines (rake of 011°) (Fig. 3.3B). Prominent, well-exposed, NNW-striking strike-ridges of Tecomate basin deposits (e.g. *Tmr4*, ash marker in *Tcg3*) are deflected in a clockwise sense and are NNE-striking proximal to the dextral Yawassag fault (Fig. 3.3A). The Kunkaak fault and these basin deposits are both truncated by the fault and not observed northeast of the fault. Both the slickenline orientation and bed deflection suggest that dextral strike-slip is the dominant type of motion on the Yawassag fault, despite its moderate dip. Near the northwestern shoreline of this study area, we map a right step in the Yawassag fault, connected by a northwest dipping normal fault (Fig. 3.3B). The lack of any correlative Miocene units along the ~8 km onshore exposure of the Yawassag fault, suggests at least that much dextral displacement since late Miocene time.

Although Gastil and Krummenacher (1977b) considered the Yawassag fault to primarily be a dextral fault, they also considered it to have accommodated significant down-to-the-southwest dip slip. The relatively deeper structural levels exposed northeast of the fault (Fig. 3.3B) is consistent with this notion. Here, in the Hinzime domain, exposures predominantly

consist of crystalline basement rocks with very few exposures of middle(?) Miocene volcanic rocks. In contrast, in the Sierra Kunkaak domain southwest of the fault, middle to late Miocene sedimentary and volcanic units are more common.

3.6b2 Additional Strike-slip Faults

Additional strike-slip faults, both dextral and sinistral, deform rocks on northeastern Isla Tiburón (Fig. 3.3B). Near the southern end of its mapped trace, the Kunkaak fault is cut by a zone of second-order, NW-striking, dextral-oblique normal faults that dip moderately to the southwest, with <1 km of apparent dextral displacement (Figs. 3.3B and 3.8G). Although the area of fault intersection is poorly exposed, concealed by Quaternary deposits, this NW-striking fault zone disrupts and rotates the otherwise continuous strike-ridge exposures in both the hanging wall and foot wall of the Kunkaak fault. The easternmost splay of this zone appears to kinematically link with the Kunkaak fault, where it may have reactivated the Kunkaak fault with dextral-oblique slip. Such reactivation could be responsible for the presence of fault-bounded slivers of *Ttsf* and *Kt* along the Kunkaak fault that are difficult to explain via solely dip-slip motion (Figs. 3.3B and 3.8G). This dextral-oblique fault zone could be a branch of the Infiernillo fault, the southwesternmost branch of the Coastal Sonora Fault Zone postulated to exist between Isla Tiburón and the mainland to the southeast (see Bennett et al., 2013). Three NE-striking sinistral faults also cut basin fill rocks with apparent sinistral displacements of up to ~500m. These adjacent faults and extension-related folds do not appear to deform the Yawassag fault. From this it may be surmised that either the Yawassag fault post-dates these other faults, or that slip on these second-order structures was contemporaneous with slip on the Yawassag fault as

part of a wrench zone, similar to the structural relationship observed along the La Cruz fault across southern Isla Tiburón.

3.6b3 Kunkaak fault

The Kunkaak fault is a significant, north-northwest striking, gently- to moderately-dipping dextral-normal fault that intersects the Yawassag fault (Fig. 3.3B). This fault juxtaposes latest Miocene volcanic and sedimentary units (e.g. *Tcg3*, *Tmr3*, *Tmr4*) in the hanging wall against mostly metasedimentary basement (e.g. *Pzms*) in the foot wall. The fanning-dip geometry observed in the Tecomate basin fill suggests basin accumulation was coeval with dip-slip on the Kunkaak fault and tilting of its hanging wall. This geometry also suggests that the dip of the Kunkaak fault may shallow with depth in a listric sense (Figs. 3.8F and 3.8G). However, because pre-rift units (e.g. *Ttsf*) in the foot wall of the Kunkaak fault are tilted by a similar amount, the foot wall and hanging wall blocks may also have experienced domino-style block tilting. Total dip-slip displacement on the Kunkaak fault is estimated to be up to ~2.7 km, measured on correlative basement nonconformity surfaces across the fault (Fig. 3.8G).

3.6b4 Tecomate fault

The Tecomate fault is another significant, north-northwest-striking, west-dipping normal fault exposed along the westernmost exposures of the Yawassag fault study area (Fig. 3.3B). This fault is structurally related to Kunkaak fault, as dip-slip on both structures created tectonic accommodation for Tecomate basin fill. The Tecomate fault juxtaposes latest Miocene volcanic and sedimentary units (e.g. *Tcg3*, *Tmr3*, *Tmr4*) and older Quaternary alluvium (*Qoa*) in the hanging wall against similar units in the foot wall, structurally duplicating tilt blocks of

Tecomate basin fill. Fault scarps up to 10 m-high are observed in older Quaternary alluvial deposits (*Qoa*). This fault also appears to cut through basement exposures at the southernmost mapped reaches in this study area (Fig. 3.3B). Oskin (2002) estimates ~3 km of total dip-slip displacement across the Tecomate fault. Along strike to the south, the Tecomate fault serves as the bounding structure between the Sierra Kunkaak and the Tecomate basin (Fig. 3.2A; Oskin, 2002). Significant dip-slip on the Tecomate fault has formed the large, topographically prominent modern-day central valley of Isla Tiburón, Valle de Tecomate.

3.6b5 Hinzime fault

The Hinzime fault is a normal fault in the Hinzime domain, northeast of the Yawassag fault (Fig. 3.3B). This NNE-striking structure dips westward and juxtaposes Miocene volcanic units (e.g. *Trhh*, *Tbhh*) against crystalline basement (*Kt*). Total dip-slip displacement on the Hinzime fault is loosely constrained to be ~2.7 km, measured on correlative basement nonconformity surfaces across the fault.

3.6b6 Additional Normal Faults and Related Folds

Smaller-scale west-dipping normal faults are mapped in the western and northwestern portions of this study area (Fig. 3.3B). Recent aeolian deposits (*Qae*) commonly obscure the precise location and connectivity of these normal faults. These faults must juxtapose isolated exposures of Tecomate basin units of broadly similar age (e.g. *Tcg3*, *Tmr3*, *Tmr4*) and may represent a zone of normal faulting related to the northern reaches of the Tecomate fault. Dip-slip displacement on any of these normal faults is unlikely to exceed tens to a few hundred meters. One NE-striking fault is observed near the southern end of the mapped Tecomate basin deposits

(Fig. 3.3B). This fault appears to be sub-vertical or may dip steeply to the southeast. Approximately 200 m of down-to-the-southeast dip-slip motion on this structure may be the cause of the ~500 m apparent dextral offset across this NE-striking fault.

Extension-related folds also deform rocks on northeastern Isla Tiburón. A gentle syncline with an interlimb angle of ~150° is observed in the hanging wall of the Kunkaak fault, immediately west of and parallel to the fault trace (Fig. 3.3B). This syncline deforms deposits of latest Miocene non-marine conglomerate (e.g. *Tcg3*) that overlie the Tuffs of Mesa Cuadrada (Figs. 3.8F and 3.8G). The axial plane trace of this syncline displays ~100 m of apparent sinistral displacement along a NE-striking strike-slip fault.

3.7 DISCUSSION

3.7a Timing of Faulting and Basin Formation on Isla Tiburón

3.7a1 Middle to Late(?) Miocene Normal Faulting and Basin Formation

Evidence for the earliest extension-related faulting comes from the La Cruz fault study area on southern Isla Tiburón (Fig. 3.3A). Here, several down-to-the-west normal faults are observed cutting early Miocene volcanic rocks and controlling deposition of overlying middle Miocene pyroclastic rocks and sedimentary strata. This early normal faulting includes the Sauzal, Colorado, and Hihitiij normal faults, each of which displays at least 1 km of dip slip. Additional N to NE-striking normal faults appear to be coeval with slip on these more significant faults, particularly in the southeastern portion of the La Cruz domain (Figs. 3.3A and 3.8D).

It appears that relative motions across the Colorado and Sauzal faults were similar during this early phase of normal faulting. For both, their hanging wall blocks tilted and rotated by greater amounts relative to their foot wall blocks, forming an angular unconformity only within

their hanging wall blocks. Kinematics of slip on these normal faults is constrained from syn-rift sediments (*Tcg1*) that accumulated in sedimentary basins above the hanging walls of the Sauzal fault and Colorado fault, both northeast and southwest of the La Cruz dextral fault. Thick sections of these syn-rift sediments appear to be restricted to a 5 - 8 km-wide region immediately adjacent and west of these faults (Fig. 3.3A). Both hanging wall basins contain up to 60 m-thick deposits of the ~12.2 Ma Tuff of San Felipe (*Ttsf*). In the hanging wall of the Colorado fault, middle Miocene conglomerate and Tuff of San Felipe overlie early Miocene basalt flows above an angular unconformity (Fig. 3.8A), suggesting faulting and tilting had commenced prior to ~12.2 Ma. In the hanging wall of the Sauzal fault, middle Miocene sediments and the Tuff of San Felipe overlie poorly-stratified volcanic breccia and lava flows, where the presence of a similar angular unconformity is likely, but difficult to verify (Fig. 3.8E). In the foot wall of the Colorado fault the contact between early Miocene volcanic rocks and middle Miocene strata correlative to the syn-rift strata appears to be conformable. Though the Tuff of San Felipe is absent, the slightly younger ~12.2 Tuff of Ensenada de La Cruz and the overlying Rhyolite Flows of Punta Amarillo are present and are tilted approximately the same amount as the underlying early Miocene rocks (Figs. 3.8C and 3.8D). In the foot wall of the Sauzal fault, exposures of these syn-rift sediments and the ~12.2 Ma Tuff of Ensenada de La Cruz are very limited. Where exposed, these overlie early Miocene volcanic rocks above an erosional unconformity, and are tilted by a similar amount as the underlying units (Fig. 3.8E).

The age of onset of normal faulting on the Sauzal fault and Colorado fault is poorly constrained, but post-dates ~19 Ma, the age of the youngest dated pre-rift units (e.g. *Tb*) that are cut by these normal faults. These normal faults were certainly active by ~12.2 Ma, as thick deposits of the Tuff of San Felipe appear to be restricted to the hanging wall of these faults (Fig.

3.3A), suggesting that a west-facing, fault-controlled escarpment controlled the spatial extent of ash-flow tuff emplacement (Figs. 3.8A and 3.8E). A minimum age for this normal faulting is ~6.9 Ma, the age of the La Cruz basin fill that consistently buries and caps these normal faults.

3.7a2 Late Miocene to Pliocene(?) Strike-slip Faulting and Basin Formation

In both the La Cruz and Yawassag fault study areas (Fig. 3.3), we document structural relationships that constrain the onset of activity on the first-order, NW-striking, La Cruz and Yawassag strike-slip faults. Slip on the La Cruz fault commenced between 12 and 8 Ma, based on cross-cutting relationships and the age of strata at the base of the La Cruz basin that formed adjacent to the fault. The La Cruz fault cross-cuts older sedimentary basins formed in the hanging wall of the Sauzal and Colorado faults. This relationship shows that strike-slip faulting commenced after ~12.2 to 12.3 Ma, the ages of the Tuff of Ensenada de La Cruz and Tuff of San Felipe, respectively, that are present within these, and related basins. Additional information on the age of faulting is preserved within syn-tectonic deposits of the La Cruz basin. Dips within the oldest of these deposits (*Tcg2*) shallow progressively up-section from 31 - 34°, conformable with underlying middle Miocene strata, to 13 - 17° beneath the Basalt Breccia of Alta Sauzal (*Tbas*), with a ~7.9 Ma maximum age of emplacement. Slightly younger, more widespread conglomerate (*Tcg3*) overlies these earliest basin deposits above a minor (5 - 10°) angular unconformity (Fig. 3.8C). Along strike to the northwest, we document a ~6.9 Ma ash bed interstratified near the base of a highly deformed section of *Tcg3* within the La Cruz fault zone (Fig. 3.8B). Along the northwesternmost onshore exposure of the La Cruz fault, adjacent marine strata accumulated above an angular unconformity cut across early Miocene volcanic rocks. Here, Oskin and Stock (2003a) and I (Chapter 2 of this thesis) document a ~6.4 Ma ash-flow tuff at the base of this

basin, below the marine strata, which supports a similar history of latest Miocene activity on the La Cruz fault.

Slip on the La Cruz fault appears to have ceased largely by 4 Ma. At Hipat Mesa, relatively undeformed deposits of non-marine conglomerate (*Tcg4*) and the Tuffs of Hipat Mesa (*Tthm*) bury and cap syn-tectonic La Cruz basin fill (Figs. 3.3A and 3.4A). No isotopic ages exist for these capping units. However, these units lie at the same stratigraphic and topographic position as a ~4.0 Ma dike-fed lava flow near the southwestern tip of the island (Chapter 2 of this thesis).

On northeastern Isla Tiburón, syn-tectonic deposits of the Tecomate basin preserve a record of activity on the Kunkaak and Tecomate normal faults, and indirectly constrain slip on the Yawassag fault (Fig. 3.3B). At least 2 km of syn-tectonic conglomerate and pyroclastic material accumulated within the adjacent Tecomate basin, coeval with 5 - 6 km of combined dip-slip on the Kunkaak and Tecomate normal faults. Non-marine sandstone and conglomerate deposits in the Tecomate basin overlie older middle Miocene volcanic rocks, such as the ~12.2 Ma Tuff of San Felipe, above an angular unconformity. Conglomerate within the Tecomate basin displays a continuous, up-section fanning-dip geometry, indicative of its syn-tectonic association (Fig. 3.8G). Near the base of this conglomerate a ~7.0 Ma interstratified ash bed constrains the onset of this tilting and basin formation. From this it is inferred that slip on the Kunkaak fault commenced shortly before 7 Ma, broadly synchronous with the onset of strike-slip faulting on the La Cruz fault. Though the direct association of subsidence of the Tecomate basin with dextral motion on the Yawassag fault is unclear, the northern end of the Kunkaak fault must either merge or be cross-cut by the Yawassag fault. This relationship indirectly constrains the onset of slip on the Yawassag dextral fault to have begun in latest Miocene time, either shortly before or

after 7 Ma. If the latter is true, at least 8 km of dextral slip occurred on the Yawassag fault and this motion post-dates formation of the Tecomate basin (post-6.4 Ma). However, paleomagnetic results (Chapter 1 of this thesis) indicate that up to ~70% of the total ~30° of clockwise vertical-axis block rotations in this study area occurred prior to 6.4 Ma, suggesting that a form of dextral deformation (block rotation) was active by that time. An additional, less significant zone of dextral-oblique normal faults also cuts obliquely through this study area and likely also reactivated the Kunkaak fault with dextral-normal slip (Figs. 3.3B and 3.8G). No undeformed units cap these faults and related basin deposits. Thus, the cessation of transtensional fault activity on northeastern Isla Tiburón is poorly constrained, but must post-date the ~6.4 Ma age of the Tuffs of Mesa Cuadrada, which are present within the Tecomate basin fill and cross-cut by strike-slip faults.

The kinematic history and timing of activity for the Tecomate basin and the Kunkaak, Tecomate, and Yawassag faults are strikingly similar to the history of events that Bennett et al. (2013) document for the Coastal Sonora Fault Zone, 30 -50 km to the southeast along strike of this rift-segment-bounding transform fault system (Fig. 3.1). Here on the Sonora mainland, syn-tectonic basin-fill accumulation and clockwise vertical-axis block rotation commenced between 11.5 and 7 Ma, with nearly all fault-related basin subsidence and most of the tectonic tilting occurring after 7 Ma. Similar to northeastern Isla Tiburón, the Kino basin was subsequently cut and dextrally offset by NW-striking dextral faults, while this late-stage dextral shear was accommodated by further clockwise vertical-axis rotation of the Punta Chueca basin (Bennett et al., 2013).

3.7b New Constraints for Total Dextral Offset Along the La Cruz Fault

Prior to this study, total dextral displacement along the La Cruz fault was not well constrained (Oskin and Stock, 2003b). The results of our detailed mapping (Fig. 3.3A) reveal new correlative rock units that may be used to constrain its slip. We use a simplified geologic and structural map (Fig. 3.9A) of the present-day distributions of these units to draw connections between the La Cruz and Sauzal structural domains southwest and northeast of the fault, respectively, and to justify estimates of total dextral displacement (Fig. 3.9B). These units may also prove useful in a future study to determine offset between Isla Tiburón and Isla Angel de al Guarda, across the Tiburón transform fault.

The broadest and oldest correlative units we document across the La Cruz fault are two sequences of early Miocene volcanic and sedimentary rocks (Fig. 3.9A). The first sequence consists of basalt flows and discontinuous beds of reddish volcaniclastic sandstone and lacustrine limestone. Over much of the La Cruz domain, these units lie near the base of the early Miocene section (Fig. 3.3A). The second sequence consists of andesitic flows and breccias, which are consistently found to stratigraphically overlie the basalt flows. The basaltic sequence is observed across the western and central portions of the La Cruz domain, where it is relatively thick and widespread. It also occurs within the eastern portion of the Sauzal domain, where it is relatively thin (Fig. 3.3A), and overlies older andesitic rocks that are not exposed in the La Cruz domain. The overlying sequence of andesitic flows and breccias is observed primarily within the Sauzal domain, but importantly it also occurs within the La Cruz domain adjacent to the La Cruz fault. We document that exposures of the basalt and sediment sequence thins from west to east (Fig. 3.3A) and speculate that this thinning pattern continues across the La Cruz fault, where it explains the relatively thin layer of basalt exposed within the Sauzal domain (Fig. 3.8C).

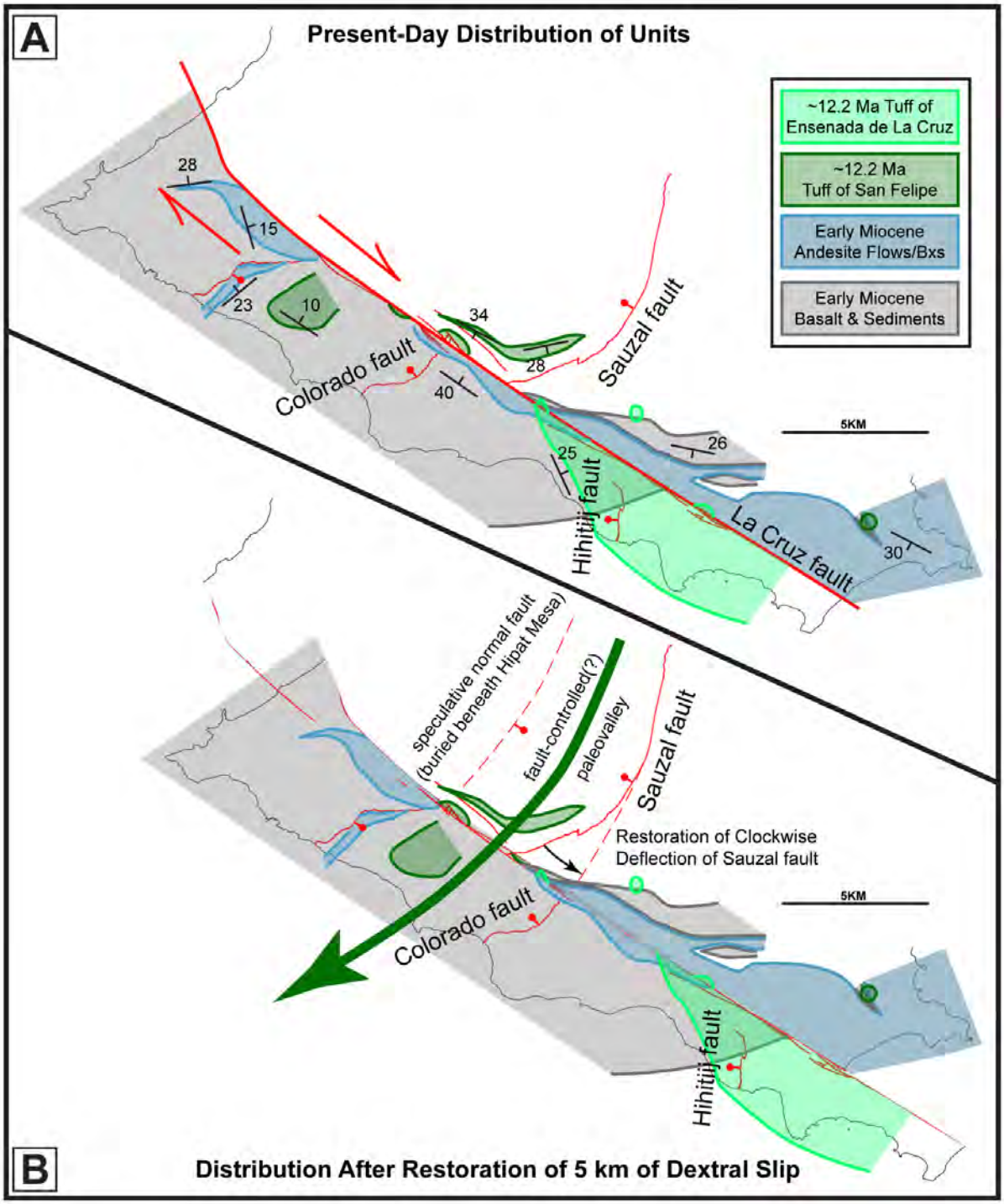

Figure 3.9
(A) Present-day distribution of correlative map units across the La Cruz strike-slip fault.
(B) Preferred restoration of ~5 km of dextral slip brings correlative map units into general alignment. Deposits of the ~12.2 Ma Tuff of San Felipe were restricted to a fault-controlled paleovalley, which was subsequently offset by the dextral La Cruz fault.

Oppositely, the andesitic sequence appears thickest to the northeast (Figs. 3.8C, 3.8D, and 3.8E) and is relatively thinner to the southwest (Figs. 3.3A and 3.8B). Direct correlation of individual lava flows or map units of the same thickness is complicated by unknown amounts of subsequent down-to-the-northeast vertical motion across the La Cruz fault and moderate amounts of block tilting. Such vertical motion has juxtaposed disparate levels and thicknesses of volcanic stratigraphy of adjacent basaltic and andesitic volcanic complexes to the southwest and northeast, respectively. These factors preclude a robust and unique estimate of dextral offset across the La Cruz fault using these sequences. However, restorations of ~5 -15 km of dextral motion bring these similar regions into general juxtaposition (Fig. 3.9). Thus, the total post-early Miocene dextral offset on the La Cruz fault is likely less than the minimum of 28 km predicted by Oskin and Stock (2003b).

We document a more robust correlation of latest middle Miocene units across the La Cruz fault (Fig. 3.9). Northeast of the fault, we map and date exposures of the ~12.2 Ma Tuff of San Felipe (*Ttsf*), which are exposed in an ~4.5 km-long, ENE-striking, south-dipping belt that is gradually deflected in a clockwise sense to more ESE-striking proximal to the dextral La Cruz fault (Figs. 3.3A and 3.8E). These *Ttsf* exposures are underlain by non-marine conglomerate (*Tcg1*). *Ttsf* is overlain by additional coarse conglomerate (*Tcg1*), which contains up to two interbedded, discontinuous, white and yellow ash beds just above its basal contact with *Ttsf*. Southwest of the La Cruz fault, we map and date similar exposures of *Ttsf*, discontinuously exposed in a ~4 km-wide, gently NE-dipping belt (Figs. 3.3A and 3.8A). Here, coarse conglomerate deposits (*Tcg1*) both underlie and overlie *Ttsf*, similar to the sequence observed northeast of the La Cruz fault. Locally, we observe similar, discontinuous ash beds intercalated within the lowest, *Tcg1* deposits immediately above *Ttsf*. These 4 - 5 km-wide belts of *Ttsf*

(measured along strike in a ~NW-SE direction) may be correlative exposures of an elongate, NE-SW trending, fault-controlled paleovalley that accumulated deposits of the Tuff of San Felipe. An edge of this paleovalley is observed in only one location, at its eastern end, northeast of the La Cruz fault, where 60 m-thick *Ttsf* deposits abruptly pinch out over a distance of ~150 m (Fig. 3.3A). The other edge of this paleovalley northeast of the La Cruz fault, and both edges of this paleovalley southwest of the fault, are not directly observed. At these locations, exposures of thick *Ttsf* end, either buried beneath younger deposits (e.g. *Tcg3*, *Tthm*) or project into the air above the Gulf of California. Using the mapped extent of the *Ttsf* belts on each side of the La Cruz fault as minimum widths of this NE-SW-trending paleovalley, we estimate that it has been dextrally offset 5 ± 2 km across the La Cruz fault (Fig. 3.9). Restoration of this dextral motion brings the Colorado fault and Sauzal fault into close alignment (Fig. 3.9B), suggesting that these faults, which share similar kinematic and timing histories, may be correlative structures and were subsequently offset by dextral slip on the La Cruz fault. This fault correlation remains uncertain as it is complicated by subsequent dip-slip motion on the La Cruz fault that exposes different structural levels across it. The fault-controlled paleovalley of *Ttsf* likely connected to a more widespread and continuous sheet of *Ttsf* deposits documented by Oskin et al. (2001) and Oskin and Stock (2003b) in the Sierra Menor and beneath Valle de Tecomate to the northwest and north, respectively (Fig. 3.2A). This paleovalley also likely continued to the southwest, toward the Tiburón transform fault. We speculate that *Ttsf* exposures documented on Isla Angel de la Guarda (Stock et al., 2008; Skinner et al., 2012), ~90 - 100 km to the northwest (Fig. 3.1), may correlate to the *Ttsf* exposures on southern Isla Tiburón, providing a potential tie-point for constraining post-12.3 Ma dextral displacement across the Tiburón transform fault.

We also identify correlative exposures of the ~12.2 Ma Tuff of Ensenada de la Cruz (*Tlc*) across the La Cruz fault (Fig. 3.3A). Southwest of the La Cruz fault, outcrops of *Tlc* vary along strike from ~50 m-thick, densely-welded deposits in the southeast (Fig. 3.8D) to thin (<10 m) and discontinuous, slightly- to non-welded deposits in the northwest (Fig. 3.8C). Northeast of the La Cruz fault, *Tlc* deposits are very discontinuous, observed only ~5 - 10 m-thick in isolated exposures (e.g. Fig. 8E). Thus, due to its discontinuous exposure across the fault, *Tlc* is a poor marker for estimating total dextral displacement across the La Cruz fault. However, its limited distribution is a useful datum that corroborates our estimates of dextral displacement of the *Ttsf* paleovalley (Fig. 3.9).

Younger, late Miocene (post-8 Ma) units also correlate across the La Cruz fault, including the La Cruz basin deposits (*Tcg3*). The basal contact of these deposits is cut and offset by the multiple strands of the dextral La Cruz fault and *Tcg3* deposits are commonly highly faulted and folded within the La Cruz fault zone (Fig. 3.3A). Corresponding, highly deformed marine strata in the Southwest Isla Tiburón basin accumulated between 6.4 Ma and 6.0 Ma and are dextrally offset no more than 1 km along the La Cruz fault (Chapter 2 of this thesis). Thus, the majority of the 5 ± 2 km of dextral displacement along the La Cruz fault must have occurred between ~12.2 and ~6.0 Ma, and the majority of syn-tectonic basin accumulation occurred after ~7.9 Ma.

3.7c Synchronous Onset of Transform Faulting in the Gulf of California

Dextral strike-slip faults and related sedimentary basins on Isla Tiburón initiated during latest Miocene time, regionally consistent and synchronous with the onset of transform faulting and more focused and oblique transtensional deformation along a significant length of the

Pacific-North America plate boundary in northwest Mexico and southernmost California (Fig. 3.10). Tectono-stratigraphic records from both conjugate rifted margins of the Gulf of California preserve a history of transform faulting that initiated in the latter half of proto-Gulf time, ca. 9 - 6 Ma (cf. Seiler et al., 2011; Fig. 10).

Direct evidence for latest Miocene onset of focused transtension in the form of mapped strike-slip faults and/or documentation of clockwise vertical-axis block rotation is restricted to a few onshore exposures adjacent to the northern Gulf of California. On the eastern, Sonoran rift margin, the majority of strike-slip faulting, clockwise block rotation, and transtensional basin formation took place after ca. 7 Ma in the Coastal Sonora Fault Zone (Fig. 3.1; Bennett et al., 2013). The Yawassag fault and related Tecomate basin on northeastern Isla Tiburón is the northwesternmost onshore exposure of this transtensional belt of deformation, which we demonstrate here also initiated ca. 7 Ma or later. These findings are consistent with latest Miocene to Pliocene (7 - 4 Ma) apatite fission track ages documented throughout coastal Sonora, which are interpreted as a minimum age for the onset of exhumation related to transtensional shearing (Lugo-Zazueta et al., 2010). Further to the southeast, along structural strike, Herman and Gans (2006) document a zone of significant late Miocene (~9 Ma) dextral deformation and clockwise vertical-axis block rotation in the Sierra el Aguaje (Fig. 3.10) that Bennett et al. (2013) speculate may be related to the Coastal Sonora Fault Zone. Structurally outboard of the Coastal Sonora Fault Zone, to the southwest, we document similar timing for the La Cruz fault on southern Isla Tiburón, with activity by 7 Ma, which was complete by 4 Ma.

On the western, Baja California rift margin (Fig. 3.1), direct geologic evidence suggests that the majority of transtensional deformation also commenced in latest Miocene time ca. 9 -7 Ma. In northeastern Baja California, on the conjugate rift margin to Isla Tiburón and coastal

Figure 3.10 Paleo-tectonic map of proto-Gulf of California, restored to ~6 - 7 Ma. Main map shows restored positions of documented latest Miocene transtensional faulting and basin formation (white circles). These locales define a NNW-trending proto-Gulf of California shear zone, where earliest transform faulting initiated in the latter half of proto-Gulf time, ca. 9 - 6 Ma. See Discussion section in text for details. Plots tied to each locale show available information about the timing and magnitude of tectonic subsidence (green) and tilting (blue). The onset of rapid basin subsidence appears to have occurred in a synchronous fashion in latest proto-Gulf time (vertical gray box). At the Punta Chueca and Santa Rosa basins, thermochronologic data (black bar) further constrain the onset of rift-related exhumation. Late Miocene position of cities as small black squares: Y-Yuma, SD-San Diego, PP-Puerto Penasco, SF-San Felipe, P-Puerticitos, G-Guaymas

(INSET MAP) As inset map in Figure 1, showing present-day locations of latest Miocene transtensional faulting discussed in text, including those shown in their restored positions in the main figure. FCV-Fish Creek-Vallecitos basin, AB-Altar basin, SRB-Santa Rosa basin, CS-Coastal Sonora & Isla Tiburón basins, SA-Sierra el Aguaje, G-Eastern Guaymas basin, SB-Southeastern Baja California, AS-Alarcon rift segment

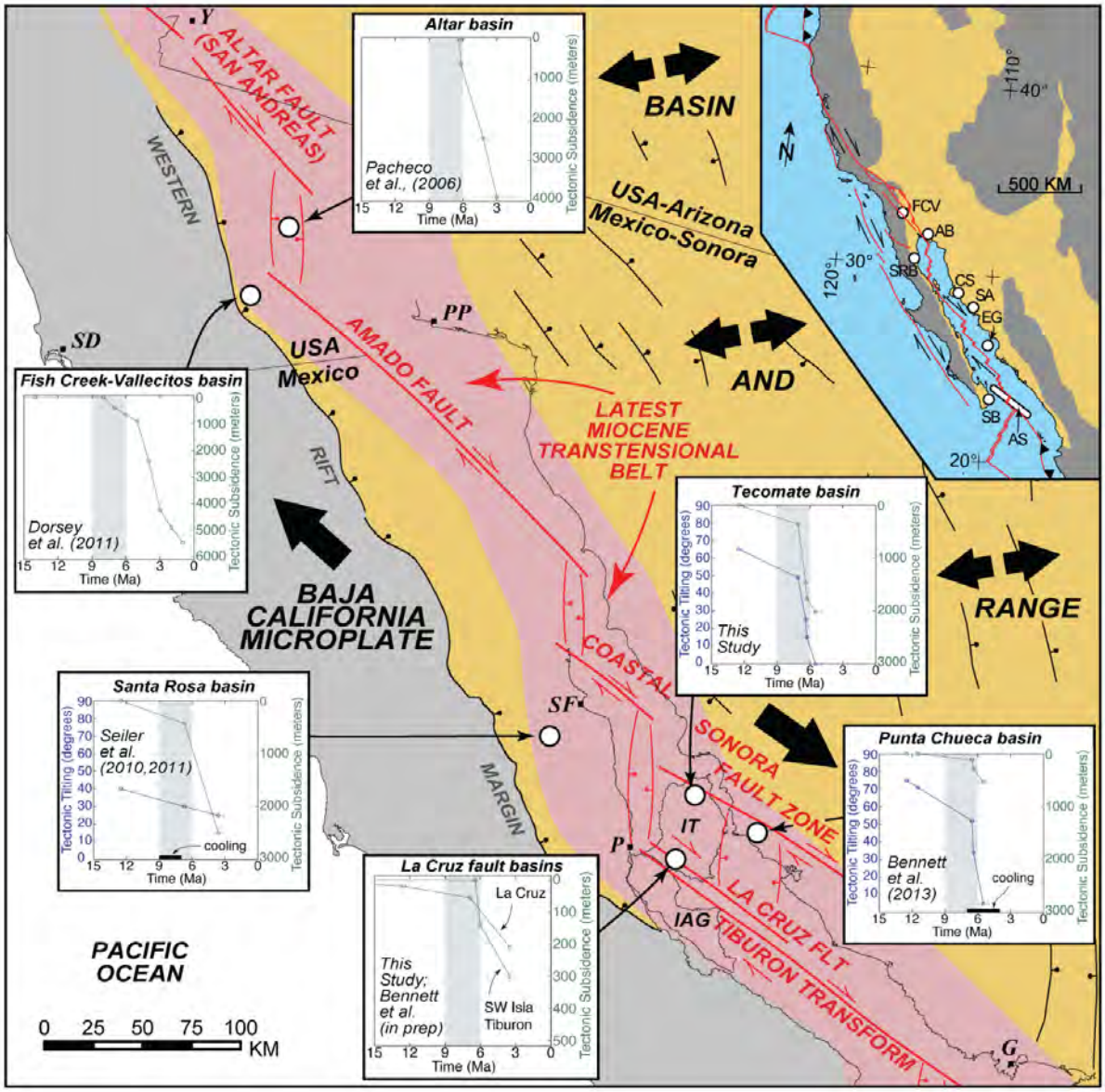
Altar basin
Pacheco et al., (2006)
Time (Ma)
Tectonic Subsidence (meters)
Fish Creek-Vallecitos basin
Dorsey et al. (2011)
Santa Rosa basin
Seiler et al. (2010,2011)
cooling
Tectonic Tilting (degrees)
Tecomate basin
This Study
Punta Chueca basin
Bennett et al. (2013)
La Cruz fault basins
La Cruz
This Study; Bennett et al. (in prep)
SW Isla Tiburon
ALTAR FAULT (SAN ANDREAS)
WESTERN
RIFT
MARGIN
AMADO FAULT
LATEST MIOCENE TRANSTENSIONAL BELT
COASTAL
SONORA FAULT ZONE
LA CRUZ FLT
TIBURON TRANSFORM
BASIN
AND
RANGE
USA-Arizona
Mexico-Sonora
USA
Mexico
BAJA CALIFORNIA MICROPLATE
PACIFIC OCEAN
0 25 50 75 100 KM
500 KM
FCV
AB
SRB
CS
SA
EG
SB
AS
Y
SD
PP
SF
P
IT
IAG
G

Sonora (Fig. 3.10), Lewis and Stock (1998a,b) and Seiler et al. (2010) document a series of syn-tectonic basins related to regional dextral shear, which was accommodated via clockwise vertical-axis block rotation, sinistral slip on NE-striking strike-slip faults, and east- to southeast-directed extension above detachment faults. Basins formed adjacent to and above these faults, respectively, host growth strata with basal depositional ages between 6 and 7 Ma (Boehm, 1984; Seiler et al., 2010). Low-temperature thermochronologic analysis of normal faults that controlled basin formation indicates an onset of exhumation related to oblique rifting between 9 - 7 Ma (Fig. 3.10; Seiler et al., 2011).

Indirect evidence for the onset of transform faulting comes from geological and geophysical examination of pull-apart basins kinematically linked to significant dextral strike-slip faults. These data are also relatively sparse, but examples exist along a >1,000 km-long length of the Gulf of California (Fig. 3.10). At the northwestern end, subsidence in the Salton Trough, in the hanging wall of the West Salton Detachment fault, presumably linked to dextral motion south of the southern San Andreas fault, began at 8.0 ± 0.4 Ma (Dorsey et al., 2007; 2011). In the Altar desert of northwesternmost Sonora, southeast of the Salton Trough, (Fig. 3.10), Pacheco et al. (2006) document the onset of syn-tectonic sediment accumulation in the Altar pull-apart basin ca. 7 - 6 Ma. This basin formed above the hanging wall of the Altar detachment fault, coeval with top-to-the-northwest extension that was kinematically linked to dextral strike-slip motion on the NW-striking Altar fault, a southeastward continuation of the San Andreas fault. Approximately 350 km southeast of Isla Tiburón, offshore Sinaloa and along strike with the Ballenas transform fault, Miller and Lizarralde (2013) document ~7 Ma deposits of marine evaporite that floor transtensional marine basins that formed during oblique opening of the Guaymas rift segment (Fig. 3.10). In the southernmost Gulf of California, across the Alarcon

rift segment (Fig. 3.10), Sutherland et al. (2012) document a phase of oblique extension ca. 8 - 5 Ma, supported by the presence of syn-rift deposits that overlie volcanic rocks as young as 11 - 9 Ma, and are located adjacent to related strike-slip faults. The timing of this transtensional deformation is broadly synchronous with the ~9 - 8 Ma onset of basement exhumation documented on the adjacent rift margin in southernmost Baja California (Fig. 3.10; Kohn et al., 2010). Sutherland et al. (2012) also suggest an earlier phase of transtension ca. 14 -11 Ma, though direct evidence for its association with dextral strike-slip faulting is lacking from their geophysical data. Alternatively, formation of these middle Miocene basins could be due to east-west extension, similar to that accommodated by the Sauzal and Colorado normal faults on Isla Tiburón.

In summary, there is widespread evidence of a tectonic reorganization in the Gulf of California rift in the late Miocene, between 7 and 9 Ma (Fig. 3.10). This transition led to formation of a more intensive, localized, and oblique rift, characterized by the development of long transform faults, linked pull-apart basins, and a 50 to 100 km-wide belt of clockwise vertical-axis block rotations (Chapter 1 of this thesis). This zone accrued several tens of km of dextral displacement in a few million years – a strain rate comparable to that of the plate boundary that eventually developed here. Though earlier proto-gulf deformation was likely transtensional in character (c.f. Gans, 1997; Fletcher et al., 2007), it was probably more diffuse, more akin to the back-arc extension that preceded it within the Mexican Basin and Range than the nascent plate-boundary dextral shear zone that followed.

3.7d Implications for Latest Miocene Rift Localization in Northwestern Mexico

Based on regional synchronicity of intense oblique deformation on the margins of the northern Gulf of California, beginning only 1 to 3 Myr prior to full rift localization, it appears that localization was facilitated by the development of long transform faults. Slip on these transform faults, opening of intervening pull-apart basins, and crustal thinning in flanking regions of large-magnitude extension and block rotation, set the stage for subsequent crustal rupture and opening of the Gulf of California. The timing and kinematic setting of this transition from diffuse transtension to focused and highly oblique rifting is conspicuously similar to a significant azimuthal change in PAC-NAM relative plate motion predicted by the global plate circuit model by Atwater and Stock (1998). During chron 4, a magneto-chron time interval from 8.8 - 7.5 Ma (Lourens et al., 2004), the PAC-NAM relative plate motion vector rotated 15 - 20° clockwise at the latitude of the Gulf of California. This effectively increased the obliquity of rifting by reducing the angle between the relative plate motion and the regional trend of the plate boundary, drawn from the Salton Sea to the Rivera triple junction at the mouth of the Gulf of California. Analog clay models of oblique rifts illustrate the diverse structural styles that develop from variable angles of rift obliquity (Withjack and Jamison, 1986; Clifton et al., 2000; Clifton and Schlische, 2001). Importantly, only highly oblique rifts, with ≤30° between relative plate motion and the plate boundary, develop significant strike-slip faults in these models (Clifton et al., 2000). The clockwise shift for a reference point that tracks this relative motion across the central Gulf of California alters the angle of rift obliquity from ~30° to <15° during chron 4. Thus, the Gulf of California appears to have crossed a critical structural threshold during latest Miocene time, at ~ 8 Ma, when an increase in rift obliquity spurred the synchronous

development of major dextral transform faults along much of the rift, resulting in a focused zone of oblique divergence along which rifting eventually proceeded to full localization by 6 Ma.

Thus, although a global plate circuit model indicates that rapid (~5 cm/yr) PAC-NAM dextral-oblique motion was underway by ~12.3 Ma at the latitude of Baja California (Atwater and Stock, 1998), development of significant, embedded dextral transform faults within the rift was delayed by 3 - 4 Myr, until ~9 - 8 Ma. The proto-Gulf shear zone that eventually developed probably bore similarities to the Walker Lane belt of the western Basin and Range province of California and Nevada (Faulds et al., 2005; Henry and Faulds, 2006). In both areas, the shear zone developed along the axis of the former, subduction-related volcanic arc (Hausback, 1984; Umhoefer et al., 2001; Busby et al., 2012). This zone of thermally weakened and gravitationally unstable lithosphere was slightly oblique (more northerly) to the azimuth of Pacific-North America relative plate motion. The *en echelon* patterns of oblique deformation that developed resemble model predictions of oblique extension across pre-existing weak zones (van Wijk, 2005; Brune et al., 2012). If this proto-Gulf shear zone was only active for 1 - 2 Myr, then no more than ~100 km of PAC-NAM dextral shear could have accrued during proto-Gulf time. This is consistent with our estimates of total dextral shear across Isla Tiburón and with estimates in coastal Sonora by Bennett et al. (2013) and northeastern Baja California (Lewis and Stock, 1998a), while in conflict with tectonic models that invoke much larger magnitudes (150 - 250 km) of proto-Gulf dextral deformation here (e.g. Nicholson et al, 1994; Gans, 1997; Wilson et al, 2005; Fletcher et al., 2007; Seiler et al., 2010). Older, distributed transtension across the western Mexican Basin and Range (Fig. 3.1 inset) likely contributes additional dextral slip to the full plate-boundary budget (e.g. Gans, 1997), but no significant, pre-9 Ma strike-slip faults have been discovered to date that compare with the proto-Gulf transform faults in westernmost Sonora and

on Isla Tiburón. Additional proto-Gulf-age dextral faulting related to PAC-NAM relative motion has been documented offshore, west of Baja California (e.g. Fletcher et al., 2007; Brothers et al., 2012).

Following the development of this proto-Gulf shear zone, the Gulf of California progressed to a localized rift, became host to a marine seaway, and proceeded to continental rupture. Intense oblique-divergent motion throughout latest Miocene time caused lithospheric thinning and subsidence that formed incipient pull-apart basins at or below sea level. Sufficient thinning and subsidence within this proto-Gulf shear zone allowed the regionally synchronous marine flooding of the northern Gulf of California ca. 6.5 - 6.3 Ma (Oskin and Stock, 2003a; Chapter 2 of this thesis). Full rift localization in the Gulf of California occurred within the core of this proto-Gulf shear zone, but was delayed until ~6 Ma (Oskin et al., 2001; Oskin and Stock, 2003b), at least 1 to 2 Myr after the onset of transform faulting. Eventually, within the northern Gulf of California, extreme crustal thinning across pull-apart basin detachment faults (Gastil and Fenby, 1991; González-Fernández et al., 2005) facilitated Pliocene-Pleistocene continental rupture along its western edge (Martín-Barajas et al., 2010). Consequently, protracted, Oligo-Miocene westward-migrating extension (cf. Aragón-Arreola and Martín-Barajas, 2007), culminating with a late Miocene increase in rift obliquity, led to the present-day strongly asymmetric rifted margins flanking the northern Gulf of California (Aragón-Arreola and Martín-Barajas, 2006). The Baja California margin is relatively narrow, <50 km, while the Sonora margin encompasses a ~300 km-wide extensional province (Fig. 3.1 inset; Stock and Hodges, 1989). This asymmetric geometry resembles other, more mature, rifted continental margins (Louden and Chian, 1999) and model predictions of continental break-up (Bassi, 1995;

Huismans and Beaumont, 2003). But in the case of the Gulf of California, this end result was strongly influenced by the evolving rift obliquity.

Continental rupture and formation of new oceanic rift basins requires focused strain (Buck, 1991). Due to its infancy, the Gulf of California preserves a rare onshore record of early continental break-up processes, and serves as an example of how rift obliquity and formation of transform faults helps facilitate continental rupture. Intrinsically, oblique rifts develop *en echelon* patterns of transform faults and connected pull-apart basins (Withjack and Jamison, 1986; van Wijk, 2005). Sub-vertical strike-slip faults are relatively unaffected by buoyancy and flexural forces (e.g. Forsyth, 1992) that otherwise restrict fault-slip on non-vertical, normal faults; restrictions that can drive rift widening during orthogonal rifting (Buck, 1991). Thus, strike-slip faults tend to be longer-lived and susceptible to fault weakening and shear heating (Leloup et al., 2002), processes that allow shear zones to further persist in their location (Kaus and Podladchikov, 2006) and accumulate larger displacements. Furthermore, normal faults typically experience horizontal axis rotation and evolve to more shallow dips with continued slip, leaving them in non-optimal orientation for accumulation of large displacement (c.f. Brady et al., 2000). Sub-vertical strike-slip faults, on the other hand, can tolerate such fault plane rotation across releasing or restricting bends, allowing them to be long-lived, grow in length, and accommodate large displacements. Additionally, unlike strike-slip faults, the length of any single normal fault found in a traditional, orthogonal rift setting may be limited in its growth by the thickness of the brittle crust (Jackson and White, 1989).

Highly oblique rift geometries, where the strike-slip faults that bound rift segments (transform faults) are kinematically linked to adjacent pull-apart basins, may favor the formation of large-offset, translithospheric detachment faults (e.g. Tucholke et al., 1998) and are likely

more efficient at localizing the strain necessary for continental rupture than orthogonal rifting (Brune et al., 2012). Several structural and geophysical studies throughout the Gulf of California and Salton Trough demonstrate the abundance of large-offset normal faults kinematically linked to zones of transform faults with high transtensional strain rates (e.g. Axen and Fletcher, 1998; González-Fernández et al., 2005; Pacheco et al., 2006; Martín-Barajas, 2010; Seiler et al., 2010; Dorsey et al., 2011; Bennett et al., 2013), consistent with the notion that an oblique, *en echelon* rift architecture enhances the ability for rupturing continental lithosphere and formation of a new oceanic rift basin.

3.8 CONCLUSIONS

The Gulf of California preserves a rare, youthful onshore record of oblique continental break-up processes, where transform faults kinematically linked to adjacent pull-apart basins appear to have efficiently localized the strain necessary for continental rupture, consistent with numerical modeling studies (e.g. Brune et al., 2012). Rift-related structures and syn-tectonic basins on Isla Tiburón, a proximal onshore exposure of the rifted North America margin in the Gulf of California, preserve a two-phase record of fault activity and basin formation. On southern Isla Tiburón, an early phase of east-west extension on the Sauzal and Colorado normal faults initiated sometime after ~19 Ma and was ongoing by ~12.2 Ma. Extensional faults and related basin deposits were subsequently buried by younger, syn-tectonic sediments of the non-marine La Cruz basin and cross-cut by the northwest-striking La Cruz strike-slip fault, which was active ~7 - 4 Ma. Reconstruction of the distribution of pre-rift and syn-rift volcanic units permits an estimate of 5 ± 2 km of total dextral slip across the La Cruz fault (Fig. 3.9). On northeastern Isla Tiburón, the Tecomate basin accumulated syn-tectonic sediments above the

hanging wall of the Kunkaak normal fault. The Tecomate basin is floored by the ~12.2 Ma Tuff of San Felipe, and contains deposits of non-marine conglomerate and intercalated 7.1 - 6.4 Ma volcanic rocks. The Yawassag fault and other minor strike-slip faults subsequently cut and truncated the Kunkaak fault and Tecomate basin-fill via ≥8 km of post-6.4 Ma dextral strike-slip. The La Cruz and Yawassag faults were significant NW-striking, strike-slip structures that developed during latest Miocene time and are likely representative components of transform fault systems that bound the Upper Delfín-Upper Tiburón rift segment (Fig. 3.1). These structures were later lengthened offshore, to the northwest, and acted as plate boundary transform faults that accommodated earliest (late Miocene-Pliocene) oblique opening and pull-apart basin formation in the northern Gulf of California (Oskin and Stock, 2003b; Martín-Barajas et al., 2010).

Latest Miocene (~8 - 6 Ma) onset of strike-slip faulting and related basin formation on Isla Tiburón is synchronous with tectono-stratigraphic records of oblique rifting and pull-apart basin formation from both conjugate rifted margins in the northern Gulf of California and along a significant length of the Pacific-North America plate boundary in northwest Mexico and southernmost California. At several locations along the >1,000 km-long reconstructed plate boundary, evidence for the onset of transform faulting and related, focused oblique rifting appear to concentrate, in both time and space, along a narrow, NNW-trending proto-Gulf of California shear zone, where earliest transform faulting initiated in the latter half of proto-Gulf time, ca. 9 - 6 Ma (cf. Seiler et al., 2011; Fig. 10). Earlier proto-gulf deformation, which was possibly transtensional in character (c.f. Gans, 1997; Fletcher et al., 2007) and probably more diffuse, transitioned to more intensive, localized, and oblique rifting, characterized by the development of long transform faults, linked pull-apart basins, and a 50 to 100 km-wide belt of clockwise

vertical-axis block rotations (Chapter 1 of this thesis). Strain localization and recent continental rupture in the Gulf of California was likely facilitated by this transition to highly oblique rifting and the development of transform faults. The timing of this transition corresponds to a clockwise azimuthal shift in Pacific-North America relative motion ca. 8.8 - 7.5 Ma, which reorganized plate motions (Atwater and Stock, 1998) and amplified the effects of rift obliquity within the Gulf of California. Consequently, the Gulf of California rift crossed a critical structural threshold that prompted the synchronous development of major dextral transform faults along its length, resulting in a focused zone of oblique divergence. Shortly following (1 - 3 Myr) the development of this proto-Gulf shear zone, the Gulf of California became host to a marine seaway ca. 6.5 - 6.0 Ma (Oskin and Stock, 2003a; Chapter 2 of this thesis) co-located and coeval with full localization of the incipient plate boundary (Oskin et al., 2001; Oskin and Stock, 2003b). Thus, although rapid (~5 cm/yr) PAC-NAM dextral-oblique motion commenced ~12.3 Ma at the latitude of Baja California (Atwater and Stock, 1998), localization of the plate boundary was delayed until ~6 Ma, following a transition to more oblique rifting and upon the development of major transform faults. The record from the proto-Gulf of California illustrates how highly oblique rift geometries enhance the ability of continental lithosphere to rupture and, ultimately, lead to the formation of new oceanic rift basins.

ACKNOWLEGMENTS

Funding from the National Science Foundation Tectonics and MARGINS programs, awards #0739017 and #0904337, an ExxonMobil Geoscience Grant, a Geological Society of America Graduate Student Research Grant, a Northern California Geological Society Richard Chambers Memorial Scholarship, and a UC Davis Cordell Durrell scholarship made this research

possible. Permission to enter Isla Tiburón was granted by the Secretaría de Medio Ambiente y Recursos Naturales-Comisión Nacional de Areas Naturales Protegidas and the native Cumcaác (Seri) tribe. We thank A. Martín-Barajas for assistance with permit acquisition. Discussions with R. Dorsey and A. Forte helped to improve this manuscript. We thank M. Kunk and J. Wooden for assistance with our $^{40}Ar/^{39}Ar$ and U/Pb geochronology data, respectively. M. Tappa, M. Iglecia, A. Gauer, J. Ford, and E. Stevens all provided great company, safety, and support while conducting fieldwork on Isla Tiburón. T. Donovan, G. Smart, and the Prescott College Kino Bay Center for Cultural and Ecological Studies staff provided incredible logistical support and comfortable accommodations while conducting fieldwork. We thank the Molina Villa-Lobos family (Ernesto, Francisco, and Esequel) of the of the native Cumcaác (Seri) tribe for their superb boatmanship and safekeeping during our field research.

Table 3.1 $^{40}Ar/^{39}Ar$ step-heating data for Isla Tiburón samples.

Step	Temp. °C	%^{39}Ar of total	Radiogenic Yield (%)	$^{39}Ar_k$ (moles x 10^{-12})	$^{40}Ar^*/^{39}Ar_k$	Apparent K/Ca	Apparent K/Cl	Apparent Age (Ma)	Error (Ma)
TIB-10-34	***basalt matrix***	*J = 0.004767 ± 0.30%*		*wt = 276.2 mg*	*#282&283KD57*				
A	600	1.1	3.2	0.0373	0.627	1.24	28	5.38	± 0.74
B	700	8.6	13.5	0.3066	1.006	1.78	43	8.63	± 0.16
C	800	12.0	25.6	0.4259	0.992	0.78	52	8.51	± 0.08
D	850	7.6	25.7	0.2722	0.969	0.37	61	8.32	± 0.16
E	900	7.1	27.1	0.2532	1.109	0.24	72	9.51	± 0.83
F	950	6.6	20.3	0.2336	1.028	0.21	67	8.82	± 0.12
G	1000	6.6	13.9	0.2364	1.154	0.26	51	9.89	± 0.10
H	1050	7.0	12.8	0.2490	1.249	0.28	46	10.71	± 0.69
I	1100	3.5	11.0	0.1258	1.120	0.28	43	9.60	± 0.48
J	1150	3.8	11.7	0.1360	1.201	0.23	41	10.30	± 0.21
K	1200	3.1	11.5	0.1118	1.137	0.17	40	9.75	± 0.28
L	1250	2.2	12.1	0.0780	1.119	0.10	40	9.60	± 0.24
M	1350	16.2	11.5	0.5782	1.607	0.11	39	13.77	± 0.14
N	1450	12.8	11.9	0.4554	1.627	0.11	42	13.94	± 0.46
O	1650	1.7	11.2	0.0611	2.107	0.09	39	18.03	± 1.74
Total Gas		100	16.4	3.5605	1.247	0.42	49	10.69	
TIB-10-3	***dacite-andesite matrix***	*J = 0.004712 ± 0.30%*		*wt = 867.0 mg*	*#284&285KD57*				
A	600	0.2	0.6	0.0047	5.064	0.86	12	42.54	± 14.35
B	700	1.1	4.2	0.0248	2.252	1.04	48	19.04	± 2.42
C	800	4.1	20.2	0.0958	1.633	0.87	175	13.83	± 0.20
D	850	4.5	60.0	0.1050	2.432	0.71	447	20.55	± 0.14
E	900	7.3	80.6	0.1701	2.546	0.72	1635	21.51	± 0.07
F	950	18.9	89.1	0.4395	2.529	0.78	0	21.37	± 0.05
G	1000	17.9	88.7	0.4168	2.461	0.76	0	20.80	± 0.04
H	1050	15.5	84.8	0.3598	2.437	0.64	4371	20.60	± 0.05
I	1100	9.7	75.1	0.2259	2.446	0.55	1176	20.67	± 0.06
J	1150	6.4	61.0	0.1480	2.465	0.50	424	20.83	± 0.09
K	1200	5.3	52.7	0.1238	2.460	0.56	217	20.79	± 0.14
L	1250	3.8	46.8	0.0883	2.460	0.51	134	20.79	± 0.16
M	1350	3.8	24.3	0.0893	2.701	0.31	40	22.81	± 0.20
N	1450	0.7	5.2	0.0161	5.169	0.09	12	43.41	± 3.36
O	1650	0.8	3.2	0.0187	7.451	0.08	11	62.25	± 2.16
Total Gas		100	72.1	2.3266	2.406	0.66	983	20.34	

Ages calculated assuming an initial $^{40}Ar/^{36}Ar = 295.5 \pm 0$.
All precision estimates are at the one sigma level of precision.
Ages of individual steps do not include error in the irradiation parameter J.
No error is calculated for the total gas age.

Table 3.2 $^{40}Ar/^{39}Ar$ laser total fusion data of single-crystal k-feldspar from volcanic rocks from Isla Tiburón.

Hole number	$^{39}Ar_k$ (Moles)	Radiogenic Yield (%)	$\frac{^{40}Ar^*}{^{39}Ar_k}$	K/Ca	K/Cl	Age (Ma)		Error (Ma)
TIB-10-36b	*Sonora, Mexico*	***sanidine***	*J = 0.004606 ± 0.25%*		*#204KD57*			
8	5.73E-14	28.7	1.436	3.2	2632	**11.89**	**±**	**0.20**
9	2.29E-14	72.1	1.438	3.0	20000	**11.91**	**±**	**0.24**
17	8.54E-14	36.3	1.448	4.1	2174	**12.00**	**±**	**0.16**
18	6.45E-14	59.6	1.457	5.0	2778	**12.06**	**±**	**0.16**
19	6.57E-14	43.1	1.459	3.9	3704	**12.09**	**±**	**0.17**
14	2.27E-14	63.4	1.461	5.5	4762	**12.10**	**±**	**0.26**
13	3.23E-14	38.9	1.468	4.7	3571	**12.15**	**±**	**0.30**
6	2.16E-14	52.1	1.471	5.3	2439	**12.19**	**±**	**0.28**
11	5.48E-14	77.8	1.472	2.7	3571	**12.19**	**±**	**0.11**
10	4.06E-14	53.1	1.473	4.2	4348	**12.20**	**±**	**0.17**
3	6.71E-14	54.8	1.473	3.6	4762	**12.20**	**±**	**0.15**
7	3.64E-14	64.7	1.481	4.7	4545	**12.26**	**±**	**0.19**
12	3.22E-14	87.3	1.483	2.9	1724	**12.28**	**±**	**0.17**
5	2.46E-14	24.2	1.483	3.9	2041	**12.28**	**±**	**0.37**
15	7.16E-14	81.9	1.485	3.7	20000	**12.30**	**±**	**0.09**
16	1.12E-13	61.0	1.496	5.5	10000	**12.39**	**±**	**0.10**
2	6.17E-14	96.1	1.501	7.1	***	**12.43**	**±**	**0.09**
1	6.97E-14	54.3	1.510	2.3	2632	**12.51**	**±**	**0.15**
4del	*3.81E-14*	*55.5*	*1.529*	*4.5*	*5263*	*12.66*	*±*	*0.19*
		MSWD = 1.20		**Weighted Mean Age =**		**12.26**	**±**	**0.07**
TIB-10-41	*Sonora, Mexico*	***sanidine***	*J = 0.004607 ± 0.25%*		*#202KD57*			
3	4.83E-14	79.8	1.423	4.8	4348	**11.78**	**±**	**0.32**
13	1.36E-13	37.4	1.431	9.3	7692	**11.85**	**±**	**0.14**
14	8.61E-14	47.8	1.433	5.0	9091	**11.87**	**±**	**0.18**
4	7.30E-14	92.8	1.435	9.5	***	**11.89**	**±**	**0.24**
8	5.54E-14	52.9	1.446	9.6	***	**11.98**	**±**	**0.26**
5	3.84E-14	65.4	1.450	5.2	7692	**12.01**	**±**	**0.42**
11	1.46E-13	44.3	1.453	5.0	5556	**12.04**	**±**	**0.12**
16	1.34E-13	61.6	1.456	6.2	9091	**12.05**	**±**	**0.12**
15	8.29E-14	80.9	1.469	3.4	5556	**12.17**	**±**	**0.16**
17	9.77E-14	34.0	1.472	6.5	2174	**12.19**	**±**	**0.18**
2	1.35E-13	89.5	1.475	8.5	50000	**12.22**	**±**	**0.11**
18	6.28E-14	28.8	1.477	4.4	2128	**12.23**	**±**	**0.27**
10	1.27E-13	70.2	1.480	5.5	***	**12.25**	**±**	**0.12**
12	9.47E-14	77.0	1.481	5.8	11111	**12.27**	**±**	**0.15**
9	4.28E-14	20.7	1.490	3.8	2564	**12.34**	**±**	**0.38**
6	9.51E-14	73.8	1.503	8.2	25000	**12.44**	**±**	**0.15**
1	8.67E-14	71.8	1.506	9.3	***	**12.47**	**±**	**0.17**
		MSWD = 1.31		**Weighted Mean Age =**		**12.14**	**±**	**0.08**

(Cont.)

Table 3.2 (cont.) $^{40}Ar/^{39}Ar$ laser total fusion data of single-crystal k-feldspar from volcanic rocks from Isla Tiburón.

Hole number	$^{39}Ar_k$ (Moles)	Radiogenic Yield (%)	$^{40}Ar^*/^{39}Ar_k$	K/Ca	K/Cl	Age (Ma)		Error (Ma)
TIB-9-12	*Sonora, Mexico*	***sanidine***	*J = 0.004497 ± 0.25%*		*#205KD57*			
12del	*1.27E-13*	*79.7*	*1.487*	*10.2*	*5882*	*12.02*	*±*	*0.07*
5	5.74E-14	78.5	1.488	18.0	11111	**12.03**	**±**	**0.11**
10	1.18E-13	79.1	1.502	13.8	11111	**12.15**	**±**	**0.07**
2	4.42E-14	68.3	1.504	4.2	5882	**12.16**	**±**	**0.14**
14	1.29E-13	69.6	1.505	8.0	4762	**12.16**	**±**	**0.09**
15	1.71E-13	75.1	1.508	7.1	4167	**12.19**	**±**	**0.06**
11	1.67E-13	69.3	1.510	9.0	4762	**12.21**	**±**	**0.07**
4	6.62E-14	72.3	1.512	3.9	2273	**12.22**	**±**	**0.11**
3	1.27E-13	73.0	1.512	9.2	5000	**12.23**	**±**	**0.06**
6	8.68E-14	75.6	1.514	8.4	5556	**12.24**	**±**	**0.09**
16	1.30E-13	71.6	1.515	6.7	7692	**12.25**	**±**	**0.07**
13	1.03E-13	66.0	1.517	7.0	3226	**12.26**	**±**	**0.10**
9	4.58E-14	58.0	1.518	4.7	3571	**12.27**	**±**	**0.16**
8	6.44E-14	70.8	1.518	4.0	2564	**12.28**	**±**	**0.12**
1del	*6.87E-14*	*79.0*	*1.540*	*5.8*	*4000*	*12.45*	*±*	*0.10*
7del	*9.09E-14*	*33.1*	*1.572*	*4.9*	*2041*	*12.71*	*±*	*0.14*
		MSWD = 0.41			**Weighted Mean Age =**	**12.20**	**±**	**0.05**
TIB-10-10	*Sonora, Mexico*	***sanidine***	*J = 0.004495 ± 0.25%*		*#206KD57*			
2del	*5.33E-14*	*54.9*	*1.431*	*4.3*	*9091*	*11.57*	*±*	*0.18*
1del	*3.54E-14*	*45.2*	*1.451*	*3.1*	*4000*	*11.73*	*±*	*0.22*
3	3.86E-14	52.0	1.483	4.0	4167	**11.98**	**±**	**0.19**
8	4.86E-14	43.9	1.488	4.1	7143	**12.02**	**±**	**0.19**
13	6.91E-14	46.8	1.495	4.3	33333	**12.08**	**±**	**0.13**
15	8.09E-14	61.5	1.498	4.1	11111	**12.11**	**±**	**0.10**
14	5.03E-14	46.4	1.502	4.0	2778	**12.14**	**±**	**0.16**
16	3.34E-14	52.5	1.502	0.6	3571	**12.14**	**±**	**0.21**
18	3.67E-14	50.6	1.506	4.7	5263	**12.17**	**±**	**0.20**
9	4.39E-14	37.7	1.508	4.2	4167	**12.19**	**±**	**0.20**
12	4.22E-14	35.6	1.519	1.3	3704	**12.27**	**±**	**0.24**
7	5.30E-14	75.9	1.524	3.1	***	**12.31**	**±**	**0.14**
5	5.99E-14	42.5	1.524	4.9	3125	**12.32**	**±**	**0.17**
4	4.02E-14	43.8	1.529	3.0	3704	**12.36**	**±**	**0.20**
11	3.86E-14	52.3	1.533	3.7	2857	**12.39**	**±**	**0.22**
10	5.07E-14	33.3	1.537	4.2	5000	**12.42**	**±**	**0.20**
17	5.59E-14	51.4	1.550	4.1	1667	**12.52**	**±**	**0.16**
		MSWD = 0.85			**Weighted Mean Age =**	**12.21**	**±**	**0.09**
TIB-10-49	*Sonora, Mexico*	***sanidine***	*J = 0.004498 ± 0.25%*		*#203KD57*			
6	5.96E-14	23.4	1.452	8.6	2000	**11.74**	**±**	**0.24**
14	4.42E-14	53.3	1.454	8.6	2439	**11.76**	**±**	**0.17**
12	9.30E-14	34.8	1.470	6.3	3448	**11.89**	**±**	**0.15**
9	3.79E-14	55.9	1.479	5.0	3030	**11.96**	**±**	**0.19**
11	5.05E-14	69.7	1.481	6.2	6250	**11.98**	**±**	**0.13**
3	4.64E-14	46.5	1.490	4.7	2000	**12.05**	**±**	**0.18**

(Cont.)

Table 3.2 (cont.) $^{40}Ar/^{39}Ar$ laser total fusion data of single-crystal k-feldspar from volcanic rocks from Isla Tiburón.

Hole number	$^{39}Ar_k$ (Moles)	Radiogenic Yield (%)	$\frac{^{40}Ar^*}{^{39}Ar_k}$	K/Ca	K/Cl	Age (Ma)		Error (Ma)
TIB-10-49 (Cont.)								
8	5.70E-14	56.0	1.493	4.3	5263	**12.08**	**±**	**0.14**
10	1.09E-13	67.6	1.500	9.5	5000	**12.13**	**±**	**0.08**
5	3.64E-14	61.4	1.512	4.5	4348	**12.23**	**±**	**0.18**
15	1.27E-13	50.5	1.521	10.9	4545	**12.30**	**±**	**0.10**
4	4.05E-14	50.2	1.522	4.8	2703	**12.31**	**±**	**0.19**
13	5.40E-14	54.6	1.527	3.4	5556	**12.35**	**±**	**0.15**
7	3.48E-14	63.8	1.531	3.9	5882	**12.38**	**±**	**0.19**
1del	*2.66E-14*	*50.7*	*1.567*	*3.4*	*4167*	*12.67*	*±*	*0.27*
2del	*3.28E-14*	*34.2*	*1.573*	*3.1*	***	*12.72*	*±*	*0.25*
		MSWD = 1.71		**Weighted Mean Age =**		**12.12**	**±**	**0.08**
TIB-09-25	*Sonora, Mexico*	***sanidine***	*J = 0.004398 ± 0.25%*		*#190KD53*			
3	1.18E-14	95.8	0.870	59.7	4000	**6.89**	**±**	**0.03**
29	3.21E-15	97.1	0.881	74.9	14286	**6.98**	**±**	**0.07**
31	5.26E-15	96.7	0.882	55.6	33333	**6.98**	**±**	**0.03**
7	8.80E-15	96.3	0.886	62.5	7692	**7.02**	**±**	**0.04**
4	7.40E-15	83.3	0.891	66.1	8333	**7.05**	**±**	**0.05**
37	4.46E-15	91.4	0.892	52.8	10000	**7.07**	**±**	**0.05**
19	4.62E-15	97.0	0.897	79.3	5556	**7.10**	**±**	**0.04**
11	8.63E-15	91.2	0.898	67.3	10000	**7.11**	**±**	**0.04**
13	8.86E-15	99.4	0.899	81.3	8333	**7.12**	**±**	**0.02**
12	9.04E-15	95.7	0.901	50.5	5556	**7.13**	**±**	**0.04**
20	9.65E-15	99.1	0.903	79.4	***	**7.15**	**±**	**0.03**
40	4.01E-15	98.9	0.904	57.3	9091	**7.15**	**±**	**0.05**
30	2.64E-15	99.3	0.904	34.7	4545	**7.16**	**±**	**0.07**
2	9.82E-15	99.8	0.907	87.3	0	**7.18**	**±**	**0.03**
18	7.45E-15	99.1	0.908	152.9	11111	**7.19**	**±**	**0.03**
38	6.62E-15	98.3	0.908	188.7	25000	**7.19**	**±**	**0.03**
6	1.01E-14	96.7	0.911	70.9	2273	**7.21**	**±**	**0.03**
41	1.40E-15	89.3	0.926	104.4	12500	**7.33**	**±**	**0.14**
22	8.21E-15	97.5	1.465	73.8	5556	11.59	±	0.03
		MSWD = 3.46		**Weighted Mean Age =**		**7.11**	**±**	**0.09**
TIB-09-25	*Sonora, Mexico*	***plagioclase***	*J = 0.004398 ± 0.25%*		*#190KD53*			
28	5.70E-16	67.4	0.751	0.6	***	**5.95**	**±**	**0.31**
5	1.35E-15	77.6	0.799	0.6	5263	**6.33**	**±**	**0.27**
24	6.75E-16	57.7	0.801	0.8	2778	**6.34**	**±**	**0.29**
9	1.16E-15	58.9	0.804	0.6	2857	**6.37**	**±**	**0.26**
8	9.78E-16	74.7	0.810	0.7	3846	**6.42**	**±**	**0.31**
10	2.74E-15	46.1	0.820	1.5	2941	**6.49**	**±**	**0.15**
26	6.82E-16	81.1	0.825	0.6	***	**6.53**	**±**	**0.26**
25	9.62E-16	83.0	0.838	0.6	***	**6.63**	**±**	**0.19**
15	7.72E-16	87.4	0.847	0.8	***	**6.71**	**±**	**0.25**
14	1.59E-15	88.6	0.857	0.9	3125	**6.79**	**±**	**0.15**
36	9.24E-16	80.6	0.872	0.5	3846	**6.90**	**±**	**0.21**

(Cont.)

Table 3.2 (cont.) $^{40}Ar/^{39}Ar$ laser total fusion data of single-crystal k-feldspar from volcanic rocks from Isla Tiburón.

Hole number	$^{39}Ar_k$ (Moles)	Radiogenic Yield (%)	$\frac{^{40}Ar^*}{^{39}Ar_k}$	K/Ca	K/Cl	Age (Ma)		Error (Ma)
TIB-09-25 (Cont.)								
17	1.08E-15	91.4	0.883	0.7	2703	**6.99**	**±**	**0.18**
27	1.08E-15	67.8	0.883	0.6	1299	**6.99**	**±**	**0.23**
21	1.24E-15	83.2	0.889	0.5	***	**7.04**	**±**	**0.16**
42	8.77E-16	97.9	0.918	0.6	2632	**7.27**	**±**	**0.22**
23	6.51E-16	89.8	0.951	0.4	6250	**7.53**	**±**	**0.28**
34	5.72E-16	94.3	0.963	0.6	8333	**7.63**	**±**	**0.31**
16	9.03E-16	100.0	0.964	0.4	***	**7.63**	**±**	**0.20**
33	6.26E-16	88.3	0.972	0.8	2703	**7.69**	**±**	**0.27**
32	1.06E-15	87.9	0.983	0.6	6667	**7.79**	**±**	**0.18**
1	7.34E-16	66.5	0.993	0.8	1587	**7.86**	**±**	**0.42**
39	5.62E-16	100.0	1.047	0.5	2273	**8.29**	**±**	**0.33**
35	4.97E-16	100.0	1.049	0.8	4000	**8.30**	**±**	**0.35**
		MSWD = 5.93		**Weighted Mean Age =**		**7.00**	**±**	**0.50**

Analyses in gray italics are not used to calculate the weighted mean age

Table 3.3 U-Th-Pb analytical data for LA-ICPMS spot analyses on zircon grains for volcanic rocks from Isla Tiburón.

				CORRECTED RATIOS										CORRECTED AGES (Ma)									
	U# (ppm)	Th# (ppm)	Th/U	$^{207}Pb/^{206}Pb^{\dagger}$	±1s*	$^{207}Pb/^{235}U^{\dagger}$	±1s*	$^{206}Pb/^{238}U^{\dagger}$	±1s*	$^{208}Pb/^{232}Th^{\dagger}$	±1s*	Rho	% disc**	$^{206}Pb/^{238}U$	±1s*	$^{207}Pb/^{235}U$	±1s*	$^{207}Pb/^{206}Pb$	±1s*	$^{208}Pb/^{232}Th$	±1s*	Best age (Ma)	1s
Sample **TIB-10-52**		Mount ICGEO-17 (January 2011)																					
Zircon_**37**	688	444	0.58	0.0576	0.0032	0.0078	0.0004	0.0010	0.00001	0.0003	0.00001	0.240	19	6.4	0.1	7.9	0.4	513	122	5.9	0.2	6.4	± 0.1
Zircon_**12**	386	196	0.45	0.0677	0.0044	0.0094	0.0007	0.0010	0.00002	0.0003	0.00001	0.310	32	6.5	0.1	9.5	0.7	859	137	6.2	0.1	6.5	± 0.1
Zircon_**29**	469	390	0.75	0.0673	0.0095	0.0094	0.0014	0.0010	0.00002	0.0003	0.00001	0.370	28	6.5	0.1	9.0	1.0	846	299	6.2	0.1	6.5	± 0.1
Zircon_**22**	602	368	0.55	0.0648	0.0032	0.0090	0.0005	0.0010	0.00001	0.0003	0.00001	0.190	27	6.6	0.1	9.1	0.5	769	104	6.3	0.2	6.6	± 0.1
Zircon_**23**	373	203	0.49	0.0678	0.0043	0.0094	0.0006	0.0010	0.00002	0.0003	0.00001	0.240	31	6.6	0.1	9.5	0.6	863	132	6.5	0.2	6.6	± 0.1
Zircon_**34**	361	161	0.40	0.0474	0.0040	0.0066	0.0006	0.0010	0.00002	0.0003	0.00002	0.240	1	6.6	0.1	6.7	0.6	71	178	5.7	0.4	**6.6**	**± 0.1**
Zircon_**25**	342	166	0.44	0.0734	0.0038	0.0104	0.0006	0.0010	0.00002	0.0004	0.00002	0.320	36	6.7	0.1	10.5	0.6	1026	106	7.1	0.4	**6.7**	**± 0.1**
Zircon_**4**	332	162	0.44	0.0552	0.0059	0.0079	0.0009	0.0010	0.00002	0.0003	0.00001	0.210	16	6.7	0.1	8.0	0.9	420	234	6.6	0.2	**6.7**	**± 0.1**
Zircon_**6**	329	147	0.40	0.0529	0.0046	0.0076	0.0007	0.0010	0.00002	0.0003	0.00001	0.240	13	6.7	0.1	7.7	0.7	326	192	6.6	0.2	**6.7**	**± 0.1**
Zircon_**8**	373	195	0.47	0.0726	0.0047	0.0105	0.0007	0.0010	0.00002	0.0003	0.00001	0.260	37	6.7	0.1	10.6	0.7	1004	134	6.4	0.1	**6.7**	**± 0.1**
Zircon_**1**	492	279	0.51	0.0548	0.0037	0.0079	0.0006	0.0011	0.00001	0.0004	0.00001	0.270	14	6.8	0.1	7.9	0.6	405	153	7.1	0.2	**6.8**	**± 0.1**
Zircon_**13**	319	150	0.42	0.0660	0.0051	0.0095	0.0008	0.0011	0.00002	0.0003	0.00002	0.230	29	6.8	0.1	9.6	0.8	806	164	6.9	0.4	**6.8**	**± 0.1**
Zircon_**15**	464	259	0.50	0.0625	0.0089	0.0090	0.0013	0.0011	0.00002	0.0003	0.00001	0.250	24	6.8	0.1	9.0	1.0	692	307	6.5	0.2	**6.8**	**± 0.1**
Zircon_**7**	364	174	0.43	0.0581	0.0051	0.0084	0.0008	0.0011	0.00002	0.0003	0.00001	0.290	20	6.8	0.1	8.5	0.8	533	196	6.6	0.1	**6.8**	**± 0.1**
Zircon_**17**	490	276	0.51	0.0781	0.0065	0.0115	0.0010	0.0011	0.00002	0.0003	0.00001	0.410	43	6.9	0.1	12.0	1.0	1150	169	6.4	0.1	**6.9**	**± 0.1**
Zircon_**18**	358	182	0.46	0.0671	0.0059	0.0100	0.0009	0.0011	0.00002	0.0003	0.00001	0.250	32	6.9	0.1	10.1	0.9	842	185	6.6	0.1	**6.9**	**± 0.1**
Zircon_**19**	412	182	0.40	0.0734	0.0076	0.0109	0.0012	0.0011	0.00002	0.0003	0.00001	0.270	37	6.9	0.1	11.0	1.0	1025	217	6.5	0.1	**6.9**	**± 0.1**
Zircon_**28**	410	195	0.43	0.0667	0.0066	0.0099	0.0010	0.0011	0.00002	0.0003	0.00001	0.220	31	6.9	0.1	10.0	1.0	830	211	6.6	0.1	**6.9**	**± 0.1**
Zircon_**35**	350	167	0.43	0.0738	0.0046	0.0107	0.0007	0.0011	0.00002	0.0003	0.00002	0.270	36	6.9	0.1	10.8	0.7	1036	127	6.9	0.4	**6.9**	**± 0.1**
Zircon_**2**	219	99	0.41	0.0624	0.0084	0.0094	0.0013	0.0011	0.00002	0.0003	0.00001	0.200	22	7.0	0.1	9.0	1.0	689	287	6.8	0.2	**7.0**	**± 0.1**
Zircon_**21**	242	108	0.40	0.0796	0.0089	0.0119	0.0014	0.0011	0.00003	0.0003	0.00001	0.370	42	7.0	0.2	12.0	1.0	1187	230	6.5	0.2	**7.0**	**± 0.2**
Zircon_**24**	334	170	0.46	0.0670	0.0068	0.0101	0.0011	0.0011	0.00002	0.0003	0.00001	0.250	30	7.0	0.1	10.0	1.0	837	217	6.7	0.1	**7.0**	**± 0.1**
Zircon_**30**	331	153	0.42	0.0809	0.0052	0.0122	0.0009	0.0011	0.00002	0.0003	0.00001	0.410	43	7.0	0.1	12.3	0.9	1219	129	6.6	0.1	**7.0**	**± 0.1**
Zircon_**33**	406	204	0.45	0.0718	0.0102	0.0108	0.0016	0.0011	0.00002	0.0003	0.00001	0.250	36	7.0	0.1	11.0	2.0	979	296	6.6	0.2	**7.0**	**± 0.1**
Zircon_**9**	304	147	0.43	0.0680	0.0084	0.0102	0.0013	0.0011	0.00002	0.0003	0.00001	0.220	30	7.0	0.1	10.0	1.0	868	260	6.7	0.2	**7.0**	**± 0.1**
Zircon_**39**	287	131	0.41	0.0618	0.0077	0.0093	0.0012	0.0011	0.00003	0.0003	0.00001	0.280	22	7.0	0.2	9.0	1.0	669	266	6.8	0.2	**7.0**	**± 0.2**
Zircon_**16**	279	99	0.32	0.0635	0.0055	0.0096	0.0008	0.0011	0.00002	0.0004	0.00002	0.170	26	7.2	0.1	9.7	0.8	724	186	7.3	0.4	**7.2**	**± 0.1**
Zircon_**26**	233	103	0.40	0.0789	0.0066	0.0117	0.0010	0.0011	0.00002	0.0004	0.00002	0.260	40	7.2	0.1	12.0	1.0	1170	168	7.5	0.4	7.2	± 0.1
Zircon_**31**	202	83	0.37	0.0641	0.0096	0.0093	0.0014	0.0011	0.00003	0.0004	0.00003	0.200	20	7.2	0.2	9.0	1.0	746	317	7.1	0.6	7.2	± 0.2
Zircon_**11**	219	94	0.38	0.0705	0.0084	0.0111	0.0014	0.0011	0.00003	0.0003	0.00001	0.220	34	7.3	0.2	11.0	1.0	944	246	7.0	0.2	7.3	± 0.2
Zircon_**3**	249	114	0.41	0.0667	0.0081	0.0104	0.0013	0.0011	0.00002	0.0004	0.00001	0.210	34	7.3	0.1	11.0	1.0	827	254	7.0	0.2	7.3	± 0.1
Zircon_**5**	234	107	0.41	0.0750	0.0117	0.0117	0.0019	0.0011	0.00002	0.0003	0.00001	0.230	39	7.3	0.1	12.0	2.0	1068	324	6.9	0.2	7.3	± 0.1
Zircon_**14**	269	104	0.35	0.0655	0.0057	0.0102	0.0009	0.0012	0.00002	0.0004	0.00002	0.210	28	7.4	0.1	10.3	0.9	791	186	7.3	0.4	7.4	± 0.1
n = 33																		**Weighted $^{206}Pb/^{238}U$ mean age =**				**6.87**	**± 0.07**
																						MSWD = 2.0; n = 22	
Sample **TIB-09-25**		Mount ICGEO-7 (October 2009)																					
TIB25-**27**	1551	752	0.45	0.0476	0.0018	0.0063	0.0003	0.0010	0.00001	0.0003	0.00001	0.240	3	6.2	0.1	6.4	0.3	81	84	6.2	0.2	6.2	± 0.1
TIB25-**8**	1122	591	0.48	0.0586	0.0031	0.0078	0.0004	0.0010	0.00001	0.0003	0.00001	0.250	20	6.3	0.1	7.9	0.4	554	113	6.5	0.2	6.3	± 0.1
TIB25-**23**	1160	397	0.31	0.0462	0.0016	0.0064	0.0002	0.0010	0.00001	0.0003	0.00002	0.200	2	6.4	0.1	6.5	0.2	9	68	6.8	0.5	6.4	± 0.1
TIB25-**19**	626	503	0.74	0.0531	0.0043	0.0078	0.0007	0.0011	0.00002	0.0003	0.00001	0.210	13	6.9	0.1	7.9	0.7	331	181	6.8	0.2	**6.9**	**± 0.1**
TIB25-**11**	609	147	0.22	0.0504	0.0029	0.0075	0.0005	0.0011	0.00002	0.0003	0.00001	0.270	8	7.0	0.1	7.6	0.5	212	129	6.9	0.2	**7.0**	**± 0.1**
TIB25-**32**	713	283	0.37	0.0518	0.0038	0.0078	0.0006	0.0011	0.00002	0.0003	0.00001	0.320	11	7.0	0.1	7.9	0.6	275	164	6.9	0.2	**7.0**	**± 0.1**
TIB25-**15**	990	303	0.28	0.0514	0.0041	0.0079	0.0007	0.0011	0.00001	0.0004	0.00001	0.290	10	7.1	0.1	7.9	0.7	260	179	7.0	0.3	**7.1**	**± 0.1**
TIB25-**7**	392	157	0.37	0.0607	0.0072	0.0097	0.0013	0.0012	0.00003	0.0004	0.00001	0.390	25	7.5	0.2	10	1.0	629	258	7.2	0.2	**7.5**	**± 0.2**
TIB25-**38**	393	134	0.31	0.0555	0.0049	0.0096	0.0009	0.0013	0.00002	0.0004	0.00001	0.240	16	8.1	0.1	9.7	0.9	431	197	7.9	0.2	8.1	± 0.1
TIB25-**10**	341	114	0.31	0.0502	0.0035	0.0091	0.0007	0.0013	0.00002	0.0004	0.00002	0.190	8	8.5	0.1	9.2	0.7	203	154	8.4	0.4	8.5	± 0.1
TIB25-**35**	389	185	0.44	0.0546	0.0036	0.0149	0.0011	0.0020	0.00004	0.0006	0.00001	0.290	15	12.7	0.3	15	1.0	397	149	12.5	0.3	12.7	± 0.3
TIB25-**34**	345	152	0.40	0.0645	0.0039	0.0181	0.0012	0.0020	0.00003	0.0006	0.00001	0.340	27	13.1	0.2	18	1.0	759	126	12.6	0.2	13.1	± 0.2
TIB25-**37**	74	41	0.52	0.0613	0.0092	0.0172	0.0027	0.0021	0.00008	0.0008	0.00007	0.240	20	13.6	0.5	17	3.0	649	331	15.0	1.0	13.6	± 0.5
TIB25-**3**	544	252	0.43	0.0605	0.0029	0.0213	0.0011	0.0026	0.00003	0.0008	0.00003	0.230	21	16.5	0.2	21	1.0	621	103	16.2	0.6	16.5	± 0.2
TIB25-**13**	900	236	0.24	0.0491	0.0009	0.0713	0.0015	0.0105	0.00009	0.0036	0.00005	0.420	3	67.6	0.6	70	1.0	151	44	73.0	1.0	67.6	± 0.6
TIB25-**16**	671	121	0.17	0.0496	0.0012	0.0928	0.0028	0.0136	0.00018	0.0043	0.00006	0.510	3	87.0	1.0	90	3.0	175	56	87.0	1.0	87.0	± 1.0
TIB25-**20**	276	140	0.47	0.0540	0.0015	0.1053	0.0031	0.0142	0.00012	0.0045	0.00009	0.290	11	90.6	0.8	102	3.0	373	63	90.0	2.0	90.6	± 0.8
TIB25-**31**	276	193	0.64	0.0517	0.0013	0.1014	0.0028	0.0142	0.00012	0.0044	0.00008	0.330	7	90.8	0.8	98	3.0	271	59	89.0	2.0	90.8	± 0.8
TIB25-**21**	269	103	0.35	0.0504	0.0018	0.0989	0.0040	0.0142	0.00016	0.0045	0.00005	0.370	5	91.0	1.0	96	4.0	212	81	91.0	1.0	91.0	± 1.0

(Cont.)

Table 3.3 (cont.) U-Th-Pb analytical data for LA-ICPMS spot analyses on zircon grains for volcanic rocks from Isla Tiburón.

				CORRECTED RATIOS										CORRECTED AGES (Ma)									
	U[#] (ppm)	Th[#] (ppm)	Th/U	$^{207}Pb/^{206}Pb^{\dagger}$	±1s*	$^{207}Pb/^{235}U^{\dagger}$	±1s*	$^{206}Pb/^{238}U^{\dagger}$	±1s*	$^{208}Pb/^{232}Th^{\dagger}$	±1s*	Rho	% disc**	$^{206}Pb/^{238}U$	±1s*	$^{207}Pb/^{235}U$	±1s*	$^{207}Pb/^{206}Pb$	±1s*	$^{208}Pb/^{232}Th$	±1s*	Best age (Ma)	1s
Sample **TIB-09-25** (Cont.)																							
TIB25-**39**	208	70	0.31	0.0464	0.0018	0.0907	0.0039	0.0142	0.00017	0.0045	0.00021	0.360	-3	91.0	1.0	88.0	4.0	19	80	91.0	4.0	91.0	± 1.0
TIB25-**14**	215	100	0.43	0.0505	0.0016	0.0991	0.0033	0.0142	0.00013	0.0044	0.00011	0.270	5	91.1	0.8	96.0	3.0	220	74	89.0	2.0	91.1	± 0.8
TIB25-**18**	264	171	0.60	0.0539	0.0029	0.1063	0.0060	0.0143	0.00014	0.0045	0.00005	0.200	11	91.6	0.9	103.0	6.0	366	120	90.2	0.9	91.6	± 0.9
TIB25-**17**	264	139	0.49	0.0481	0.0013	0.0952	0.0026	0.0144	0.00013	0.0045	0.00009	0.340	0	92.0	0.8	92.0	2.0	104	60	91.0	2.0	92.0	± 0.8
TIB25-**22**	300	138	0.42	0.0493	0.0011	0.0975	0.0023	0.0144	0.00012	0.0044	0.00009	0.370	2	92.0	0.8	94.0	2.0	163	51	89.0	2.0	92.0	± 0.8
TIB25-**4**	181	64	0.33	0.0496	0.0024	0.0985	0.0054	0.0144	0.00021	0.0046	0.00008	0.450	3	92.0	1.0	95.0	5.0	178	110	92.0	2.0	92.0	± 1.0
TIB25-**6**	180	67	0.34	0.0510	0.0022	0.1015	0.0045	0.0144	0.00014	0.0045	0.00014	0.230	6	92.3	0.9	98.0	4.0	241	98	91.0	3.0	92.3	± 0.9
TIB25-**5**	452	177	0.36	0.0508	0.0017	0.1018	0.0037	0.0145	0.00020	0.0050	0.00012	0.400	5	93.0	1.0	98.0	3.0	229	76	100.0	2.0	93.0	± 1.0
TIB25-**33**	241	72	0.28	0.0497	0.0018	0.1001	0.0039	0.0146	0.00015	0.0046	0.00005	0.310	4	93.5	1.0	97.0	4.0	182	81	93.0	1.0	93.5	± 1.0
TIB25-**30**	710	215	0.28	0.0482	0.0010	0.1044	0.0023	0.0157	0.00014	0.0050	0.00008	0.420	0	100.7	0.9	101.0	2.0	111	47	101.0	2.0	100.7	± 0.9
TIB25-**2**	237	87	0.34	0.0608	0.0022	0.1688	0.0089	0.0202	0.00050	0.0062	0.00015	0.630	18	129.0	3.0	158.0	8.0	631	79	125.0	3.0	129.0	± 3.0
TIB25-**1**	1609	495	0.28	0.0871	0.0010	2.5152	0.0362	0.2096	0.00145	0.0621	0.00042	0.560	4	1227.0	8.0	1276.0	10.0	1362	21	1218.0	8.0	1362.0	± 21.0
n = 31																						**Weighted $^{206}Pb/^{238}U$ mean age =**	**7.03 ± 0.19**
																							MSWD = 2.0; n = 5

[#]U and Th concentrations (ppm) are calculated relative to analyses of trace-element glass standard NIST 612.
[†]Isotopic ratios ratios are corrected relative to PLE standard zircon for mass bias and down-hole fractionation (PLE, Plešovice = ~337 Ma; Sláma *et al.*, 2008). Common Pb corrections were made using the Andersen Method (Andersen, 2002).
[*]All errors in isotopic ratios and ages are absolute and given at the 1-sigma level except for the Weighted Mean $^{206}Pb/^{238}U$ age that is reported at the 2-sigma level.
[**]Percentage discordance obtained using the following equation (100*[(age $^{207}Pb/^{235}U$)-(age $^{206}Pb/^{238}U$)]/age $^{207}Pb/^{235}U$). Positive and negative values indicate normal and inverse discordance, respectively.
Individual zircon ages in bold were used to calculate the weighted mean $^{206}Pb/^{238}U$ age and MSWD (Mean Square of Weigthed Deviates) using the computacional program Isoplot (Ludwig , 2003).

Bibliography

Abbott, P. L., and Smith, T. E., 1989, Sonora, Mexico, Source for the Eocene Poway Conglomerate of Southern California: Geology, v. 17, no. 4, p. 329-332.

Al-Zoubi, A., and ten Brink, U., 2002, Lower crustal flow and the role of shear in basin subsidence: an example from the Dead Sea basin: Earth and Planetary Science Letters, v. 199, p. 67-79.

Andersen, T., 2002, Correction of common lead in U-Pb analyses that do not report Pb-204: Chemical Geology, v. 192, no. 1-2, p. 59-79.

Aragón-Arreola, M., and Martín-Barajas, A., 2006, Rift-to-drift transition in the Gulf of California, in Proceedings Lithospheric Rupture in the Gulf of California-Salton Trough Region - NSF Margins RCL Workshop, Ensenada, Mexico.

Aragón-Arreola, M., and Martín-Barajas, A., 2007, Westward migration of extension in the northern Gulf of California, Mexico: Geology, v. 35, no. 6, p. 571-574.

Aragón-Arreola, M., Morandi, M., Martín-Barajas, A., Deldago-Argote, L., and González-Fernández, A., 2005, Structure of the rift basins in the central Gulf of California: Kinematic implications for oblique rifting: Tectonophysics, v. 409, p. 19-38.

Atwater, T., and Stock, J. M., 1998, Pacific North America plate tectonics of the Neogene southwestern United States: An update: International Geology Review, v. 40, no. 5, p. 375-402.

Axen, G. J., and Fletcher, J. M., 1998, Late Miocene-Pliocene extensional faulting, northern Gulf of California and Salton Trough, California: International Geological Review, v. 40, no. 3, p. 217-244.

Bassi, G., 1995, Relative importance of strain rate and rheology for the mode of continental extension: Geophys. J. Int., v. 122, p. 195-210.

Beck, M. E., 1980, Paleomagnetic record of plate-margin tectonic processes along the western edge of North America: Journal of Geophysical Research, v. 85, p. 7115-7131.

Bennett, S. E. K., 2009, Transtensional Rifting in the Late Proto-Gulf of California Near Bahía Kino, Sonora, México [M.S.]: University of North Carolina-Chapel Hill, 122 p.

Bennett, S. E. K., Oskin, M. E., and Iriondo, A., 2013, Transtensional Rifting in the Proto-Gulf of California, near Bahía Kino, Sonora, México: Geological Society of America Bulletin.

Bialas, R. W., and Buck, W. R., 2009, How sediment promotes narrow rifting: Application to the Gulf of California: Tectonics, v. 28, no. TC4014, doi:10.1029/2008TC002394.

Boehm, M. C., 1984, An overview of the lithostratigraphy, biostratigraphy, and paleoenvironments of the late Neogene San Felipe Marine Sequence, Baja California, Mexico, in Frizzell, V. A., ed., Geology of the Baja California Peninsula, Volume 39: Los Angeles, California, Society of Economic Paleontologists and Mineralogists, Pacific Section, p. 253-265.

Brady, R., Wernicke, B., and Fryxell, J., 2000, Kinematic evolution of a large-offset continental normal fault system, South Virgen Mountains, Nevada: Geological Society of America Bulletin, v. 112, no. 9, p. 1375-1397.

Brothers, D., Harding, A., Gonzalez-Fernandez, A., Holbrook, W. S., Kent, G., Driscoll, N., Fletcher, J., Lizarralde, D., Umhoefer, P., and Axen, G., 2012, Farallon slab detachment and deformation of the Magdalena Shelf, southern Baja California: Geophysical Research Letters, v. 39.

Brune, S., Popov, A., and Sobolev, S. V., 2012, Modeling suggests that oblique extension facilitates rifting and continental break-up: Journal of Geophysical Research, v. 117.

Buck, R. W., 1991, Modes of continental extension: Journal of Geophysical Research, v. 96, p. 20161-20178.

Buck, W. R., Lavier, L. L., Poliakov, A. N. B., Rohr, K., Jackson, J., Chadwick, A., Osmaston, M., Kusznir, N., Brun, J.-P., Roberts, A., and Geli, L., 1999, How to Make a Rift Wide: Philosophical Transactions: Mathematical, Physical and Engineering Sciences, v. 357, no. 1753, p. 671-693.

Busby, C. J., Koerner, A., Hagan, J., and Andrews, G., 2012, Sierra Crest graben: a Miocene Walker Lane Pull-apart in the Ancestral Cascades Arc at Sonora Pass, in Hughes, N., and Hayes, G., eds., Geological Excursions, Sonora Pass Region of the Sierra Nevada, Far Western Section, National Association of Geoscience Teachers field guide, p. 8-36.

Butler, R. L., 1992, Paleomagnetism, Cambridge, MA, Blackwell Scientific Publications, 319 p.:

Carreño, A. L., 1985, Biostratigraphy of the Late Miocene to Pliocene on the Pacific island Maria Madre, Mexico: Micropaleontology, v. 31, no. 2, p. 139-166.

Carreño, A. L., 1992, Neogene microfossils from the Santiago Diatomite, Baja California Sur, Mexico: Paleontología Mexicana, v. 59.

Carreño, A. L., and Smith, J. T., 2007, Stratigraphy and correlation for the ancient Gulf of California and Baja California peninsula, Mexico: Bulletins of American Paleontology, v. 371, p. 146.

Cas, R. A. F., and Wright, J. V., 1987, Volcanic successions, modern and ancient, London, Allen and Unwin, 528 p.:

Cassidy, M., 1990, Marine stratigraphy and paleontology of southwest Isla Tiburón, Gulf of California, Mexico [Master of Science: San Diego State University, 177 p.

Chester, F. M., 1995, A Rheologic Model For Wet Crust Applied to Strike-slip Faults: Journal of Geophysical Research-Solid Earth, v. 100, no. B7, p. 13033-13044.

Christie-Blick, N., and Biddle, K. T., 1985, Deformation and basin formation along strike-slip faults, in Biddle, K. T., and Christie-Blick, N., eds., Strike-slip deformation, Basin Formation, and Sedimentation, Volume SEPM Special Publication, p. 1-34.

Clifton, A. E., and Schlische, R. W., 2001, Nucleation, growth, and linkage of faults in oblique rift zones: Results from experimental clay models and implications for maximum fault size: Geology, v. 29, no. 5, p. 455-458.

Clifton, A. E., Schlische, R. W., Withjack, M. O., and Ackermann, R. V., 2000, Influence of rift obliquity on fault-population systematics: results of experimental clay models: Journal of Structural Geology, v. 22, p. 1491-1509.

Cotton, M. L., and Von der Haar, S., 1980, Microfossils from Cerro Prieto geothermal wells, Baja California, Mexico, in Proceedings Conference: 2. symposium on the Cerro Prieto Geothermal Field, Baja California, Mexico, p. 11.

Darin, M. H., 2011, Late Miocene Extensional Deformation in the Sierra Bacha, coastal Sonora, México: Implications for the Kinematic Evolution of the Proto-Gulf of California [M.S.]: University of Oregon, 95 p.

Dean, M. A., 1996, Neogene Fish Creek Gypsum and associated stratigraphy and paleontology, southwestern Salton Trough, California, in Abbott, P. L., and Seymour, D. C., eds., Sturzstroms and detachment faults, Anza-Borrego Desert State Park, California, Volume 24: San Diego, CA, South Coast Geological Society, p. 123-148.

Delgado-Argote, L. A., López-Martínez, M., and Perrilliat, M. C., 2000, Geologic reconnaissance and age of volcanism and associated fauna from sediments of Bahia de Los Angeles Basin, central Gulf of California, in Stock, J., Aguirre, G., and Delgado, H., eds., Cenozoic tectonics and volcanism of Mexico, Volume 334: Boulder, CO, Geological Society of America, p. 111-121.

Demarest, H. H., 1983, Error analysis for the determination of tectonic rotation from paleomagnetic data: Journal of Geophysical Research, v. 88, p. 4321-4328.

Dorsey, R. J., 2010, Age of Oldest Marine Deposits in the Northern Gulf of California and Salton Trough, in Proceedings CRevolution 2—Origin and evolution of the Colorado River system.

Dorsey, R. J., and Burns, B., 1994, Regional stratigraphy, sedimentology, and tectonic significance of Oligocene-Miocene sedimentary and volcanic rocks, northern Baja California, Mexico: Sedimentary Geology, v. 88, p. 231-251.

Dorsey, R. J., Fluette, A., McDougall, K., Housen, B. A., Janecke, S. U., Axen, G. J., and Shirvell, C. R., 2007, Chronology of Miocene-Pliocene deposits at Split Mountain Gorge, Southern California: A record of regional tectonics and Colorado River evolution: Geology, v. 35, no. 1, p. 57-60.

Dorsey, R. J., Housen, B. A., Janecke, S. U., Fanning, C. M., and Spears, A. L. F., 2011, Stratigraphic record of basin development within the San Andreas fault system: Late Cenozoic Fish Creek-Vallecito basin, southern California: Geological Society of America Bulletin, v. 123, no. 5-6, p. 771-793.

Dorsey, R. J., Umhoefer, P. J., and Renne, P. R., 1995, Rapid subsidence and stacked Gilbert-type fan deltas, Pliocene Loreto basin, Baja California Sur, Mexico: Sedimentary Geology, v. 98, no. 1–4, p. 181-204.

Eberly, L. D., and Stanley, T. B. j., 1978, Cenozoic stratigraphy and geologic history of southwestern Arizona: Geological Society of America Bulletin, v. 89, p. 921-940.

England, P., 1983, Constraints on extension of continental lithosphere: Journal of Geophysical Research, v. 88, p. 1145-1152.

Escalona-Alcázar, F. J., and Delgado-Argote, L. A., 2001, Estudio de la deformación en las islas San Lorenzo Y Las Animas, Golfo de California: Implicaciones sobre su desplazamiento como bloque Rígido desde el Pliocene Tardio: Geos, v. 20, no. 1, p. 8-20.

Farr, T. G., Rosen, P. A., Caro, E., Crippen, R., Duren, R., Hensley, S., Kobrick, M., Paller, M., Rodriguez, E., Roth, L., Seal, D., Shaffer, S., Shimada, J., Umland, J., Werner, M., Oskin, M., Burbank, D., and Alsdorf, D., 2007, The shuttle radar topography mission: Reviews of Geophysics, v. 45, no. 2.

Faulds, J. E., Henry, C. D., and Hinz, N. H., 2005, Kinematics of the northern Walker Lane: An incipient transform fault along the Pacific-North American plate boundary: Geology, v. 33, no. 6, p. 505-508.

Fenby, S. S., and Gastil, R. G., 1991, Geologic-Tectonic Map of the Gulf of California and Surrounding Areas, in Dauphin, J. P., and Simoneit, B. R. T., eds., AAPG Memoir 47: The Gulf and Peninsular Province of the Californias, Volume 47, p. 79-83.

Ferrari, L., Lopez-Martinez, M., Aguirre-Diaz, G., and Carrasco-Nunez, G., 1999, Space-time patterns of Cenozoic arc volcanism in central Mexico: From the Sierra Madre Occidental to the Mexican Volcanic Belt: Geology, v. 27, no. 4, p. 303-306.

Fisher, S. R., 1953, Dispersion on a Sphere: Proceedings of the Royal Society of London. Series A, Mathematical and Physical Sciences, v. 217, no. 1130, p. 295-305.

Fletcher, J. M., Grove, M., Kimbrough, D., Lovera, O., and Gehrels, G. E., 2007, Ridge-trench interactions and the Neogene tectonic evolution of the Magdalena shelf and southern Gulf of California: Insights from detrital zircon U-Pb ages from the Magdalena fan and adjacent areas: Geological Society of America Bulletin, v. 119, no. 11/12, p. 1313-1336.

Forsyth, D. W., 1992, Finite extension and low-angle normal faulting: Geology, v. 20, p. 27-30.

Gans, P. B., 1997, Large-magnitude Oligo-Miocene extension in southern Sonora: Implications for the tectonic evolution of northwest Mexico: Tectonics, v. 16, no. 3, p. 388-408.

Gastil, R. G., and Fenby, S. S., 1991, Detachment faulting as a mechanism for tectonically filling the Gulf of California during dilation, in Dauphin, J. P., and Simoneit, B. R. T., eds., AAPG Memoir 47: The Gulf and Peninsular Province of the Californias, Volume 47, p. 371-375.

Gastil, R. G., and Krummenacher, D., 1977a, Reconnaissance geologic map of coastal Sonora between Puerto Lobos and Bahia Kino, GSA Map and Chart Series MC-16: Geological Society of America, scale 1:150,000.

Gastil, R. G., and Krummenacher, D., 1977b, Reconnaissance geology of coastal Sonora between Puerto Lobos and Bahia Kino: Geological Society of America Bulletin, v. 88, no. 2, p. 189-198.

Gastil, R. G., and Krummenacher, D., 1978, A reconnaissance geologic map of the west-central part of the state of Nayarit, Mexico: GSA Map and Chart Series MC-24, scale 1:200,000, scale 1:200,000.

Gastil, R. G., Lemone, D. V., and Stewart, W. J., 1973, Permian Fusulinids from near San Felipe, Baja California: American Association of Petroleum Geologists Bulletin, v. 57, no. 4, p. 746-747.

Gastil, R. G., Neuhaus, J., Cassidy, M., Smith, J. T., Ingle, J. C., and Krummenacher, D., 1999, Geology and paleontology of southwestern Isla Tiburón, Sonora, Mexico: Revista Mexicana de Ciencias Geologicas, v. 16, no. 1, p. 1-34.

Gilbert, G. K., 1885, The topographic features of lake shores, U. S. Geological Survey, Annual Report, 5th (1883-1884), p. 69-123.

Gómez-Ponce, M., 1971, Sobre la presencia de estratos marinos del Mioceno en el estado de Sonora, Mexico: Revista del Instituto Mexicano del Petroleo, v. 3, no. 4, p. 77-78.

Gómez-Valencia, A. M., and Vidal-Solano, J., 2010, Reconocimiento Septentrional del Gran Depósito Ignimbrítico Hiperalcalino del Mioceno Medio en el NW de México: Geoquímica y Petrografía de una Facie Distal en la Región de Ráyon, Sonora, in Proceedings Reunión Anual, Unión Geofísica Mexicana, Volume 30.

González-Fernández , A., Danobeitia, J. J., Deldago-Argote, L., Michaud, F., Cordoba, D., and Bartolome, R., 2005, Mode of extension and rifting history of upper Tiburon and upper Delfin basins, northern Gulf of California: Journal of Geophysical Research, v. 110, p. 1-17.

Gonzalez-Leon, C. M., Valencia, V. A., Lopez-Martinez, M., Bellon, H., Valencia-Moreno, M., and Calmus, T., 2010, Arizpe sub-basin: A sedimentary and volcanic record of Basin and Range extension in north-central Sonora, Mexico: Revista Mexicana de Ciencias Geologicas, v. 27, no. 2, p. 292-312.

Goudie, A. S., and Sperling, C. H. B., 1977, Long distance transport of foraminiferal tests by wind in the Thar Desert, northwest India: Journal of Sedimentary Petrology, v. 47, no. 2, p. 630-633.

Hamilton, W., 1961, Origin of the Gulf of California: Geological Society of America Bulletin, v. 72, no. 9, p. 1307-1318.

Hausback, B. P., 1984, Cenozoic volcanic and tectonic evolution of Baja California Sur, Mexico, in Frizzell, V. A., Jr., ed., Geology of the Baja California Peninsula, Volume 39: Los Angeles, California, Pacific Section of the Economic Paleontologists and Mineralogists, p. 219-236.

Helenes, J., and Carreño, A. L., 1999, Neogene sedimentary evolution of Baja California in relation to regional tectonics: Journal of South American Earth Sciences, v. 12, p. 589-605.

Helenes, J., Carreño, A. L., and Carillo, R. M., 2009, Middle to late Miocene chronostratigraphy and development of the northern Gulf of California: Marine Micropaleontology, v. 72, p. 10-25.

Henry, C., and Faulds, J., 2006, The Walker Lane and Gulf of California: Related Expressions of Pacific-North America Plate Boundary Development, in Proceedings RCL-Cortez Workshop: Lithospheric Rupture in the Gulf of California-Salton Trough Region, Ensenada, Mexico.

Henry, C. D., and Aranda Gomez, J. J., 1992, The real southern basin and range: Mid Cenozoic to Late Cenozoic extension in Mexico: Geology, v. 20, no. 8, p. 701-704.

Herman, S. W., and Gans, P., 2006, A paleomagnetic investigation of large scale vertical axis rotations in coastal Sonora: evidence for transtensional proto-Gulf deformation: Geological Society of America Abstracts with Programs, v. 38, no. 7, p. 311.

Hernández-Méndez, G. L., Stock, J., Vidal-Solano, J., and Paz-Moreno, F. A., 2008, Paleomagnetic Constraints on the Extent of the Miocene Tuff of San Felipe/Tuff of Hermosillo, Sonora, Mexico, in Proceedings Geological Society of America Annual Meeting, Denver, CO.

Holt, J. W., Stock, J. M., and Holt, E. W., 2000, An age constraint on Gulf of California rifting from the Santa Rosalía basin, Baja California Sur, Mexico: GSA Bulletin, v. 112, no. 4, p. 540-549.

Hopper, J. R., and Buck, W. R., 1996, The effect of lower crustal flow on continental extension and passive margin formation: Journal of Geophysical Research, v. 101, no. B9, p. 20,175-120,194.

Huismans, R. S., and Beaumont, C., 2003, Symmetric and asymmetric lithospheric extension: Relative effects of frictional-plastic and viscous strain softening: Journal of Geophysical Research, v. 108, no. B10.

Huismans, R. S., and Beaumont, C., 2011, Depth-dependent extension, two-stage breakup and cratonic underplating at rifted margins: Nature, v. 473.

Ingersoll, R. V., 1988, Tectonics of sedimentary basins: Geological Society of America Bulletin, v. 100, no. 11, p. 1704-1719.

Jackson, J. A., and White, N. J., 1989, Normal faulting in the upper continental crust: observations from regions of active extension: Journal of Structural Geology, v. 11, no. 1-2, p. 15-&.

Jones, C. H., 2002, User-driven Integrated Software Lives: "PaleoMag" Paleomagnetics Analysis on the Macintosh: Computers and Geosciences, v. 28, no. 10, p. 1145-1151.

Karig, D. E., and Jensky, W., 1972, The Proto-gulf of California: Earth and Planetary Science Letters, v. 17, p. 169-174.

Kaus, B. J. P., and Podladchikov, Y. Y., 2006, Initiation of localized shear zones in viscoelastoplastic rocks: Journal of Geophysical Research, v. 111, no. B04412.

Keogh, M., 2010, Stratigraphic Analysis of Late Miocene to Early Pliocene (?) Sedimentary Rocks, SW Isla Tiburón, Sonora, Mexico [B.S.]: University of Oregon, 76 p.

Kirschvink, J. L., 1980, The least-squares line and plane and the analysis of paleomagnetic data: Geophys. J. R. Astron. Soc., v. 62, p. 699-718.

Kluesner, J. W., 2011, Marine Geophysical Study of Cyclic Sedimentation and Shallow Sill Intrusion in the Floor of the Central Gulf of California [PhD]: University of California, San Diego, 213 p.

Kohn, B. P., Fletcher, J., Grove, M., Lovera, O., Gleadow, A. J. W., and Foster, D. A., 2010, Cenozoic basement evolution and the timing of continental rifting, southern Gulf Extensional Province, Baja California Peninsula, Mexico: evidence from integrated thermochronology, in Proceedings Thermo2010 - 12th International Conference on Thermochronology, Glasgow, Scotland, p. 221-221.

Kusznir, N. J., and Park, R. G., 1987, The extensional strength of the continental lithosphere: its dependence on geothermal gradient, and crustal composition and thickness, in Coward, M. P., Dewey, J. F., and Hancock, P. L., eds., Continental Extension Tectonics, Volume Special Publication No 28, Geological Society.

Larson, R. L., Menard, H. W., and Smith, S. M., 1968, Gulf of California: a result of ocean floor spreading and transform faulting: Science, v. 161, p. 781-784.

Lavier, L. L., and Manatschal, G., 2006, A mechanism to thin the continental lithosphere at magma-poor margins: Nature, v. 440, p. 324-328.

Lavier, L. L., and Steckler, M. S., 1997, The effect of sedimentary cover on flexural strength of continental lithosphere: Nature, v. 389, p. 476-479.

Lee, J., Miller, M., Crippen, R., Hacker, B., and Ledesma-Vazquez, J., 1996, Middle Miocene extension in the Gulf extensional province, Baja California: Evidence from the southern Sierra Juárez: GSA Bulletin, v. 108, no. 5, p. 505-525.

Leloup, P. H., Ricard, Y., Battaglia, J., and Lacassin, R., 1999, Shear heating in continental strike-slip shear zones: model and field examples: Geophysical Journal International, v. 136, no. 1, p. 19-40.

Lewis, C. J., 1996, Stratigraphy and geochronology of Miocene and Pliocene volcanic rocks in the Sierra San Fermín and southern Sierra San Felipe, Baja California, Mexico: Geofisica Internacional, v. 35, p. 1-31.

Lewis, C. J., and Stock, J. M., 1998a, Paleomagnetic evidence of localized vertical-axis rotation during Neogene extension of the Sierra San Fermín, northeastern Baja California, Mexico: JGR, v. 103, p. 2455-2470.

Lewis, C. J., and Stock, J. M., 1998b, Late Miocene to recent transtensional tectonics in the Sierra San Fermín, northeastern Baja California, Mexico: J. Structural Geology, v. 20, p. 1043-1063.

Lizarralde, D., Axen, G. J., Brown, H. E., Fletcher, J. M., González-Fernández, A., Harding, A. J., Holbrook, W. S., Kent, G. M., Paramo, P., Sutherland, F., and Umhoefer, P. J., 2007, Variation in styles of rifting in the Gulf of California: Nature, v. 448, p. 466-469.

Lonsdale, P., 1989, Geology and tectonic history of the Gulf of California, in Winterer, E. L., Hussong, D. M., and Decker, R. W., eds., The Eastern Pacific Ocean and Hawaii, Geology of North America, Volume N: Boulder, CO, Geological Society of America, p. 499-521.

Louden, K. E., and Chian, D., 1999, The deep structure of non-volcanic rifted continental margins: Philosophical Transactions of the Royal Society of London, v. 357, p. 767-804.

Lourens, L., Hilgen, F., Shackleton, N. J., Laskar, J., and Wilson, D., 2004, The Neogene Period, in Gradstein, F. M., Ogg, J. G., and Smith, A. G., eds., A Geologic Time Scale 2004.

Ludwig, K. R., 2003, Mathematical-statistical treatment of data and errors for Th-230/U geochronology: Uranium-Series Geochemistry, v. 52, p. 631-656.

Lugo-Zazueta, R. E., Kohn, B. P., Gleadow, A. J. W., Calmus, T., Ramos-Velázquez, E., and Fletcher, J., 2010, Low temperature thermochronology of the eastern Gulf of California: a sheared continental margin, Sonora, Mexico, in Proceedings Thermo2010 - 12th International Conference on Thermochronology, Glasgow, Scotland, p. 137-137.

Mar-Hernández, E., González-Escobar, M., and Martín-Barajas, A., 2012, Tectonic framework of Tiburon Basin, Gulf of California, from seismic reflection evidence: International Geology Review, v. 54, no. 11, p. 1271-1283.

Martín-Barajas, A., González-Escobar, M., Fletcher, J. M., Pacheco, M., and Mar-Hernández, E., 2010, Continental Rupture Controlled by Low-Angle Normal Faults in the Northern Gulf of California: Analysis of Seismic Reflection Profiles, in Proceedings AGU Fall Meeting, San Francisco.

Martín-Barajas, A., Tellez-Duarte, M., and Stock, J. M., 1997, The Puertecitos Formation: Pliocene volcaniclastic sedimentation along an accommodation zone in northeastern Baja California, in Johnson, M. E., and Ledesma-Vasquez, J., eds., Pliocene Carbonate and Related Facies Flanking the Gulf of California, Baja California, Mexico: Geological Society of America Special Paper 318, Geological Society of America, p. 1-24.

Martin-Barajas, A., Vazquez-Hernandez, S., Carreno, A. L., Helenes, J., Suarez-Vidal, F., and Alvarez-Rosales, J., 2001, Late Neogene stratigraphy and tectonic control on facies evolution in the Laguna Salada Basin, northern Baja California, Mexico: Sedimentary Geology, v. 144, no. 1-2, p. 5-35.

McCloy, C., Ingle, J. C., and Barron, J. A., 1988, Neogene stratigraphy, foraminifera, diatoms, and depositional history of Maria Madre Island, Mexico: Evidence of early Neogene marine conditions in the southern Gulf of California: Marine Micropaleontology, v. 13, no. 3, p. 193-212.

McDougall, K., 2008, Late Neogene marine incursion and the ancestral Gulf of California, in Reheis, M., Herschler, R., and Miller, D., eds., Late Cenozoic Drainage History of the Southwestern Great Basin and Lower Colorado River Region: Geologic and Biotic Perspectives, Volume 439: Geological Society of America Special Paper, p. 355-373.

McDougall, K., Poore, R. Z., and Matti, J. C., 1999, Age and environment of the Imperial Formation near San Gorgonio Pass, California: Journal of Foraminiferal Research, v. 29, no. 1, p. 4-25.

Miller, N. C., and Lizarralde, D., 2013, Thick evaporites and early rifting in the Guaymas Basin, Gulf of California: Geology, v. 41, no. 2, p. 283-286.

Molina-Cruz, A., 1994, Biostratigraphy and paleoceanographic significance of the radiolarians from the protomouth of the Gulf of California: Ciencias Marinas, v. 20, no. 4, p. 441-465.

Nagy, E. A., 2000, Extensional deformation and paleomagnetism at the western margin of the Gulf Extensional Province, Puertecitos Volcanic Province, northeastern Baja California, Mexico: GSA Bulletin, v. 112, no. 6, p. 857-870.

Nagy, E. A., Grove, M., and Stock, J. M., 1999, Age and stratigraphic relationships of pre- and syn-rift volcanic deposits in the northern Puertecitos Volcanic Province, Baja California, Mexico: Journal of Volcanology and Geothermal Research, v. 93, p. 1-30.

Nagy, E. A., and Stock, J. M., 2000, Structural controls on the continent-ocean transition in the northern Gulf of California: Journal of Geophysical Research, v. 105, no. B7, p. 16,251-216,269.

Neuhaus, J., 1989, Volcanic and nonmarine stratigraphy of southwest Isla Tiburón, Gulf of California, Mexico [Master of Science: San Diego State University, 170 p.

Nicholson, C., Sorlien, C. C., Atwater, T., Crowell, J. C., and Luyendyk, B. P., 1994, Microplate capture, rotation of the western Transverse Ranges, and initiation of the San Andreas transform as a low-angle fault system: Geology, v. 22, p. 491-495.

Olguín-Villa, A. E., 2010, Estudio Físico y Químico del Volcanismo Hiperalcalino en la Región de Cataviña, Baja California [B.S.]: Universidad de Sonora, 87 p.

Onstott, T. C., 1980, Application of the Bingham distribution function in paleomagnetic studies: Journal of Geophysical Research, v. 85, p. 1500-1510.

Ortlieb, L., 1991, Quaternary vertical movements along the coasts of Baja California and Sonora, in Dauphin, J. P., and Simoneit, B. R. T., eds., The Gulf and Peninsular Province of the Californias, Volume 47: Tulsa, Oklahoma, The American Association of Petroleum Geologists, p. 447-480.

Oskin, M., 2002, Tectonic Evolution of The Northern Gulf of California, Mexico, Deduced from Conjugate Rifted Margins of the Upper Delfín Basin [Ph.D.]: California Institute of Technology, 481 p.

Oskin, M., and Martín-Barajas, A., 2003, Continental edge tectonics of Isla Tiburón, Sonora Mexico, in Alcayde, M., and Caballero, A. G., eds., Geological Transects Across Cordilleran Mexico, Volume 1: Mexico, D.F., Universidad Nacional Autónoma de México, p. 53-70.

Oskin, M., Stock, J., and Martín-Barajas, A., 2001, Rapid localization of Pacific-North America plate motion in the Gulf of California: Geology, v. 29, no. 5, p. 459-462.

Oskin, M., and Stock, J. M., 2003a, Marine incursion synchronous with plate-boundary localization in the Gulf of California: Geology, v. 31, p. 23-26.

Oskin, M., and Stock, J. M., 2003b, Pacific-North America plate motion and opening of the Upper Delfín basin, northern Gulf of California: Geological Society of America Bulletin, v. 115, p. 1173–1190.

Otvos, E. G., and Bock, W. D., 1976, Massive long-distance transport and redeposition of Upper Cretaceous planktonic foraminifers in Quaternary sediments: Journal of Sedimentary Petrology, v. 46, no. 4, p. 978-984.

Pacheco, M., Martín-Barajas, A., Elders, W., Espinosa-Cardena, J. M., Helenes, J., and Segura, A., 2006, Stratigraphy and structure of the Altar basin of NW Sonora: Implications for the history of the Colorado River delta and the Salton trough: Revista Mexicana de Ciencias Geologicas, v. 23, no. 1, p. 22.

PEMEX, 1985, Proyecto de inversión San Felipe. estudio de evaluación de cuencas, prospecto San Felipe.

Perch-Nielsen, K., 1985, Cenozoic calcareous nannofossils, in Bolli, H. M., Saunders, J. B., and Perch-Nielsen, K., eds., Plankton Stratigraphy: Cambridge Earth Sciences Series, Cambridge University Press, p. 427–554.

Ramos-Velázquez, E., Calmus, T., Valencia, V., Iriondo, A., Valencia-Moreno, M., and Bellon6, H., 2008, U-Pb and 40Ar/39Ar geochronology of the coastal Sonora batholith: New insights on Laramide continental arc magmatism: Revista Mexicana de Ciencias Geológicas, v. 25, no. 2, p. 314-333.

Schaaf, P., Roldan-Quintana, J., and Calmus, T., 1999,Terrane Reconnaissance in NE Sonora, Mexico, in the Light of Sr-Nd-Pb Isotopic Data From Coastal Belt Granitoids, in Proceedings AGU Fall Meeting.

Seiler, C., Fletcher, J., Kohn, B. P., Gleadow, A. J. W., and Raza, A., 2011, Low-temperature thermochronology of northern Baja California, Mexico: Decoupled slip-exhumation

gradients and delayed onset of oblique rifting across the Gulf of California: Tectonics, v. 30, no. TC3004.

Seiler, C., Fletcher, J. M., Quigley, M. C., Gleadow, A. J. W., and Kohn, B. P., 2010, Neogene structural evolution of the Sierra San Felipe, Baja California: Evidence for proto-Gulf transtension in the Gulf Extensional Province?: Tectonophysics, v. 488, p. 87-109.

Simon, J. I., Renne, P. R., and Mundil, R., 2008, Implications of pre-eruptive magmatic histories of zircons for U-Pb geochronology of silicic extrusions: Earth and Planetary Science Letters, v. 266, no. 1-2, p. 182-194.

Skinner, S., Stock, J., and Martín-Barajas, A., 2012, Characterization of the Tuff of San Felipe on Isla Angel de la Guarda, Baja California, Mexico, in Proceedings Geological Society of America, Cordilleran Section Meeting, Queretaro, Mexico.

Slama, J., Kosler, J., Condon, D. J., Crowley, J. L., Gerdes, A., Hanchar, J. M., Horstwood, M. S. A., Morris, G. A., Nasdala, L., Norberg, N., Schaltegger, U., Schoene, B., Tubrett, M. N., and Whitehouse, M. J., 2008, Plesovice zircon - A new natural reference material for U-Pb and Hf isotopic microanalysis: Chemical Geology, v. 249, no. 1-2, p. 1-35.

Smith, J. T., 1991, Cenozoic marine mollusks and paleogeography of the Gulf of California, in Dauphin, J. P., and Simoneit, B. R. T., eds., The Gulf and Peninsular Province of the Californias: American Association of Petroleum Geologists Memoir 47, Volume 47: Tulsa, Oklahoma, American Association of Petroleum Geologists, p. 637-666.

Smith, J. T., (personal communication to Oskin, M.) Color field photograph of monomict volcanic breccia intercalated with marine rocks, collected in Arroyo 3 on southwest Isla Tiburón (reported in Smith et al., 1985).

Smith, J. T., Smith, J. G., Ingle, J. C. J., Gastil, R. G., Boehm, M. C., Roldan, Q. J., and Casey, R. E., 1985, Fossil and K-Ar age constraints on upper middle Miocene conglomerate, SW Isla Tiburón, Gulf of California, in Proceedings Geological Society of America, Cordilleran Section, 81st annual meeting, Vancouver, British Columbia, Volume 17, p. 409.

Stock, J., Martín-Barajas, A., Martinez-Lopez, M., and Chapman, A., 2008, Net slip across the Ballenas Transform fault measured from offset ignimbrite deposits, AGU Fall Meeting.

Stock, J., Paz-Moreno, F. A., Martin, K., and Lin, D., 2006, The 12.5 Ma Tuff of San Felipe: a major structural marker horizon in northwestern Mexico, in Proceedings Lithospheric Rupture in the Gulf of California-Salton Trough Region - NSF Margins RCL Workshop, Ensenada, Mexico.

Stock, J. M., 1989, Sequence and geochronology of Miocene rocks adjacent to the main gulf escarpment: Southern Valle Chico, Baja California Norte, Mexico: Geofisica Internacional, v. 28, no. 5, p. 851-896.

Stock, J. M., 1997, Age and source of pumice lapilli within the San Felipe marine sequence, northeast Baja California: International meeting on the Geology of the Baja California Peninsula, Ensenada, Baja California Norte, April 6-9, 1997.

Stock, J. M., 2000, Relation of the Puertecitos Volcanic Province, Baja California, to development of the plate boundary in the Gulf of California, in Delgado-Granados, H., Aguirre-Diaz, G., and Stock, J. M., eds., Cenozoic Tectonics and Volcanism of Mexico, Geological Society of America Special Paper 334: Boulder, Colorado, Geological Society of America, p. 143-155.

Stock, J. M., and Hodges, K. V., 1989, Pre-Pliocene extension around the Gulf of California and the transfer of Baja California to the Pacific Plate: Tectonics, v. 8, no. 1, p. 99-115.

Stock, J. M., and Hodges, K. V., 1990, Miocene to Recent structural development of an extensional accommodation zone, northeastern Baja California, Mexico: Journal of Structural Geology, v. 12, no. 3, p. 315-328.

Stock, J. M., Lewis, C. J., and Nagy, E. A., 1999, The Tuff of San Felipe: an extensive middle Miocene pyroclastic flow deposit in Baja California, Mexico: Journal of Volcanology and Geothermal Research, v. 93, p. 53-74.

Stock, J. M., and Molnar, P., 1988, Uncertainties and implications of the Late Cretaceous and Tertiary position of North America relative to the Farallon, Kula, and Pacific plates: Tectonics, v. 7, no. 6, p. 1339-1384.

Stump, T. E., 1979, The Evolutionary Biogeography of the West Mexican Pectinidae (Mollusca: Bivalvia) [PhD]: San Diego State University, 520 p.

Sutherland, F. H., Kent, G. M., Harding, A. J., Umhoefer, P. J., Driscoll, N. W., Lizarralde, D., Fletcher, J. M., Axen, G. J., Holbrook, W. S., González-Fernández , A., and Lonsdale, P., 2012, Middle Miocene to early Pliocene oblique extension in the southern Gulf of California: Geosphere, v. 8, no. 4, p. 752-770.

Tucholke, B. E., Lin, J., and Kleinrock, M. C., 1998, Megamullions and mullion structure defining oceanic metamorphic core complexes on the mid-Atlantic ridge: Journal of Geophysical Research-Solid Earth, v. 103, no. B5, p. 9857-9866.

Umhoefer, P. J., 2011, Why did the Southern Gulf of California rupture so rapidly?—Oblique divergence across hot, weak lithosphere along a tectonically active margin: GSA Today, p. 4-10.

Umhoefer, P. J., Dorsey, R. J., Willsey, S., Mayer, L., and Renne, P., 2001, Stratigraphy and geochronology of the Comondú Group near Loreto, Baja California Sur, Mexico: Sedimentary Geology, v. 144, p. 125-147.

Unruh, J., Humphrey, J., and Barron, A., 2003, Transtensional model for the Sierra Nevada frontal fault system, eastern California: Geology, v. 31, no. 4, p. 327-330.

Valencia-Moreno, M., Ruiz, J., Ochoa-Landín, L., Martínez-Serrano, R., and Vargas-Navarro, P., 2003, Geochemistry of the Coastal Sonora batholith, Northwestern Mexico: Can. J. Earth Sci., v. 40, p. 819-831.

van Wijk, J., Adams, D. A., and Murphy, M. A., 2011, Pull-apart basin evolution: insights from numerical models, in Proceedings AGU Fall Meeting.

van Wijk, J. W., 2005, Role of weak zone orientation in continental lithosphere extension: Geophysical Research Letters, v. 32, no. 2.

van Wijk, J. W., 2007, Numerical Models of Oblique Rifting: Application to the Gulf of California, in Proceedings AGU Spring Meeting.

Vidal-Solano, J., Lozano Santa Cruz, R., Zamora, M. O., and Mendoza-Cordova, A., 2010, Correlación geoquímica e implicaciones tectónicas de la Ignimbrita Hiperalcalina ampliamente distribuida en el NW de México: WD-FRX en secciones de roca, in Proceedings Actas INAGEQ, XX Congreso Nacional de Geoquímica, Temixco, Morelos, México, Volume 16.

Vidal-Solano, J., Moreno, F. A. P., Alexander Iriondo c, d., Demant, A., and Cochemé, J.-J., 2005, Middle Miocene peralkaline ignimbrites in the Hermosillo region (Sonora, Mexico): Geodynamic implications: C.R. Geoscience, v. 337, p. 1421-1430.

Wang, Y., Forsyth, D. W., and Savage, B., 2009, Convective upwelling in the mantle beneath the Gulf of California: Nature, v. 462.

Wells, R. E., and Hillhouse, J. W., 1989, Paleomagnetism and tectonic rotation of the lower Miocene Peach Springs Tuff: Colorado Plateau, Arizona, to Barstow, California: Geological Society of America Bulletin, v. 101, p. 846-863.

Wilson, D., McCrory, P., and Stanley, R., 2005, Implications of volcanism in coastal California for the Neogene deformation history of western North America: Tectonics, v. 24.

Winker, C. D., 1987, Neogene Stratigraphy of the Fish Creek–Vallecito Section, Southern California: Implications for Early History of the Northern Gulf of California and Colorado Delta [PhD]: University of Arizona, 494 p.

Withjack, M. O., and Jamison, W. R., 1986, Deformation produced by oblique rifting: Tectonophysics, v. 126, p. 99-124.

Xie, X., and Heller, P. L., 2009, Plate tectonics and basin subsidence history: Geological Society of America Bulletin, v. 121, no. 1-2, p. 55-64.